Metasurface Technology for Electromagnetic Medical Devices

Razzicchia, Eleonora

Awarding institution:
King's College London

KING'S COLLEGE LONDON

DOCTORAL THESIS

Metasurface Technology for Electromagnetic Medical Devices

Author:
Eleonora RAZZICCHIA

Supervisors:
Dr. Panagiotis KOSMAS and
Dr. Efthymios KALLOS

A thesis submitted in fulfilment of the requirements
for the degree of Doctor of Philosophy
in the

Microwave Imaging Group
Department of Engineering
Faculty of Natural and Mathematical Sciences

July 4, 2023

Declaration of Authorship

I, Eleonora RAZZICCHIA, declare that this thesis titled, "Metasurface Technology for Electromagnetic Medical Devices" and the work presented in it are my own. I confirm that:

- This work was done wholly or mainly while in candidature for a research degree at this University.
- Where any part of this thesis has previously been submitted for a degree or any other qualification at this University or any other institution, this has been clearly stated.
- Where I have consulted the published work of others, this is always clearly attributed.
- Where I have quoted from the work of others, the source is always given. With the exception of such quotations, this thesis is entirely my own work.
- I have acknowledged all main sources of help.
- Where the thesis is based on work done by myself jointly with others, I have made clear exactly what was done by others and what I have contributed myself.

Signed: Eleonora Razzicchia

Date: 04/07/2023

Abstract

Eleonora RAZZICCHIA

Metasurface Technology for Electromagnetic Medical Devices

Over the last two decades, metamaterials and metasurfaces have been used to fabricate innovative antenna designs, offering advanced and cost-effective solutions compared to conventional radiating systems. This thesis investigates the feasibility of combining metasurface design concepts and imaging techniques to create innovative microwave imaging systems.

Microwave imaging is a valid alternative to the current imaging techniques because it is non-invasive and uses non-ionising radiation. Furthermore, it can be a portable and ergonomic technology. Stroke detection and differentiation is one of the most promising microwave imaging applications and has drawn the interest of many groups worldwide. Stroke is a neurological disorder which occurs when blood supply to a part of the brain is interrupted or reduced (ischemic stroke), or when a blood vessel breaks and bleeds into the brain (hemorrhagic stroke). Stroke is a medical emergency and prompt treatment is crucial. Thus, patients' survival depends on a quick diagnosis through the use of an efficient imaging method. Therefore, there is increasing interest in developing new diagnostic tools, such as microwave brain imaging scanners, to supplement the current imaging modalities. Developing these devices requires designing systems with increasing number of sensors (i.e., antennas). Using advanced materials can not only improve the characteristics of these antennas, but also enhance detection by tackling the impedance mismatch problem that electromagnetic waves encounter when probing human tissue.

This research work presents an approach to enhance the hardware of a custom-made brain imaging scanner with an innovative metasurface film based on a Jerusalem cross resonator. This metasurface design has been tested through full-wave simulations and experiments, using several setups and antenna types. The results presented in this thesis suggest that the proposed metasurface enhances the "weak" signal scattered by a stroke-mimicking target placed in a brain phantom volume. This translates into more accurate tomographic and radar image reconstructions. As a further analysis, the feasibility of developing a more compact and ergonomic microwave brain

imaging scanner was investigated. To this end, a new array based on metasurface-enhanced antennas was proposed. Even in this case, the results suggest that the metasurface antenna loading increases the signal difference due to the presence of a stroke-mimicking target and improves the quality of the reconstructed images. The last part of this thesis is focused on other clinical applications of metasurface technology, including cerebrovascular imaging, breast cancer detection, hyperthermia monitoring and microwave thermal ablation monitoring.

All the metasurface designs proposed in this thesis are tailored to fulfil specific requirements and achieve the desired goals (e.g., impedance-matching, improved field penetration into the human tissue, enhanced antenna designs), depending on the microwave imaging prototype and its application. In conclusion, this research work suggests that incorporating metasurface structures into the hardware of microwave imaging systems might lead towards the development of innovative, compact and ergonomic medical devices with the desired clinical accuracy.

Acknowledgements

Firstly, I would like to express my sincere gratitude to my first supervisor Prof. Panagiotis Kosmas for his continuous support during my Ph.D and related research, but also for his patience, motivation, and immense knowledge. I could not have imagined a better mentor. Beside my first advisor, I would like to thank Dr. Efthymios Kallos for his insightful comments and encouragement, but also for the hard questions which led me to widen my research from various perspectives. The guidance of both my supervisors has helped me from the first day of research to the submission of this thesis. My sincere thanks also goes to my lab colleagues for the stimulating discussions, for the hard times we have been working together before deadlines, and for all the fun we have had in the last three years. Above all, I would like to acknowledge Pan Lu, Olympia Karadima and Navid Ghavami, for providing all the reconstruction images presented in the thesis. I am equally grateful to my colleagues Syed Ahsan and Wei Guo, who designed and tested the monopole antennas used in many of my experiments. A big thanks also goes to Ioannis Sotiriou, who helped me plan my lab work. Besides my co-workers, I want to thank all the EMERALD consortium. This work would not have been possible without the strong collaboration of all the groups involved in this network. Last but not the least, I would like to thank my grandmother, my parents, and my brothers, for supporting me spiritually throughout this journey and my life in general.

Contents

List of Figures

List of Tables

List of Abbreviations

2D	Two-Dimensional
3D	Three-Dimensional
ABS	Acrylonitrile Butadiene Styrene
AVA	Antipodal Vivaldi Antenna
CBF	Cerebral Blood Flow
CNR	National Research Council of Italy
CSF	Cerebrospinal Fluid
CT	Computed Tomography
CVA	Cerebrovascular
DBIM	Distorted Born Iterative Method
DNG	Double-Negative
DPS	Double-Positive
DS-SRR	Double-Square Split-Ring Resonator
EDTA	Ethylenediaminetetraacetic Acid
EM	Electromagnetic
EMA	Effective Medium Approximation
EMERALD	ElectroMagnetic imaging for a novel genERation of medicAL Devices
EMT	Effective Medium Theory
FEM	Finite Element Method
FDTD	Finite Difference Time Domain
FIT	Finite Integration Technique
HP	Huygens Principle
ICH	Intra-cerebral Haemorrhage (or Intracranial Haemorrhage)
IREA	Institute for the Electromagnetic Sensing of the Environment
IV	Intravenous
KCL	King's College London
LHM	Left-Handed Materials
MM	Metamaterial
MIMO	Multiple-Input Multiple-Output
MTS	Metasurface
MRI	Magnetic Resonance Imaging

MTA	Microwave Thermal Ablation
MUT	Material Under Test
MWI	Microwave Imaging
MWT	Microwave Tomography
NC	Negative Control
NRI	Negative Refractive Index
NZI	Near-Zero Index
PEC	Perfect Electric Conductive
PET	Positron Emission Tomography
PLC	Primary Liver Cancer
PMC	Perfect Magnetic Conductive
PoliTo	Politecnico di Torino
PSMA	Printed Square Monopole Antenna
RF	Radio Frequency
RHM	Right-Handed Materials
SAH	Subarachnoid Haemorrhage
SAM	Specific Anthropomorphic Mannequin
SNG	Single-Negative
SRR	Split-ring Resonator
SVD	Singular Value Decomposition
TACE	Trans-Arterial Chemoembolization
TE	Transverse Electric
TL	Transmission Line
TLM	Transmission Line Method
TM	Transverse Magnetic
t-PA	Tissue Plasminogen Activator
TR	Time-Reversal
TSVD	Truncated Singular Value Decomposition
TUIL	Technische Universität Ilmenau
TwIST	Two-Step Iterative Shrinkage/Thresholding
UWB	Ultra-Wideband
VNA	Vector Network Analyser
WP2	Second Work Package

Physical Constants

ϵ_0	$8.85 \times 10^{-12} Fm^{-1}$
μ_0	$4\pi \times 10^{-7} Hm^{-1}$

To my Grandma

Chapter 1

Introduction

This chapter presents the main research topic of this thesis, the motivation of the proposed research and a literature review relevant to the subject of study. The contributions of this work to the field of research with a list of relevant publications and the description of the thesis's structure are shown in Section 1.7 and Section 1.8, respectively. The literature review presented in this chapter focuses on microwave imaging (MWI) for brain stroke detection and the use of metamaterials (MMs) and metasurfaces (MTSs) for imaging applications. A more detailed introduction on MMs, MM modelling, and MWI is presented in Chapter 2.

1.1 Motivation

Currently, medical imaging and healthcare in general are facing several challenges, which cause a growing burden of care on medical services. For example, the development of minimally invasive and personalised technologies is a challenge involving several research fields. In this context, the need for medical imaging equipment worldwide is expected to grow driven by the global rise of various pathologies such as cancer, cardiovascular diseases, brain disorders and lung diseases [1]. This is further enhanced by the increasing ageing population, as elderly people are highly susceptible to diseases, especially cancer, osteoporosis or stroke. For stroke, in particular, incidences are predicted to rise considerably due to the increase of population over 65 years, especially in low-to-middle-income countries [2].

In this framework, medical imaging technologies, such as computed tomography (CT) and magnetic resonance imaging (MRI) play a key role, being the essential clinical tool to deliver accurate initial diagnosis. Especially in the case of brain stroke, early diagnosis and treatment is critical, as the brain loses millions of cells every second following the incident. This leads to irreparable and permanent damage or even death. Furthermore, as treatments differ based on the stroke type, an incorrect diagnosis could prove lethal for the patient. For this reason, there is an increasing interest

in developing new diagnostic tools, such as microwave brain imaging scanners, to supplement and support current modalities.

Similar to other imaging modalities, medical imaging based on microwave technology requires designing systems with increasing number of sensors (i.e., antennas). Using advanced materials can not only improve the characteristics of these antennas, but also enhance detection by tackling the impedance mismatch problem that electromagnetic (EM) waves encounter when probing human tissue. This mismatch is mainly due to the skin, which reflects the incident waves. As a consequence, the reduction of the transmitted energy inevitably limits the accuracy of the applied sensing techniques. The main goal of this project was to develop and test an impedance-matching MTS to improve the resolution of a custom-made microwave system for brain stroke's detection. In addition, to demonstrate the wide applicability of MTS technology and its potential to improve microwave medical devices, the same concept was tested in other medical applications.

1.2 Research Topic and Project's Structure

The main research topic of this thesis involves the design, realization and characterization of MTSs, that can improve the performance of medical imaging systems. These MTSs are integrated into the hardware of several EM devices, which operate in conjunction with strong and robust imaging algorithms.

The topic of this research is closely related to the Horizon 2020 MCSA EMERALD (ElectroMagnetic imaging for a novel genERation of medicAL Devices) project. The scientific objective pursued by the EMERALD action is to accelerate translation of research in EM medical imaging into clinical prototypes through a network of 13 early stage researchers. The EMERALD consortium involves academic institutions, industrial partners, hospitals and medical centres. The research presented in this thesis was aligned with tasks and objectives of EMERALD's second work package (WP2), which focused on the use of MTS technology to improve microwave medical devices. In particular, the main goal of Year 1 was to employ MM science for the design of a MTS which could increase the penetration of microwave energy into the human body. To this end, the first few months of research were dedicated to the understanding of MM theory and modelling. Then, after optimization of the most promising design, the final prototype was fabricated and tested in house. This was done in collaboration with the EMERALD's industrial partner MediWise (Medical Wireless Sensing Ltd., London, UK), which has strong expertise in developing such technology. Moreover, the designed MTS has been adapted to a custom-made MWI system for intra-cerebral haemorrhage detection with simplified phantoms mimicking the head.

In Years 2 and 3, the use of MTSs for the microwave brain imaging prototype developed by KCL (King's College London, London, UK) was tested in house through new simulation and experimental studies, using both microwave tomography (MWT) and radar algorithms. Beside that, new MTSs were designed for deployment in other microwave medical prototypes fabricated within the EMERALD network. In Year 2, a new MTS film was designed for the cerebrovascular (CVA) imaging device developed by PoliTo (Politecnico di Torino, Turin, Italy). This system consists of a low-complexity MWI scanner for monitoring brain stroke. Then, MTS technology was applied to the hardware of the hyperthermia monitoring prototype developed by TUIL (Technische Universität Ilmenau, Ilmenau, Germany). Year 3 was dedicated to the study of MTS components for two more devices, one for breast cancer detection and one for liver's ablation monitoring. Similar to Year 2, these objectives were pursued via two 2-month secondments in the groups developing these prototypes: MITOS Medical Technologies (Istanbul, Turkey) and CNR-IREA (Institute for the Electromagnetic Sensing of the Environment and National Research Council of Italy, Naples, Italy), respectively.

1.3 Pathophysiology and Treatment of Stroke

Brain strokes are either ischaemic (i-stroke), when there is a blocked blood supply in a part of the brain (e.g. a blood clot restricts the blood flow), or haemorrhagic (h-stroke), when there is a burst blood supply. There are two main types of h-stroke: intra-cerebral haemorrhage, or intracranial haemorrhage (ICH), which occurs when we have a bleeding in the brain, and subarachnoid haemorrhage (SAH), which consists of bleeding on the surface of the brain.

Acute vascular occlusion, which is rarely complete, is the central event in acute i-stroke. This precipitates the primary injury by limiting the flow of oxygen and glucose to a region of the brain. The residual cerebral blood flow (CBF) depends on the degree of obstruction and the availability of collateral flow. Because the brain relies on a continuous supply of nutrients to meet its metabolic demands, the amount of injury is proportional to the duration and severity of the ischaemia [3]. Thus, following an accurate diagnosis, receiving the appropriate treatment within 4.5 hours of the onset symptoms plays an important role in saving the patient's life [4]. An intravenous (IV) injection of recombinant tissue plasminogen activator (t-PA), also called alteplase, is the gold standard treatment for i-stroke [5].

Treatment differs in the case of h-stroke. When admitted to hospital with a brain haemorrhage, emergency surgery is sometimes needed to remove blood, to relieve any pressure that has built up, or to repair the blood vessels. If the stroke is caused by a burst aneurysm, an operation may be necessary to seal it and stop it bleeding again

[6]. The outcome of ICH varies depending on haematoma volume, location, extension to ventricles, and other factors. Overall, compared to ischemic stroke, ICH leads to higher mortality and more severe disability [7].

1.4 Current Imaging Techniques for Brain Stroke Detection

Currently, stroke detection and classification relies on imaging methods such as CT and MRI. In particular, CT may be used to confirm the diagnosis and determine whether a stroke is ischaemic or haemorrhagic, whereas MRI can identify and further localize the stroke's site. Although these techniques provide highly valuable diagnostic information, they are expensive, time-consuming (not able to provide real time images) and not portable (due to relevant size of the devices). For the latter reason, both these tools cannot be easily used by paramedics to perform bedside diagnosis or found in ordinary ambulances [8]. Furthermore, a recent study has demonstrated that radiation from CT scans is associated with increased risk of cancer [9], while MRI exposes the patient to a strong magnetic field and needs more time and patient's cooperation to be performed [10]. For these reasons, there is an increasing interest in developing new diagnostic tools to supplement these current imaging modalities. In this framework, MWI may represent an interesting alternative [11].

1.5 Microwave Imaging

Among all the emerging EM techniques, MWI has great diagnostic potential in various clinical applications such as breast cancer detection, stroke detection, cardiac imaging, bone imaging and localization of in-body radio frequency (RF) sources [12–14]. This imaging technique is based on differentiation of dielectric properties of the biological tissue under study [15]. Array of antennas are used to transmit low-power microwaves into the region of interest and receive the resulting scattered signal. The spatial distribution of dielectric properties throughout the tissue volume is then estimated using reconstruction algorithms that are applied to the acquired data [16].

Despite MWI methods initially focused on diagnosing breast cancer, MWI techniques for brain stroke detection and classification are drawing the interest of many groups worldwide [11, 17–20]. Although its resolution is lower than MRI, ultrasound, and X-Ray imaging, MWI presents many advantages [21]. First, it is a non-invasive and safe technique, as its uses non-ionizing radiation power in very low doses (low-power EM waves). Moreover, its data acquisition time can range from milliseconds to

a few seconds. This can allow a quick assessment of the stroke, which is crucial for proper drug administration [19]. Another appealing property of MWI is its economical sustainability for the healthcare system: MWI has the potential to provide mobile, low-cost imaging platforms well suited to the healthcare needs.

However, developing a valid system for brain imaging is a challenging task. For example, to achieve an operational MWI system for detecting a bleeding in the brain, it is necessary to find a compromise between resolution and penetration depth into the brain tissue, which is located inside of an EM shield comprising the skull and the cerebrospinal fluid (CSF) [21]. A valid MWI system should maximize the incident power coupled into the tissue of interest and ensure acceptable spatial resolution images [22]. To maximize the amount of incident power penetrating into the brain tissue, compact antennas operating below 2 GHz and immersed in a lossy dielectric medium are recommended [22]. According to this requirement, there are several possible MWI head scanner designs that could be considered. Headband, helmet structures or specific chambers [23], for example, cover only portion of the head to allow the use of a coupling medium for the operating antennas.

The dielectric medium reduces unwanted multipath signals and broadens the frequency range of operation [24], but at the same time affects the detection of useful "weak" signals. One way to increase the transmitted power and improve the received signal is to place a MM film in front of the skin, which can act as an impedance-matching layer [25, 26]. This approach is motivated by previous numerical studies which have demonstrated that MTSs can suppress unwanted reflections and enhance transmission near a specific frequency [27, 28].

1.6 Metamaterials in Medical Sensing and Imaging

MMs and MTSs are engineered materials exhibiting unique EM properties which are not shown by naturally occurring materials. Nowadays, different MTSs based on resonating structures, such as split-ring resonators (SRRs), have been developed for several applications, including sensing and imaging. These structures present many advantages relative to conventional materials, such as high flexibility in the design process [29].

Recently, MM-based technologies have attracted an increased attention in biosensing, from the microwave to the optical frequencies. In the microwave spectrum, layers of SRRs have been used for biomolecular [30] and early cancer detection [31, 32], MRI [33–36], and imaging in the near-field [37, 38] and far-field [39]. Computational imaging systems for security-screening applications have also used frequency-diverse MTS apertures in the K-band frequencies [40–43].

With the advent of innovative devices involving MMs, one of the challenges in MWI for biomedical applications is integrating MM technology into the current diagnostic systems [44]. A relevant aspect is the possibility of using focusing lenses. At terahertz frequencies, highly efficient gradient lens based on MTS structures can efficiently manipulate the spatial field distribution and focuses the incident beam, working efficiently even at wide angles of incidence [45]. In terms of MWI applications, it has been demonstrated that the field generated by a localized source can be focused on a specific point by a flat slab. Thus, a target could be inspected by scanning a focal point, moving the source (in front of the slab) in different directions [46].

Flat MM slabs can be also used as a matching medium to couple EM energy into the region of interest. Impedance mismatch occurs when EM waves propagate between mediums with different permittivity and permeability values, resulting in reduction of the transmitted energy. This issue becomes significant in diagnostic imaging and other non-invasive biomedical applications, such as non-invasive glucose sensing [25, 26]. Thus, we can achieve impedance-matching and improve the transmitted power by placing a MM film that acts as an impedance-matching coating in front of the skin. Candidates for this purpose include layers of SRRs, which have been already shown to enhance the field penetration in the human tissue for breast imaging [47].

1.7 Contributions and Relevant Publications

My contributions to this research study are related to the design of new hardware components for EM imaging systems. In particular, the originality of the work resides in improving the efficacy of several MWI systems for clinical applications by incorporating innovative MM structures into the antenna arrays. The results shown in the following chapters, suggest that MTSs can greatly enhance MWI, paving the way towards the realisation of innovative systems with the desired clinical accuracy.

Each MM structure proposed in this thesis is tailored to fulfil specific requirements (depending on the MWI prototype) and achieve the desired goals (e.g., impedance-matching, improved field penetration into the human tissue, enhanced antenna designs). More specifically, as mentioned in Section 1.2, my main goal was to contribute to a KCL project which aims to develop a MWI system for detecting stroke. Thus, while the research in this thesis focuses on improving the quality of the signals transmitted and received by this MWI system, validating this enhancement requires using tools (algorithmic and experimental) which have been developed in collaboration with other researchers within the scope of a broader project. The researchers that contributed to this work are listed in the acknowledgments. Besides that, new MTSs were designed for deployment in other microwave medical prototypes fabricated by

other research groups within the EMERALD network. Chapter 5 and 6 present the summary of the collaborations with these EMERALD's partners. All the necessary references for the complete understanding of the systems developed by these external groups are provided in the thesis.

The publications related to the contributions of this research are stated as follows, with the relevant chapters given in brackets:

Journals

- E. Razzicchia, I. Sotiriou, H. Cano-Garcia, E. Kallos, G. Palikaras and P. Kosmas, *"Feasibility Study of Enhancing Microwave Brain Imaging Using Metamaterials"*, Sensors, 19(24), 5472, 2019. (Chapter 3)
- E. Razzicchia, P. Lu, W. Guo, O. Karadima, I. Sotiriou, N. Ghavami, E. Kallos, G. Palikaras and P. Kosmas, *"Metasurface-Enhanced Antennas for Microwave Brain Imaging"*, Diagnostics, 11(3), 424, 2021. (Chapter 4)
- N. Ghavami, E. Razzicchia, O. Karadima, P. Lu, W. Guo, I. Sotiriou, E. Kallos, G. Palikaras and P. Kosmas, *"The Use of Metasurfaces to Enhance Microwave Imaging: Experimental Validation for Tomographic and Radar-based Algorithms"*, IEEE Open Journal of Antennas and Propagation, December 2021. (Chapter 3)

Conferences

- S. Ahsan, M. Koutsoupidou, E. Razzicchia, I. Sotiriou and P. Kosmas, *"Advances towards the Development of a Brain Microwave Imaging Scanner"*, 13th European Conference on Antennas and Propagation (EuCAP), Krakow, Poland, 31 March - 5 April 2019. (Chapter 3)
- E. Razzicchia, M. Koutsoupidou, H. Cano-Garcia, I. Sotiriou, E. Kallos and G. Palikaras, *"Metamaterial Designs to Enhance Microwave Imaging Applications"*, International Conference on Electromagnetics in Advanced Applications (ICEAA), Granada, Spain, 9-13 September 2019. (Chapter 3)
- O. Karadima, E. Razzicchia and P. Kosmas, *"Image Improvement through Metamaterial Technology for Brain Stroke Detection"*, 14th European Conference on Antennas and Propagation (EuCAP), Copenhagen, Denmark, 15-20 March 2020. (Chapter 3)
- E. Razzicchia, N. Ghavami, S. Ahsan and P. Kosmas, *"Feasibility Study on Improving Microwave Stroke Detection using Metamaterials"*, 2020 IEEE AP-S Symposium on Antennas and Propagation, Montréal, Quebec, Canada, July 5-10, 2020. (Chapter 3)

- E. Razzicchia, N. Ghavami, D. O. Rodriguez Duarte, J. A. Tobon Vasquez, F. Vipiana, P. Kosmas, *"Benefits of Employing Metasurfaces on the Design of a Microwave Brain Imaging Scanner"*, International Conference on Electromagnetics in Advanced Applications (ICEAA), Honolulu, Hawaii, USA, 9-13 August 2021. (Chapter 5)

- E. Razzicchia, P. Lu, W. Guo and P. Kosmas, *"A New Metasurface-Enhanced Microstrip Patch Antenna for Haemorrhagic Stroke Detection"*, 15th European Conference on Antennas and Propagation (EuCAP), Dusseldorf, Germany, 22-26 March 2021. (Chapter 4)

- E. Razzicchia, A. Prokhorova, M. Helbig and P. Kosmas, *"Feasibility Study of Enhancing Temperature Change Detection through Metamaterial Technology for Hyperthermia Monitoring"*, URSI GASS 2021, Rome, Italy, 28 August - 4 September 2021. (Chapter 6)

- E. Razzicchia, A. Janjic, N. Ghavami, I. Akduman, M. Cayoren and P. Kosmas, *Metasurface-Enhanced Antenna for Microwave Breast Imaging*, 16th European Conference on Antennas and Propagation (EuCAP), Madrid, Spain, 27 March - 1 April 2022. (Chapter 5)

1.8 Thesis's Structure

The thesis is structured as follows. Chapter 2 presents some basic background theory necessary for a complete understanding of the presented work. Chapter 3 presents the initial unit cell MTS designs for impedance-matching, as well as experiments and simulations of a planar head model that was developed to test the full MTS structure. Furthermore, the chapter demonstrates in numerical simulations and MWI experiments how the proposed design might be integrated into MWI scanners for brain stroke's detection. Chapter 4 presents simulation studies for a MTS-enhanced antenna operating in air, without the use of a coupling liquid. Chapter 5 and Chapter 6 investigate further microwave applications of MM technology for medical devices. Finally, Chapter 7 summarises the thesis' findings and proposes future directions to develop this research further.

Chapter 2

Background Theory

This chapter reviews the theoretical background on which the findings presented in this thesis are based. Section 2.1 presents a more detailed review on metamaterials (MMs), MM modelling and a more detailed introduction to metasurfaces (MTS) for tissue impedance-matching. Section 2.2 is dedicated to microwave imaging (MWI) theory and presents the formulations of two MWI algorithms. Basic concepts on microwave networks, antenna theory and material characterization are summarized in Appendices A, B and C, respectively.

2.1 Metamaterials and Metasurfaces

A MM is an engineered material consisting of periodically arranged metallic elements which are on a size scale much smaller than the wavelength of the incident electromagnetic (EM) wave [48]. These materials can manipulate EM wave beams and exhibit some unique EM properties which are not found in naturally occurring materials. Surface-type MMs (MMs which are very thin in the third dimension) are generally called metafilms or MTSs. Because of the two-dimensional (2D) nature of their structures, MTSs occupy less physical space and can exhibit lower losses. Thus, the main advantages of MTSs include their low level of absorption in comparison with bulky MMs, and easy integration due to their thin profile [49]. For instance, a cavity or a resonator can be made smaller using MTSs rather than bulk MMs [50].

MMs were first known as left-handed materials (LHM) or negative refractive index (NRI) materials. The concept of LHM was first developed by the Russian physicist Victor Veselago in 1967 [51]. He predicted the existence of materials that could allow the propagation of EM waves with an electric field, magnetic field and phase vector that form a left-handed triad, opposite to the commonly known right-handed triad of conventional materials. He also demonstrated that such materials are allowed by Maxwell's equations [51]. Other important EM properties which were proposed by Veselago for these materials include the reversal of Snell's Law, the reversal of the Doppler effect and the reversal of Vavilov-Cerenkov radiation [51].

Due to the lack of experimental verification, MMs did not attract interest until microstructures built from non-magnetic conducting sheets were shown to exhibit an effective magnetic permeability [52]. In 2001, the first artificial LHM was made using a combination of wires and SRRs [53]. SRRs are resonant due to internal capacitance and inductance [54] and their EM properties strongly depend on the geometry rather than the composition [36]. Thus, depending on the type of resonator, different propagation characteristics can be tailored to the desired requirements.

Initially the concept of MM was associated with creating structures that exhibit negative permittivity and permeability. Then, research efforts to reduce the inherent losses and widen the operation bandwidth of LHM, broadened the concept of MMs. This was promoted by gradient index media used to bend EM waves [55] and invisible cloaks [56, 57]. Nowadays, a composite material does not require negative permittivity or permeability to be termed as MM. The term includes any material capable of manipulating EM waves (such as blocking, absorbing, enhancing, bending waves) to achieve benefits that go beyond what is possible with conventional materials. Another interesting feature to mention is that, in the specific case of MTSs, it is possible to achieve abrupt changes in amplitude and phase using very thin films (layers with subwavelength thickness) in place of electrically long structures.

Material Categorization

Figure 2.1 shows the different combination of permittivity and permeability that can be achieved. The first quadrant ($\epsilon > 0$ and $\mu > 0$) represents right-handed materials (RHM) or "double-positive" (DPS) materials. In RHM, electric field, magnetic field, and wave vectors follow the right-hand thumb rule for the direction of propagation. The second quadrant ($\epsilon < 0$ and $\mu > 0$) represents electric plasma or "epsilon-negative" materials. These materials support evanescent waves, which exhibit a rapidly decaying field amplitude in a certain spatial direction, without contributing to energy transport in that direction. The third quadrant ($\epsilon < 0$ and $\mu < 0$) corresponds to LHM materials, which are characterized by backward propagating waves. In the case of LHM, the electric field, magnetic field and the wave vectors follow a left-hand thumb rule for the direction of propagation. The forth quadrant ($\epsilon > 0$ and $\mu < 0$) represents magnetic plasma or "permittivity-negative" materials.

In general, if a material has negative values of ϵ and μ, it can be defined as "double-negative" (DNG) material. The materials with one negative parameter (quadrants two and four) will be called "single-negative" (SNG). If both ϵ and μ are zero or very close to zero, the materials will be called "zero-index" materials or "near-zero index" (NZI) materials, respectively.

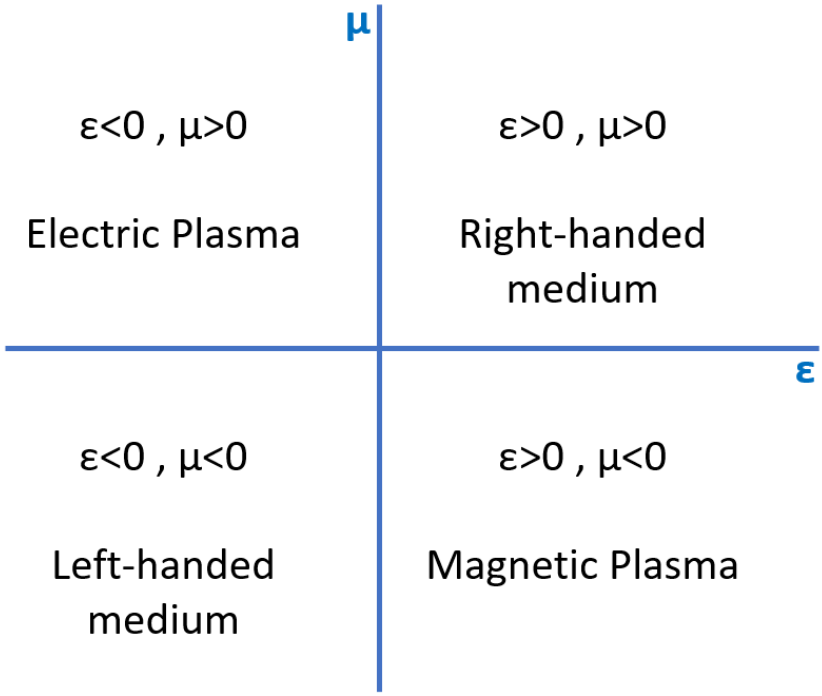

FIGURE 2.1: Material categorization based on values of permittivity and permeability.

2.1.1 Propagation of Waves in Left-Handed Materials

As MMs are engineered materials with properties not found in nature, it is important that Maxwell's equations are satisfied to obtain physical meaningful results. Maxwell's equations in differential form are given as follows:

$$\nabla \times \vec{E} = -\frac{\partial \vec{B}}{\partial t} \tag{2.1}$$

$$\nabla \times \vec{H} = \frac{\partial \vec{D}}{\partial t} + \vec{J} \tag{2.2}$$

$$\nabla \cdot \vec{D} = \rho \tag{2.3}$$

$$\nabla \cdot \vec{B} = 0 \tag{2.4}$$

where $\vec{E}$ (V/m) is the electric field density, $\vec{B}$ (W/m^2) is the magnetic flux density, $\vec{H}$ (A/m) is the magnetic field density, $\vec{D}$ (C/m^2) is the electric flux density, $\vec{J}$ (A/m^2) is the electric current density and ρ (C/m^3) is the electric charge density. For a dielectric material, the constitutive relations are the following:

$$\vec{D} = \epsilon_0 \vec{E} + \vec{P} = \epsilon_0(1 + \chi_e)\vec{E} = \epsilon_0 \epsilon_r \vec{E} = \epsilon \vec{E} \tag{2.5}$$

$$\epsilon = \epsilon' - j\epsilon'' \tag{2.6}$$

$$\vec{B} = \mu(\vec{H} + \vec{M}) = \mu_0(1 + \chi_m)\vec{H} = \mu_0\mu_r\vec{H} = \mu\vec{H} \tag{2.7}$$

$$\mu = \mu' - j\mu'' \tag{2.8}$$

where $\vec{P} = \epsilon_0\chi_e\vec{E}$ and $\vec{M} = \chi_m\vec{H}$ are the electric and magnetic polarization, and χ_e and χ_m are the electric and magnetic susceptibility, respectively.

To transform Maxwell's equations from their original derivation in the time domain to the frequency domain, we replace all sources and field quantities by their phasor equivalents and replace all time-derivatives of quantities with $j\omega$ times the phasor equivalent:

$$\nabla \times \vec{E} = -j\omega\vec{B} \tag{2.9}$$

$$\nabla \times \vec{H} = j\omega\vec{D} + \vec{J} \tag{2.10}$$

$$\nabla \cdot \vec{D} = \rho \tag{2.11}$$

$$\nabla \cdot \vec{B} = 0 \tag{2.12}$$

Let us consider a plane monochromatic wave $e^{-j\vec{k}\cdot\vec{r}}$ propagating in a medium characterised by material constant ϵ and μ, where $\vec{k}$ is the wave vector and $\vec{r}$ is a position vector. The magnitude of the wave vector is the wave number of the wave (inversely proportional to the wavelength), and its direction is ordinarily the direction of wave propagation. Equations (2.9) and (2.10) can be written as:

$$\vec{k} \times \vec{E} = -\omega\mu\vec{H} \tag{2.13}$$

$$\vec{k} \times \vec{H} = \omega\epsilon\vec{E} \tag{2.14}$$

It may be seen from the above equations that when the material constant ϵ and μ are both positive, the vectors $\vec{E}$, $\vec{H}$ and $\vec{k}$ constitute a right-handed set, whereas for negative ϵ and μ, we have a left-handed set [58].

The wave vector $\vec{k}$ is along the direction of the phase velocity ($v_p = \omega/k$), which is the speed at which the phase of a wave propagates through space. The energy flux carried by the wave is determined by the Poynting vector:

$$\vec{S} = \vec{E} \times \vec{H} \tag{2.15}$$

According to equation 2.15, the vector $\vec{S}$ always forms a right-handed set with the vectors $\vec{E}$ and $\vec{H}$. Thus, for RHM, $\vec{S}$ and $\vec{k}$ are in the same direction, whereas, for LHM, these vectors points in different directions. The Poynting vector also tells us the direction of the group velocity ($v_g = \partial\omega/\partial k$). The group velocity of a wave is the velocity with which the overall envelope shape of the wave's amplitudes propagates

through space. Thus, it is clear that LHM are materials with a so-called negative group velocity (see Figure 2.2) [51].

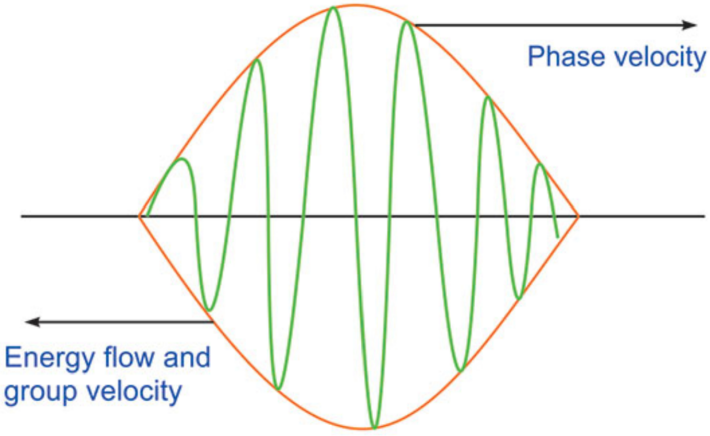

FIGURE 2.2: Wave with the group velocity and phase velocity going in different directions. The phase velocity, i.e., the peaks and troughs (green lines), is positive and moves forward. The group velocity, i.e., the envelope of the wave (orange lines), is negative and moves backward.

Normally Incident Plane Wave on a Double Negative Slab

Let us consider a DNG slab of thickness d which has an infinite extend in the transverse direction of propagation of an incident plane wave (Figure 2.3). Assuming the medium before and after the slab is characterized by ϵ_1 and μ_1 and the slab is characterized by ϵ_2 and μ_2. For a normally incident plane wave, the transmission and reflection coefficients for the slab are:

$$R = \frac{\eta_2 - \eta_1}{\eta_2 + \eta_1} = \frac{1 - e^{-j2k_2}}{1 - [(\eta_2 - \eta_1)/(\eta_2 + \eta_1)]^2 e^{-j2k_2 d}} \tag{2.16}$$

$$T = \frac{4\eta_1\eta_2}{(\eta_2 + \eta_1)^2} = \frac{e^{-j2k_2}}{1 - [(\eta_2 - \eta_1)/(\eta_2 + \eta_1)]^2 e^{-j2k_2 d}} \tag{2.17}$$

where $k_i = \omega\sqrt{\epsilon_i}\sqrt{\mu_i}$ is the wave number and $\eta_i = \frac{\sqrt{\epsilon_i}}{\sqrt{\mu_i}}$ is the wave impedance (with $i = 1, 2$). If we consider a matched DNG medium ($\eta_1 = \eta_2$), it follows that $R = 0$ and $T = e^{-j2k_2 d} = e^{+j2|k_2|d}$. Thus, a DNG medium would add a positive phase to the wave passing through the slab, whereas in a DPS medium the wave would experience a negative phase variation. This means that a matched DNG slab could be used to compensate for phase changes incurred by the passage of a plane wave through a DPS slab, meaning that one can force $k_{DPS}d_{DPS} + k_{DNG}d_{DNG} = 0$. This is an appealing feature of MMs, which can lead to interesting applications [59].

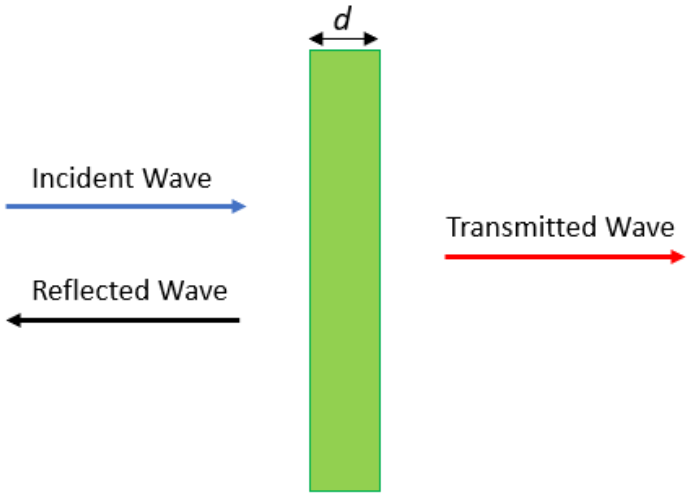

FIGURE 2.3: Plane-wave scattering from a DNG slab.

Negative Refraction

The phenomenon of negative refraction can be studied by considering an obliquely incident wave on a DPS/DNG interface (Figure 2.4). At the interface, the law of reflection and Snell's Law are the following:

$$\theta_{\text{refl}} = \theta_{\text{inc}} \tag{2.18}$$

$$\theta_{\text{transm}} = sgn(n_2)sin^{-}1(\frac{n_1}{|n_2|}sin\theta_{\text{inc}}) \tag{2.19}$$

If the index of refraction of a medium is negative, then the refracted angle is also "negative" [59]. It follows that we have an anomalous reflection with respect to conventional RHMs, as shown in Figure 2.4. Anomalous reflection refers to the phenomenon in which waves do not follow the "traditional" Snell's law and are subject to reflection at abnormal angles.

The wave and Poynting vectors associated with this oblique scattering problem are:

$$k_{\text{inc}} = k_1(cos\theta_{\text{inc}}\hat{z} + sin\theta_{\text{inc}}\hat{x}) \tag{2.20}$$

$$k_{\text{refl}} = k_1(-cos\theta_{\text{inc}}\hat{z} + sin\theta_{\text{inc}}\hat{x}) \tag{2.21}$$

$$k_{\text{trans}} = k_2(cos\theta_{\text{trans}}\hat{z} + sin\theta_{\text{trans}}\hat{x}) \tag{2.22}$$

$$S_{\text{inc}} = \frac{1}{2}\frac{|E_0^2|}{\eta_1}(cos\theta_{\text{inc}}\hat{z} + sin\theta_{\text{inc}}\hat{x}) \tag{2.23}$$

$$S_{\text{refl}} = \frac{1}{2}\frac{|RE_0^2|}{\eta_1}(-cos\theta_{\text{inc}}\hat{z} + sin\theta_{\text{inc}}\hat{x}) \tag{2.24}$$

$$S_{\text{trans}} = \frac{1}{2}\frac{|TE_0^2|}{\eta_2}(cos\theta_{\text{trans}}\hat{z} + sin\theta_{\text{trans}}\hat{x}) \tag{2.25}$$

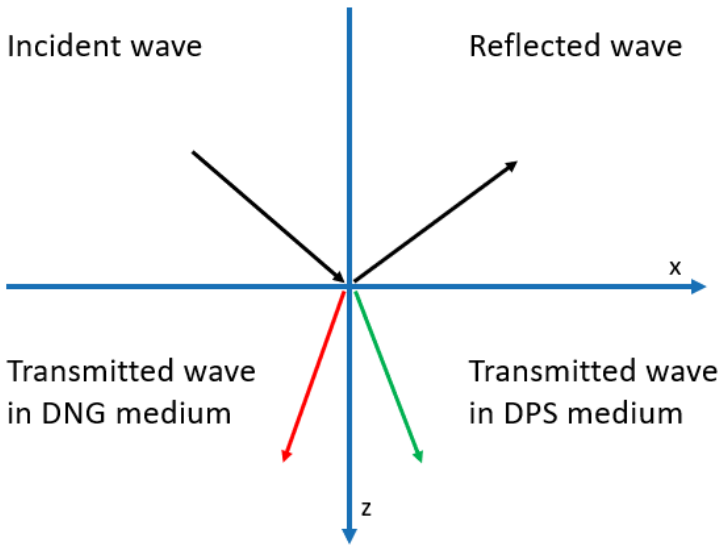

FIGURE 2.4: Scattering of a wave obliquely incident upon a DPS/DNG interface [59].

If the transmitted wave is propagating in a DPS medium, the Poynting and wave vectors are in the same direction. However, assuming that the transmitted wave is propagating in a DNG medium (with a refractive index less than zero), the transmitted wave and Poynting vector point in opposite directions:

$$k_{\text{trans}} = -|n_2|\frac{\omega}{c}(cos|\theta_{\text{trans}}|\hat{z} - sin|\theta_{\text{trans}}|\hat{x}) \tag{2.26}$$

$$S_{\text{trans}} = \frac{1}{2}\frac{|TE_0^2|}{\eta_2}(|cos\theta_{\text{trans}}|\hat{z} - sin|\theta_{\text{trans}}|\hat{x}) \tag{2.27}$$

2.1.2 Impact of Metamaterials on Radiating Systems

MMs have interesting properties useful for design of EM system, due to their capability of providing artificial values of permittivity and permeability. For this reason, MMs can be used to manipulate size, efficiency, bandwidth and directivity of structures for radiating and scattering applications. Resonances arising in electrically small regions of space where single and DNG materials are paired with common DPS materials were shown to have a great potential for overcoming the limits generally associated with several EM problems. For instance, the use of MTS-based coatings to enhance the

radiation and matching properties of electrically small antennas and magnetic dipole antennas has been studied in [60–62].

"Zero-index" MMs, which are media with permittivity and permeability with zero or near-zero values, may have strong impact in some applications despite their non-resonant character, since they combine anomalous wave interactions with relatively larger bandwidth and lower losses. It has been demonstrated that these MMs can be used to achieve high directivity antennas [63, 64]. A signal propagating in a "zero-index" MM stimulates a spatially static field structure that varies in time. Thus, the phase at any point will have the same constant value once the steady state is reached. This coherent response causes the phase across the output face of the MM slab to be uniform. Moreover, from Snell's Law, all of the outgoing wave vectors will be normal to the interface. Consequently, this effective aperture will produce the highest-directivity beam [65]. "Zero-index" MMs have also been used to achieve high efficiency antennas [66]. As their refractive index is zero or near-zero, the wavelength in the medium is effectively infinite and the resonance is independent of the physical dimensions. The physical size of an antenna can thus be made smaller than a half-wavelength. Moreover, the perfectly uniform current distribution associated with the zero-order mode may also decrease the overall loss resistance of the system and, hence, provide a higher overall efficiency [65].

2.1.3 Metamaterial Modelling

The design of MMs is an essential path between theory and practice and it is critical to achieve the desired performance in an experimental environment. In this section, an introduction about analytical and numerical modelling is presented. Furthermore, a more detailed discussion about MTS modelling for tissue impedance-matching is proposed.

Analytical Methods

As MTSs typically consist of multiple unit cells across a surface area (or a few surface layers), one method to design these structures is to use transmission line (TL) models with cascading elements. Using this approach, it is possible to calculate the EM performance of the whole MTS stack [67]. Analytical methods use analytical expressions to describe the interaction of plane waves with periodic unit cells. To use these methods, it is necessary to apply the following constraints:

1. The period of the MTS's pattern must be smaller than the effective wavelength;

2. The separation between the metallic features must be smaller than the period of the MTS's pattern.

These constraints allow us to transform our complex EM problem to an equivalent transmission line circuit (Figure 2.5).

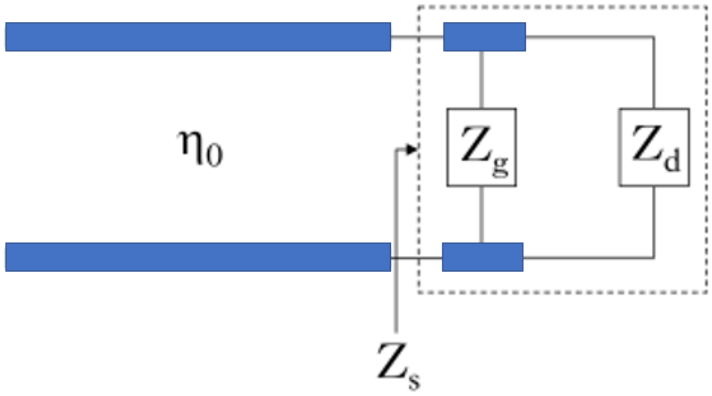

FIGURE 2.5: Transmission line equivalent circuit of the structure made of periodic unit cells where the Z_s is the MTS impedance, Z_g is the impedance of the metallic patches' grid, Z_d is the impedance of the dielectric substrate and η_0 is the characteristic impedance of free space.

Here a simple case where an array of patches placed on a dielectric substrate (ϵ_r) is examined. The combination of these two layers is the MTS. Following the formalism presented by Capolino [68] and Luukkonen et al. [69], the MTS's impedance Z_s is the impedance of the parallel of the metallic grid impedance Z_g and the dielectric substrate impedance Z_d.

$$Z_s = \frac{Z_g Z_d}{Z_g + Z_d} \tag{2.28}$$

For an obliquely incident transverse electric (TE)-polarized plane wave, the impedance of the dielectric slab Z_d is obtained by:

$$Z_d^{\mathrm{TE}}(\omega, \theta) = \frac{j\eta_0}{\sqrt{\epsilon_r - sin^2\theta}} tan(k_{nd}h) \tag{2.29}$$

The same impedance for an obliquely incident transverse magnetic (TM)-polarized plane wave is:

$$Z_d^{\mathrm{TM}}(\omega, \theta) = \frac{j\eta_0}{\sqrt{\epsilon_r - sin^2\theta}} tan(k_{nd}h)(1 - \frac{sin^2\theta}{\epsilon_r}) \tag{2.30}$$

where $k_{nd} = \omega\sqrt{\epsilon_0\mu_0}\sqrt{\epsilon_r - sin^2\theta}$ is the wave number in the dielectric slab in the normal direction and h is the thickness of the dielectric slab.

To calculate the impedance of the patch array shown in Figure 2.6, the Babinet principle [70] is applied to a grid consisting of a strip mesh with square holes, resulting in the grid impedance of the complementary structure (array of patches):

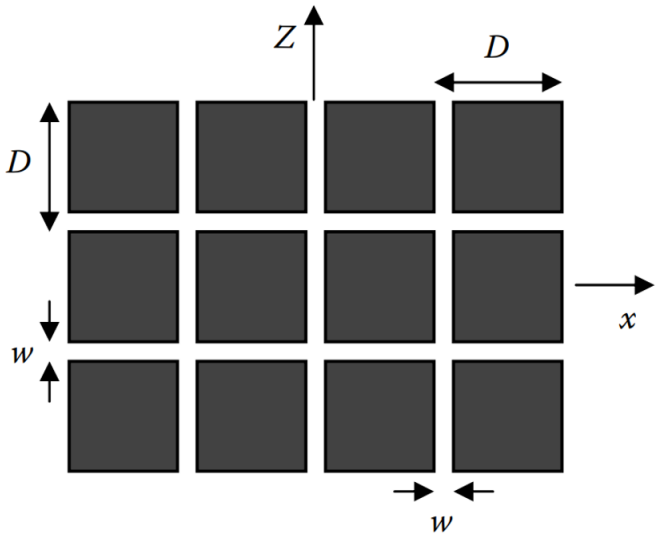

FIGURE 2.6: Array of square patches. D is the width of the square patches and w the distance between them.

$$Z_g^{\mathrm{TE}} = -j\frac{\eta_{eff}}{2\alpha(1-\frac{1}{2}(\frac{k_z}{k_{eff}})^2)} \tag{2.31}$$

$$Z_g^{\mathrm{TM}} = -j\frac{\eta_{eff}}{2\alpha} \tag{2.32}$$

where $\eta_{eff} = \frac{\eta_0}{\sqrt{\epsilon_{eff}}}$, $\epsilon_{eff} = \frac{\epsilon_r+1}{2}$, $k_{eff} = k_0\sqrt{\epsilon_{eff}}$, $k_z = k_0 sin\theta$ and α is the grid parameter of an electrically dense array of ideally conductive strips:

$$\alpha = -\frac{k_{eff}D}{\pi} ln(csc(\frac{\pi w}{2D})) \tag{2.33}$$

In Equation (2.33), D is the width of the square patches and w is the gap between them ($w << D$). Using the above equations, the total impedance $Z_s^{TE,TM}$ of the MTS can be calculated over a wide frequency range by inserting equations (2.31) or (2.32) (for the grid) and (2.29) or (2.30) (for the substrate) into (2.28).

This method can be also applied to more complex structures, such as, for example, a MTS consisting of a metallic pattern made of Jerusalem crosses printed on a dielectric substrate. In this case, we can write the grid impedance in terms of an effective inductance L_g and an effective capacitance C_g:

$$Z_g^{TE} = j\omega L_g + \frac{1}{j\omega C_g} \tag{2.34}$$

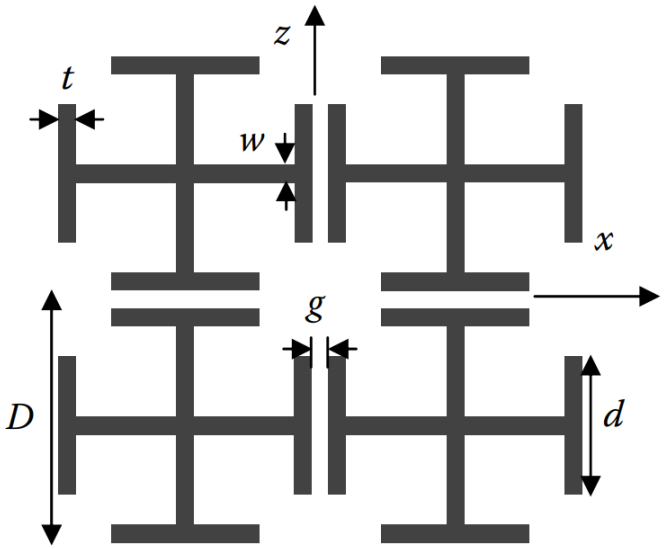

FIGURE 2.7: Feature dimensions (t, d, g, w) of the Jerusalem cross-shaped resonators.

$$Z_g^{TM} = j\omega L_g(1 - (\frac{k_z}{k_{eff}})^2) + \frac{1}{j\omega C_g} \tag{2.35}$$

where the inductance L_g is:

$$L_g = \frac{\eta_{eff}\alpha}{2\omega} \tag{2.36}$$

Here, the parameter α is given by Equation (2.33) and η_{eff}, ϵ_{eff}, and k_{eff} are the parameters of the effective medium described above. The effective capacitance can be calculated as:

$$C_g = \frac{\epsilon_0\epsilon_r d}{\pi}(ln(csc(\frac{\pi g}{2D})) + F) \tag{2.37}$$

where F is as follows:

$$F = \frac{Qu^2}{(1 + Q(1-u)^2)} + (\frac{du(3u-2)}{4\lambda})^2 \tag{2.38}$$

with:

$$Q = \sqrt{1 - (\frac{d}{\lambda})^2} \tag{2.39}$$

$$u = cos^2(\frac{\pi g}{2d}) \tag{2.40}$$

Once obtaining the total impedance Z_s from Equation (2.28), this can be used to optimize the MTS structure to achieve targeted responses. For instance, Z_s can be used to calculate the reflection coefficient on a MTS layer as a function of the structure's geometry (period, gap, thickness, etc.). Subsequently, the optimal set of geometric parameters which minimize reflection in a desired frequency range can be found through

numerical techniques (e.g. gradient descent optimization).

Numerical Simulations

Numerical methods for designing MMs are based on large amount of full-wave simulations and S-Parameters retrievals. However, as several numerical simulations are generally required to optimize the constitutive parameters of a single MM particle, this method might be very time consuming [71]. Furthermore, when the MM devices are complicated, the total number of MM particles could be very large. For example, invisible cloaks in the microwave regime contains tens of thousands of different particles [72]. This means that it will take a few weeks or months to complete an overall optimization of the MM's parameters.

Effective medium theory (EMT) provides an easier and faster way to design MMs. Effective medium approximations (EMAs) are based on the analytical and theoretical modelling of the macroscopic properties of a MM. At the constituent level, MM properties vary and are inhomogeneous. Thus, precise calculation of the many constituent values is nearly impossible. EMAs are acceptable approximations which describe useful parameters, including the effective permittivity and permeability, as a whole. For example, averaging the multiple values of the constituents that make up a MM allow us to avoid a large number of simulations [73]. However, these approximations are typically used to model bulk MMs, which are three-dimensional (3D) MMs. For 2D structures, more accurate results are obtained through full-wave simulations. Numerical simulations are usually performed using time domain or frequency domain solvers, the latter being the most common method used to design MMs. In CST Microwave Studio®, two time domain solvers are available, which both work on hexahedral meshes. One is based on the Finite Integration Technique (FIT), just called "Transient solver", the second one is based on the transmission line method (TLM) and is referred to as "TLM solver". With respect to other CST's solvers, both these methods allow a fast and memory efficient computation, together with a robust hexahedral meshing to successfully simulate extremely complex structures. CST's frequency domain solver uses Finite Element Method (FEM) to solve Maxwell's equations. A special feature of the frequency domain solver is the support of both hexahedral and tetrahedral meshes. An important difference between the transient solver and the frequency domain solver is the number of frequency samples that are calculated. Whereas in the time domain the number of frequency samples has almost no influence on the solver time, a classical frequency domain calculation has to carry out the simulation frequency point by frequency point. Every frequency point requires a

complete solver run. The frequency domain solver does however use special broadband frequency sweep techniques in order to derive the full broadband spectrum from a relatively small number of frequency samples [74].

Unit cell numerical characterization and optimization in CST

The traditional method to model a MTS unit cell with properties not found in RHMs (e.g., constitutive parameters close to zero, negative permittivity and/or permeability over some frequencies), is to use split ring resonators and wires. All the MTS unit cells presented in this thesis are based on common resonator shapes: Jerusalem cross, double square-split ring resonator (DS-SRR) and split-ring resonator (SRR). All these elements have negative permittivity and/or permeability over some frequencies and exhibit their own electric and magnetic responses described by ϵ and μ. The unit cell constitutive parameters can be extracted in CST from the calculated scattering parameters. As an example, the full characterization process of the first MTS unit cell presented in this thesis is reported in Section 3.2.1.

However, in many cases, the numerical simulation of a single unit cell does not fully achieve the desired results. This happens because, in the MTS structure, the unit cells are arranged in periodic arrays and the EM waves interact with them as a homogeneous medium. In this thesis, all the MTS single elements were modelled using CST unit cell boundary conditions and their structure was adjusted iteratively to achieve the desired S-Parameters. In CST frequency domain, unit cell boundary conditions virtually repeat the MTS single element periodically. Thus, the whole structure can be easily optimized by changing the geometric features of the single unit cell (e.g., dimensions of the metal wires, dielectric substrate thickness, etc.) in order to achieve the desired goals. The most robust algorithm used to perform unit cell optimization is the "Trust Region Framework" algorithm. This algorithm first defines a region around the current best solution, in which a certain model (usually a quadratic model) can to some extent approximate the original objective function. Then, the algorithm takes a step forward. If a notable decrease is gained after the step forward, then the model is considered to be a good representation of the original objective function. If the improvement is too subtle or even a negative improvement is gained, then the model is not to be considered as a good representation of the original objective function within that region. The size of the "trust region" in each iteration would depend on the improvement previously made.

The design and optimization of all the MTS unit cells proposed in this thesis were performed numerically through CST. The adopted design procedure consists in changing the resonators' geometry and and size through several simulations. Then, small

refinements of the structure were made using the "Trust Region Framework" algorithm.

2.1.4 Metasurface design for tissue impedance-matching: analytical and numerical modelling

Transmission line modelling

Several research studies [75, 76] have demonstrated that the TL model can be a very valuable tool to describe the physical interactions that occur when a travelling plane wave propagates across a certain medium. In first approximation, we can represent the portion of the human body placed in the close proximity of our source of excitation as a homogeneous medium. This medium has average dielectric properties of the considered body region, which is made of various tissues. If the tissue is several wavelengths thick, we can make the assumption that the TL terminates on this biological load, which is characterized by an equivalent impedance Z_L:

$$Z_L = \sqrt{\frac{\mu_0}{\epsilon_0 \epsilon_L}} \tag{2.41}$$

A convenient way to study a more complex biological structure, such as the head, is to consider an equivalent TL in which each section corresponds to a tissue layer [77], as sketched in Figure 2.8. In such a model, Z_{skin}, Z_{bone}, Z_{csf} and Z_{brain} denote the characteristic impedances of skin, bone, cerebrospinal fluid (CSF) and brain, respectively. The characteristic impedance of the n-th section is:

$$Z_n = \sqrt{\frac{\mu_0}{\epsilon_0 \epsilon_n}} \tag{2.42}$$

where ϵ_n is the complex permittivity of the corresponding tissue. The length of each section can be chosen according to the thickness values found in literature [78–81]. Using the TL modelling, we can calculate the total transmission coefficient T, which allows us to quantify the amount of incoming power that penetrates into the brain. This coefficient is defined as:

$$T = 1 - \Gamma \tag{2.43}$$

where Γ is the reflection coefficient at the section AA', which corresponds to the interface between the MTS and the skin (see Figure 2.8). This coefficient is defined as:

$$\Gamma = \frac{Z_{AA'} - Z_s}{Z_{AA'} + Z_s} \tag{2.44}$$

In the previous equation, Z_s is the impedance of the MTS and $Z_{AA'}$ represents the total impedance of the head, which can be evaluated according to the impedance transfer equation [82].

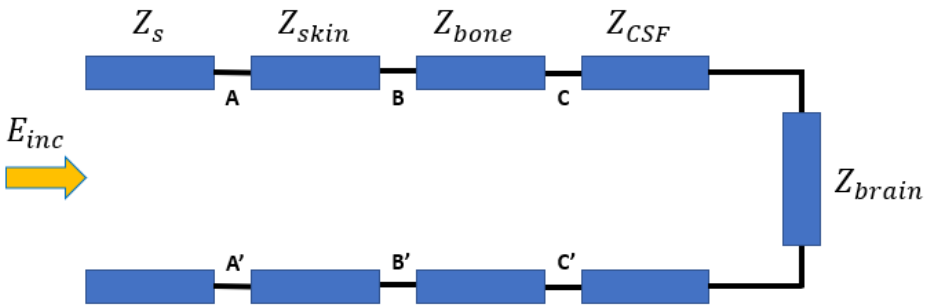

FIGURE 2.8: TL equivalent circuit of the human head, where Z_{skin}, Z_{bone}, Z_{csf} and Z_{brain} denote the characteristic impedances of skin, bone, CSF and brain, respectively. Z_s is the impedance of the MTS and $Z_{AA'}$ represents the total impedance of the head.

A way to design the MTS consists in minimizing the reflection coefficient Γ at the interface with the skin. Thus, once calculated the impedance that minimizes Γ, the optimal structural parameters to match the this impedance value can be retrieved (as explained in section 2.1.3).

Using a more complex approach, it is also possible to evaluate the impedance offered by the source. This can be retrieved using Schelkunoff's definition of wave impedance:

$$Z_{source} = Z_0 \frac{\frac{j}{k_0 r} + \frac{1}{(k_0 r)^2} - \frac{j}{(k_0 r)^3}}{\frac{j}{k_0 r} + \frac{1}{(k_0 r)^2}} \tag{2.45}$$

where Z_0 is the free space impedance, k_0 is the free space wave number and r is the distance from the source to the observation point. The impedance behaviour of the source (e.g., capacitive or inductive) is an important information that can be used for the MTS design. In particular, the MTS can be realized in order to show an impedance that mitigates Z_{source}. For example, for a short dipole, the impedance offered by the source shows a capacitative behaviour (Z_{source} = 238 - j106). Therefore, the matching-impedance MTS should mitigate this capacitive reactance. Based on this assumption, one of the possible MTS design could be a wire grid with an inductive behaviour [77].

Cascade connection of 2-port networks

Another approach to design a MTS for tissue-impedance matching is using a cascade connection of 2-port networks. Each 2-port network is characterized by an $ABCD$

matrix. A more detailed explanation of the $ABCD$ matrix and its relation with the S-Parameters is given in Appendix A. According to this formalism, the substrate of the MTS can be modelled as a lossless medium (ϵ''=0, σ=0) of thickness l and propagation constant β, whereas the metal grid can be linked to its admittance value Y_g. For simplicity, one could model the whole MTS stack, rather than each individual layer. Thus, the whole MTS can be modelled as an admittance matrix and the tissue slabs can be represented by TLs with losses.

For instance, if the MTS is applied on a skin slab (setup shown in Figure 2.9), the total ABCD matrix can be written as:

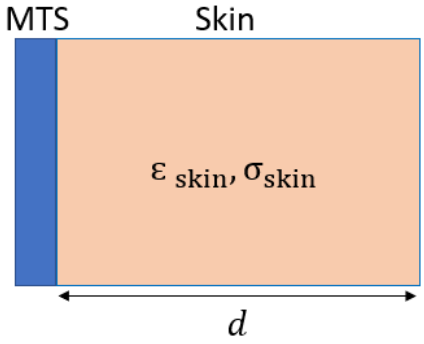

FIGURE 2.9: MTS applied on a skin slab of thickness d. This setup can be modelled as a 2-port cascade network.

$$\begin{bmatrix} A & B \\ C & D \end{bmatrix} = \begin{bmatrix} A_s & B_s \\ C_s & D_s \end{bmatrix} \begin{bmatrix} A_{skin} & B_{skin} \\ C_{skin} & D_{skin} \end{bmatrix} \tag{2.46}$$

with:

$$\begin{bmatrix} A_s & B_s \\ C_s & D_s \end{bmatrix} = \begin{bmatrix} 1 & 0 \\ Y_s & 1 \end{bmatrix} \tag{2.47}$$

$$\begin{bmatrix} A_{skin} & B_{skin} \\ C_{skin} & D_{skin} \end{bmatrix} = \begin{bmatrix} cosh(jk_0\sqrt{\epsilon_{skin}}d_s) & Z_{skin}sinh(jk_0\sqrt{\epsilon_{skin}}d_s) \\ \frac{1}{Z_{skin}}sinh(jk_0\sqrt{\epsilon_{skin}}d_s) & cosh(jk_0\sqrt{\epsilon_{skin}}d_s) \end{bmatrix} \tag{2.48}$$

where $ABCD_s$ and $ABCD_{skin}$ are the matrices which characterize the MTS and the skin, respectively. k_0 is the wave number in free space, d is the skin slab's thickness, ϵ_{skin} is the complex permittivity of the skin and $Z_{skin} = \frac{Z_0}{\sqrt{\epsilon_{skin}}}$ is the skin's characteristic impedance. The total $ABCD$ matrix can be then related to the S-parameter for transmission using the following equation:

$$S_{21} = \frac{2}{A + \frac{B}{Z_0} + CZ_0 + D} \tag{2.49}$$

At this point, the S_{21} parameter can be maximized and the optimal admittance Y_s for the MTS can be found. Finally, this admittance can be related to the structural parameters of the unit cell (as discussed in section 2.1.3).

Numerical modelling

As discussed in the previous subsections, analytical methods can be used to calculate the equivalent impedance (Z_s) or admittance (Y_s) of the periodic MTS and correlate it to the dimensions of the metallic features. However, analytical methods are not always possible to implement. For example, for more complex structures containing multiple metallic features (such as the unit cell presented in Chapter 3), there is no analytical expression for Z_s, and more accurate results are obtained by performing full-wave simulations and optimisation of the whole MTS stack. Furthermore, numerical methods allow us to take into account the tissue's inhomogeneous structure at the design stage, without introducing any computational complexity. In this thesis, all the MTS structures designed for impedance-matching purposes were modelled using CST and were optimized in order to achieve an increased transmission through complex multi-layer biological tissues. For instance, the MTS unit cell presented in Chapter 3 has been designed to maximize transmission through a planar head model comprising seven tissue layers. It is also important to point out that, to the end of modelling MTSs for tissue impedance-matching, it might be convenient to optimize the whole structure (e.g., number of unit cells) in front of the illuminating antenna. Thus, it might be useful to take advantage of numerical software to simulate the MTS layer in front of the antenna model.

2.2 Microwave Imaging

Microwave-based imaging refers to the image reconstruction process of an object using microwave frequencies. Diagnostic approaches in microwave brain imaging include both microwave tomography (MWT) as well as radar techniques, which can provide faster image processing [83]. MWT is a form of quantitative imaging technique. The reconstructed image using MWT estimates the complex permittivity distribution of different tissues inside the part of the body which is illuminated by EM waves. In contrast, radar algorithms employed by ultra-wideband (UWB) head imaging systems, for example, provide only qualitative information. This means that the permittivity values of different tissues inside the brain are not estimated, but rather a map of strong scattered energy is produced.

2.2.1 Microwave Tomography Imaging

The MWT imaging problem is a specific example of what is known as EM inverse scattering. Given the incident field(s) and the EM characteristic of the background medium (ϵ_b,μ_b), the problem consists of determining the EM and morphologic properties of a scattering system from the measurement of the scattered field(s).

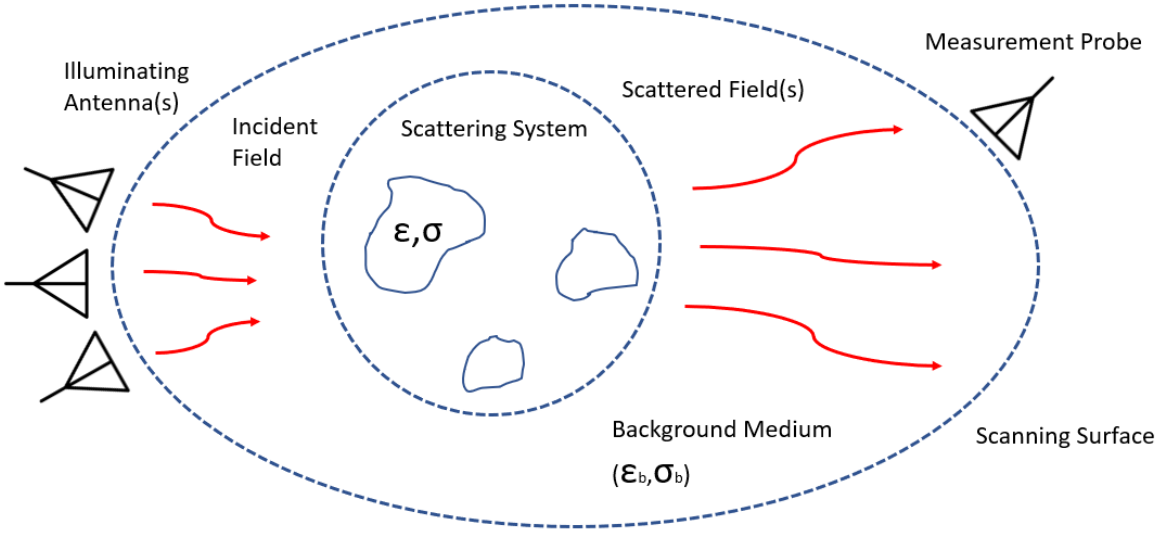

FIGURE 2.10: Schematics of inverse scattering problem.

Direct (forward) scattering problem

The direct EM scattering problem satisfies the following Helmholtz equation:

$$\nabla \times \frac{1}{\mu} \nabla \times \vec{E}(r) - \omega^2 \epsilon \vec{E}(r) = -j\omega \vec{J}_0(r) \tag{2.50}$$

where r is the position vector and $\vec{J}_0$ is the source. The behaviour of the electric field can be described in terms of the system impulse response. Since both the input (excitation current) and the output (field quantities) are vector quantities, the impulse response must be a dyadic quantity. The solution of equation 2.50 inside a region V is given by:

$$\vec{E}(r) = -j\omega\mu \int_V \vec{J}_0(r') \cdot G(\vec{r'}, r) dr' \tag{2.51}$$

where $\vec{G}$ is the dyadic Green's function (impulse response for free space) [84]. The formulation of the dyadic Green's function is given below:

$$\begin{aligned}\vec{G}(r',r) &= [I + \frac{\nabla'\nabla'^2}{k}]g(r',r) \\ &= \begin{bmatrix}1 & 0 & 0\\ 0 & 1 & 0\\ 0 & 0 & 1\end{bmatrix} g(r,r') + \begin{bmatrix}\frac{\partial^2}{\partial x^2} & \frac{\partial^2}{\partial x\partial y} & \frac{\partial^2}{\partial x\partial z}\\ \frac{\partial^2}{\partial y\partial x} & \frac{\partial^2}{\partial y^2} & \frac{\partial^2}{\partial y\partial z}\\ \frac{\partial^2}{\partial z\partial x} & \frac{\partial^2}{\partial z\partial y} & \frac{\partial^2}{\partial z^2}\end{bmatrix} \\ &= \begin{bmatrix}k^2 + \frac{\partial^2}{\partial x^2} & \frac{\partial^2}{\partial x\partial y} & \frac{\partial^2}{\partial x\partial z}\\ \frac{\partial^2}{\partial y\partial x} & k^2 + \frac{\partial^2}{\partial y^2} & \frac{\partial^2}{\partial y\partial z}\\ \frac{\partial^2}{\partial z\partial x} & \frac{\partial^2}{\partial z\partial y} & k^2 + \frac{\partial^2}{\partial z^2}\end{bmatrix} \frac{g(r',r)}{k^2}\end{aligned} \tag{2.52}$$

where

$$g(r',r) = \frac{e^{ik|r'-r|}}{4\pi|r'-r|} \tag{2.53}$$

is the scalar Green's function. As $\vec{G}(r',r) = \vec{G}^T(r,r')$, 2.51 can be also written as:

$$\vec{E}(r) = -j\omega\mu \int_V \vec{G}(r,r') \cdot \vec{J}_0(r')dr' \tag{2.54}$$

Inverse scattering problem

Subtracting the known background terms $\nabla \times \frac{1}{\mu_b}\nabla \times \vec{E}(r) - \omega^2\epsilon_b\vec{E}(r)$ from both sides of equation 2.50, the following inverse scattering equation is obtained:

$$\nabla \times (\frac{1}{\mu} - \frac{1}{\mu_b})\nabla \times \vec{E}(r) - \omega^2(\epsilon - \epsilon_b)\vec{E}(r) = -j\omega\vec{J}_0(r) - \nabla \times \frac{1}{\mu_b}\nabla \times \vec{E}(r) + \omega^2\epsilon_b\vec{E}(r) \tag{2.55}$$

The solution of 2.54 can be obtained as:

$$\begin{aligned}\vec{E}(r) = -j\omega \int_V \mu_b\vec{G}(r,r') \cdot \vec{J}_0(r')dr' + \omega^2 \int_V \mu_b(\epsilon - \epsilon_b)\vec{G}(r',r) \cdot \vec{E}(r')dr' \\ - \int_V \mu_b\vec{G}(r,r') \cdot \nabla' \times (\frac{1}{\mu} - \frac{1}{\mu_b})\nabla' \times \vec{E}(r')dr'\end{aligned} \tag{2.56}$$

where the first term on the right side of the equation is the known incident field $\vec{E}_{inc}(r')$. For $\mu_b = \mu$, 2.55 is reduced to:

$$\vec{E}(r) = \vec{E}_{inc}(r) + \omega^2\mu_0\epsilon_0 \int_V \delta_\epsilon(r')\vec{G}(r,r') \cdot \vec{E}(r')dr' \tag{2.57}$$

where $\vec{E}$ is the total field, $\delta_\epsilon = \epsilon_r(r') - \epsilon_b(r')$ is the contrast of the relative permittivity, and the integral term (extended to the reconstruction region V) contains information on the scatter. This equation is non-linear, due to the fact that the total field is related to the permittivity's contrast. As the electric field $\vec{E}$ is unknown inside the reconstruction domain, approximations are needed. Born approximation replaces the total field $\vec{E}(r)$

inside the integral term with the known incident field $\vec{E}_{inc}(r)$:

$$\vec{E}(r) \approx \vec{E}_{inc}(r) \tag{2.58}$$

Thus, it follows that:

$$\vec{E}(r) \approx \vec{E}_{inc}(r) + \omega^2 \mu_0 \epsilon_0 \int_V \delta_\epsilon(r') \vec{G}(r, r') \cdot \vec{E}_{inc}(r') dr' \tag{2.59}$$

The equation above is the so-called "first-order Born approximation" and it is valid for solving weak scatterer problems [85].

Distorted Born iterative method

The distorted Born iterative method (DBIM) is an iterative algorithm for solving the EM inverse scattering problem, which is used to estimate the spatial distribution of the tissue's dielectric properties inside a region V of the human body [86]. The 2D DBIM considers that the non-linear inverse scattering problems for each transceiver pair is linearized and approximated by the following equation:

$$\vec{E}_s(r_n, r_m) = \vec{E}_t(r_n, r_m) - \vec{E}_b(r_n, r_m) = \omega^2 \mu_0 \epsilon_0 \int_V \delta_\epsilon(r) \vec{G}(r_n, r) \cdot \vec{E}_b(r, r_m) dr \tag{2.60}$$

where E_t, E_s, E_b are the total, scattered and background electric fields, respectively, r_n and r_m are the transmitting and receiving antenna locations, ω is the angular frequency, μ_0 is the permeability of free space, ϵ_0 is the permittivity of free space, and $\vec{G}$ is the Green's function for the background medium:

$$\vec{G}(r_n, r) = \frac{j}{\omega \mu_0 I} \vec{E}_b(r, r_n) \tag{2.61}$$

The difference δ_ϵ between the relative complex permittivity of the reconstructed region, $\epsilon_r(r)$, and the background medium, $\epsilon_b(r)$, is defined as: $\delta_\epsilon(r) = \epsilon_r(r) - \epsilon_b(r)$. The scalar integral equation above assumes 2D transverse-mode propagation, and is only an approximation of the 3D inverse problem at hand. Despite this loss in information, the 2D approximation can produce images of acceptable quality in many MWI problems arising in medical applications.

At each DBIM iteration i, the integral equation can be discretized for each transceiver pair as:

$$\vec{E}_s(r_n, r_m) = \omega^2 \mu_0 \epsilon_0 \sum \delta_\epsilon(r) \vec{G}(r_n, r) \cdot \vec{E}_b(r, r_m) \tag{2.62}$$

leading to an ill-posed linear system as:

$$\mathbf{A}\delta_\epsilon = b \tag{2.63}$$

where $\mathbf{A}$ is an $M \times N$ matrix ($M \ll N$) and b is the $M \times 1$ vector of the scattered fields. M is the number of transmitting-receiving pairs and N are the voxels of the reconstruction region V. The matrix $\mathbf{A}$ is calculated at each DBIM iteration by the forward solver, which provides $\vec{E}_b$ for a known background ϵ_b. The background field is used to build the linear system above, which is then solved by an inverse solver. Finally, the background profile is updated by $\epsilon_b^{i+1}(r) = \epsilon_b^i(r) + \delta_\epsilon(r)$ and the DBIM continues to next iteration $i+1$. The forward solver uses the finite difference time domain (FDTD) method. This method simulates the EM wave propagation of the direct, "forward" problem based on Maxwell's equations. Furthermore, this implementation uses a single-pole Debye model to model frequency-dependent materials, such as brain tissues, as:

$$\frac{\varepsilon}{\varepsilon_0} = \varepsilon_\infty + \frac{\Delta\varepsilon}{1 + j\omega\tau} + \frac{\sigma_s}{j\omega\varepsilon_0} \tag{2.64}$$

The system in 2.63 is ill-posed because it does not satisfy the Hadamard's conditions, which define well-posed problems. According to these conditions, a well-posed problems should have the properties that a solution exists, the solution is unique and it is continuously depending on the initial conditions. To guarantee a reliable solution for the considered inverse scattering problem, advanced inverse solvers are required. For this purpose, iterative solvers are usually used, because they are more robust respect with direct solvers.

Iterative shrinkage/thresholding methods

The two-step iterative shrinkage/thresholding (TwIST) algorithm is employed as the solver of the ill-posed linear inverse problem at each DBIM iteration. Thresholding algorithms solve the ill-conditioned linear system $Ax = b$, by finding a solution x which minimizes the least squares error function as $F(x) = \frac{1}{2}\|Ax - b\|^2 + \lambda\|x\|_1$. The regularization term $\lambda\|x\|_1$ stabilizes the solution by limiting its l_1-norm. The general structure of the TwIST algorithm for solving this minimization problem is given by [87]:

$$\begin{aligned} x_{t+1} &= (1-\alpha)x_{t-1} + (\alpha-\beta)x_t + \beta C_\lambda(x_t) \\ C_\lambda(x) &= \Psi_\lambda(x + A^T(y - Ax)) \end{aligned} \tag{2.65}$$

The parameters for the TwIST algorithm are calculated as:

$$\kappa = \frac{\xi_1}{\xi_m} \tag{2.66}$$

$$\rho = \frac{1-\sqrt{\kappa}}{1+\sqrt{\kappa}} \tag{2.67}$$

$$\alpha = \rho^2 + 1 \tag{2.68}$$

$$\beta = \frac{2\alpha}{\xi_1 + \xi_m} \tag{2.69}$$

where ξ_1 and ξ_m are the smallest and largest eigenvalues of $A^T A$, respectively. The shrinkage/thresholding operation is a soft-thresholding function, calculated as $\Psi_\lambda(x) = sign(x)\max\{0, |x| - \lambda\}$. At each TwIST step, the new solution is updated based on two previous solutions and the soft-thresholding operation. As the linear system can be extremely ill-conditioned for MWI problems, the TwIST parameters above must be optimised specifically for the problem at hand [88].

The stopping criterion of the TwIST algorithm can be set based on a tolerance value, which is the normalised difference between the previous and current values of $F(x)$ and is defined as $tol = \frac{F(x_{k+1})-F(x_k)}{F(x_k)}$. The TwIST algorithm stops when tol is smaller than a preset value, usually in range between 10^{-4} and 10^{-1}. This early termination of the iterative algorithm serves as additional regulator, with a similar effect to the Tikhonov approach [86]. The Tikhonov regularisation is another inverse solver for linear systems, which minimises the function $F(x) = \frac{1}{2}||Ax - b||_2^2 + ||\Gamma x||_2^2$ for some chosen Tikhonov matrix $\Gamma = \alpha I$. This regularisation improves the conditioning of the problem and enables to express the solution as $x = (A^T A + 2\alpha^2 I)^{-1} A^T b$ [85].

The l_1-problem $F(x) = \frac{1}{2}\|Ax - b\|^2 + \lambda\|x\|_1$ can be regularised further by employing the Pareto curve method, which provides the optimal trade-off between the residual error $\|Ax - b\|^2$ and the norm of the solution $\|x\|_1$ (similar to the L-curve method for l_2-problems) [89]. To reduce the computational cost, a practical approach for selecting λ is based on the form $\lambda = \delta\|A^T b\|_\infty$, where δ is factor with $0 < \delta < 1$ [89].

2.2.2 Ultra-wideband Radar Imaging

In contrast to tomography, the UWB radar approach solves a simpler computational problem by seeking only to identify the significant scatterers [90, 91]. In order to reconstruct the image, beam-forming techniques of varying complexity are required. Current beam-forming techniques use time domain processing algorithms. One method is confocal imaging which employs simple delay-and-sum beam-forming [92]. Time-reversal (TR) based approaches have also been proposed in [93]. TR is based on the following assumption: if the scattered fields at the receiver are time-reversed and computationally re-radiated into the medium, focusing is achieved at the source point.

In this thesis, an imaging method based on the Huygens principle (HP) is used. The HP states that: "Each locus of a wave excites the local matter which re-radiates a secondary wavelets, and all wavelets superpose to a new, resulting wave (the envelope of those wavelets), and so on" [94]. Therefore, we consider what would happen if we apply the HP using the field measured on the external surface of the object under investigation as locus of a wave. Then, in order to exploit such a strategy, the field inside the object is calculated as the superposition of the fields radiated by the observation points. Using HP to forward propagate the waves removes the need to solve inverse problems and, consequently, no matrix generation/inversion is required [95].

Formulation of the Huygens Principle-based Algorithm

The radar-based Huygens algorithm, initially presented in [96], has already shown its potential for use in medical applications in [97, 98]. Considering an imaging region of interest such as the human head which is illuminated by a transmitter TX_m (operating at a frequency range f_i) and R receivers (with receiver r at location ρ_r measuring the field $E_{rm}(f_i)$ from transmitter m at frequency f_i), the Huygens algorithm measures the field on the external surface of the medium $E_{rm}(f_i)$ and back-propagates it virtually inside the imaging domain. In this way, the internal field within the medium is reconstructed as:

$$E_{\mathrm{HP}}(\rho, m, f_i) = \sum_{r=1}^{R} E_{rm}(f_i) G(k|\rho_r - \rho|) \tag{2.70}$$

where $G(k_1|\rho_r - \rho|) = \frac{1}{4\pi} e^{-jk_1|\rho_r - \rho|}$ indicates the Green's function as defined in [96] at locations ρ, while k represents the complex wave number of the background medium. It should be pointed out that the algorithm uses the free space Green's function instead of 0-th order Hankel function for 2D radar reconstructions. This has been done to preserve a better generalization of the algorithm and a uniform formulation for a future extension to 3D imaging scenarios [99].

To calculate the total intensity, all the transmitting positions and all the recorded frequencies are summed incoherently as shown below:

$$I_{\mathrm{HP}}(\rho) = \sum_{m=1}^{M} \left[\sum_{i=1}^{I} E_{\mathrm{HP}}(\rho, m, f_i) \right]^2 \tag{2.71}$$

Chapter 3

Impedance-Matching Metasurface for Brain Imaging

This chapter presents the microwave brain imaging prototype developed by King's College London (KCL) and proposes an innovative metasurface (MTS) design as a hardware advancement for this system. This MTS structure has been incorporated in different setups, and its interaction with electromagnetic (EM) waves has been studied both experimentally and by using CST Microwave Studio®. The results presented in this chapter show that the proposed MTS can enhance the penetration of the transmitted signals into experimental and numerical human head phantoms. This leads to an improvement of the transceivers' ability to detect useful "weak" signals, which may translate in higher-quality reconstruction images. It is important to emphasize that the proposed MTS film has been tested on two different types of monopole antennas. The near-field characterization of these antennas and their design process and optimization are reported in the references provided throughout the thesis. In particular, the design process and experimental comparison of these antenna is reported in [100, 101]. The enhancement in the imaging reconstruction process obtained for both the antenna designs (using tomographic and radar-based algorithms) strengthens the claim of the MTS having a positive impact on microwave brain imaging.

3.1 Microwave Brain Imaging Prototype for Brain Stroke Detection and Differentiation

Figure 3.1 shows the custom-made microwave imaging (MWI) setup [102] developed by KCL, which is compatible for both radar and tomographic configurations. This setup comprises a 300 mm diameter cylindrical tank, shielded by an RF absorbing sheet from Laird Technologies. The transmitting and receiving antennas are positioned in a circular ring inside the acrylic tank and surround the head phantom model shown in Figure 3.1. Vertical and horizontal mounts are used to adjust the position of

the antennas with precision and accuracy. Transmitter and receiver are connected to the multi-port vector network analyser (VNA) Keysight M9019A.

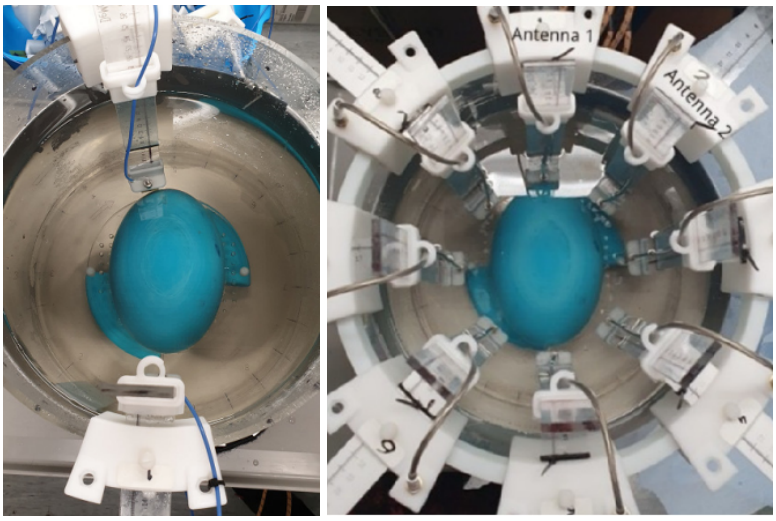

(**a**) (**b**)

FIGURE 3.1: Measurement hardware and setup for (**a**) radar, and (**b**) tomography.

For tomography measurements, an elliptical 8-antenna array is immersed inside the tank. The 8 antennas are positioned as close as possible to the head phantom's external surface and perform both as receivers and transmitters, creating an 8×8 scattering matrix which is fed into the two-dimensional (2D) DBIM-TwIST algorithm. Meanwhile, only two antennas are used for the radar measurements, one performing as transmitter, and the other as receiver. For each radar-based measurement, the transmitting antenna is positioned 30 mm away from the elliptical brain phantom at its larger axis of 170 mm, while the receiving antenna is placed closer at only 10 mm away from the largest axis of the brain phantom. For each transmitter position, the receiving antenna is rotated radially (anti-clockwise) with 15° steps, measuring the external field of the phantom at 24 receiving positions. Both types of measurements record a frequency band of 0.5 to 2 GHz. In all cases, the antennas are immersed in a 90% glycerol-water mixture (with permittivity of $\approx$17 at 1 GHz), which is used as matching medium. This solution is obtained by mixing 9 L of glycerol and 1 L of distilled water. The permittivity value of the matching medium was chosen in order to ensure acceptable spatial resolution images [22].

The head model, which represents only the upper portion of the head, is also immersed inside the matching medium contained in the imaging tank. In a practical system, this could be achieved, for example, by delimiting the imaging chamber with a membrane where the head conforms to. The coupling liquid is supposed to cover

only part of the head, similarly to the chamber shown in [23]. The head model consists of a three-dimensional (3D) printed ABS (Acrylonitrile Butadiene Styrene) elliptic mould, containing a gelatin-oil mixture based on the phantom preparation method described in [103]. The 3D printed mould with a length of 170 mm and width of 120 mm was used as a holder for the liquid phantom that, once solidified, can mimic the brain. Furthermore, it acts as an additional phantom layer during image reconstruction.

The haemorrhagic or ischaemic stroke is mimicked by inserting a cylindrical target of 30 mm diameter in the gel-based brain phantom. This is done through creating a hole in the phantom, and extracting a part of the brain mixture using a cylindrical mould, resulting in the creation of a cylindrical cavity with a diameter of 30 mm. Next, the cavity is filled with gel phantoms resembling the bleeding in haemorrhagic stroke or the low-oxygenated tissue in ischaemic stroke. An accurate description of the phantom preparation methodology is illustrated in Section 3.4.2.

3.2 Metasurface Design

3.2.1 Unit Cell Metasurface Design

The MTS design proposed in this chapter is based on simulation studies to achieve a transmission improvement through lossy biological tissues. To this end, a first MTS unit cell was designed to act as an impedance-matching layer in the presence of a simplified planar model of the head. The design of the unit cell was initially based on a plane wave analysis inspired by [25, 104]. This analysis is tailored to the desired operation bandwidth (selected as 0.5-2.0 GHz for our head imaging application) and is based on a slab model of tissue layers interacting with the MTS [105]. The planar head model is shown in Figure 3.2, and comprises seven flat tissue layers placed in the following order: skin, cortical bone (outer layer), cancellous bone, cortical bone (inner layer), cerebrospinal fluid (CSF), grey matter and white matter. Grey and white matter make up the central nervous system. In the brain, the grey matter is the outermost layer, whereas white matter is the deeper brain tissue. CSF forms a liquid cushion that protects the brain and also helps it to receive nourishment. Cancellous bone separates the inner and outer layers of the cortical bone of the skull. The thickness of the different tissues are reported in Table 3.1. The dielectric properties of the tissues at 1 GHz were taken from [106]. The interaction of this setup with a linearly polarized plane wave in the 0.5–2 GHz frequency range was modelled in CST. The S-parameters were calculated considering "Port 1" before the lossy dielectric medium (thickness = 5 mm, permittivity ϵ' = 18 and conductivity σ= 1.3 S/m at 1 GHz) and "Port 2" after the white matter layer.

FIGURE 3.2: Simulation setup with planar head model comprising seven tissue layers. The thickness of each tissue's slab is indicated in the table below (Table 3.1).

TABLE 3.1: Thickness of each tissue's slab for the planar head model shown in Figure 3.2.

Numbering	Tissue	Thickness
1	Skin	2.8 mm
2	Cortical bone (outer layer)	1.8 mm
3	Cancellous bone	2.3 mm
4	Cortical bone (inner layer)	1.4 mm
5	CSF	4.2 mm
6	Grey matter	2.5 mm
7	White matter	56.6 mm

The first MTS unit cell design (MTS1) is shown in Figure 3.3a and comprises a Jerusalem cross metallic lattice (thickness = 0.10 mm) embedded between two Rogers 3010 TM substrates (thickness = 1.27 mm, $\epsilon' = 10.2$ and $\tan\delta = 0.0022$). The two Rogers high-dielectric substrates are bonded with Rogers 3001 bonding film ($\epsilon' = 2.28$, $\tan\delta = 0.003$), as shown in Figure 3.3c.

This design was optimized manually until the performance achieved was close to the expected. In particular, as shown in Figure 3.3b (MTS2), variations in the classic Jerusalem cross design were introduced in order to reduce the reflection coefficient at 1 GHz. After that, the CST's optimizer tool "Trust Region Framework" algorithm was used to tune the wires' dimensions, setting maximum transmission across all the frequency range (0.5-2 GHz) as a goal. Figure 3.4a shows that the introduction of additional metal wires in the simple Jerusalem cross structure reduced reflection by about 3 dB at 1 GHz. In the presence of this second unit cell (MTS2), the transmission parameter is improved by about 1.5 dB in the whole frequency range with respect to the "no MTS" case-scenario. In the "no MTS" configuration, the MTS unit cell is replaced by additional dielectric medium.

The change in the reflection parameter due to the additional metallisation can be easily understood by modelling the metal sections using a lumped LC network analogy [107]. Each resonator is linked to a different equivalent circuit model. The metal

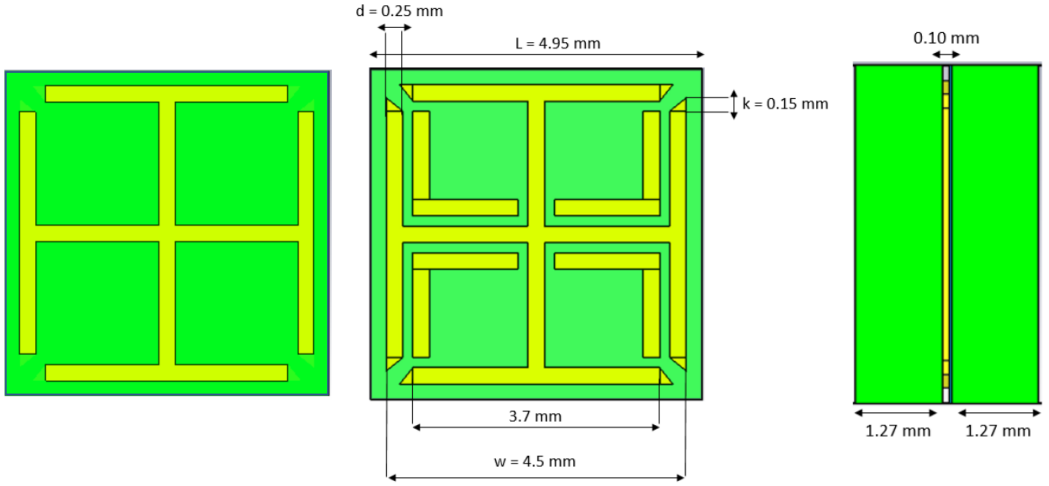

FIGURE 3.3: (**a**) First MTS unit cell design (MTS1) comprising a Jerusalem cross copper lattice embedded between two high-dielectric substrates. (**b**) MTS2 design, including additional metal wires in the simple Jerusalem cross structure. (**c**) Side-view of the MTS unit cells, showing the two Rogers high-dielectric substrates embedding the copper lattice.

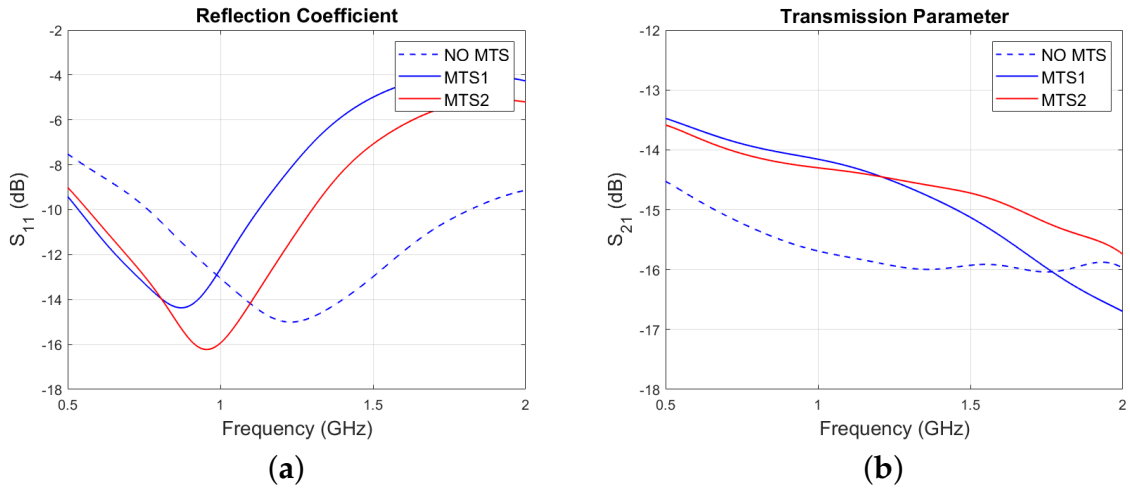

FIGURE 3.4: (**a**) Reflection parameter comparison between MTS1 and MTS2, and (**b**) transmission comparison between MTS designs and in the absence of MTS.

wires in the last design represent additional inductances and introduce new gap capacitances in the Jerusalem cross equivalent circuit shown in Figure 3.5, producing new inductive and capacitive effects.

The permittivity and permeability values for the unit cell of Figure 3.3b (MTS2) are shown in Figure 3.6. To extract these values from the S-Parameters, boundary conditions E_t=0 were assigned along the X-axis direction and boundary conditions H_t=0 were assigned along the Y-axis. Input/output ports were set along the Z-axis

FIGURE 3.5: Jerusalem cross equivalent circuit.

direction. From Figure 3.6, we can observe that both permittivity and permeability are close to zero. The real part of permittivity becomes negative in the 3.6-5 GHz frequency range. MTSs characterized by double (ϵ<0 and μ<0) or single negative (ϵ<0 and μ>0 or ϵ>0 and μ<0) structure can exhibit independent electric (E) and magnetic (H) responses described by ϵ and μ. Typically, by adjusting the structural parameters of the unit cell, one can tailor permittivity and permeability to achieve the desired response. However, as pointed out in Section 2.1.3, the numerical simulation of a single unit cell does not always fully achieve the desired goals. Thus, in this thesis, the size of the unit cell was adjusted iteratively (using unit cell boundary conditions) to achieve maximum transmission across the head model of Figure 3.2.

3.2.2 Full Metasurface Structure

Based on the unit-cell results, a periodic structure based on the optimized unit cell geometry (MTS2) was studied. In particular, with the aim of simulating a setup that could be easily fabricated to carry on the first experiments, a 15×18 unit cell MTS structure was deigned in contact with a skin slab (thickness t_1 = 1 mm). No air gaps were left between the skin and the MTS. The simulation setup included two other tissue layers: cortical bone (t_2 = 2 mm) and brain (t_3 = 7 mm). A layer of 90% glycerol-water mixture (coupling liquid) was added on the right of the metamaterial (MM) film, similarly to the setup shown in Figure 3.2. The antenna ("Port 1") proposed in [102, 104] was used to excite the full setup in the 0.5-1.5 GHz frequency range. This antenna was accurately designed to be immersed in a water-glycerol mixture, in close proximity to the head model. The antenna was characterized by studying the return loss and the transmitted signal strength [108]. A similar study is reported in [109]. "Port 2" was placed after the brain model. The S-parameters for reflection and transmission are plotted in Figure 3.8b. The results show that the improvement in transmission caused by the finite MTS structure is close to the value calculated

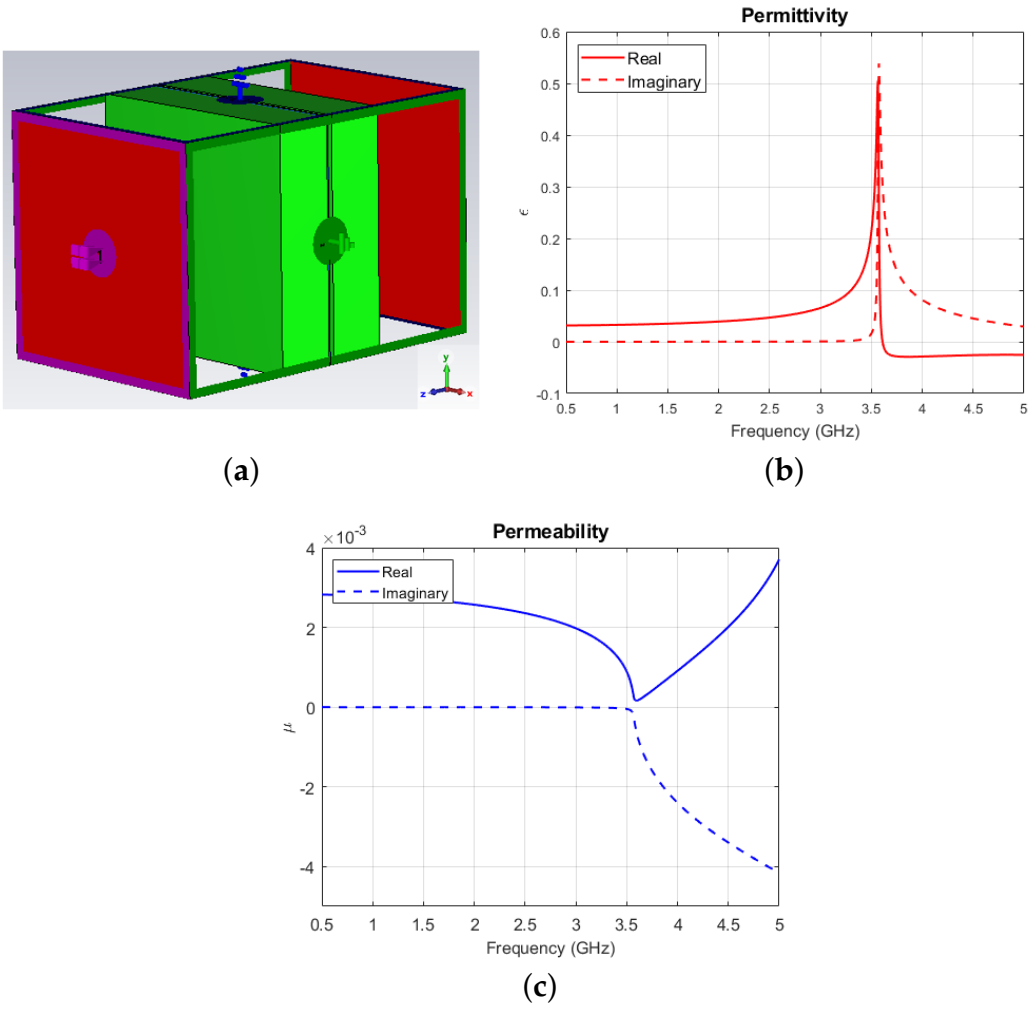

FIGURE 3.6: (**a**) Simulation setup to extract the unit cell's constitutive parameters. Boundary conditions E_t=0 are assigned along the X-axis direction and boundary conditions H_t=0 are assigned along the Y-axis. The input/output ports are set along the Z-axis direction. (**b**) Permittivity and (**c**) permeability for the unit cell shown in Figure 3.3. Both permittivity and permeability are close to zero. The real part of permittivity becomes negative in the 3.6-5 GHz frequency range.

with the unit cell approach in the previous section, suggesting that the 15×18 unit cell structure can approximate the unit cell MTS behaviour for the purposes of our application.

The following section will describe the characterization process of the adopted MTS design in detail. More specifically, the experimental testing of this impedance-matching MTS will be discussed. The results shown below demonstrate that a transmission improvement across several phantom models can be achieved by employing the proposed MTS. Furthermore, Section 3.5 and Section 3.6 demonstrate how improvements in the reconstructed images of a blood-mimicking target can be achieved by integrating the MTS in KCL's brain scanner.

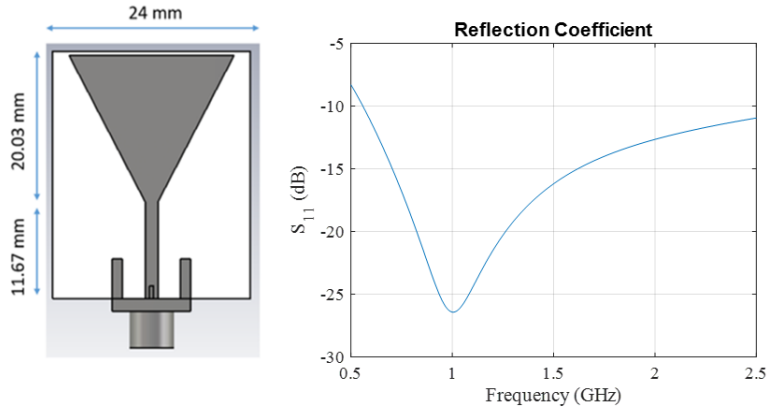

FIGURE 3.7: Design and reflection coefficient (S_{11}) of the antenna used as excitation source: The antenna consists of a triangular patch on a FR-4 substrate, with a partial ground on the back side. The S_{11} presents a deep resonance at 1 GHz, where S_{11} falls below -25 dB [104].

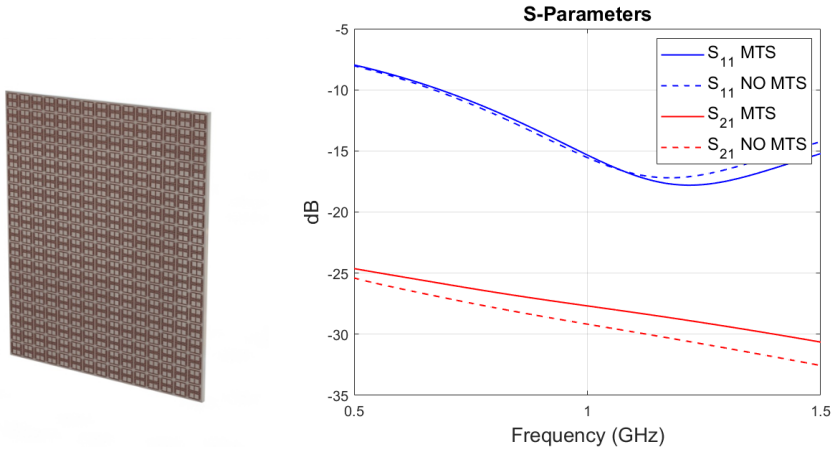

(**a**) (**b**)

FIGURE 3.8: (**a**) Finite MTS periodic structure comprising an inner metallic pattern in between two high dielectric substrates and (**b**) simulation results for the transmission S_{21} and reflection S_{11} parameters with (solid lines) and without (dashed lines) the MTS, showing an improvement in transmission of about 1.50 dB at 1 GHz in the presence of the MTS.

3.3 Simulation and Experiments of a 2-Port Setup

3.3.1 Experimental Methodology

To study the performance of the 15×18 unit cell MTS, the 2-port custom-made experimental setup shown in Figure 3.9a and Figure 3.10a was designed and fabricated. This comprises five rectangular acrylic layers ($\epsilon' = 2.53$, $\tan\delta = 0.0119$) of 240 mm width, 215 mm height, and 16 mm thickness which are placed in series in between two acrylic

tanks (300 mm × 300 mm × 250 mm). Two triangular patch antennas, each immersed in a tank, are used to transmit and receive signals in the range of 0.5-4.0 GHz using Keysight's PXI VNA (M9370A). The tanks are filled with a lossy dielectric medium made of a 90% glycerol-water mixture, which is used as immersion liquid for the employed antennas [102]. The measurements were taken at three equal antenna distances of 100 mm, 110 mm, and 130 mm, whereas the MTS was positioned on the acrylic surface close to antenna 1 and guided to the correct position using a custom designed slider to avoid any errors caused by movement. When the antennas are placed at a distance of 100 mm, antenna 1 is in its closest position to the MTS (4 mm from it).

The middle five acrylic layers were filled with various liquid phantoms, which were made to resemble different types of human tissue. These liquid phantoms were easy to fabricate and were suitable for reproducing a simple planar model of the human head. Supported by the acrylic layers, the phantoms were stacked in the following order: skin ("Layer 1"), bone ("Layer 2"), brain or blood ("Layer 3"), bone ("Layer 4"), and skin ("Layer 5"). This head model is separated from the matching liquid contained in the tanks by acrylic walls. As discussed in Section 3.1, in a practical MWI scanner, we could use a membrane to separate the head from the liquid contained in the imaging chamber [23]. Each liquid phantom was prepared using different concentrations of water in glycerol. Then, the phantoms were validated by measuring their permittivity using a dielectric probe connected to the VNA. The real part of the measured permittivity at 1 GHz is shown in Table 3.2.

TABLE 3.2: Liquid phantom composition and permittivity at 1 GHz.

Type of Phantom	**Water (%)**	**Glycerol (%)**	ϵ'
Skin	30	70	38.2
Bone	10	90	13.2
Brain	35	65	42
Blood	50	50	59.4

To investigate the impact of the proposed MTS, measurements in different experimental scenarios were conducted. First, to assess the system's sensitivity to changes in permittivity of the inner layer ("Layer 3"), the transmitted signals without MTS were measured for "Layer 3" filled with different liquids: brain phantom, blood phantom, and horse blood in EDTA (Ethylenediaminetetraacetic Acid) from TCS Biosciences (Botolph Claydon, Buckingham, UK). EDTA has an anticoagulant function and allows the best preservation of cellular components and morphology of blood cells. Subsequently, the same measurements were taken in the presence of the MTS and differences in the transmission coefficient S_{21} with and without the MTS were calculated and compared. Furthermore, to demonstrate that the MTS is able to enhance

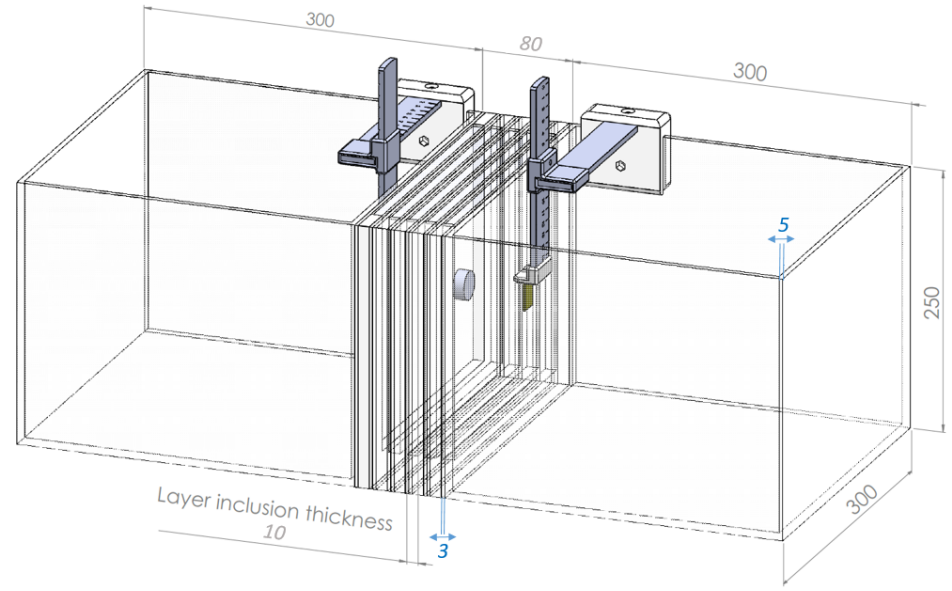

(a)

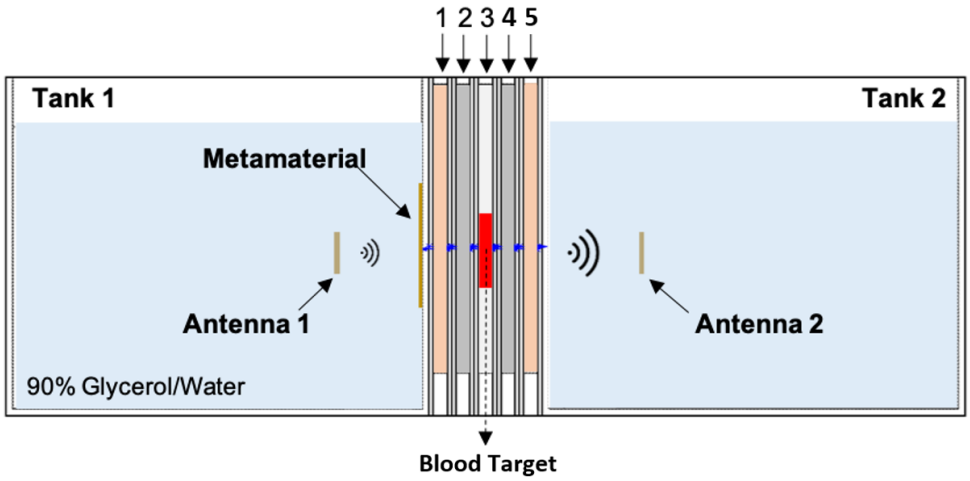

(b)

FIGURE 3.9: (**a**) Technical drawing showing the geometric dimensions of the setup expressed in millimetres. The antennas are fixed to adjustable holders. (**b**) Schematic design showing the setup in the "with target" configuration. The MTS is fixed on the acrylic surface, close to antenna 1.

the signal due to a blood-like target, a cylindrical capsule (25 mm diameter and 8 mm thickness) made of ABS ($\epsilon' = 2.74$, $\tan\delta = 0.0051$) and filled with horse blood in EDTA was included and centred in the inner layer of the setup. This blood-capsule inserted into the brain phantom is a simplified representation of a bleeding in the brain and is used as proof-of-concept to validate the MTS performance. Then, the signal difference "with target – no target" (in dB) was measured with and without the MTS. We refer to the basic setup configuration ("Layer 3" filled with brain phantom only) as the "no target" scenario. Figure 3.9b illustrates the "with target" configuration, consisting of

"Layer 3" filled with the brain phantom and including the blood capsule.

Representative configurations of the system described above were modelled using CST in the 0.5-2 GHz frequency range. As the liquid phantoms were correctly resembling the dielectric properties of all the tissues, values of permittivity and conductivity at 1 GHz were assigned from [106]. These values were already acceptable approximations of the phantom's dielectric properties for the frequency of interest. For the horse blood properties, dielectric values based on measurements (ϵ' = 58.7 at 1 GHz) were used. In addition, to further demonstrate the MTS's ability to enhance transmission, a "negative control" (NC) case was also considered, for which the MTS was replaced by a material with the same dielectric substrate and dimensions but without the metallic pattern. This allowed evaluating the effect due to the metallic pattern design.

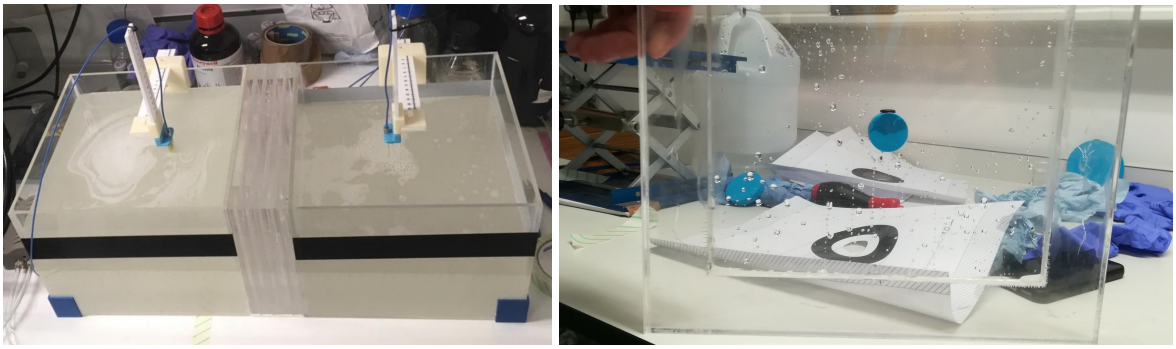

(**a**) (**b**)

FIGURE 3.10: (**a**) Experimental setup and (**b**) target capsule containing horse blood in EDTA, centered in Layer 3.

3.3.2 Results and Discussion

The experimental results shown in Figure 3.11a indicate that the measured transmission parameters vary with the dielectric properties of the liquid phantom contained in the inner layer. This demonstrates that the two-port planar system of Figure 3.10a is sensitive to changes in the dielectric properties of the inner acrylic layer. Furthermore, the MTS enhances transmission over the 0.5-1.5 GHz frequency range for all three cases of the inner layer filled with the brain phantom (Figure 3.11b), blood phantom (Figure 3.11c), or real horse blood (Figure 3.11d). In the presence of the MTS, the S_{21} coefficient is increased around 1-2 dB over the considered frequency range, with higher differences near 1.5 GHz. These measurements also suggest that, despite the physical limitations of the setup and the presence of the acrylic, which results in additional scattering, signal differences due to the MTS are still detectable. The results shown in Figure 3.11 were obtained for an antenna distance of 100 mm in the setup of

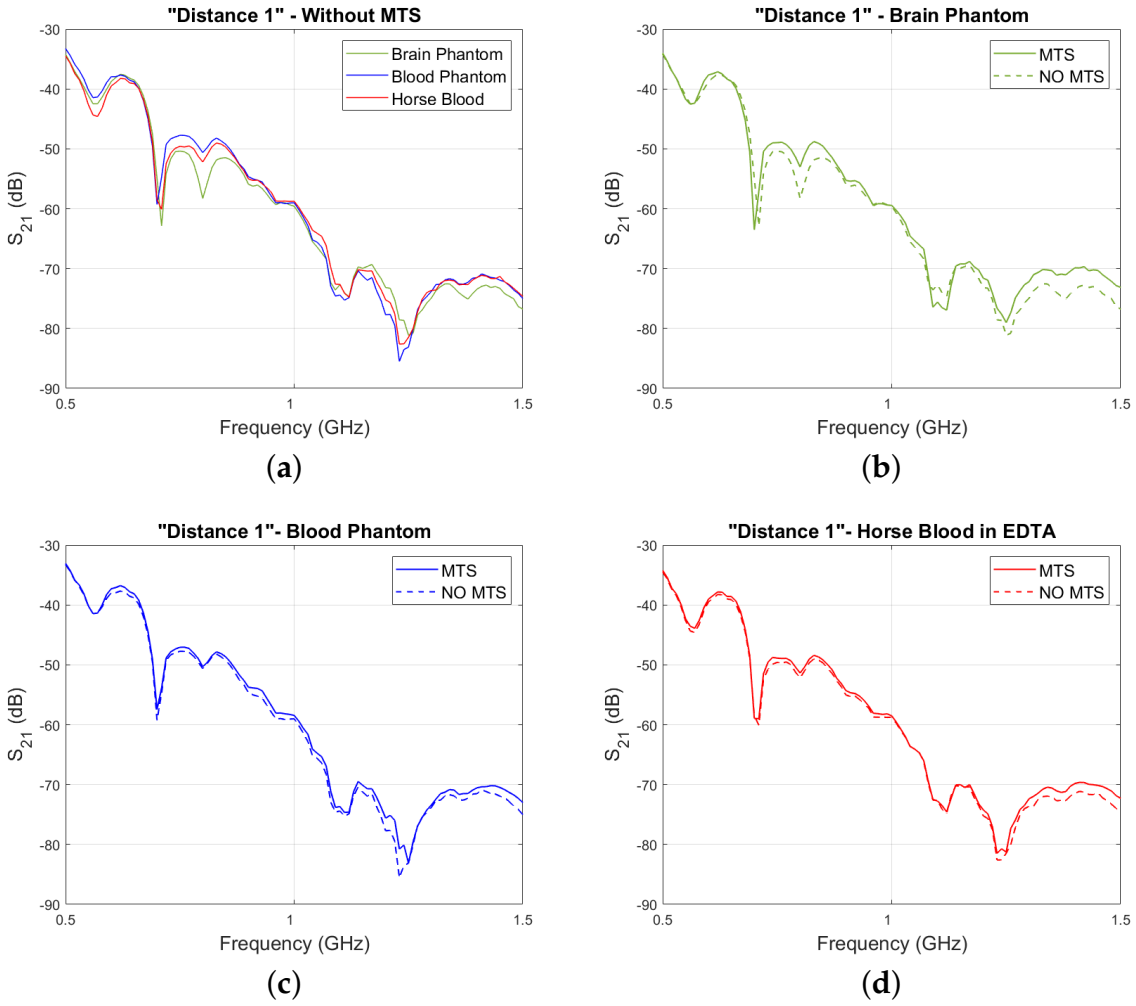

FIGURE 3.11: (**a**) Comparison of the experimentally measured transmission coefficient S_{21} for "Distance 1" without the MTS and with inner layer filled with brain phantom, blood phantom, and horse blood; (**b**) comparison of the experimentally measured transmission coefficient S_{21} for "Distance 1" with the MTS (solid lines) and without the MTS (dashed lines) when the inner layer is filled with the brain phantom, (**c**) with the blood phantom, and (**d**) with the horse blood in EDTA.

Figure 3.10a, which is the antennas' closest position to the MTS considered in these experiments (4 mm). We will refer to this configuration as "Distance 1". As the antennas in the brain scanner radiate in proximity of the head model, it is relevant to validate the MTS impact on the system when it is close to the antenna's substrate. Thus, we will focus on "Distance 1".

For the first case scenario ("Layer 3" filled with brain phantom), as shown in Figure 3.12a and Figure 3.12b, the transmission parameter was measured for other two different distances between the antennas: 110 mm and 130 mm, corresponding respectively to antenna 1 placed at 10 mm ("Distance 2") and at 20 mm ("Distance 3") from the MTS. In particular, the S_{21} parameter was first measured for all the distances with

the MTS. Then, the MTS was removed and the measurements were repeated. Thus, even if the antenna spacing was changing, the stability of the measurements was not significantly affected by the action of placing and removing the MTS in front of antenna 1. The simulations studies confirmed the experimental findings. For instance,

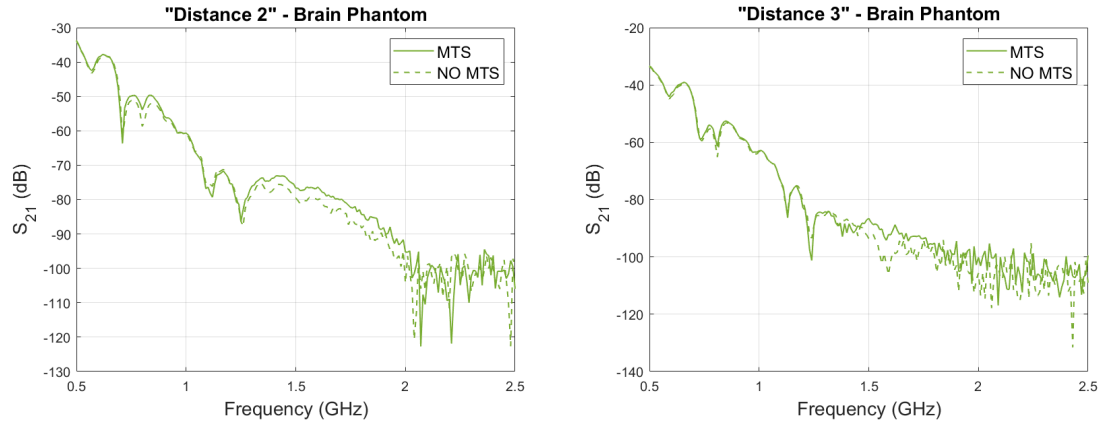

FIGURE 3.12: Experimentally measured transmission coefficient S_{21} with the MTS (solid lines) and without the MTS (dashed lines) when the inner layer is filled with the brain phantom for (**a**) "Distance 2" and (**b**) "Distance 3".

Figure 3.13 shows an overall slight increase in the S_{21} coefficient in the presence of the MTS, ranging from 1 to 3 dB in the considered frequency range. Importantly, this improvement is not observed for the NC material in these plots. These results suggest that the improvement in the transmitted signals is due to the unit cell's metallic pattern design and not to the partial replacement of the lossy immersion liquid with a lower-loss dielectric material. Furthermore, the experiments and simulations presented in this section demonstrate that the system is sensitive to changes in permittivity of the inner layer due to the "blood target" inclusion. To illustrate this, the signal difference "with target - no target" was calculated in dB and was shown to be higher in the presence of the MTS for both simulations and measurements. As the thickness of the cylindrical shell's surfaces is small (1 mm) and the ABS's permittivity is close to the acrylic's one, the ABS does not significantly affect the detectable signal difference obtained with and without the MTS. Experimental results are plotted in Figure 3.14a and show that the MTS increases the signal difference in the 0.5-0.65 GHz and 1-1.7 GHz frequency ranges. A very high signal difference of about 16.5 dB was measured around 1.1 GHz. Simulation results confirm these experimental findings. Figure 3.14b shows a similar trend and an overall enhancement of the signal difference in the 0.5-1.5 GHz frequency range. A NC case was also simulated and led to a lower signal difference than the one obtained with the MTS.

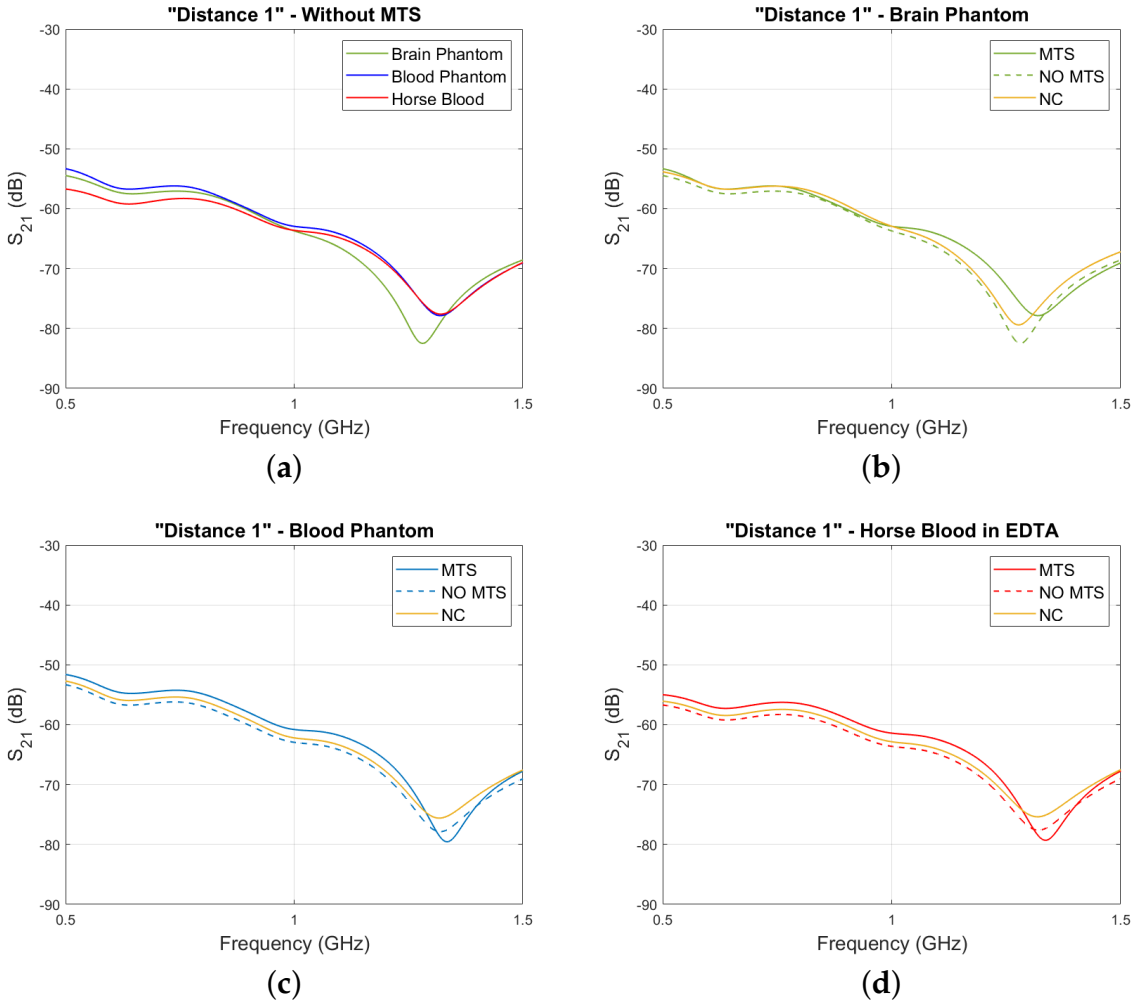

FIGURE 3.13: Same plots as Figure 3.11 for the simulated data: (**a**) comparison of the calculated transmission coefficient S_{21} without the MTS and with inner layer filled with brain phantom, blood phantom, and horse blood; (**b**) comparison of the calculated transmission coefficient S_{21} with the MTS (solid lines) and without the MTS (dashed lines) when the inner layer is filled with the brain phantom, (**c**) with the blood phantom, and (**d**) with the horse blood in EDTA. The same results for the "NC" case is plotted in yellow.

3.4 Simulations and Experiments of a Multi-Port Setup

With the aim of integrating the MTS into the brain imaging prototype described in Section 3.1, a new MTS structure was created by fitting the triangular patch antenna's surface with a suitable number of unit cells. Thus, keeping the unit cell design and size fixed, a 5×6 unit cell MTS was generated and radar and tomographic measurements were performed with the microwave multi-port system shown in Figure 3.1. It is important to emphasize that, aside from fitting the MTS to the antenna's dimensions, this design process does not require any further adjustment to the specific antenna design.

For the experimental investigation described in this section, 8 inverted triangular

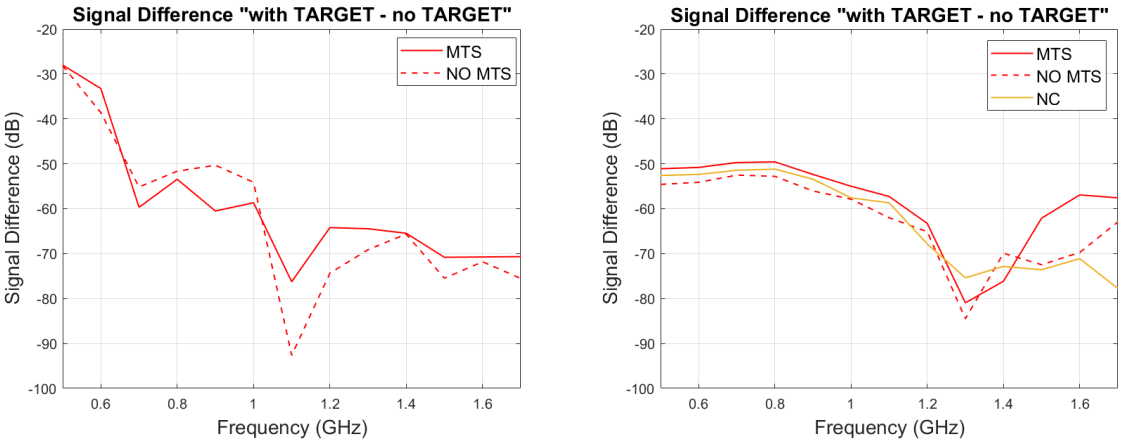

FIGURE 3.14: Signal difference "with target – no target" (dB) with (solid lines) and without (dashed lines) the MTS, which is due to the blood-filled spherical inclusion in Figure 3.10: (**a**) experimentally measured and (**b**) calculated from simulations. The same result for the "NC" case is plotted in yellow in Figure 3.14b.

patch antennas were used. Triangular antenna's photos both with and without MTS coating are depicted in Figure 3.15. An investigation carried out with the same MTS and a different type of monopole [17] is reported in Section 3.6. Before proceeding with the measurements, the experimental setup of Figure 3.1 was simulated in CST to check the functionality and performance of the MTS and the imaging algorithms described in Section 2.2 of Chapter 2.

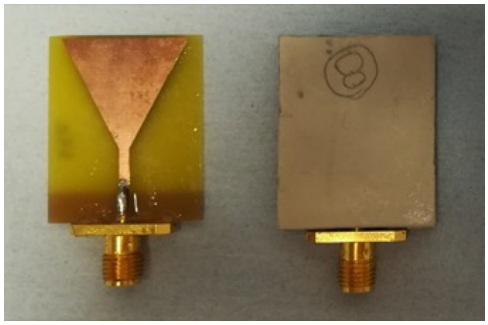

FIGURE 3.15: Triangular antenna without (left) and with MTS coating (right).

3.4.1 Impact of MTS on Antenna Performance

As shown in Figure 3.15, the MTS-enhanced antenna used for this investigation consists of the triangular antenna described in Section 3.2.2, plus a MTS superstrate loading (24.75 mm $\times$ 29.7 mm), based on the unit cell illustrated in Figure 3.3b.

Before studying the 8-port system, the interaction between two antennas in the near-field was studied in CST. Reflection and transmission parameters were calculated

(with and without MTS) for two different setups. The first setup includes two antennas placed at a distance of 127 mm and immersed in a tank filled with 90% glycerol-water mixture. The second setup includes the lossy matching medium and our elliptical head phantom. This head model includes an external plastic layer (ϵ = 2.56; tan δ = 0.0119) and average brain tissue inside (ϵ = 45.8; σ = 0.76 S/m). The antennas were closely fixed on the elliptical head phantom, along its smallest dimension, at a distance of 127 mm.

Figure 3.16 shows that the transmission coefficient S_{21} is considerably higher in the presence of the MTS in both cases, while the antenna's reflection coefficient S_{11} is not enhanced by the MTS. The transmission enhancement in Figure 3.16b is much higher than the 1.5-2 dB observed in Figure 3.11b. This may be due to the fact that a much simpler phantom (with fewer reflection layers and much lower total loss) is used in this study. It is important to notice that the MTS's impedance-matching property refers to this transmission enhancement, rather than to improving the impedance match of the antenna itself. However, improving the antenna's impedance-match is also possible, as shown in Section 3.6 with spear patch antennas, where improvements in both transmission and reflection measured coefficients were observed when using the MTS.

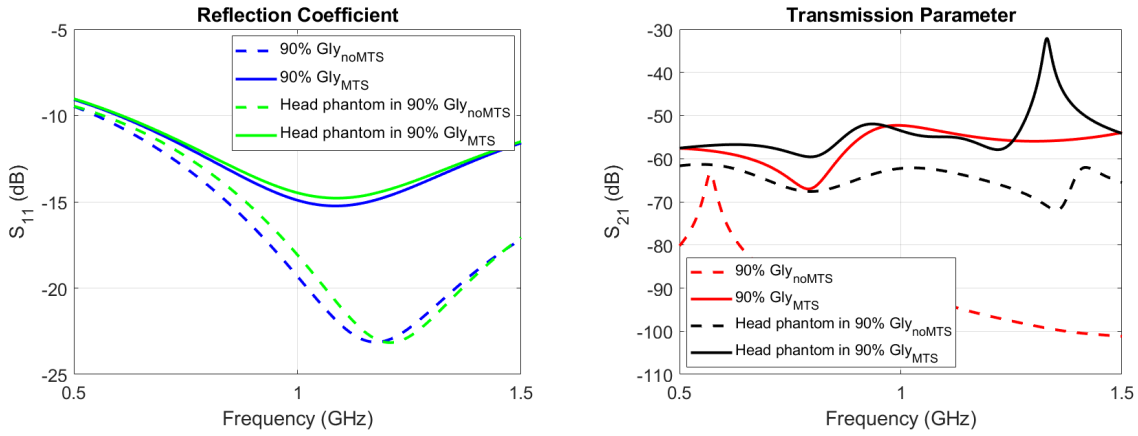

FIGURE 3.16: (a) Reflection, and (b) transmission parameters comparison with and without the MTS.

The impact of the distance of the MTS from the radiating element was also studied. To this end, two antennas were placed at a distance of 137 mm along the smallest dimension of the elliptical head phantom and the MTS superstrate loading was placed at two different positions: on the head model's surface and adjacent to the antenna's substrate. The S_{21} parameters shown in Figure 3.17 indicate that the improvement

in transmission is overall more significant when the MTS is placed adjacent to the radiating elements.

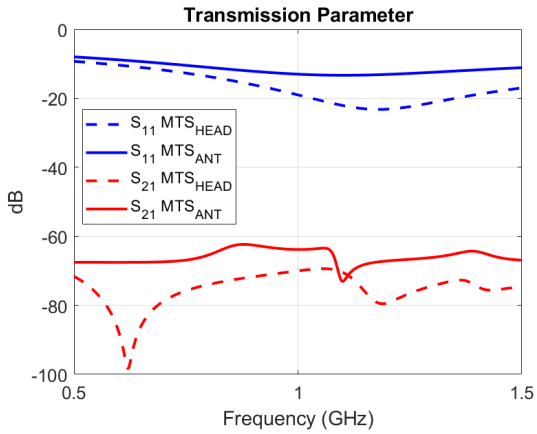

FIGURE 3.17: Reflection and transmission parameters of the MTS on the head model and adjacent to the antenna.

Figure 3.18 shows the calculated normalized electric field distributions at a representative frequency of 1.25 GHz. To isolate the MTS effect, a new "NC" scenario, where the substrate without the MTS-defining metallic elements is placed on the antennas, was simulated. Comparing the field distributions in these plots shows a stronger signal in the target area when the MTS is used, which translates into a stronger target response and hence higher data quality for the imaging system. This improvement, however, is also observed for the "NC" case of substrate-only loaded antenna. In the absence of the MTS, however, the resulting reconstructions for the substrate-only loaded antenna fail to detect the target, as discussed in Section 3.5.

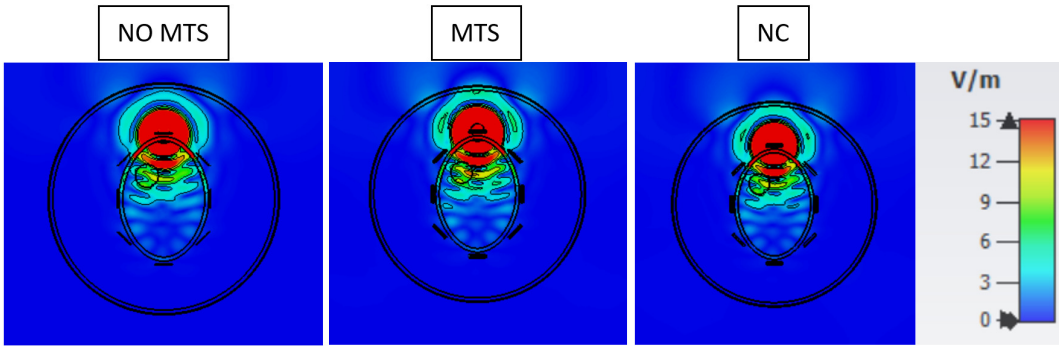

FIGURE 3.18: Normalized E-field plots for an antenna transmitting in our simulated experimental setup without MTS (left), with MTS (center), and loaded only with a substrate used as NC (right).

As the E-field plots in Figure 3.18 do not show a significant difference between the "MTS" and "NC" cases, to demonstrate the MTS's impact on the radiated field, the E-field value at two points belonging to different imaging planes and located in the

centre of the head was calculated. For all the array configurations, the E-field intensity values in those points were computed for a model of the head made of average brain only ("no target" scenario) and for the same model including a blood-mimicking target ("with target" scenario). Then, the difference between the E-field intensity values calculated in the two scenarios (ΔE) was estimated. Values of the scattered fields for the "no MTS", "MTS", and "NC" configurations are shown in Table 3.3. These values suggest that the field scattered from the target inclusion has a higher intensity when the MTS is present.

TABLE 3.3: Differences between E-field intensity values at 2 different points for "no MTS", "MTS" and "NC" configurations.

	Point1 (0,60,0) mm	**Point2 (0,43,0) mm**
ΔE (no MTS)	0.41 V/m	0.65 V/m
ΔE (MTS)	0.50 V/m	0.81 V/m
ΔE (NC)	0.47 V/m	0.76 V/m

Figure 3.19 shows the total E-field distribution on the surface of the head phantom at 1.25 GHz for antenna 1 (T1) transmitting with and without MTS. In this figure, the E-field distribution for the "NC" case-study is also included. The plots show that the MTS does not focus the E-field onto a tighter beam, but on the contrary, it widens the E-field distribution inside the head model, resulting in better signal coverage. This might be the reason why the target's response is stronger in the presence of the MTS.

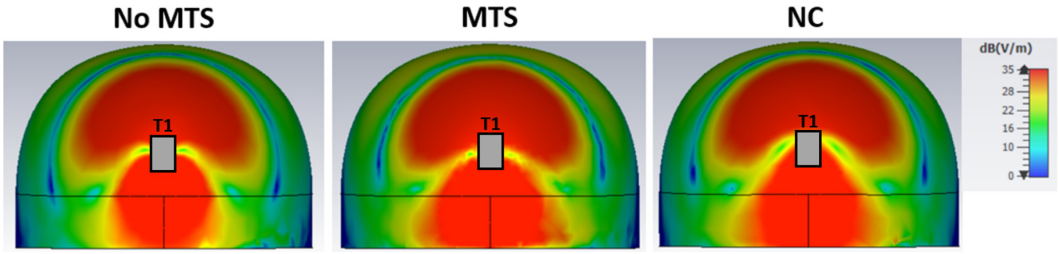

FIGURE 3.19: E-field distribution on the surface of the head phantom for the "no MTS", "MTS", and "NC" scenarios when antenna 1 (T1) is transmitting. The MTS produces a wider E-field distribution.

Moreover, the E-field distributions on the transmitting antennas for the "no MTS", "MTS", and "NC" scenarios shown in Figure 3.20 indicate that a stronger field is excited by the transmitter's substrate when the MTS is present. However, it is important to notice that this higher-field intensity on the antenna's substrate covered by the MTS sheet could be caused by the fact that the monopole's radiating part is not in direct contact with our lossy coupling medium. Thus, to validate the MTS's impact on the antenna array, the MTS's behaviour in receiving mode was studied. The simulation results suggest that the MTS seems to act as an "amplifier" of the received field. To

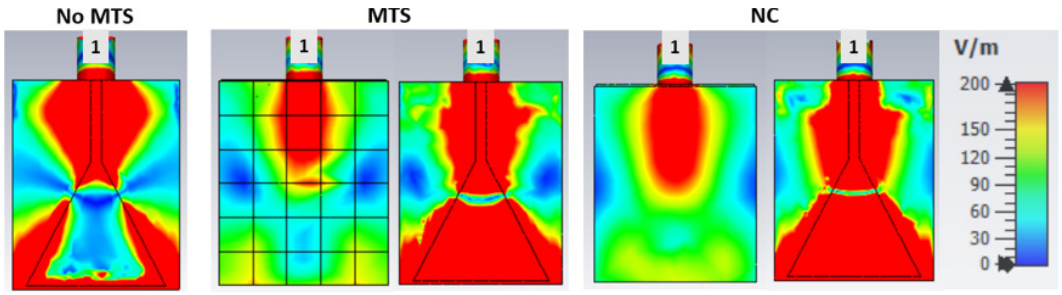

FIGURE 3.20: E-field plotted on the transmitter's substrate for the "no MTS", "MTS", and "NC" scenarios with the head model. A higher-intensity E-field is transmitted when the MTS is present.

show this enhancement, different antenna arrays immersed in matching medium only were considered. The first array includes a triangular patch transmitter (antenna 1) and 7 MTS-enhanced receivers. The second array consists of 8 triangular patch antennas, whereas the third array consists of a triangular patch transmitter and 7 negative-control receivers. The E-field was plotted on the substrate of the receiver opposite to the transmitter (with and without MTS and with NC). Figure 3.21 shows that the E-field on receiver 5 is significantly enhanced when the MTS covers the antenna's substrate. Thus, considering the same source of excitation, the MTS leads to an improvement of the received field.

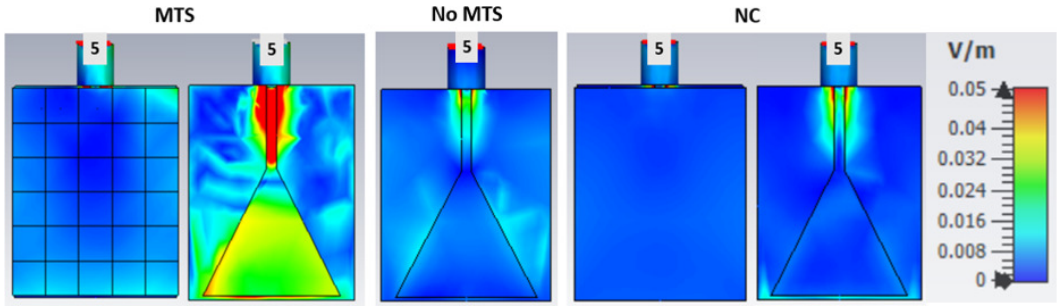

FIGURE 3.21: E-field plotted on the substrate of receiver 5 (with and without MTS and with NC loading) when antenna 1 is transmitting. A higher-intensity E-field is received when the MTS is present.

3.4.2 Experimental Methodology

To examine the performance of the radar and tomographic algorithms experimentally, gelatin-oil mixtures based on the phantom preparation method described in [103], and investigated on phantoms in [110], [111], were prepared. Two mixtures were produced to mimic the average brain and blood gels. The gel preparation process was performed in a controlled environment at ambient temperature. The materials used to fabricate

the phantoms are not toxic or harmful to health. The concentration of each material used in preparing the mixtures is presented in Table 3.4.

TABLE 3.4: Quantities of materials used for 100 ml of tissue mimicking phantoms.

	Average brain	**Blood**
Gelatin powder	11 gr	16 gr
Kerosene	13 ml	-
Propanol	2.5 ml	1.5 ml
Safflower oil	13 ml	-
Surfactant	4 ml	-
Water	60 ml	80 ml

The preparation process started with preparing a water-gelatine solution, which was mixed until the gelatine particles were fully dissolved, resulting in a transparent mixture. Next, propanol was added to remove the air bubbles from the surface. When the mixture reached 70°C, a 50% kerosene-safflower oil solution was added to the existing mixture and stirred at the same temperature, until the oil particles were fully dissolved. The mixture was stirred until the temperature dropped to 50°C, at which point surfactant was added. As a final step, the prepared mixture (at 35°C) was poured inside a thin elliptical plastic mould, as shown in Figure 3.22, and was left to cool and solidify until the next day, when measurements were preformed.

Before inserting the target into the average brain mixture, the “no target" scenario was measured using both tomography and radar antenna configurations, with both “without MTS” and “with MTS” antenna types. After performing all the “no target" measurements, the “with target" measurements were carried out, by placing a 30 mm diameter cylindrically shaped target mimicking the blood inside the average brain solution. The target was placed at a distance of 30 mm horizontally to the right and 25 mm vertically downwards from the centre of the phantom [30, -25], at an angular position of ≈320 degrees relative to the position of the first transmitting antenna. The target was prepared with a similar recipe to that of the brain, but without the use of safflower oil and kerosene (Table 3.4), providing a mixture with permittivity of ≈65 and conductivity of ≈0.4 S/m at 1 GHz, mimicking the dielectric properties of blood during haemorrhage stroke. Next, all the “with target" measurements for both tomography and radar configurations, both with and without MTS were performed.

In order to verify that the target detection for the first phantom corresponded to the haemorrhage blood target region and not to an anomaly or an artefact, one week after the first set of measurements, a second phantom was prepared. The target for the second phantom was positioned eccentrically, placed 30 mm horizontally to the left and 25 mm vertically downwards from the phantom’s centre with respect to the first antenna position [-30, -25]. This experimental procedure is reported in [112].

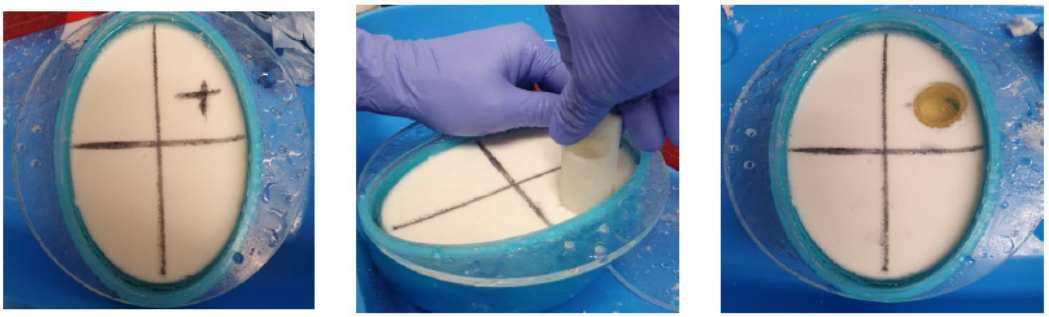

FIGURE 3.22: Elliptical brain phantom before (left) and after (right) inserting the eccentric target. The target was positioned at two different locations in the two constructed phantoms.

3.5 Results and Discussion

This section presents results from simulations and experiments which show the positive impact of the MTS deployment in a MWI system for stroke. These include reconstruction images, with and without the MTS, using the tomographic and radar algorithms, as well as comparison plots of the stroke-like target response. We note that the reconstructions presented in this section have been obtained assuming knowledge of the target response by subtracting the signals from the phantom before and after inserting the target. This assumption can only be partially realized in practice as the "no-target" scenario will not be perfectly known in real-life clinical scenarios. It allows, however, to study the impact of the MTS enhancement in the absence of errors associated with incomplete knowledge of the "no-target" scenario.

Figure 3.23 shows the 2D DBIM-TwIST results for Phantom 1 (with and without MTS) at three different frequencies using simulation data. An improvement in the target's localization, with less artefacts, can be obtained when using the MTS. Similarly, simulation results of Phantom 2 are depicted in Figure 3.24, before and after applying the MTS. It should be pointed out that for both the "no MTS" and "with MTS" cases, the same incident field model of ideal point sources has been used in the finite difference time domain (FDTD) forward solver used by the distorted Born iterative method (DBIM) algorithm. This is common practice in inverse scattering algorithms, where modelling patch antennas in the imaging algorithm is computationally challenging. The calibration method used for the experiments accounts to some extent for this mismatch between these simple antenna models and the true antennas used by our system. Moreover, it should be noted that all the reconstructed tomography images presented here represent the real part of the complex permittivity (dielectric constant) of the tissues. As shown in [110], the imaginary part (and hence the tissues' conductivity) can also be estimated, but with less accuracy.

Moving on to the radar simulation results, Figure 3.25a and Figure 3.25b show the

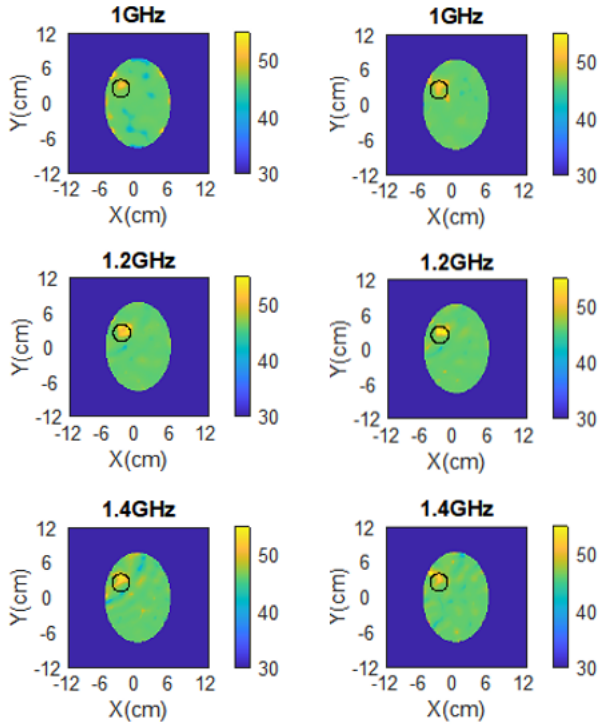

FIGURE 3.23: Reconstructed dielectric constant of Phantom 1 at three different frequencies using simulation data and antennas with (left) and without (right) the MTS.

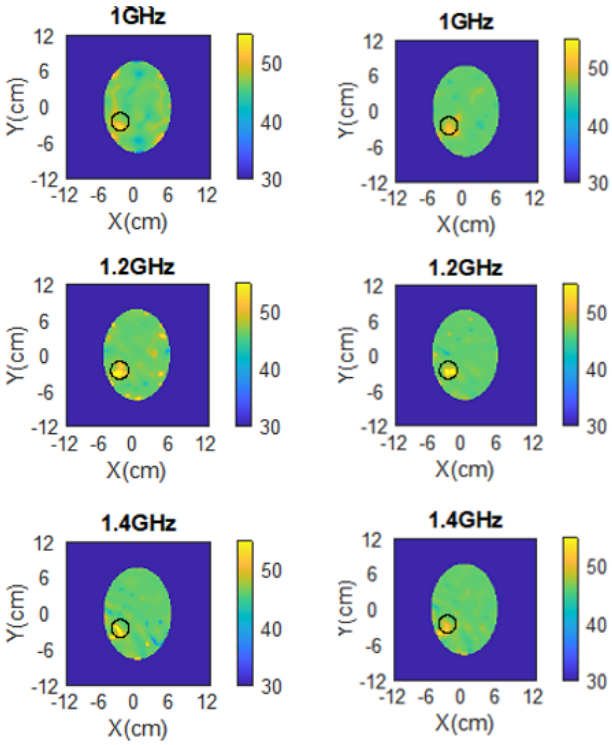

FIGURE 3.24: Reconstructed dielectric constant of Phantom 2 at three different frequencies using data from the CST model and antennas with (left) and without (right) the MTS.

normalized and adjusted reconstructed intensity images corresponding to Phantoms 1 and 2 with the MTS, respectively. The image adjustment procedure allows us to have a better and clearer visualization of the target and the region of interest, and is done here by converting intensity values lower than 0.65 to 0, and re-ranging values higher than 0.65, from 0 to 1. In both cases, the target can be localized in its approximate position without artefacts. In comparison, no detection is achieved without the use of MTS on the antennas, as depicted in Figure 3.26a and Figure 3.26b.

To demonstrate the positive impact of the MTS on radar-based detection, a "NC" scenario for Phantom 1 was simulated in CST. Although the electric field distribution plotted in Figure 5.5 for this case is very similar to the "MTS" case, the resulting reconstruction in Figure 3.27 shows a stronger ghost target close to the real one, which obstructs accurate detection. This example suggests that using the MTS can enhance detection by virtue of its transmitting and receiving properties, which increases the target response relative to other signal artefacts.

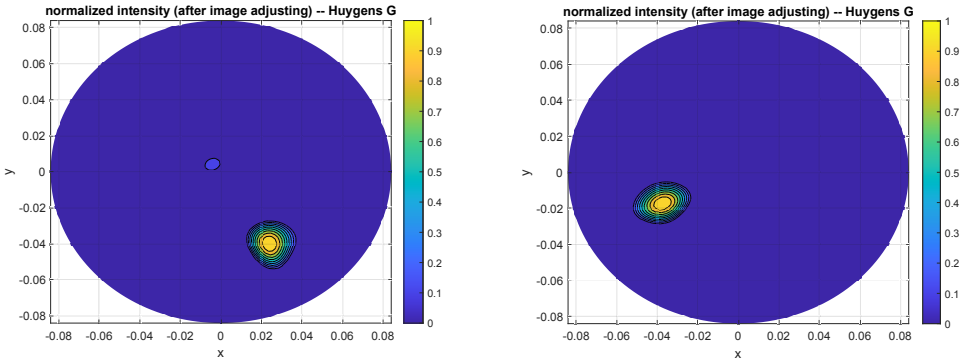

(**a**) (**b**)

FIGURE 3.25: Radar-based images after normalization and adjustment for: (**a**) Phantom 1, and (**b**) Phantom 2, using simulation data and antennas with the MTS. Axes units are meters.

Focusing now on the reconstruction results from the measurements, Figure 3.28 and Figure 3.29 show the reconstructed images using the 2D DBIM-TwIST for six different frequencies in the range of 1-1.5 GHz for Phantom 1 without and with MTS, respectively. Images illustrate the whole tank, however, the reconstruction domain contains only the brain ellipsoid inside the antenna array. These results show a clearer improvement in target detection when using the MTS than the improvement observed with the simulated data. A similar improvement can be noticed for images corresponding to Phantom 2, depicted in Figure 3.30 and Figure 3.31 before and after applying the MTS, respectively. More specifically, we can observe that the dielectric constant (real part) of haemorrhagic-mimicking target is detectable for all the frequencies albeit with some artefacts in the images. The most encouraging observation from

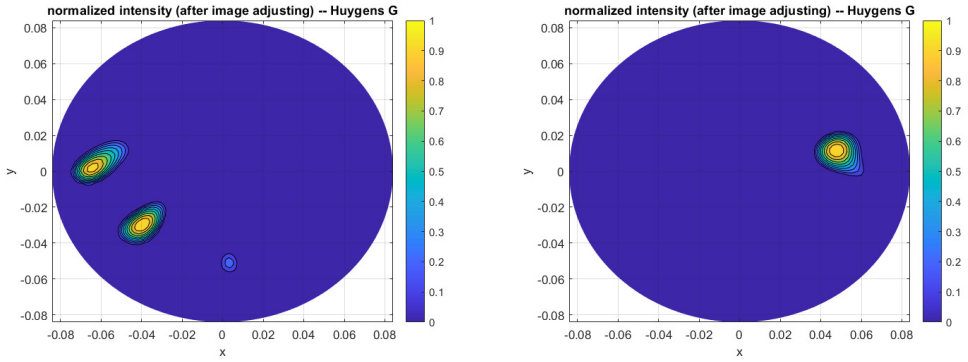

(**a**) (**b**)

FIGURE 3.26: Radar-based images after normalization and adjustment for: (**a**) Phantom 1, and (**b**) Phantom 2, using data from the CST model and antennas without the MTS. Axes units are meters.

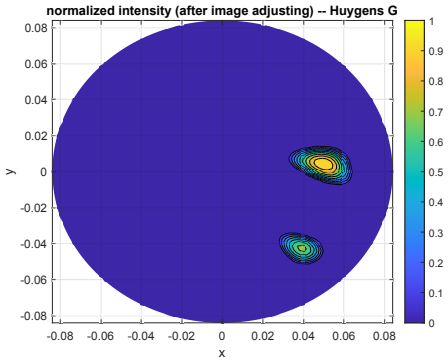

FIGURE 3.27: Radar-based image after normalization and adjustment for Phantom 1, using data from the CST model and the "NC" scenario defined in Section 3.4.1, where the antenna is loaded with a substrate only. Axes units are meters.

these figures, however, is that there is a clear distinction in the estimation of the targets' dielectric properties for the "no MTS" and "MTS" case. For instance, looking at the reconstruction images at 1.3 GHz in Figure 3.30 and Figure 3.31, we can see that, in the presence of the MTS, the permittivity values are close to 60 (measured value) in all the target's area. Furthermore, the artefacts appear to be reduced.

Referring to radar measurements, Figure 3.32 shows the S-parameter comparison for the recorded frequency band (0.5-2 GHz) of Phantom 1 without and with MTS, when the triangular antennas are closest (S_{21}), midway or 90° apart (S_{71}) and farthest to each other (S_{13-1}), respectively. From this figure, signal propagation improvement over the whole frequency band can be observed when using the MTS. A similar pattern is also observed for Phantom 2. Investigating the recorded frequency range while processing the measured data indicated a frequency range of 0.6-0.8 GHz as the optimum frequency band for image reconstruction when using the Huygens algorithm. An average gain of 4.8 dB when using the MTS is achieved in this frequency range.

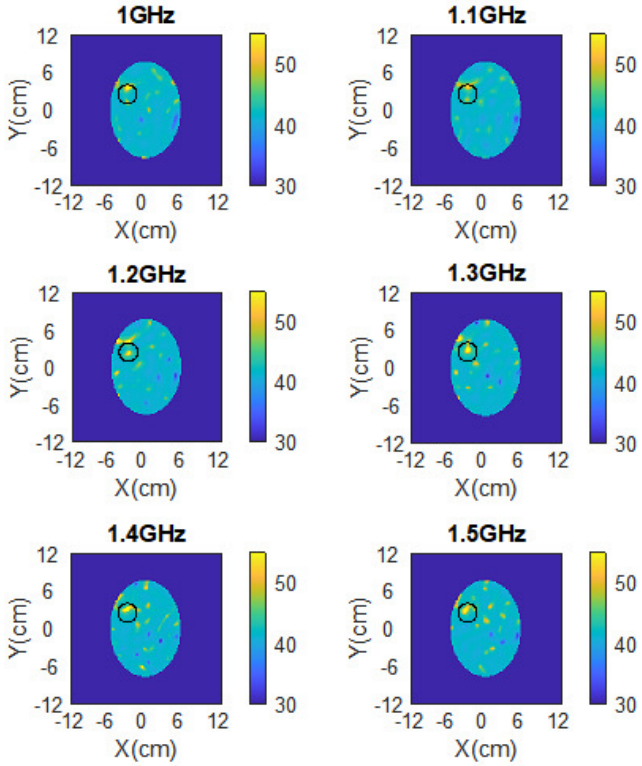

FIGURE 3.28: Reconstructed dielectric constant of Phantom 1 at different frequencies in the range of 1-1.5 GHz using experimental data and antennas without the MTS.

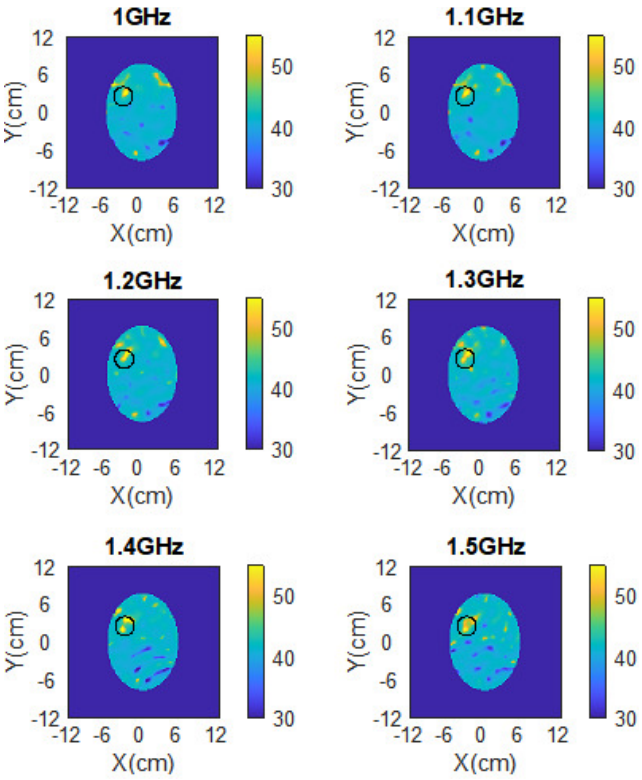

FIGURE 3.29: Reconstructed dielectric constant of Phantom 1 at different frequencies in the range of 1-1.5 GHz using experimental data and antennas with the MTS.

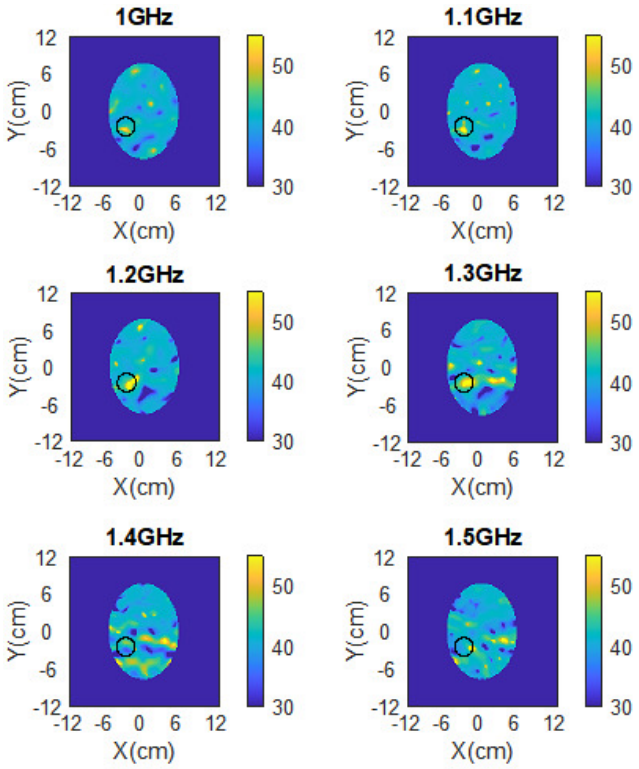

FIGURE 3.30: Reconstructed dielectric constant of Phantom 2 at different frequencies in the range of 1-1.5 GHz using experimental data and antennas without the MTS.

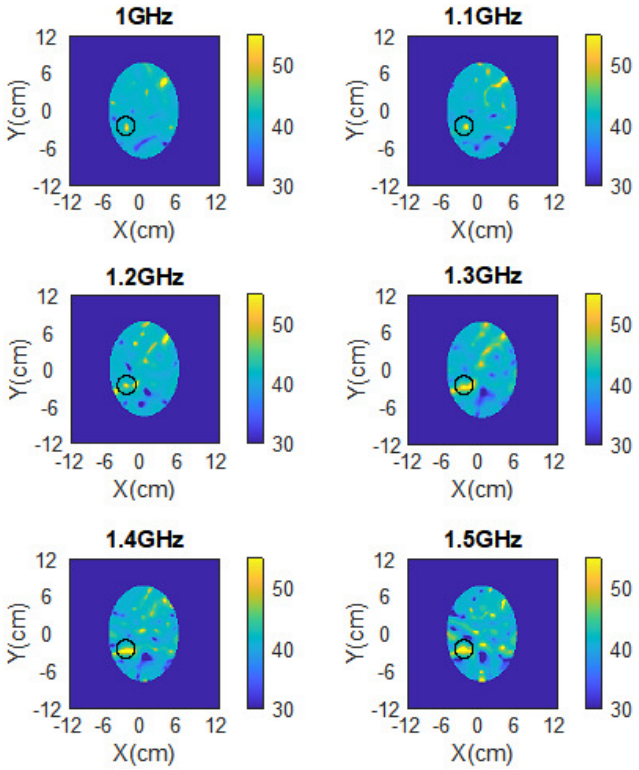

FIGURE 3.31: Reconstructed dielectric constant of Phantom 2 at different frequencies in the range of 1-1.5 GHz using experimental data and antennas with the MTS.

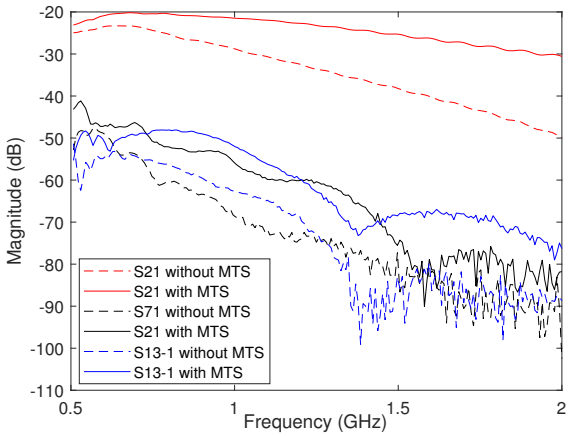

FIGURE 3.32: Magnitude (dB) plots (for Phantom 1) for different antenna distances within the 0.5-2 GHz frequency band. Solid lines represent "MTS" measurements while dashed lines represent "no MTS" measurements.

Figure 3.33a and Figure 3.33b show the intensity images of Phantom 1 without the use of MTS obtained through the Huygens algorithm, before and after image normalization and adjusting, respectively. Similarly, Figure 3.34a and Figure 3.34b represent the images of the same phantom when placing the MTS on the antennas. We can see a clear improvement of the images after the use of MTS. In Figure 3.34b, the target is localized in its approximate position without noticeable artefacts. The actual location of the target is shown with a red circle.

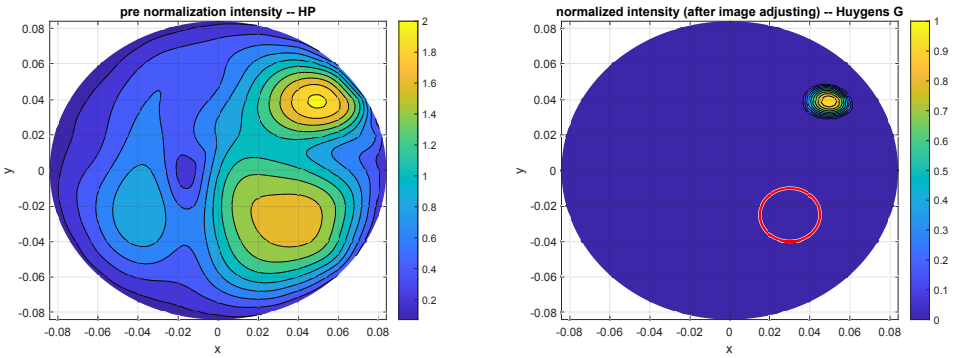

(**a**) (**b**)

FIGURE 3.33: Radar-based images for Phantom 1 using experimental data and antennas without the MTS : (**a**) images before normalizing; (**b**) images after normalization and thresholding adjustment. Axes units are meters.

Figure 3.35a and Figure 3.35b present the intensity images of Phantom 2 without the use of MTS obtained through the Huygens algorithm, before and after image normalization and adjusting, respectively. The corresponding images of the same phantom after placing the MTS design are depicted in Figure 3.36a and Figure 3.36b. Once

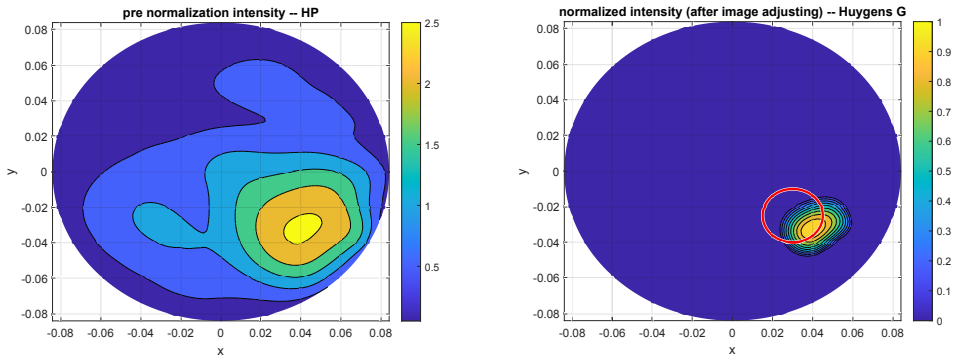

(**a**) (**b**)

FIGURE 3.34: Radar-based images for Phantom 1 using experimental data and antennas with the MTS : (**a**) images before normalizing; (**b**) images after normalization and thresholding adjustment. Axes units are meters.

again, the noticeable effect of using the MTS can be observed by comparing the images. More specifically, it must be noted that for both radar-based simulation and measurement results presented in this chapter and Chapter 5, the use of MTS enhances the detection and localization through improvement of "useful signals", thus increasing the target response relative to other signal artefacts. Such unwanted artefacts in radar imaging are predominantly generated by transmitter image and the reflections of the layers, often masking the target [113]. Still, even when employing MTS antennas a small offset is sometimes present in images corresponding to radar-based measurement result. This could be due to several factors such as the imperfect manual rotation of the antennas, the use of uniform Green's function in a non-homogenous phantom, or the use of circular arrangement of receiving antennas for imaging an elliptical phantom.

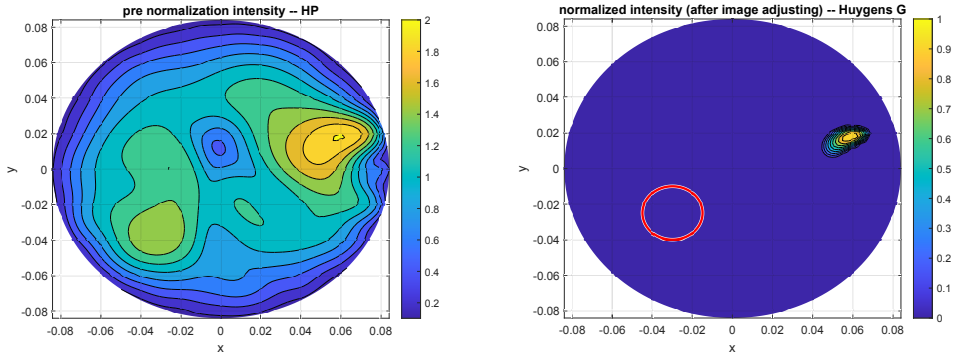

(**a**) (**b**)

FIGURE 3.35: Radar-based images for Phantom 2 using experimental data and antennas without the MTS : (**a**) Image before normalizing; (**b**) Image after normalization and thresholding adjustment. Axes units are meters.

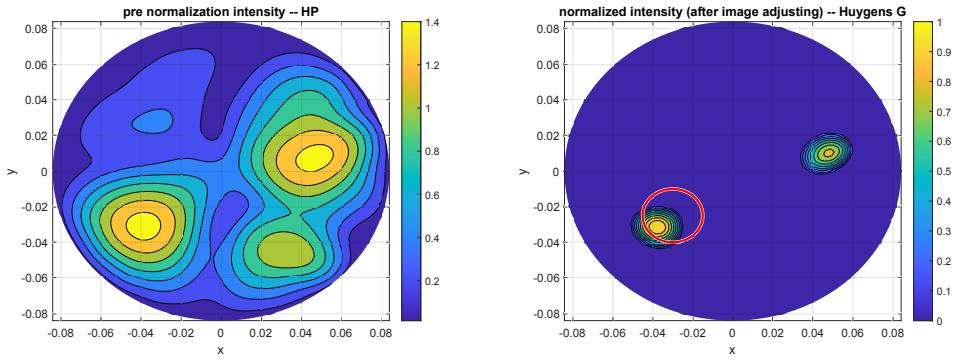

(**a**) (**b**)

FIGURE 3.36: Radar-based images for Phantom 2 using experimental data and antennas with the MTS : (**a**) image before normalizing; (**b**) image after normalization and thresholding adjustment. Axes units are meters.

It should be emphasized that as an input, the Huygens principle (HP)-based algorithm only requires the electrical properties of the background medium where the antennas are placed (in this case, 90% glycerol). Thus, measured permittivity and conductivity values of 17 and 1.1 S/m respectively were assigned to the algorithm to perform the correct reconstructions in previous figures. In order to examine the robustness of the Huygens algorithm with respect to the uncertainty in the knowledge of the electrical properties of the background medium, the reconstruction of the data from Phantom 1 was repeated first assuming a permittivity of 27 (Figure 3.37a), and then assuming a permittivity of 5 and conductivity of 0.5 S/m (Figure 3.37b). It can be observed that not having the exact knowledge of the background medium's electrical properties does not impact the detection capability, while it has a minor effect on the localization through creating an offset. An interesting point to note is that Huygens

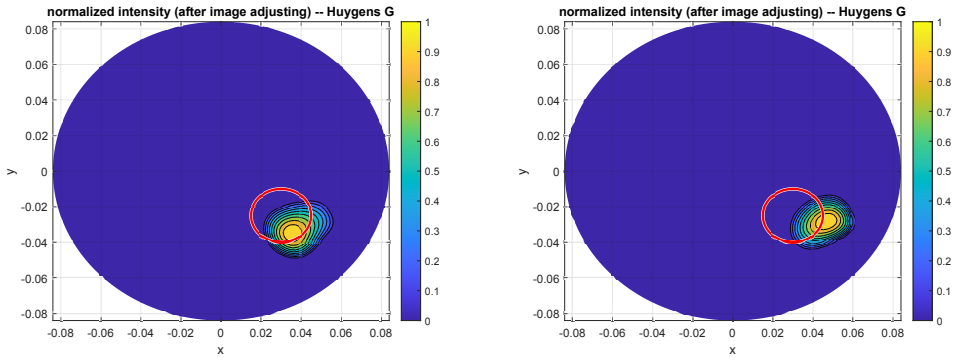

(**a**) (**b**)

FIGURE 3.37: Radar-based normalized and adjusted images for Phantom 1 using experimental data and antennas with the MTS, when assuming background electrical properties: (**a**) ϵ =27, σ=1.1 S/m; (**b**) ϵ =5, σ=0.5 S/m. Axes units are meters.

algorithm's best reconstructions are produced using a lower frequency range of 0.6-0.8 GHz (likely due to greater penetration depth) while the DBIM-TwIST performs the best at higher frequencies between 1-1.5 GHz. This can be a great consideration for a hybrid imaging algorithm that can make use of both the lower and higher measured frequency bands for an optimum image reconstruction. A further point to address would be the challenge of overcoming the "no target" reference scenario used here for image subtraction, which will be unavailable in real-life clinical scenarios.

Comparison plots of the stroke-like target response for Phantom 1 and Phantom 2 are shown in Figure 3.38 and Figure 3.39, respectively. These plots show the signal difference "with target - no target" (in dB) calculated at 1.2 GHz (central frequency for the tomographic reconstructions) using both simulation and experimental data. This difference is plotted for each transmitter, as a function of the receivers' location. The antennas are numbered clockwise starting from the transmitter. As shown in the graphs, when the MTS film is covering the antennas, it leads to an overall improvement (up to 45 dB) of the signal scattered by the blood-mimicking target. This enhancement is more visible in simulations rather than experiments. As shown in Figure 3.38b and Figure 3.39b, the target's response calculated from the experimental data is overall enhanced but not for all the receiving positions. However, it is important to notice that this differential signal measured in the presence of the MTS is higher (with respect to the "no MTS" case) in proximity of the target's location. For instance, looking at antenna 1 (Trans 1) of Figure 3.38b, we can observe an increased target's response for the receiving positions 2, 3, 7 and 8 in the presence of the MTS.

3.6 Simulations and Experiments of Multi-Port Setup with Spear Patch Antennas

3.6.1 Simulations of a Tomographic Headband Scanner

This section presents a further simulation study investigating the impact of the proposed MTS on the spear patch antenna reported in [17]. To this end, the same 5×6 unit cell MTS described in Section 3.4 was incorporated in a microwave tomography (MWT) scanner for microwave head imaging. The MWT system proposed for this numerical study is a more realistic head scanner compared with the model of the experimental system presented in Section 3.1. It consists of 12 antennas arranged uniformly inside an elliptical headband filled with a 90% glycerol-water matching medium [17]. This scanner was placed around a numerical head phantom, for which the EN 50361 Specific Anthropomorphic Mannequin (SAM) head model was used. This head model

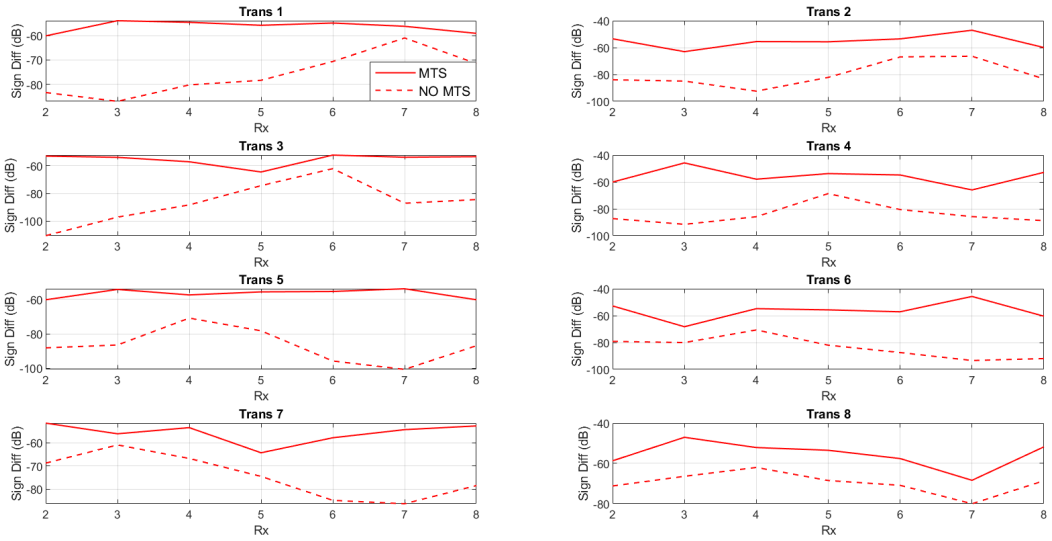

(**a**)

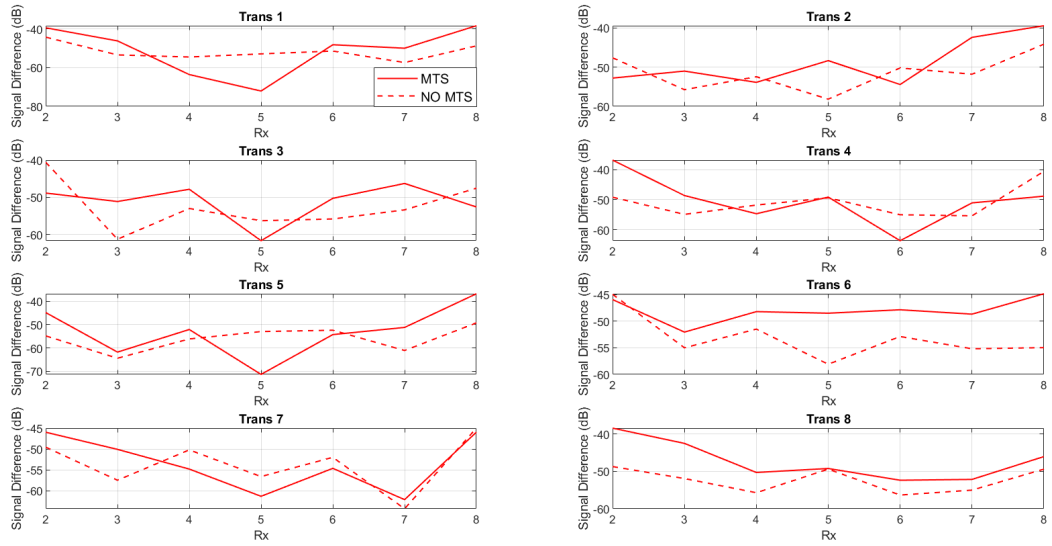

(**b**)

FIGURE 3.38: Signal difference "with target - no target" (dB) for Phantom 1 calculated at 1.2 GHz, using data (**a**) from CST and (**b**) experiments. The plots show the target's response for each transmitter, as a function of the receivers' location, with (solid lines) and without (dashed lines) MTS. The numbering of the antennas is clockwise, as shown in Figure 3.1.

includes a skull layer (bone) and average brain tissue inside. The setup is shown in Figure 3.40.

We will refer to the model with brain and bone alone as the "no target" scenario. The signal propagation in the presence of a blood-like target inside the brain volume

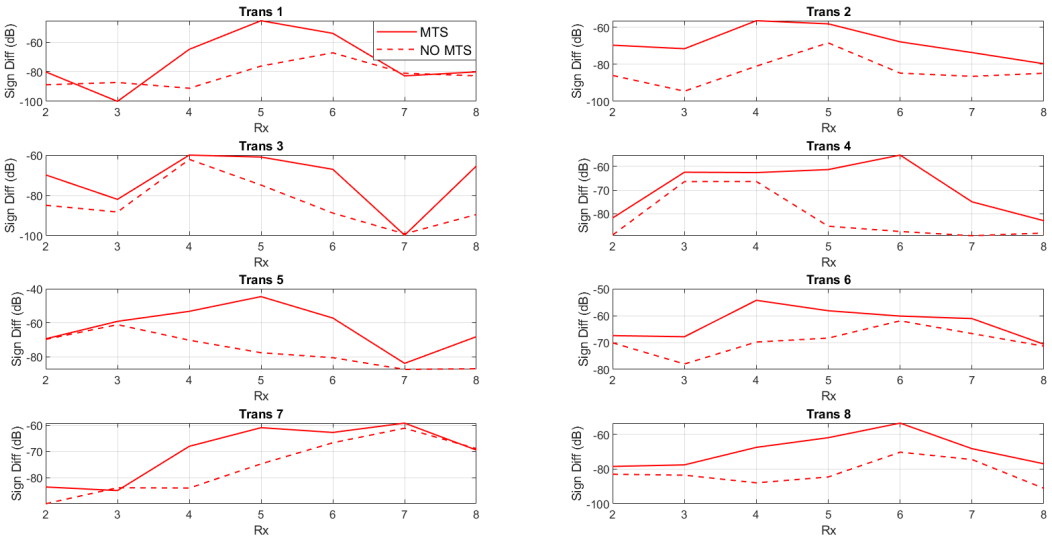

(**a**)

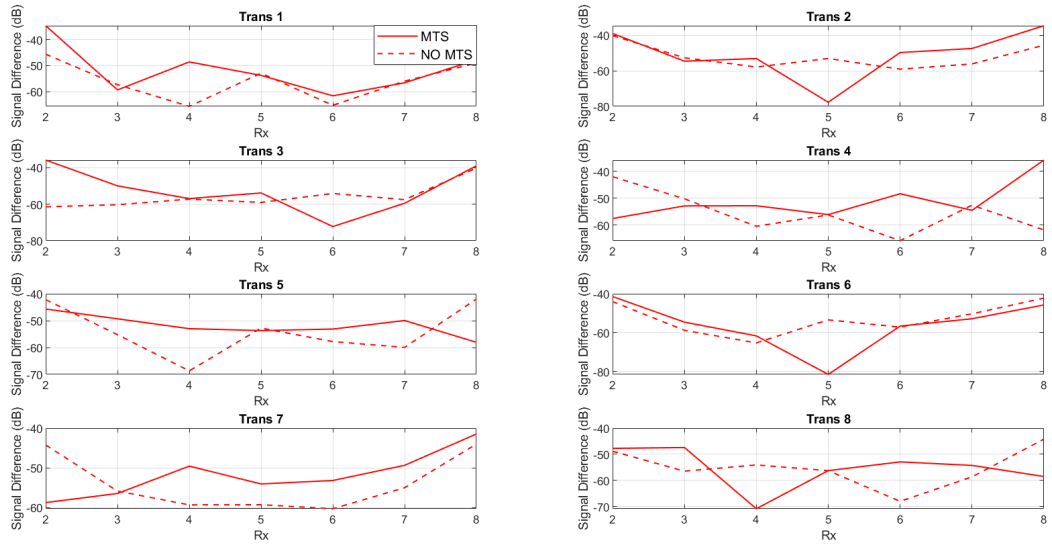

(**b**)

FIGURE 3.39: Signal difference "with target - no target" (dB) for Phantom 2 calculated at 1.2 GHz using data (**a**) from CST and (**b**) experiments. The plots show the target's response for each transmitter, as a function of the receivers' location, with (solid lines) and without (dashed lines) MTS. The numbering of the antennas is clockwise, as shown in Figure 3.1.

was also studied. The target was a cylinder of 30 mm diameter and 20 mm height and was placed in the vertical centre of the brain, in the front-left part, close to antennas 8-10 (see Figure 3.40). We will refer to this case (with the blood target introduced in the brain) as the "with target" scenario. A permittivity value of 20 and conductivity of 0.35

S/m were assigned to the bone region and values of 45.8 and 0.76 S/m were attributed to the brain tissue, respectively. The properties of blood to the aforementioned target were assigned from CST's material library.

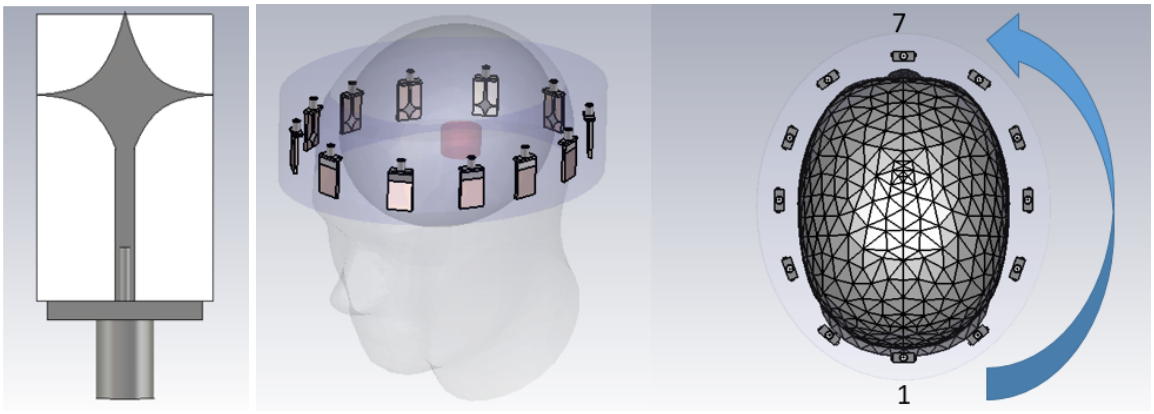

(**a**) (**b**)

FIGURE 3.40: (**a**) Spear-shaped antenna used in the headband system, operating at 1.5 GHz when immersed in the 90% glycerol coupling medium: it consists of a spear patch printed on a FR-4 substrate, with a rectangular ground on the back side. (**b**) Headband system geometry and head model: the array is close to the head, around 10 mm on average. The headband is 65 mm thick, whereas the major and minor axes of the elliptical cross section are 260 mm and 220 mm, respectively [17]. A MTS layer is placed in front of each antenna at different distances to evaluate its effect on the array's signals and the resulting reconstructed images.

The MTS was placed in front of each antenna at different distances. In particular, two case studies were investigated: the MTS was placed on the head and adjacent to the antenna's substrate. The S-parameters were measured over the 0.5-2 GHz frequency range and the signal difference "with target - no target" (in dB) with and without the MTS was calculated at relevant frequencies. Then, images of the blood-mimicking target (with and without MTS) were reconstructed thorough the 2D DBIM-TwIST algorithm.

Results and Discussion

The results presented in this section show that a significant enhancement of the "weak" signal scattered from the target is achieved in the presence of the MTS. Figure 3.41 shows the signal difference "with target – no target" (in dB) as a function of receiver location at the antenna's resonant frequency (1.5 GHz) when the MTS is placed both on the head and on the antenna's substrate. As shown in the graph, when the MTSs are close to the antenna array, it leads to an overall improvement of the signal difference compared to the case in which it is placed on the head (see Transmitters 3, 4, 7, and 9). Furthermore, the E-field plots in Figure 3.42 show that the MTS enhances the

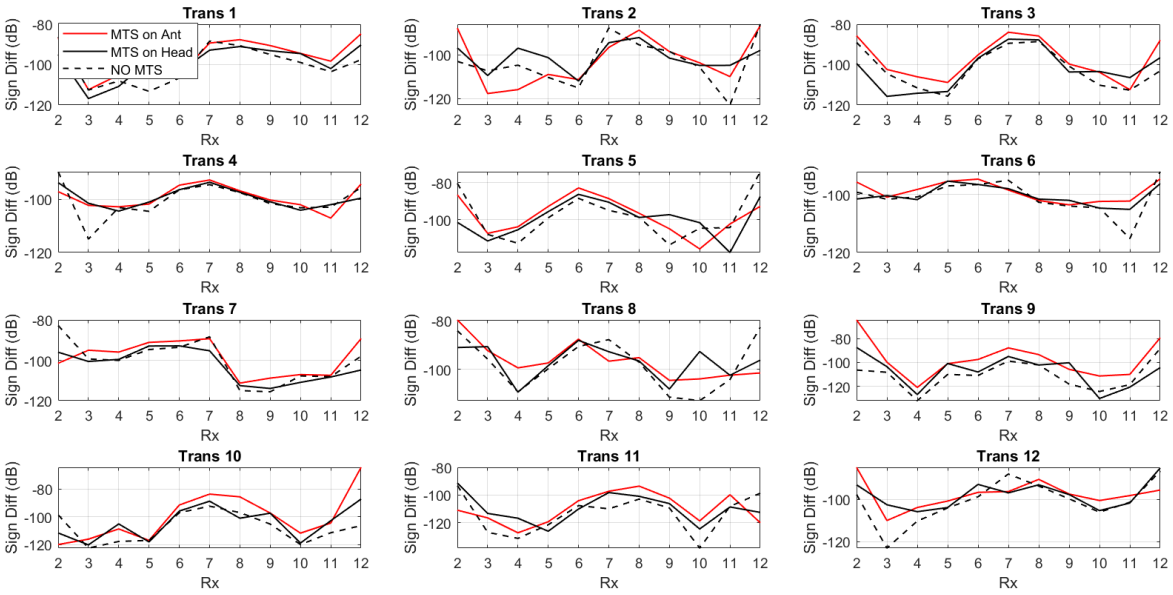

FIGURE 3.41: Signal difference "with target - no target" (dB) at 1.5 GHz as a function of the receivers' location with the MTS placed on the antenna's substrate (red solid lines), with the MTS placed on the human head (black solid lines), and without the MTS (black dashed lines). As shown in the graph, when the MTS is placed on the antenna's substrate, it leads to higher signal differences with respect to the case in which it is placed on the head.

intensity of the E-field localized in the target region and that this enhancement is more significant when it is placed adjacent to the antenna's substrate. As this enhancement translates into higher signal differences due to the target, the configuration with the MTS film placed on the antenna's substrate was further investigated.

Finally, to test the MTS's impact on image reconstructions, the 2D DBIM-TwIST algorithm [89, 114] was applied to the simulated data plotted in Figure 3.41. To this end, single-frequency and multi-frequency (frequency hopping) reconstructions were carried out, assuming approximate knowledge of the brain tissue and bone as initial guess for our DBIM-TwIST algorithm. Frequency hopping reconstruction results of the estimated dielectric contrast are shown in Figure 3.43, where five equally spaced frequencies were used in the interval 0.8-2 GHz. Comparing the images produced from data with and without the MTS shows a clear improvement in image quality when the MTSs are added to each antenna element. In particular, a reduction of artefacts and a better localization of the blood target are observed for the reconstructed permittivity's real part when the MTS is used. The same observation holds true for the single-frequency reconstructions presented in Figure 3.44 and Figure 3.45. For instance, looking at the reconstructions images at 1.3 GHz, we can clearly observe that, in the presence of the MTS, the artefacts are noticeably reduced.

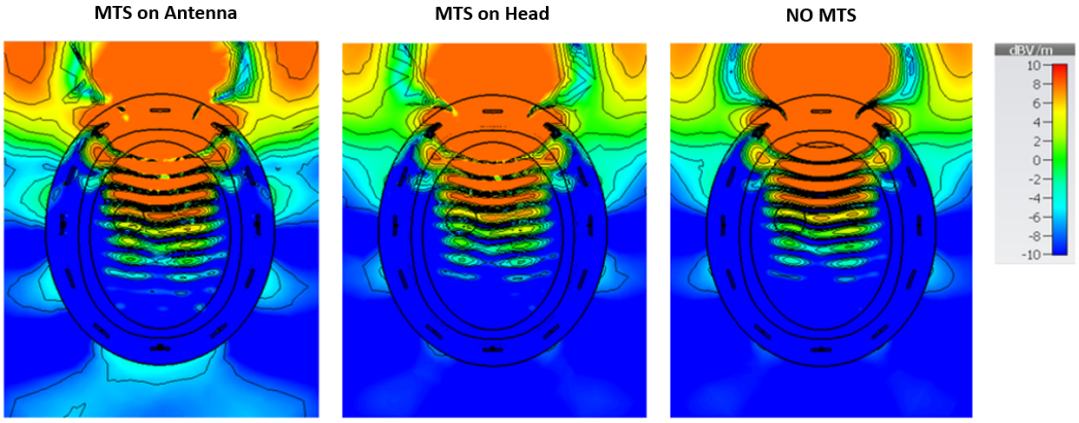

FIGURE 3.42: E-fields plotted on a transverse section of the human head model with a blood target in the brain. The MTS was placed on the antenna's substrate (left plot) and on the human head (central plot). On the right is the "no MTS" case. A higher field intensity in the target's region is shown when the MTS is placed adjacent to the antenna's substrate. In particular, the E-field values calculated inside the target at point P(X,Y) = (29 mm, 29 mm) of the transverse section are 4.8 dB (V/m) and 7.3 dB (V/m) for the MTS placed on the head and on the antenna's substrate, respectively. In the absence of the MTS, the intensity of the E-field in the same point is 3.7 dB (V/m).

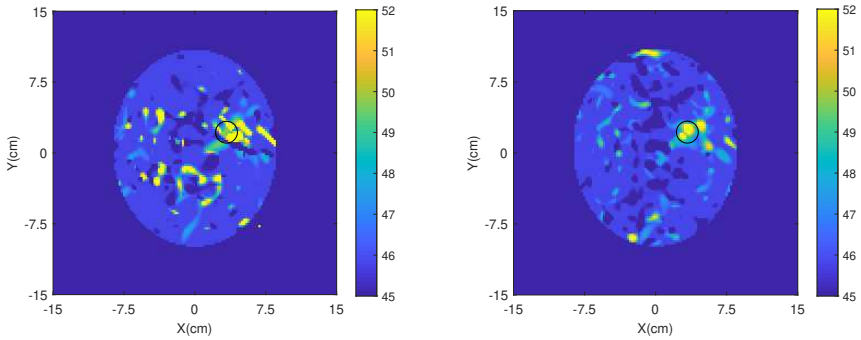

FIGURE 3.43: Reconstructed real part of permittivity with frequency hopping without the MTS (left) and with the MTS (right).

3.6.2 Simulations of a Radar Headband Scanner

The same headband scanner shown in Figure 3.40 was used to test the MTS design using the HP-based algorithm described in Section 2.2. To investigate the MTS's impact on image reconstructions, a cylindrical blood-mimicking target (40 mm height and 40 mm diameter) was placed at three different positions inside the brain volume and images were reconstructed via the radar-based algorithm.

Results and Discussion

Figure 3.46 presents the reconstructed normalized intensity images obtained for the domain inside the antenna array shown in Figure 3.40b. The blood-mimicking target

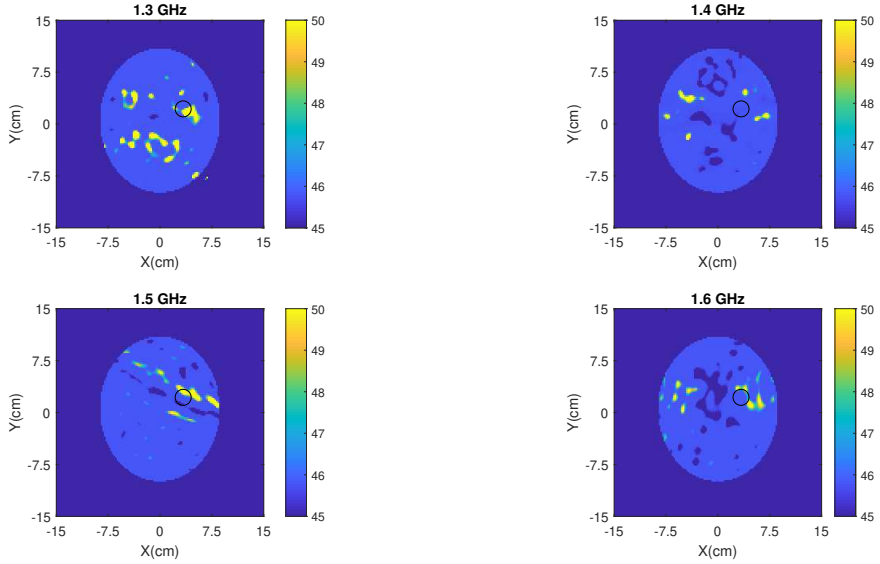

FIGURE 3.44: Single frequency reconstruction of the permittivity's real part for the same data as in Figure 3.43 at some representative frequencies (1.3 GHz, 1.4 GHz, 1.5 GHz, and 1.6 GHz) without the MTS

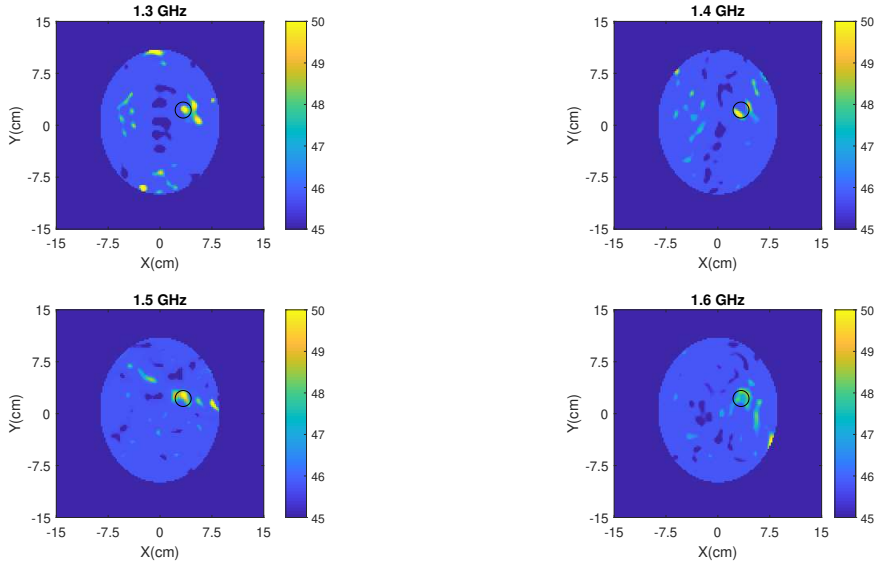

FIGURE 3.45: Single frequency reconstruction of the permittivity's real part for the same data as in Figure 3.43 at some representative frequencies (1.3 GHz, 1.4 GHz, 1.5 GHz, and 1.6 GHz) with the MTS.

was reconstructed for three different positions, with and without the MTS. These results clearly indicate that the proposed MTS design enables a correct detection and localization of the target and removes the noticeable imaging offset present when reconstructing the images without any MTS. It must be noted that the MTS enhances the detection and localization through improvement of the signals backscattered by

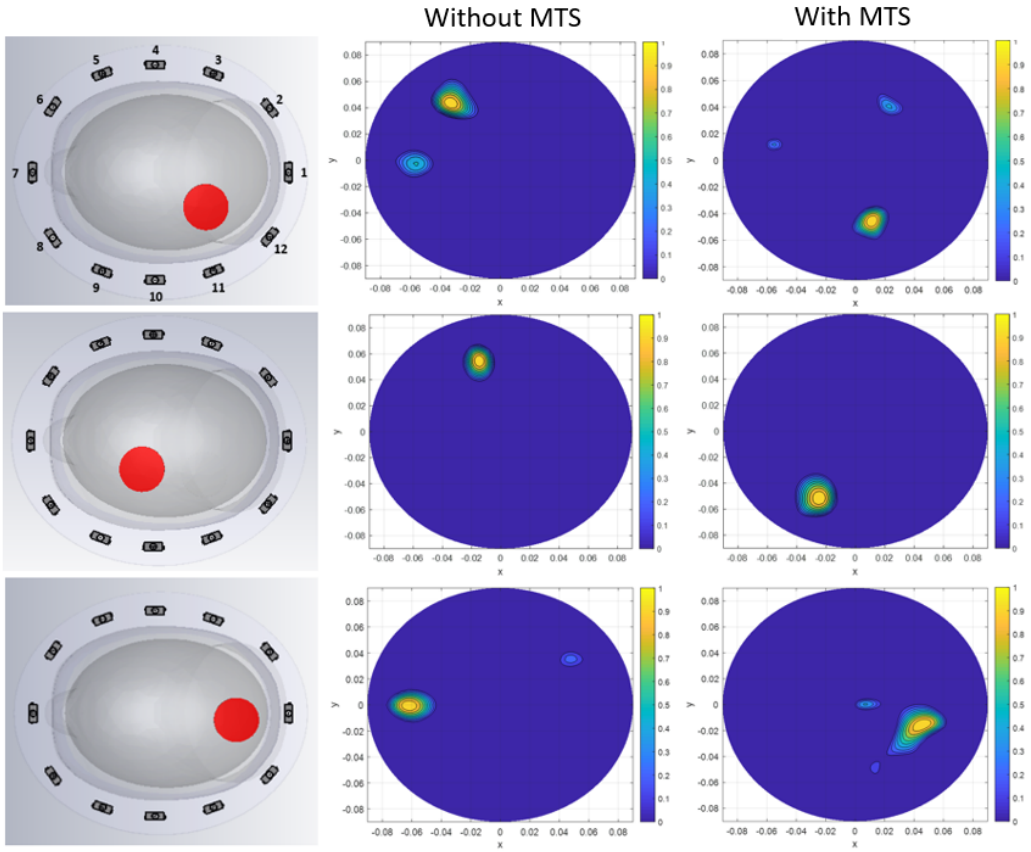

FIGURE 3.46: Reconstructed images (with and without MTS) of the blood-like target positioned at three different locations inside the brain volume.

the target, thus increasing the target's response relative to other signal artefacts, which are common in radar imaging [113]. Even when employing MTS antennas a small offset is sometimes present in images corresponding to radar-based measurement result. This could be due to the arrangement of receiving antennas (conformal to the head model) for imaging an elliptical phantom.

3.6.3 Experiments of an 8-Port Setup

To assess the impact of the MTS on the spear antenna experimentally, 8 MTS-enhanced spear patch antennas were fabricated and tested on the custom-made prototype described in Section 3.1. Gelatin-oil phantoms mimicking the properties of average brain, blood tissue and ischaemia were fabricated and images of a haemorrhagic target ("h-target") and an ischaemic target ("i-target") were reconstructed via the 2D DBIM-TWiST algorithm. A picture of the spear antenna both with and without MTS is shown below, in Figure 3.47

As for the triangular antennas, after carrying on the "no target" measurements, the 30 mm inclusion resembling the bleeding was inserted in the brain phantom and the

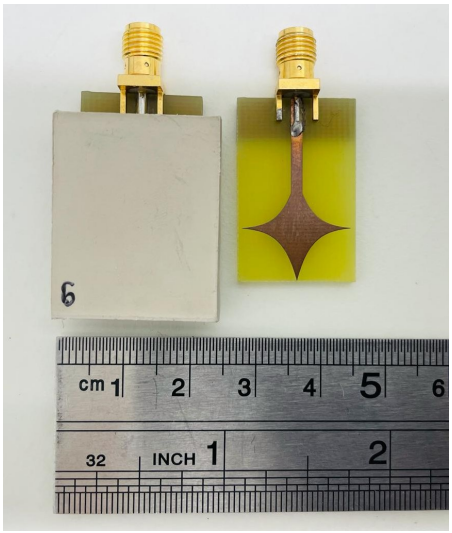

FIGURE 3.47: Photos of the spear patch antenna (right) and its MTS-enhanced version (left).

"with target" measurements were performed. Then, the blood-mimicking inclusion was substituted with the ischaemia-mimicking target and a second round of "with target" measurements was carried out. All the inclusions were positioned at the same coordinates, at an angular position of about 320 degrees relative to the position of the first transmitting antenna. The permittivity's values at 1 GHz of the coupling liquid and the phantoms used in these experiments are shown in Table 3.5.

TABLE 3.5: Permittivity of glycerol solution, brain phantom, blood-mimicking target and ischaemia-mimicking target measured at 1 GHz.

Type of Material	Permittivity at 1 GHz
90% Glycerol-water Mixture	15
Average Brain Phantom	38
Blood Phantom	65
Ischaemia Phantom	22

Figure 3.48a shows the reflection coefficient vs. frequency for the spear patch antenna number 8, while Figure 3.48b plots the transmission coefficient vs. frequency for a pair of antennas opposite to the brain phantom, along the direction containing the haemorrhage-mimicking or ischaemic-mimicking target. These plots suggest that a similar improvement in transmission is achieved if the MTS is used with the spear antennas, similar to the case of the triangular antennas.

The blood-mimicking target and the ischaemia-mimicking target were reconstructed via the 2D DBIM-TWiST algorithm. Multi-frequency reconstructions were performed using frequencies 0.7 GHz, 1.1 GHz and 1.3 GHz. The reconstructed blood phantom's

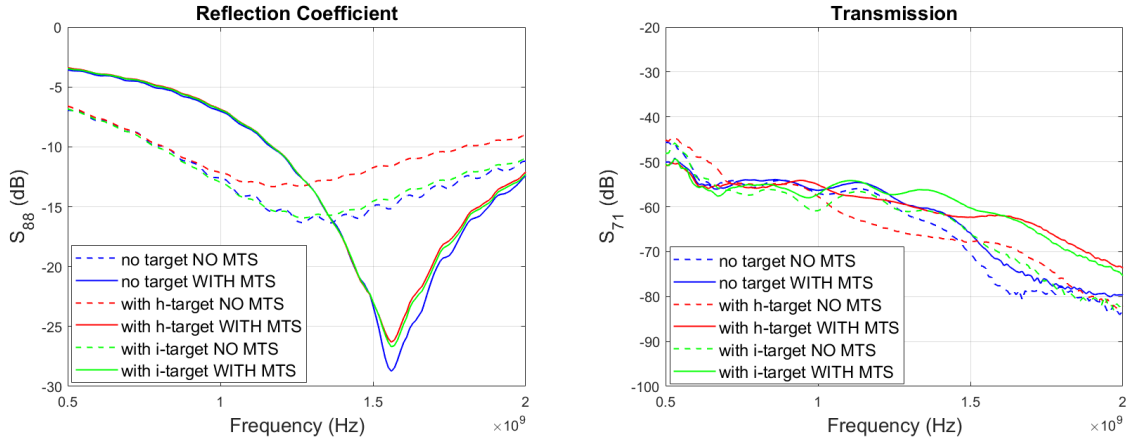

(**a**) (**b**)

FIGURE 3.48: (**a**) Measured S_{88} parameter for the spear patch antenna array in the "with h-target" (red lines), "with i-target" (green lines), and "no target" (blue lines) configuration, with (solid lines) and without MTS (dashed lines) (**b**) Measured S_{71} parameter for the spear patch antenna array in the "with h-target" (red lines), "with i-target" (green lines), and "no target" (blue lines) configuration, with (solid lines) and without MTS (dashed lines).

permittivity and ischaemia-mimicking tissue's permittivity are shown in Figure 3.49 and Figure 3.50, respectively. These images suggest that, despite the presence of some artefacts in the images, the dielectric constant (real part) of both the h-target and the i-target is detectable. Figure 3.49 shows that a better localization of the h-target is shown when the MTS films are integrated in the setup. A very promising observation is that there is a clear distinction in the permittivity's intensity values of the i-target between the "no MTS" and "MTS" case (Figure 3.50). Reconstructing the i-target is indeed very challenging, due of the low dielectric contrast between the ischaemic-mimicking tissue and brain phantom.

3.7 Conclusions

This chapter has presented preliminary numerical and experimental results which demonstrate the potential of a novel MTS structure to enhance MWI systems. In Section 3.2, a MTS unit cell design and two (finite) MTSs based on this single element were studied. First, to examine the benefits of using the MTS as an impedance-matching layer capable of improving transmission through the human head, a series of simulation studies were performed. Figure 3.4 shows that the MTS unit cell improves transmission of about 1.80 dB at 1 GHz for plane wave excitation of singular polarization if applied to a simple planar model for the human head.

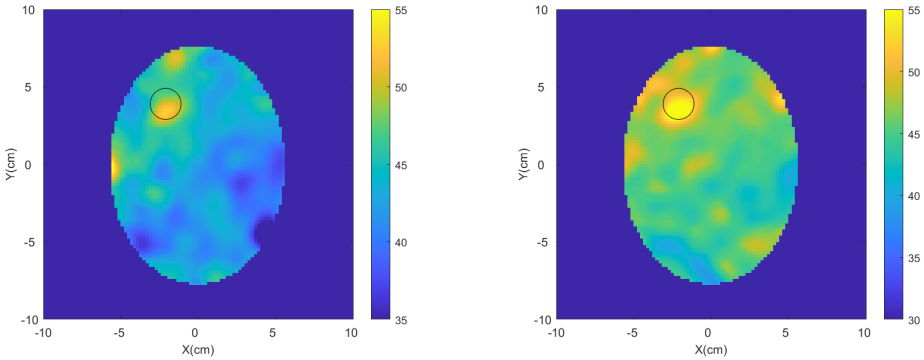

FIGURE 3.49: Frequency hopping reconstructions of the blood-mimicking target obtained from experimental data for the spear patch antenna array (**a**) without MTS and (**b**) with MTS.

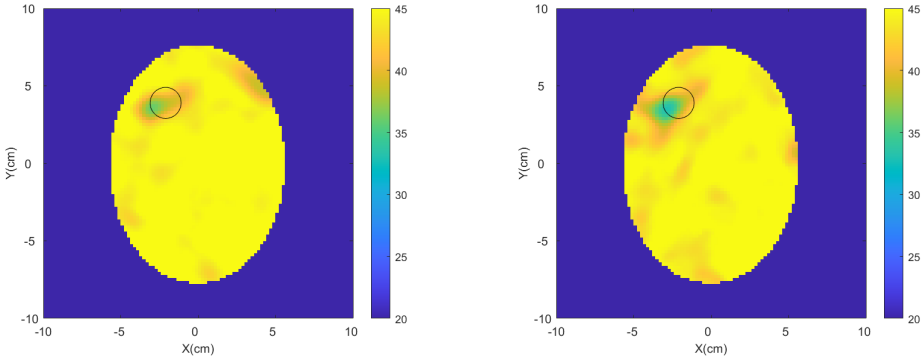

FIGURE 3.50: Frequency hopping reconstructions of the ischaemia-mimicking target obtained from experimental data for the spear patch antenna array (**a**) without MTS and (**b**) with MTS.

Subsequently, two full MTS structures were studied. The experimental results shown in Section 3.3 indicate that a 15×18 unit cell MTS incorporated in a two-port planar setup improves transmission through a simplified planar head model comprising five different tissue layers. In addition, the MTS enhances the signal scattered from a cylindrical blood target introduced in the system. Best results were obtained by placing the antennas as close as possible to the MTS layer. The simulation studies confirmed the experimental findings despite expected differences in the actual transmitted S_{21} coefficients.

Then, further simulation and experimental studies were performed to assess the impact of a 5×6 unit cell MTS on two different monopole antennas. The simulation and experimental investigation conducted for the triangular patch antenna and

presented in Section 3.5, verifies that both the radar and tomographic algorithms described in Section 2.2 can detect and localize a haemorrhagic stroke-mimicking target in its approximate location (if the background signal in the absence of the target is known). Both simulations and measurements were carried out with the custom-made MWI system shown in Figure 3.1 and the target was placed on two different locations to assess the detectability of the algorithms. The results presented in Section 3.5 have shown that the MTS permits a considerable performance enhancement resulting in improvements in both target detection and localization for both radar and tomography.

The investigation carried out for the spear patch antenna was presented in Section 3.6. Similar to the triangular antenna, the results showed that placing the MTS layer adjacent to the substrate of each spear patch antenna has a positive impact on the image reconstruction process. In this configuration, the signal difference due to the blood target inside the brain increases significantly (up to 30 dB). This increased signal difference leads to higher-quality reconstructions of the blood-like target by applying the DBIM-TwIST MWT algorithm and the HP-based algorithm. Single and multiple frequency tomographic reconstructions showed that the MTS can greatly reduce image artefacts and facilitates the localization of the target. Radar reconstruction of a blood-mimicking target placed in three different positions indicate that the MTS enables a correct detection and localization of the target. The MTS-enhanced spear patch antenna was also tested experimentally. The results shown in Section 3.6 suggest that the MTS loading enhances transmission across the head phantom and improves the matching of the in-house fabricated spear patch antenna in the 0.5–2 GHz frequency range. In particular, the signal transmitted across the head phantom, along the direction containing the blood-mimicking target, is overall increased over all the frequency range. Moreover, the antennas' reflection coefficient is reduced by several dBs when the MTS films are incorporated into the system. In conclusion, the enhancement in the imaging reconstruction process obtained for both the antenna designs (using tomographic and radar-based algorithms) strengthens the claim of the MTS having a positive impact on microwave brain imaging.

Chapter 4

Metasurface-Enhanced Antenna for Brain Imaging

This chapter presents a detailed numerical study on the performance of a new printed square monopole antenna (PSMA) operating in air, enhanced by a metasurface (MTS) superstrate loading. In microwave imaging (MWI) for clinical applications, avoiding the use of a coupling medium could be extremely beneficial from a practical point of view. This could indeed lead towards the development of more compact and ergonomic medical systems. As the monopole antennas used in the previous chapters are not matched to operate in the desired frequency band outside the coupling liquid, a new antenna design was needed. Section 4.1 will discuss how the proposed design is tailored to have specific radiation characteristics in front of the head model.

In the simulation study presented in section 4.2, a brain scanner made of 8 spear patch antennas operating in an infinite lossy matching medium is compared to two tomographic systems operating in air: an 8-PSMA system and an 8 metasurface (MTS) enhanced PSMA system. The results presented in this chapter show that the MTS superstrate enhances the antennas' reflection coefficient by around 5 dB and increases the signal difference due to the presence of a blood-mimicking target up to 25 dB, which leads to more accurate reconstructions.

4.1 MTS-Enhanced Printed Square Monopole Antenna Operating in Air

To investigate the possibility of applying microwave tomography (MWT) without employing any matching medium in between the antennas and the human head, the PSMA shown in Figure 4.1a was modelled using CST Microwave Studio®. The proposed PSMA is tailored to have specific radiation characteristics in front of the head model (omnidirectional pattern and specific operational frequency). The design is based on a square patch printed on a RT/duroid 5880 LZ low dielectric substrate

(thickness = 1.026 mm, ϵ' = 1.96, tanδ = 0.0019), with a partial ground on the backside. The antenna is fed using a SMA connector connected with a transmission line (TL). As for the monopole antenna designs shown in Chapter 3, the microstrip feeding centred in the substrate allows easy positioning of the antennas around the head. The very thin substrate with low permittivity was chosen in order to achieve a low-profile design. The vertex-fed configuration allows us to reduce the dimensions of the monopole. The dimensions of the substrate, patch and TL are shown in Figure 4.1a. In order to reduce the size of the monopole to 30 mm $\times$ 76 mm, the dimensions of the substrate were minimized through a parametric study. Furthermore, the height of the ground at the back side was further reduced to 10 mm. Although this choice lowered the directivity and narrowed the bandwidth of the antenna, it allowed to achieve high flexibility for the positioning of the antennas around the head. The reflection coefficient of the antenna measured in free space is plotted in Figure 4.2 (dashed lines). The S_{11} shows a deep resonance around 1.2 GHz, where it falls below -30 dB.

The MTS superstrate structure shown in Figure 4.1b was designed to operate as an enhancer of the antenna described above. This includes a 10 $\times$ 19 unit cell MTS film covering almost the whole antenna's surface and bonded to the front side of the PSMA through Rogers 3001 bonding film (thickness = 0.03 mm). The MTS unit cell design is based on a 0.01 mm thick double square split-ring resonator (DS-SRR) printed on a square RT/duroid 5880 LZ. The thickness of the substrate is 0.635 mm. The dimensions of the DS-SRR are shown in Figure 4.1b. First, the number and period of unit cells was manually optimized to fit the antenna's dimensions and achieve a reduced reflection coefficient. Then, the thickness of the metal wires and the gap capacitances were tailored using CST's "Trust Region Framework" algorithm by setting minimum reflection at 1.1 GHz as a goal. The reflection parameter of the loaded antenna is shown in Figure 4.2 (solid lines).

It is very important to point out that this new MTS-antenna was designed to resonate at 1 GHz in front of the head model. This frequency is one of the central frequencies to reconstruct images. Thus, the S_{11} parameter was optimized taking into account the shift in resonance obtained when placing a lossy structure, such as the head, in front of the antenna. As shown in Figure 4.2, the PSMA's reflection coefficient is reduced by 6 dB and shifted towards lower frequencies when the MTS is added on top of the antenna's substrate. Thus, the MTS shifts the PSMA's operating frequency and improves the matching of the antenna itself.

To characterise the antenna (with and without MTS) proposed in this chapter, near-field parameters should be considered. However, given that there are not many widely acceptable near-field figures of merit to help in the antenna selection and design for

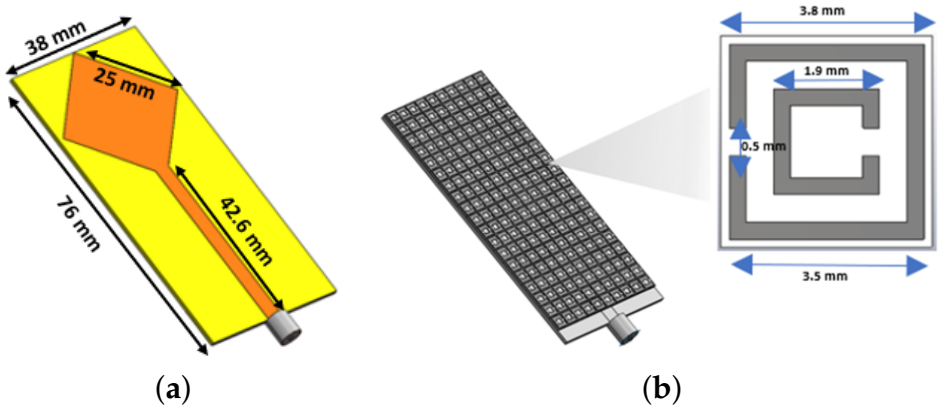

FIGURE 4.1: (**a**) Dimensions of PSMA (**b**) PSMA with MTS superstrate loading and square DS-SRR based unit cell.

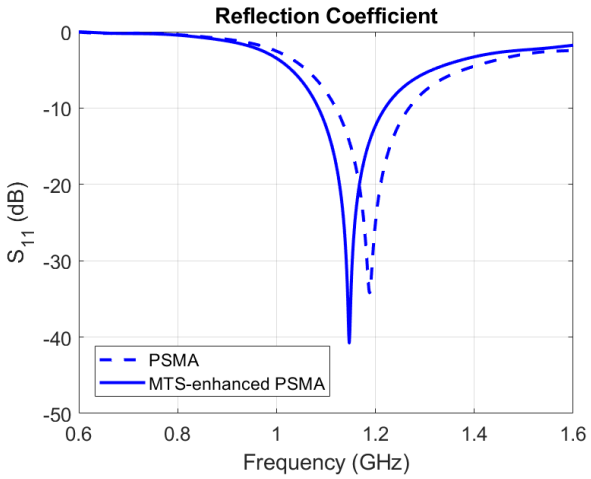

FIGURE 4.2: S_{11} parameter for the PSMA (dashed lines) and the MTS-enhanced PSMA (solid lines). The PSMA's reflection coefficient is reduced and shifted towards lower frequencies when the MTS superstrate loading is added on the antenna's substrate.

MWI applications, it is not uncommon to use just far-field characteristics as a first approach [115]. Thus, for completeness, the radiation pattern and the total efficiency of the proposed antenna at 1.1 GHz (with and without MTS superstrate loading) are shown in Figure 4.3 and Figure 4.4, respectively. Both the antennas were designed to have an omnidirectional pattern. Employing omnidirectional antennas is a very common practice in microwave brain imaging, because it allows to illuminate the whole region of interest and reduce the number of array elements. Moreover, the modification of the near-field antenna pattern due to the antenna operated in the vicinity of an unknown and variable medium, such as the head, is less pronounced for an omnidirectional antenna [116]. As shown in Figure 4.3, the MTS does not have a significant impact on the far-field directivity of the PSMA.

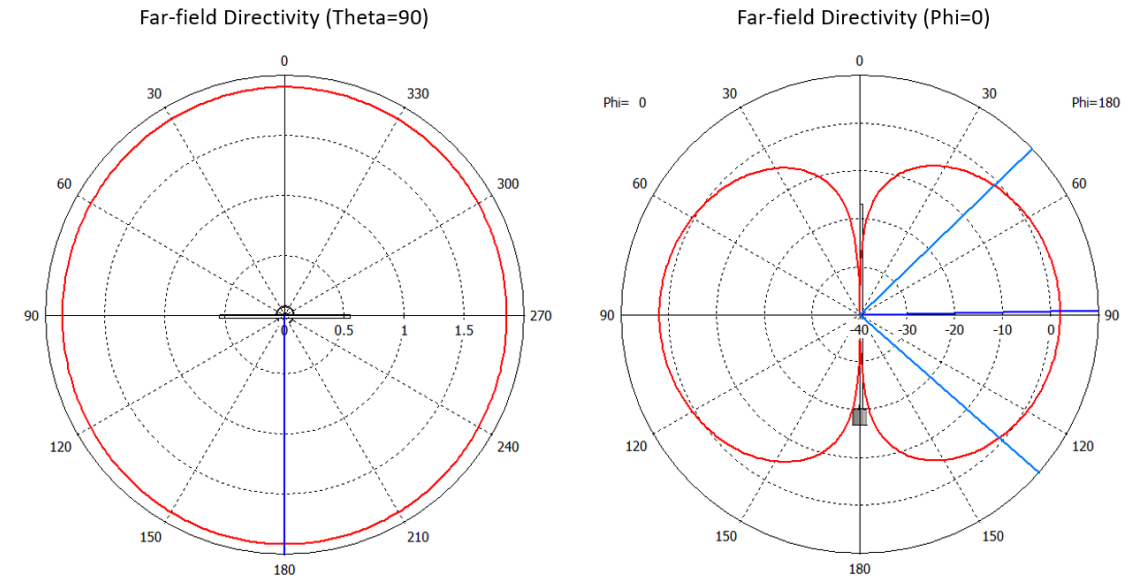

(**a**)

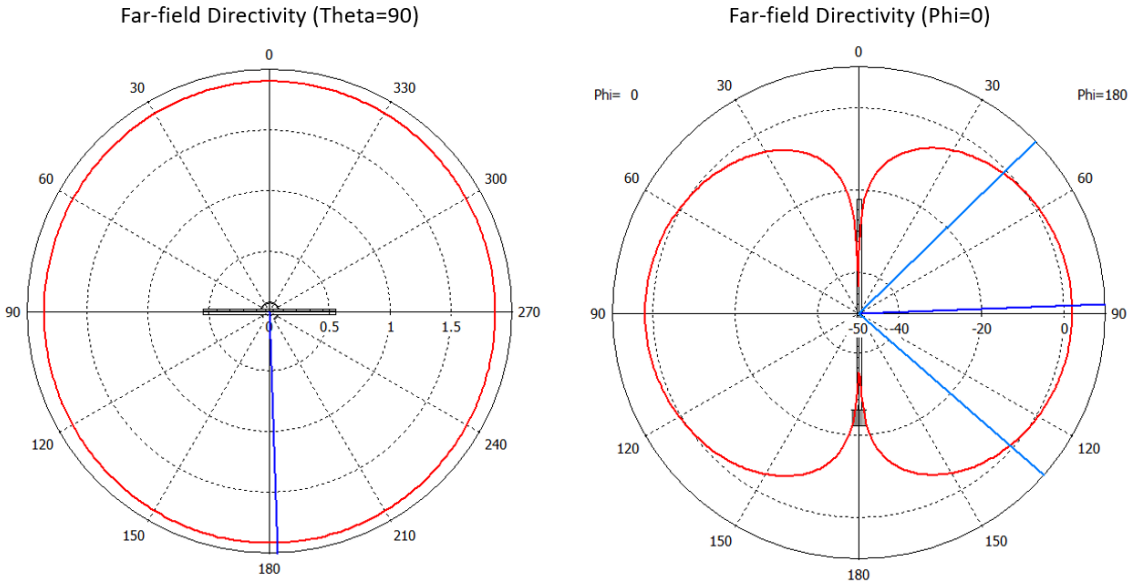

(**b**)

FIGURE 4.3: Far-field directivity at 1.1 GHz. θ=90° (left) and ϕ=0° (right) cuts for (**a**) the PSMA and (**b**) the MTS-enhanced PSMA. Light blue lines indicate the main lobe direction. No significant difference between the two radiation patterns is visible from the plots.

To evaluate the MTS impact on the antenna, near-field parameters must be investigated. Thus, as in Chapter 3, the total E-field distribution was plotted on the surface of the brain phantom shown in Figure 4.5a. The E-field was plotted at 1 GHz, for the PSMA transmitting with and without MTS. The plots in Figure 4.5b show that the MTS does not focus the E-field onto a tighter beam, but on the contrary, it widens the E-field distribution inside the head model, resulting in better signal coverage. This might be

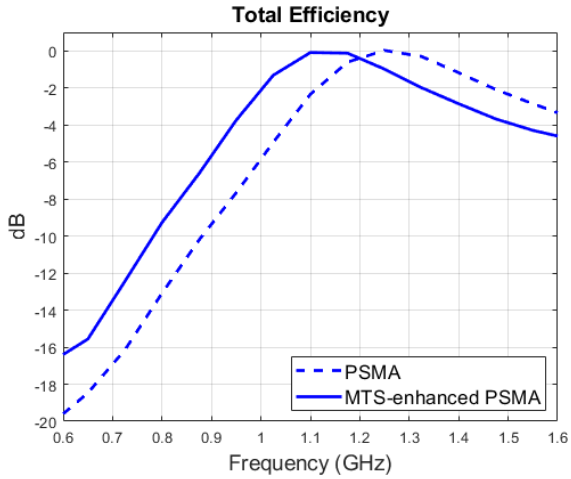

FIGURE 4.4: Total efficiency (in dB) plotted as a function of frequency for the PSMA (blue dotted lines) and the MTS-enhanced PSMA (blue solid lines). The total efficiency improved by 2 dB in the 0.6-1.1 GHz frequency range, in the presence of the MTS.

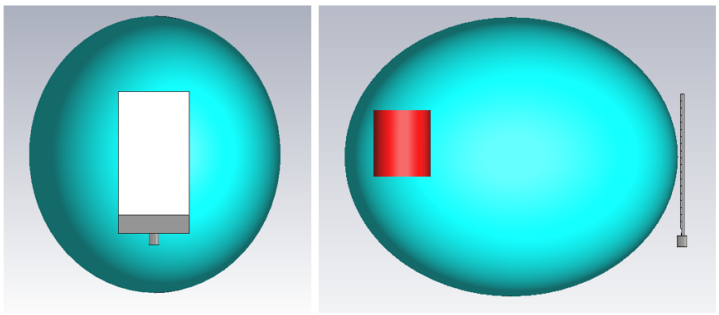

(**a**)

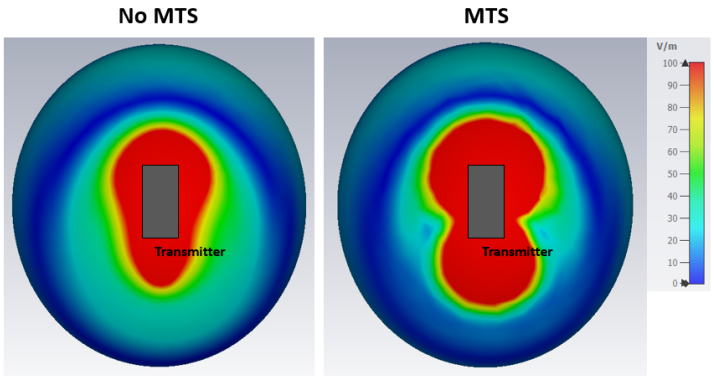

(**b**)

FIGURE 4.5: (**a**) Simulated setup with a transmitter placed in front of the brain model. A blood-mimicking target is inserted in the back side of the brain, opposite to the transmitter. (**b**) E-field distribution on the surface of the elliptical brain phantom for the "no MTS" (left) and "MTS" (right) case scenarios. The MTS superstrate loading produces a wider E-field distribution.

the reason why, as shown in the following sections, the target's response is stronger in the presence of the MTS. Figure 4.6 shows the E-field distribution on a transversal section of the brain model and on the target's surface. As shown from the plots, the E-field intensity is visibly increased when the MTS superstrate is applied on the PSMA. This is due to the response of the DS-SRRs to the applied field. When a time-varying magnetic field is applied perpendicularly to the square resonators, current loops are generated. Furthermore, the E-field couples with the end of the wires (in proximity of the splits). Thus, the resonators produce their own field, which might enhance or oppose the incident field. For this reason, the field distribution on the brain phantom model changes in the presence of the MTS superstrate.

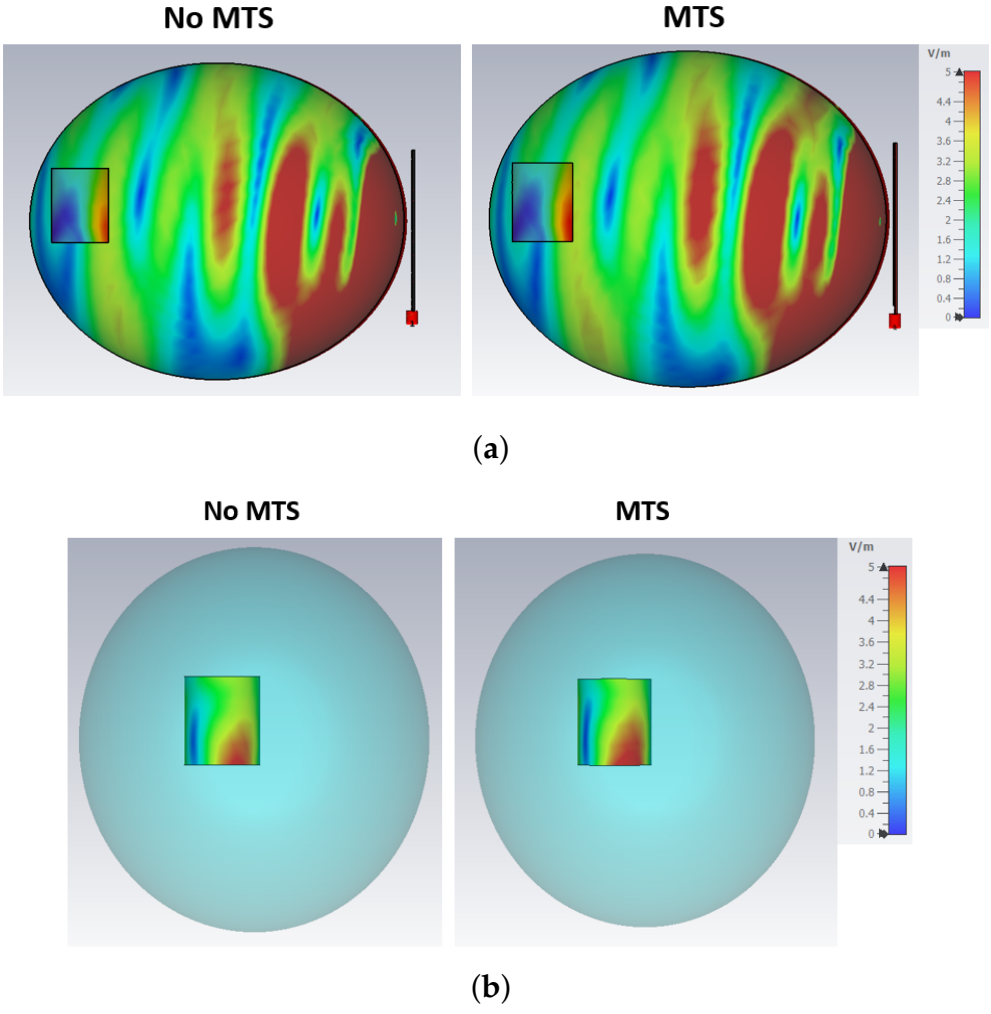

FIGURE 4.6: (**a**) E-field plotted on a longitudinal section of the brain phantom containing the blood-mimicking target, without (left) and with MTS (right). The MTS enhances the field's intensity in the centre of the brain and on the surface in the target area. (**b**) E-field distribution on the surface of the blood-mimicking target for the "no MTS" (left) and "MTS" (right) case scenarios. The MTS superstrate loading produces a wider and more intense E-field distribution on the blood-mimicking target.

4.2 PSMA and MTS-Enhanced PSMA: Comparison between Different MWT Scanners

To test the performance of the new PSMA and MTS-enhanced PSMA, three different brain scanners were studied and compared. KCL's previously developed MWT scanner for brain imaging (see Figure 3.40) consists of 12 spear patch antennas immersed in a 90% glycerol-water mixture and placed around SAM (Specific Anthropomorphic Mannequin) head model [105, 117]. A similar setup ("System 1"), including 8 spear antennas placed elliptically around SAM, was modelled in CST. The antenna array was immersed in an infinite mixture of 90% glycerol-water matching medium. The radiation pattern of the spear patch antenna is shown in Figure 4.7. These results were obtained for the antenna immersed in infinite matching medium. Total efficiency and gain values are extremely low due to the immersion liquid.

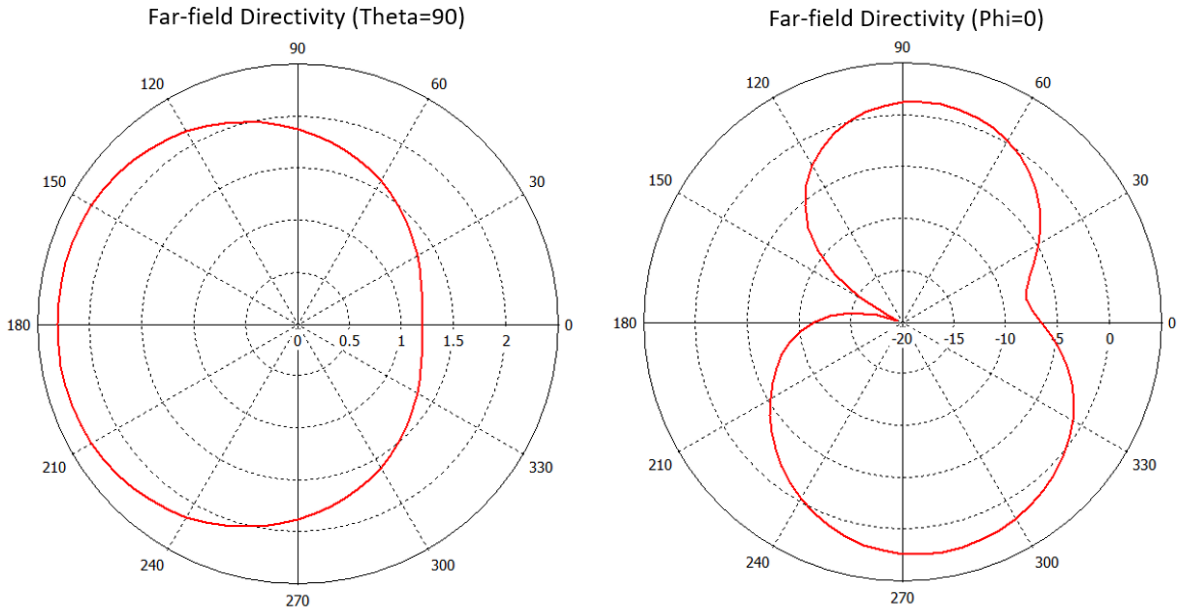

FIGURE 4.7: (**a**) θ=90° and (**b**) ϕ=0° cuts of the far-field directivity at 1.5 GHz for the spear patch antenna immersed in infinite coupling liquid.

Using the same numerical head model, other two MWT scanners operating in air were studied: "System 2", which comprises 8 PSMAs, and "System 3", which includes 8 MTS-enhanced PSMAs. In these MWT systems, the antennas were closely fixed to the head's surface. The MWT antenna arrays described above are summarised in Table 4.1. "System 1" and "System 3" are shown in Figure 4.8.

The head model is made of a nylon mould ($\epsilon' = 3.2$, $\tan\delta = 0.013$) containing an average brain numerical phantom inside ($\epsilon' = 45.8$ and $\sigma = 0.76$ S/m). We will refer to the

TABLE 4.1: MWT antenna arrays for brain imaging simulated in CST

System	Number of antennas	Type of antennas
"System 1"	8	Spear antennas
"System 2"	8	PSMAs
"System 3"	8	MTS-enhanced PSMAs

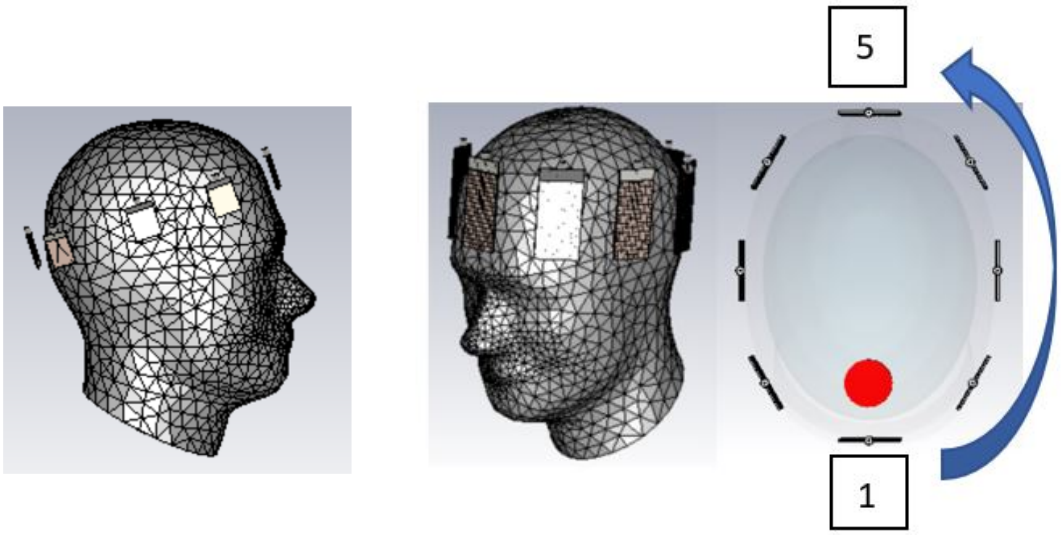

(**a**) (**b**)

FIGURE 4.8: (**a**) 8-PSMA array ("System 1") (**b**) 8-MTS-enhanced PSMA array ("System 3") and its transversal view. "System 2" is equal to "System 3" except for including non-enhanced PSMAs. The antennas are distributed conformally to the head model and are numbered anticlockwise starting from the antenna placed in front of the target.

model with brain and nylon alone as the "no target" scenario. The signal propagation in the presence of a blood-like target inside the brain volume was also studied. The target was a cylinder of 30 mm diameter and 35 mm height, placed at the back of the brain, in front of antenna 1 (see Figure 4.8b). We will refer to this case (with the blood target introduced in the brain) as the "with target" scenario. The properties of blood to the aforementioned target were assigned from CST's material library. For each antenna array, the S-parameters for reflection and transmission were calculated in CST over the 0.5–2 GHz frequency range for the "no target" configuration (head model including average brain only) and the "with target" configuration. Then, the signal difference "with target - no target" (in dB) at relevant frequencies was calculated. Finally, single and multi-frequency reconstructions were carried out by applying the 2D DBIM-TwIST algorithm [89] to the simulation data.

4.3 PSMA and MTS-enhanced PSMA: Simulation Results with different Brain Scanners

Figure 4.9 shows the reflection parameter for each of the antennas of "System 1", "System 2" and "System 3". The plots show that the presence of the MTS superstrate loading reduces the reflection coefficient of the PSMA by 5 dB. Relevant transmission parameters for "System 2" and "System 3" are shown in Figure 4.10. These parameters are slightly enhanced in the 0.5-1 GHz frequency due to the MTS loading. An improvement in the S_{36} and S_{38} parameters is also visible around 1.2 GHz. Transmission is inevitably lower for "System 1", due to the lossy matching liquid.

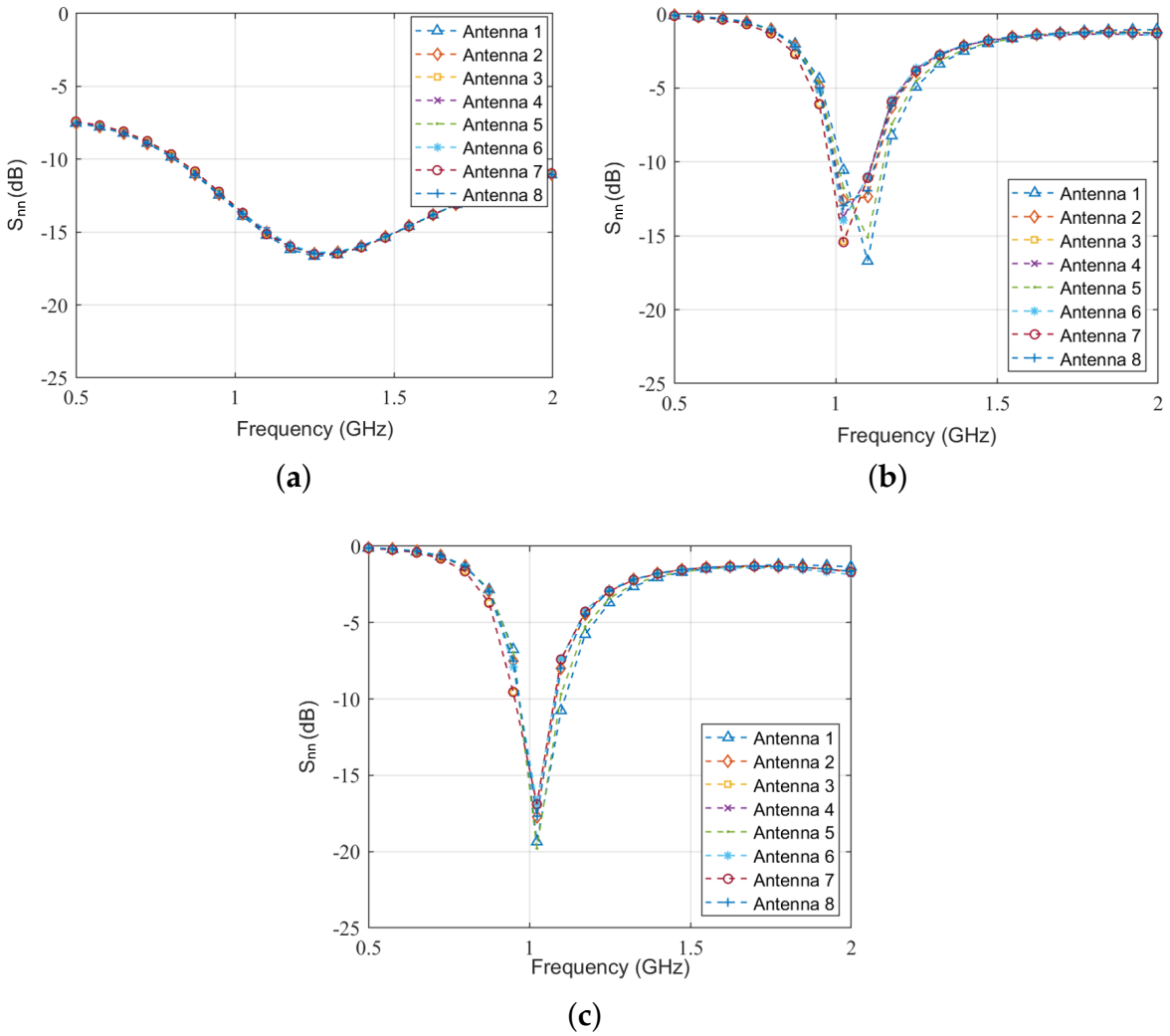

FIGURE 4.9: Calculated reflection coefficients for the "no target" scenario for (**a**) the spear patch antennas, (**b**) the PSMAs and (**c**) the MTS-enhanced PSMAs.

Figure 4.11 shows the signal difference "with target – no target" (in dB) at frequencies 1 GHz and 1.1 GHz for "System 1", "System 2" and "System 3". This differential

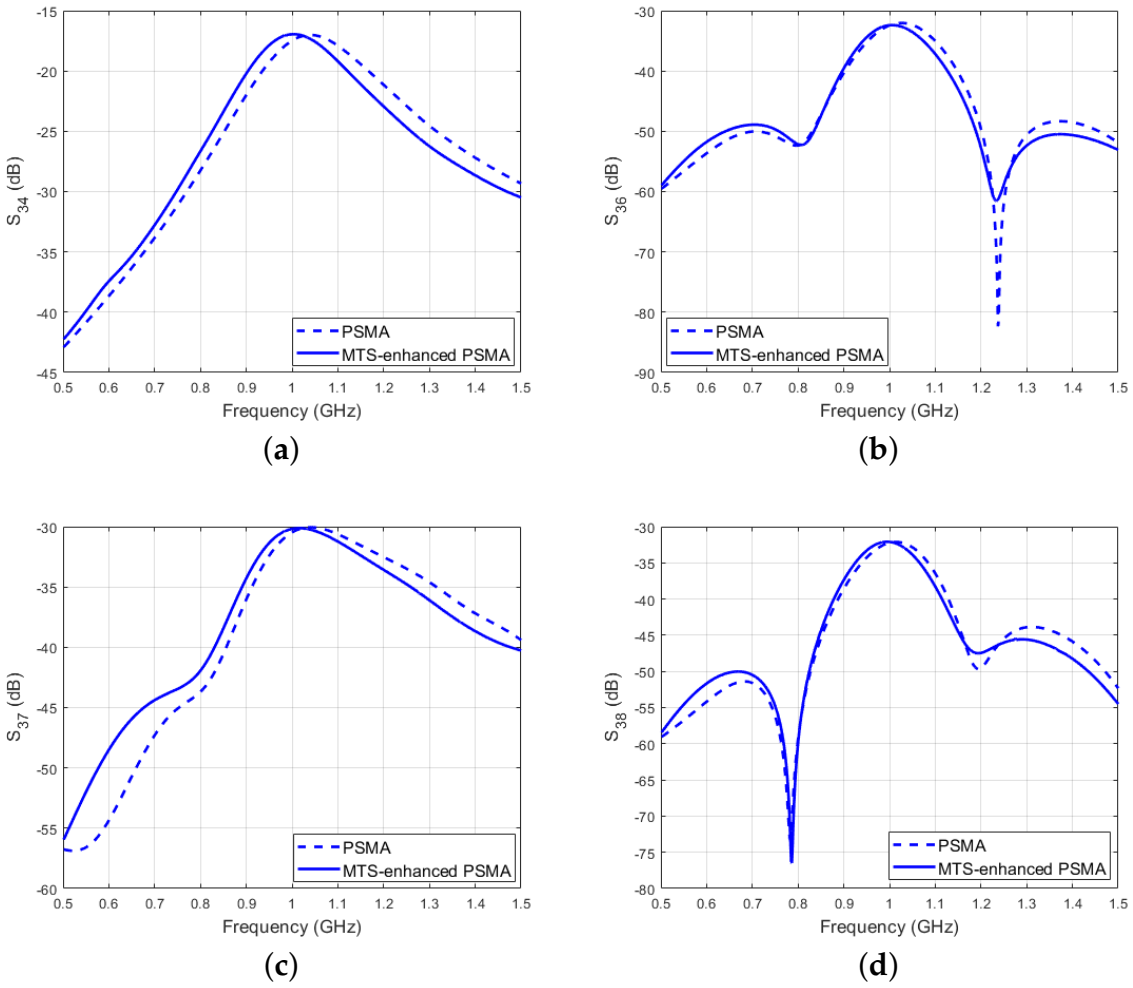

FIGURE 4.10: (**a**) S_{34}, (**b**) S_{36}, (**c**) S_{37} and (**d**) S_{38} parameter, calculated for "System 2" (blue dashed lines) and "System 3" (blue solid), in the "with target" scenario. Transmission is slightly enhanced in the 0.5-1 GHz frequency range due to the MTS superstrate. A noticeable improvement in the S_{36} and S_{38} parameters can be observed around 1.2 GHz.

signal is plotted for each transmitter, as function of the receivers' location. As shown in the graphs, when the PSMA is loaded with the MTS superstrate ("System 3"), it leads to an overall improvement of the signal backscattered by the blood-mimicking target, compared to "System 2". For instance, when antenna 1 (i.e., Trans 1, which is the transmitter in front of the blood-mimicking target) is transmitting, the target's response received by antenna 5 is improved by 10 dB at 1 GHz (see Figure 4.11a). This signal enhancement (up to 25 dB) can be observed for most of the receivers' locations and suggest that the MTS might contribute to achieve high quality reconstruction images. Another interesting point is to note that the coupling liquid severely affects the signal scattered by the blood-mimicking target, which falls below the noise level (below -100 dB). For instance, if we refer to "System 3" (black solid lines) in Figure 4.11a, we can

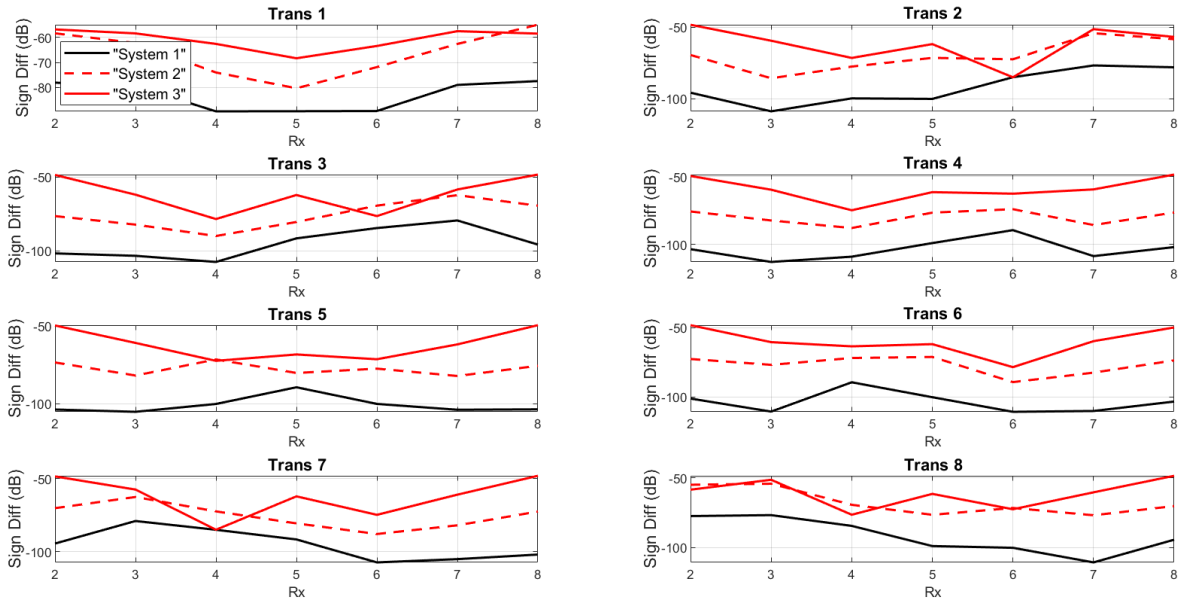

(**a**)

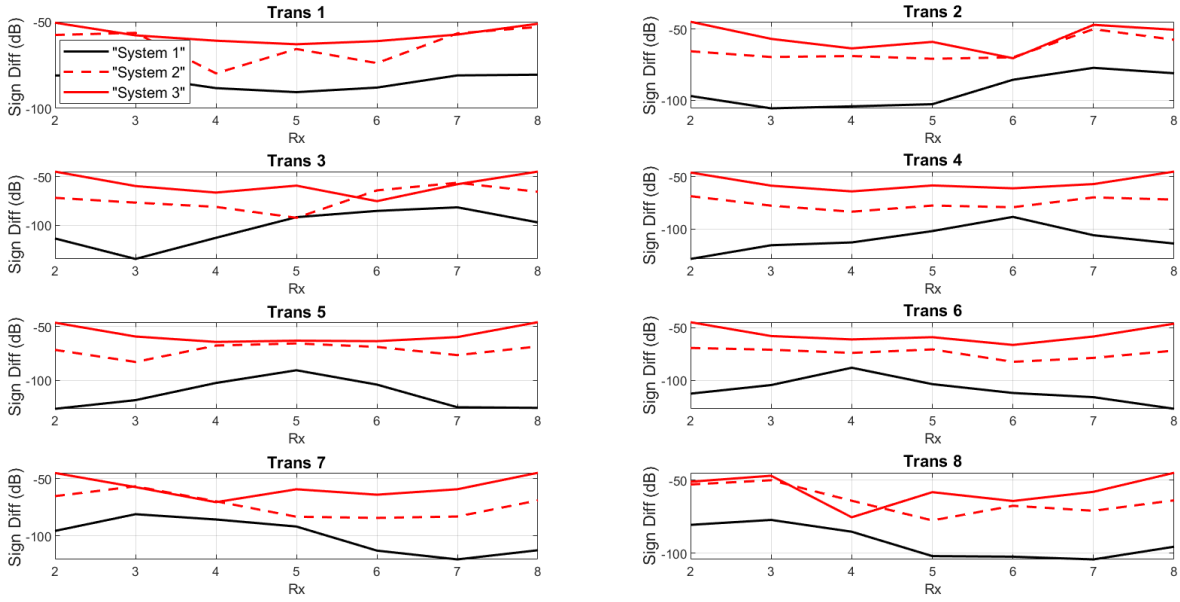

(**b**)

FIGURE 4.11: Calculated signal difference "with target - no target" (dB) for the 8-spear patch antenna array operating in infinite matching medium ("System 1"), the 8-PSMA array ("System 2") and the 8-MTS-enhanced PSMA array ("System 3") at (**a**) 1 GHz and (**b**) 1.1 GHz. The differential signal is plotted for each transmitter, as function of receiver location. The antenna numbering is anti-clockwise, as shown in Figure 4.8.

observe that, when antenna 1 is transmitting (Trans 1), the differential signal received by antenna 5 is equal to -90 dB. This suggests that the matching medium employed in "System 1" severely affects the detection of useful "weak" signals backscattered by the blood-mimicking inclusion. Thus, the feasibility of designing head scanners operating in air must be investigated.

Finally, to test the MTS's impact on tomographic reconstructions, the 2D DBIM-TwIST algorithm was applied to the simulated data plotted in Figure 4.11. Single and multiple-frequency reconstructions were carried out, assuming approximate knowledge of the dielectric properties of plastic and average brain tissue as initial guess for the algorithm. The multiple frequency (frequency hopping) reconstructions are shown in Figure 4.12. For the frequency hopping, two frequencies (1 GHz and 1.1 GHz) were used in the interval 0.5–2 GHz. As the spear patch antenna is operating at higher frequencies [17], a single frequency reconstruction at 1.6 GHz was carried out for "System 1" (see Figure 4.12a). The estimated dielectric properties at frequencies 0.9 GHz, 1 GHz and 1.1 GHz is shown in Figure 4.13. The reconstruction results presented in this section show that when employing the new PSMA operating in air ("System 2"), the blood-mimicking target is detected correctly. However, a higher contrast between the haemorrhage-mimicking target and the surrounding brain tissue is observed when the MTS is integrated in the scanner ("System 3"). The most encouraging observation from these figures is that there is a clear distinction in the estimation of the targets' dielectric properties between the "no MTS" systems ("System 1" and "System 2") and "System 3". For instance, observing the single frequency reconstruction images at 1 GHz and 1.1 GHZ in Figure 4.13, we can see how, in the presence of the MTS, the permittivity values in the target's area are close to 65 (value set in the simulations).

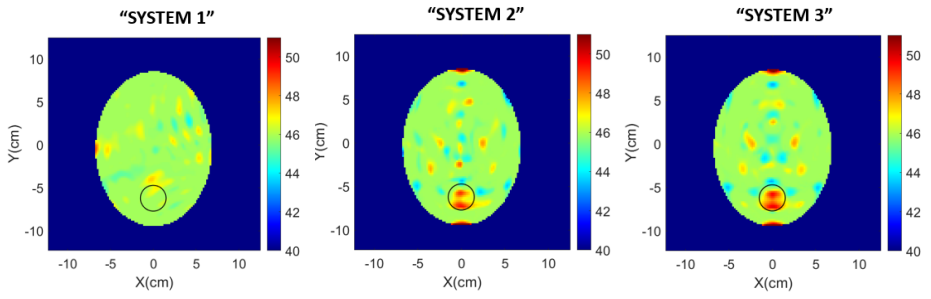

(**a**) (**b**) (**c**)

FIGURE 4.12: Real part of permittivity reconstructed from simulation data for (**a**) the 8-spear patch antenna array operating in infinite matching medium (1.6 GHz) (**b**) the 8-PSMA array operating in air (frequency hopping at 1.0 and 1.1 GHz) (**c**) the 8-MTS-enhanced PSMA array operating in air (frequency hopping at 1.0 and 1.1 GHz).

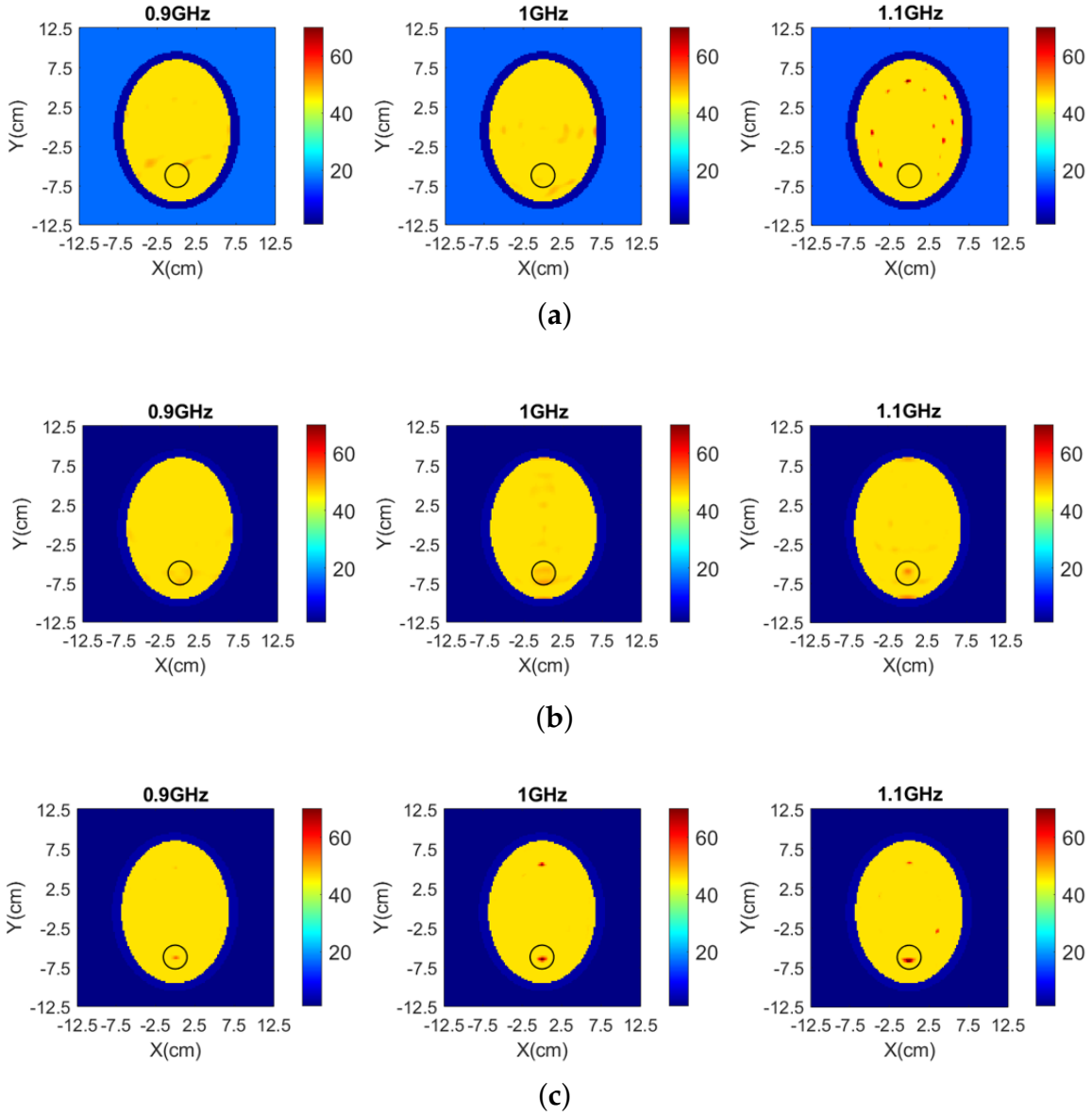

FIGURE 4.13: Real part of permittivity reconstructed from simulation data at frequencies 0.9 GHz, 1 GHz and 1.1 GHz for (**a**) the 8-spear patch antenna array operating in infinite matching medium ("System 1") (**b**) the 8-PSMA array ("System 2") and (**c**) the 8-MTS-enhanced PSMA array ("System 3") operating in air.

4.4 Conclusions

The purpose of the study proposed in this chapter was to investigate the feasibility of developing portable, compact and ergonomic microwave brain imaging scanners, capable of detecting a haemorrhage-mimicking target without the need of coupling materials. To this end, a new MTS-enhanced PSMA was modelled to test the 2D DBIM-TwIST in air. Then, three MWT scanners were tested and compared using a numerical head model made of average brain tissue and including a blood-mimicking target. For

each system, the S-Parameters were measured over the 0.5-2 GHz frequency range and the signal difference "with target - no target" (in dB) at relevant frequencies was calculated. Multiple frequency (frequency hopping) and single frequency reconstructions were also performed.

The results presented in this chapter indicate that it is possible to detect a blood-mimicking target placed inside the brain volume of a simple head model without using a bulky immersion liquid. Furthermore, the signal difference due to the presence of the target is increased in the presence of the MTS superstrate loading. This translates into higher-quality reconstruction images.

Chapter 5

Metasurfaces for Monitoring and Screening Devices

As mentioned in Chapter 1, the research presented in this thesis was aligned with tasks and objectives of EMERALD's WP2, which focused on improving the hardware of the microwave prototypes developed within the EMERALD network. All the numerical studies presented in this chapter were performed during two of the four secondments (i.e., exchange visits) planned by the EMERALD consortium. In this chapter, new metasurface (MTS) designs are proposed for monitoring and screening applications. More specifically, the first section presents an impedance-matching MTS for cerebrovascular (CVA) imaging. This design was modelled to replace the thick and bulky matching medium employed in the head scanner developed by PoliTo (Politecnico di Torino, Italy). The second section is focused on breast cancer detection. In particular, a modification of the Vivaldi antenna designed by MITOS Medical Technologies (Instanbul, Turkey) is proposed. The originality of the work presented below resides in the design procedure, which is tailored to satisfy specific requirements, depending on the prototype.

5.1 Impedance-Matching Metasurface for Cerebrovascular Imaging

This section presents a new feasibility study of enhancing microwave brain imaging using an innovative Jerusalem cross-shaped MTS. This MTS was designed to be integrated into the novel low-complexity microwave imaging (MWI) system for monitoring brain stroke developed by PoliTo. As in Chapter 4, the new MTS film was modelled to avoid the use of coupling materials between the radiating antennas and the human head. It is important to notice that the numerical study presented in this section assesses the impact of using MTS films on a different brain scanner. For this

reason, the results presented in this section further validate the benefits of using MTS technology in microwave brain imaging.

5.1.1 Cerebrovascular Imaging Device for Brain Stroke Detection and Monitoring Developed by PoliTo

The MWI device for CVA imaging developed by PoliTo is shown in Figure 5.1. It comprises a helmet with 24 monopole antennas operating in blocks of solid matching medium and a simplified model of the head. The use of a semi-flexible material (a mixture of urethane rubber and graphite powder) with custom-permittivity allows to avoid the use of coupling liquid and enables simple array arrangement [116]. This matching medium is easy to fabricate. The addition of graphite powder to the rubber is needed to increase the permittivity of the mixture to the designed value. The graphite powder increases also the conductivity. However, this remains comparable or lower with respect to the conductivity values of the common coupling materials used in medical MWI. The optimal layout of the antenna array was achieved by carrying on a rigorous design procedure, which is described in [11]. This procedure identifies the exact number and position of the antennas, which are arranged around a 3D printed anthropomorphic mannequin filled with a stable liquid phantom, resembling the dielectric properties of the average brain.

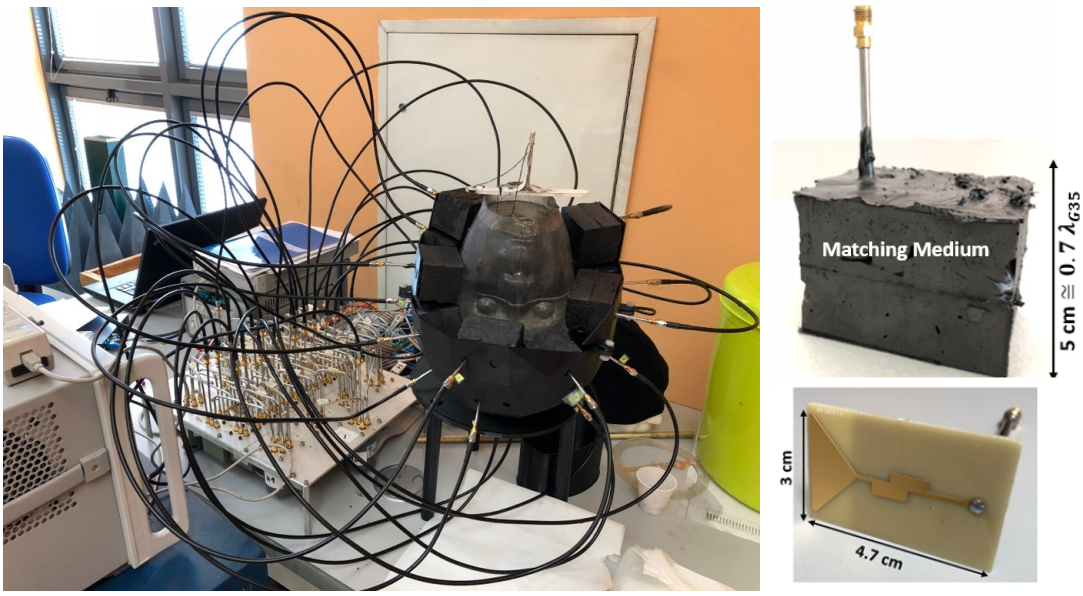

(**a**) (**b**)

FIGURE 5.1: (**a**) CVA system and (**b**) monopole antenna operating in a 5 cm thick mixture of urethane rubber and graphite powder. *Credit: PoliTo (Politecnico di Torino, Turin, Italy).*

5.1.2 Metasurface Design

The MTS film presented in this section was modelled to replace the matching medium shown in Figure 5.1. This MTS design was optimized to be placed adjacent to each antenna's substrate, in between the antenna and the head phantom.

Metasurface Unit Cell

The new Jerusalem cross-based unit cell shown in Figure 5.2a was designed to match the impedance of a planar model of the head phantom described in Section 5.5.1. This model includes a thin layer of ABS (Acrylonitrile Butadiene Styrene) and average brain. The ABS layer (ϵ'= 2.74, tanδ = 0.0051) is 2.5 mm thick, whereas the brain slab (ϵ'= 45.8 and tanδ = 0.76 S/m) has a thickness of 70 mm. The metamaterial (MM) film comprises a copper Jerusalem cross (thickness = 0.1 mm) printed on a flexible Rogers RO3010 TM substrate (thickness = 0.6 mm, ϵ'= 10.2 and tanδ = 0.0022). The unit cell was tested using CST Microwave Studio® for a plane wave excitation of linear polarization, considering "Port 1" before the MTS and "Port 2" after the phantom layer. The Jerusalem cross' geometric parameters and the substrate's thickness were optimized using CST's "Trust Region Framework" for maximum transmission in the 0.8-1.2 GHz frequency range. As a result, a transmission improvement (about 3 dB at 1 GHz) due to the presence of the MTS was shown. In addition, reflection was also greatly reduced, up to 6.5 dB at 1 GHz (see Figure 5.2b).

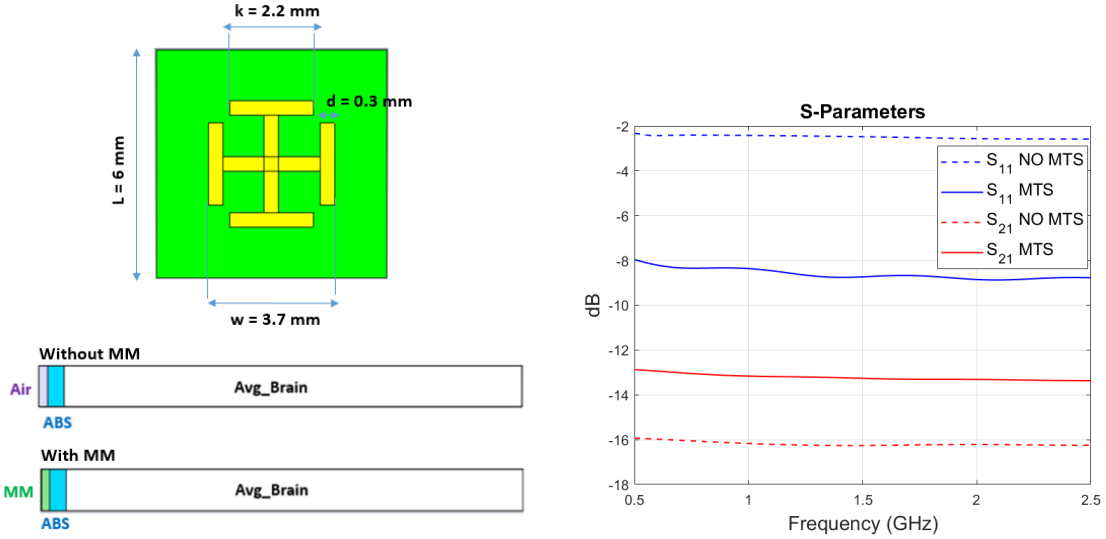

(**a**) (**b**)

FIGURE 5.2: (**a**) New MTS unit cell and simplified phantom model (**b**) S-Parameters for the setup shown in (a). In the "no MTS" configuration, the MM sheet is replaced with air.

Metasurface Full Structure

After optimizing the unit cell geometry, different dimensions for a periodic structure based on the unit cell design were tested on a planar setup comprising a thin layer of ABS (100 mm × 100 mm × 2.5 mm) and average brain (100 mm × 100 mm × 150 mm). The S-parameters for reflection and transmission were calculated for "Port 1" and "Port 2" before and after the head model, respectively. The antenna shown in Figure 5.1b was used as excitation source ("Port 1"). Figure 5.3 shows the S-Parameters obtained for different MTS dimensions (e.g. 5 by 8 unit cell MTS, 5 by 9 unit cell MTS etc...). The S-Parameters plotted in Figure 5.3 show that a higher transmission and a reduced reflection coefficient is obtained for the 5 by 8 and 9 by 8 unit cell MTS. As the size of the smallest MTS was fitting the dimensions of the antenna's substrate, this was chosen to be integrated in the system and further tested using the planar setup shown in Figure 5.4. This 2-Port setup includes a block of average brain phantom (100 mm × 100 mm × 150 mm), two layers of ABS (100 mm × 100 mm × 2.5 mm) and two monopole antennas placed in contact with the plastic slabs.

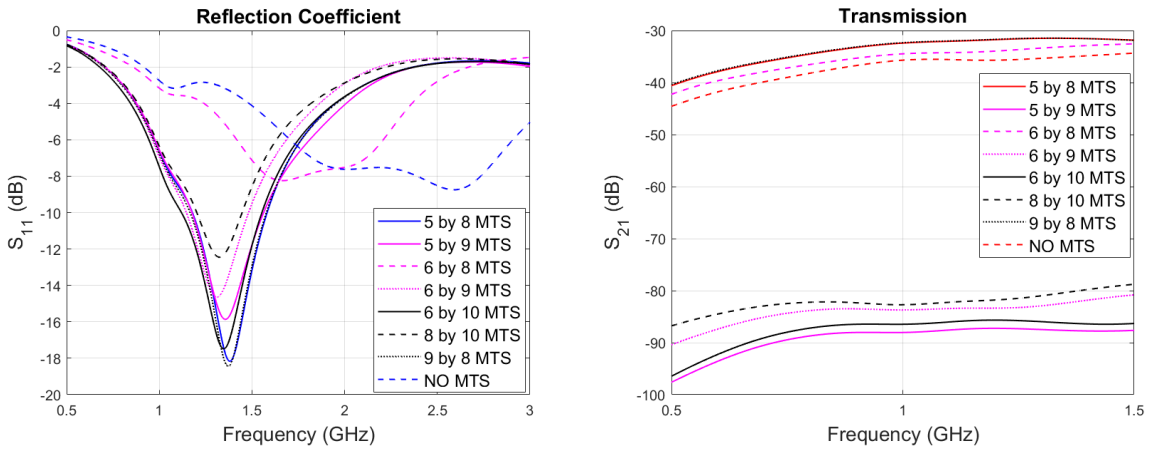

FIGURE 5.3: (**a**) Reflection and (**b**) transmission parameters obtained for MM layers of different dimensions.

To investigate whether the MTS was capable of enhancing the "weak" signal backscattered by a blood-mimicking target resembling a haemorrhagic stroke, the propagation of electromagnetic (EM) waves was studied, with and without MTS, for a phantom including only ABS and average brain ("no target" scenario) and in the presence of a blood-like target inside the average brain volume ("with target" scenario). The blood-mimicking target consists of a blood cylinder of 12 mm diameter and 10 mm height placed in the middle of the brain volume. For each configuration, the S-parameters were measured over the 0.5–1.5 GHz frequency range and the signal difference "with target – no target" (in dB) was calculated. The graph in Figure 5.4b

shows that this difference is greatly increased due to the presence of the MTS (22 dB at 1.1 GHz), suggesting that the MTS enhances the signal backscattered by the blood-mimicking target. Furthermore, the E-Field plots in Figure 5.5 show that the MTS focuses the E-field in the target's region, enhancing its intensity in that area.

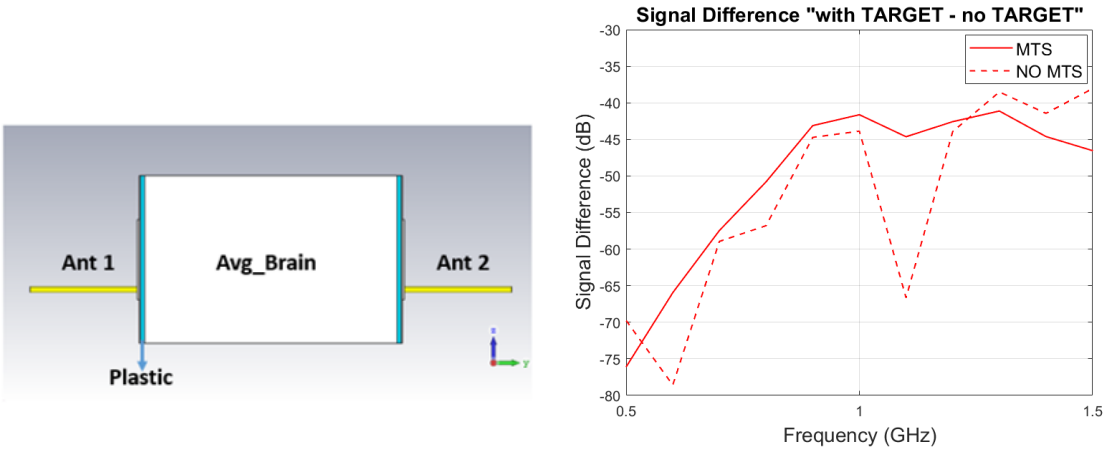

(**a**) (**b**)

FIGURE 5.4: (**a**) 2-port planar setup and (**b**) signal difference "with target - no target" (dB), with (solid lines) and without MTS (dashed lines). This differential signal is greatly enhanced in the presence of the MTS.

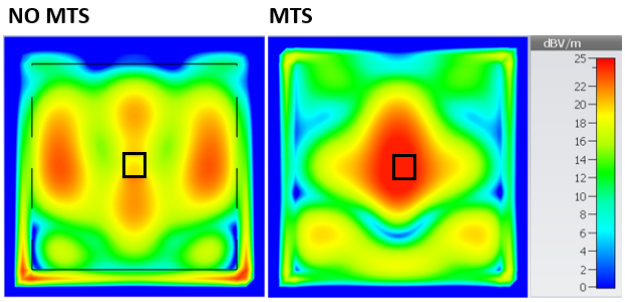

(**a**)

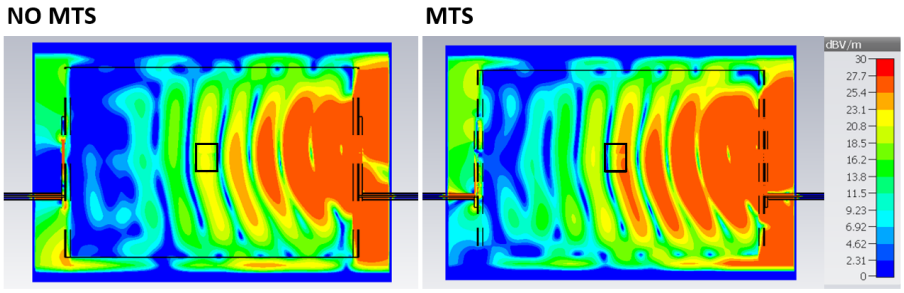

(**b**)

FIGURE 5.5: E-field plotted on (**a**) a cross-section and on (**b**) a longitudinal section of the planar brain phantom containing the blood-mimicking target.

5.1.3 Simulations of PoliTo's Device for Brain Imaging (Simplified Scanner)

2-Port Setup

After testing the MTS on planar setups, preliminary simulations with a 2-Port MWI scanner for brain haemorrhage detection were carried on. To simulate this first setup in CST, SAM head model was used. The numerical head model and the MTS antenna's coating are shown in Figure 5.6a. As with the previous simulations, the S-parameters for reflection and transmission were measured in the "no target" and "with target" configurations, with and without MTS, and the signal difference "with targer - no target" (in dB) was calculated. Figure 5.6b shows an enhancement of this differential signal in the presence of the MTS, up to 24 dB at 1.4 GHz (which is the operational frequency of the MTS-enhanced antenna). As shown in Chapter 3, this enhancement might contribute to reconstruct higher quality images. Despite the improvement in the differential signal shown in Figure 5.6b is not visible for all the frequencies in the 0.5-2 GHz range, the results shown in following subsection suggest that, for a 12-antenna array, it is possible to reconstruct images only when using the MTS. Furthermore, as for the planar setup, the E-field plots in Figure 5.7 show that the MTS enhances the field's penetration in the brain. More specifically, the plots indicate that the field's intensity at 1.3 GHz in the target region is noticeably increased in the presence of the MTS.

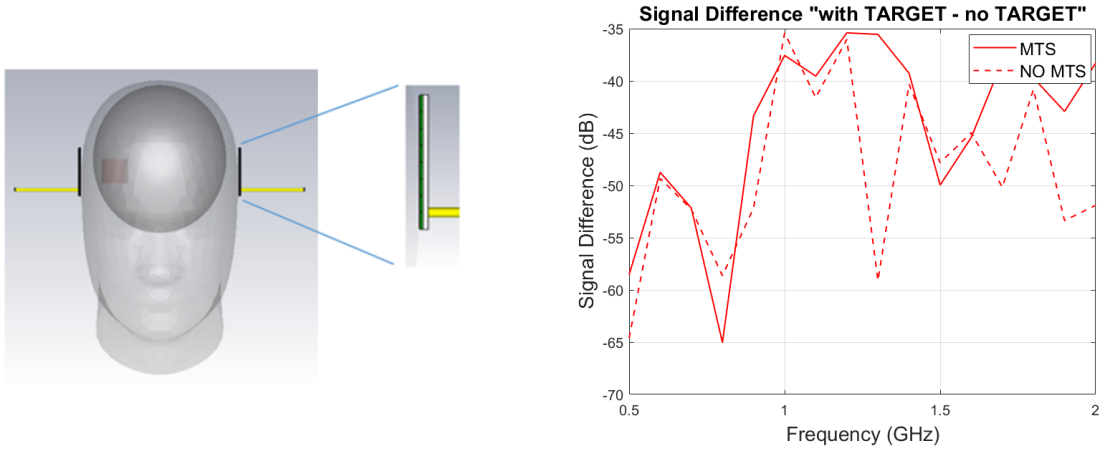

(**a**) (**b**)

FIGURE 5.6: (**a**) Proposed headband scanner and MTS-based antenna. The blood-mimicking target is inserted in the brain volume, in front of "Port 1" (**b**) Signal difference "with target - no target" (dB) with (solid lines) and without MTS (dashed lines). When the MTS is applied on the antenna's substrate, the differential signal is greatly enhanced around 1.4 GHz (which is the operational frequency of the MTS-enhanced antenna).

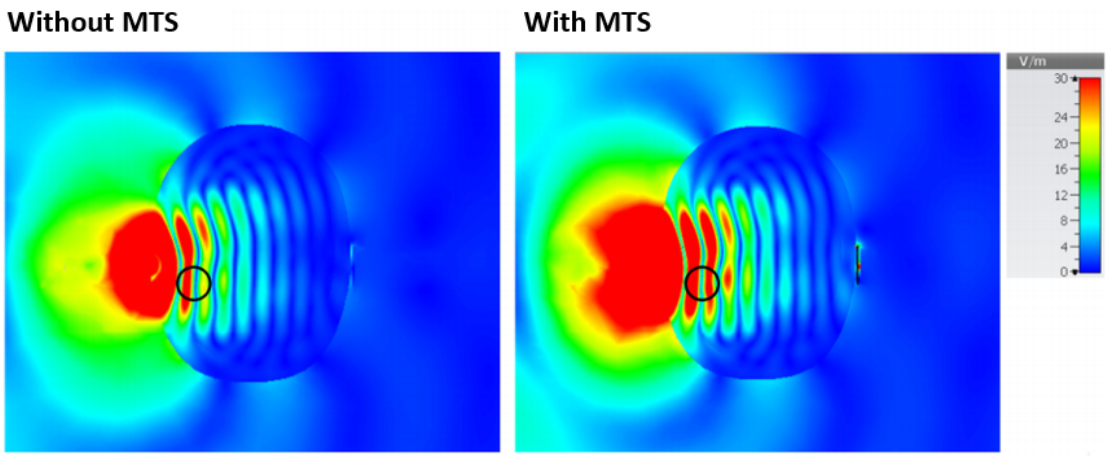

FIGURE 5.7: E-field at 1.3 GHz plotted on a transverse section of the human head model (for the "with target" configuration) with and without MTS. The field's penetration is significantly enhanced when the MTS is applied on the substrate of the transmitting antenna.

12-Port Setup

To further test the MTS's performance, the antenna array shown in Figure 5.8b was modelled. This system comprises 12 monopole antennas arranged around SAM head model. A MTS sheet was placed on the numerical head phantom, closely fixed to

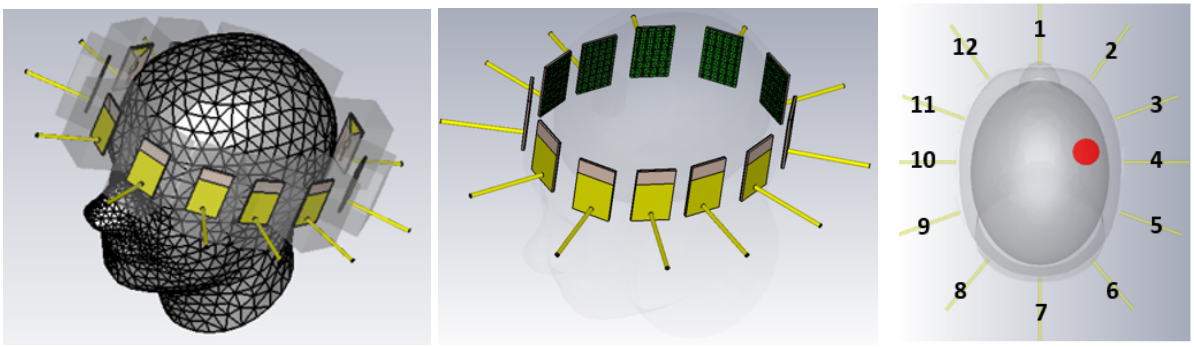

(**a**) (**b**) (**c**)

FIGURE 5.8: (**a**) 12 antenna-array operating in G35 (mixture of urethane rubber and graphite powder) (**b**) 12 antenna-array operating air plus MTS. (**c**) Target's location with respect to the antennas' position. The antennas are numbered clockwise starting from the antenna placed in front of the numerical head phantom.

the MWI antennas. Then, a blood-mimicking target of 4 cm diameter and height was inserted in the brain volume and positioned between antennas 3 and 4, as shown in Figure 5.8c. To investigate whether the MTS sheets had the capability of enhancing the "weak" signal backscattered by the blood-mimicking inclusion, this system was compared to a similar one, including 12 brick-shaped antennas. As for the previous

simulations, the S-Parameters were calculated over the whole frequency range and the signal difference "with target – no target" (in dB) was measured at 1.5 GHz, which corresponds to the resonant frequency of the antenna when operating in front of the MM slab. As shown in the Figure 5.9, the brick-shaped matching medium (G35) affects the "weak" signal scattered by the target, which also falls below the noise level. On the contrary, the differential signal is overall enhanced (up to 35 dB) in the presence of the MTS-based array.

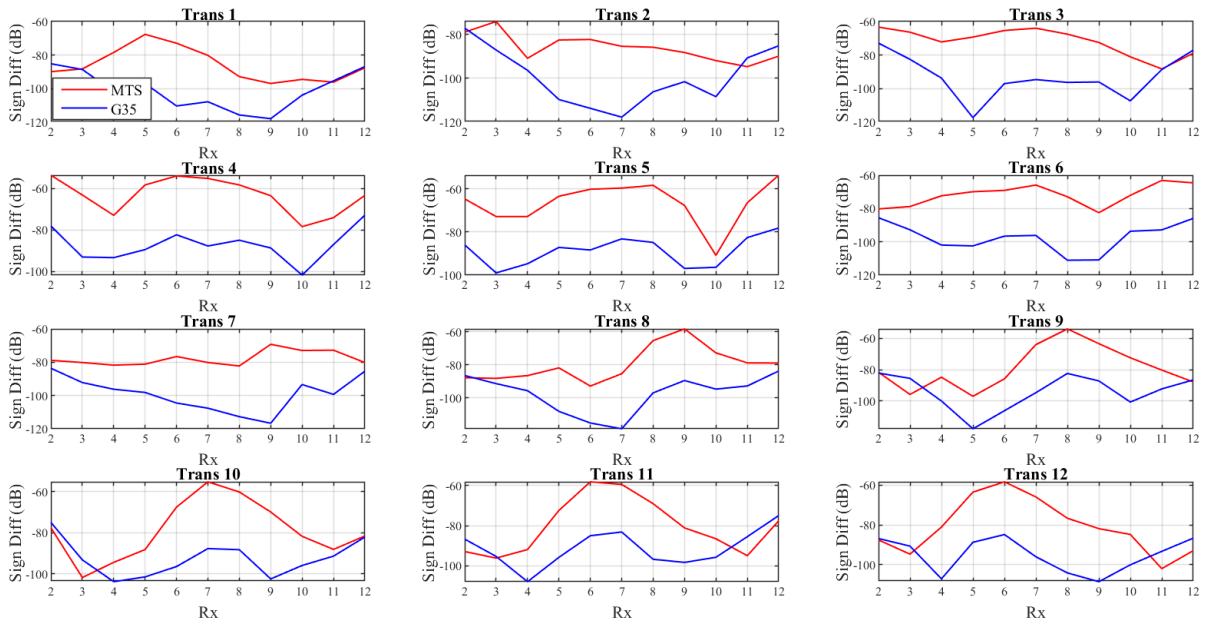

FIGURE 5.9: Differential signal plotted as function of the receivers' location at 1.5 GHz for the antenna array operating in contact with the MTS (red lines) and for the brick-shaped antenna array (blue lines). The numbering of the antennas is clockwise, as shown in Figure 5.8c. The signal difference "with target - no target" (dB) is overall enhanced (up to 35 dB) when the MTS structure is applied on the substrate of the antennas. For example, for the brick-shaped antenna system, when antenna 4 is transmitting, the signal backscattered by the target and received by antenna 10 falls below -100 dB. When the matching medium is removed and the MTS is applied on the antennas' substrate, the same signal is enhanced by about 20 dB.

Finally, to assess the possibility of achieving target's detection with the new developed brain scanners operating in air, the Huygens principle (HP)-based algorithm was applied to the simulated data of the two arrays. Figure 5.10 shows images reconstructed using data in the 0.6-0.8 GHz frequency range. As shown in Figure 5.10c, the blood-mimicking target is detected correctly in the presence of the MTS. This is due to the MTS, which improves the target's response relative to other signal artefacts.

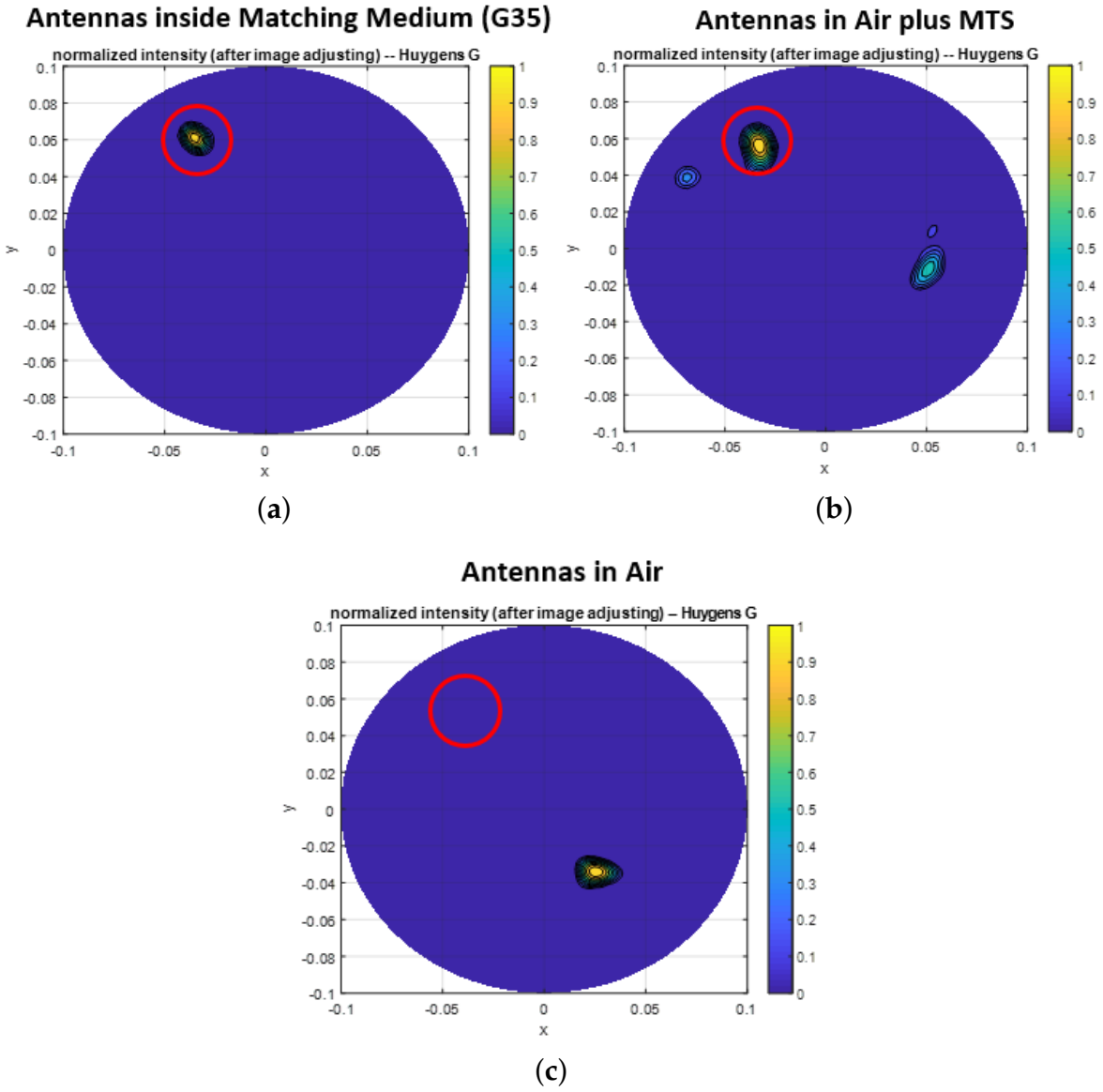

FIGURE 5.10: Images reconstructed through our HP-based algorithm after applying post-processing thresholding for (**a**) the 12 brick-shaped antenna-array, for (**b**) the 12-antenna array operating in air, in contact with the MTS sheets, and for (**c**) the 12-antenna array operating in air, without MTS sheets. The images are rotated by 90 degrees compared to Figure 5.8c.

5.2 Metasurface-Enhanced Antenna for Microwave Breast Imaging

In this section, the multi-static system for microwave breast cancer imaging reported in [118] is presented and a hardware advancement for this prototype is proposed. In particular, a MTS-enhanced antenna has been modelled to improve transmission through a breast phantom and enhance the signals scattered from a tumour-mimicking target inserted into the breast volume.

5.2.1 Microwave Imaging for Breast Cancer Detection

Breast cancer is the most common cancer in the UK population, with around 54,700 new cases diagnosed in 2017, and the most common cancer in women, globally [119]. This type of cancer occurs when cells in the breast tissue grow uncontrollably, forming a tumour, which can be seen through medical imaging or felt as a lump. In the last decades, significant research efforts in the diagnosis and treatment of breast cancer has helped in increasing the survival rates and declining the number of deaths associated with this disease. This outcome is largely due to factors such as earlier detection and personalized approach to treatment. In particular, as early diagnosis is associated with decreased breast cancer mortality, primary prevention through regular screening procedures is crucial [120].

Current techniques for early-stage breast cancer detection are X-ray mammography, ultrasound, magnetic resonance imaging (MRI), and positron emission tomography (PET). X-ray mammography, which is the most common screening procedure, uses low-energy X-rays to create images of the breast. Nowadays, regular mammograms are the best tests doctors have to perform early diagnosis of breast tumour, sometimes up to three years before it can be felt as a lump [121]. However, X-rays mammography has its limitations. First of all, it is painful (breast compression is needed during the test) and it exposes the patient to low radiations which can be harmful over time. Secondly, mammograms are not 100% accurate in detecting breast cancer and may cause psychological harm associated with false test results: about 1 out of 5 breast cancers is not found (false-negative result) and about 50% of the women getting regular mammograms over a 10-year period will be diagnosed with breast cancer at some point (false-positive result) [122]. Other harmful effects of mammography include overtreatment and unnecessary follow-up testing.

MWI is a promising alternative method to X-rays mammography because it is non-invasive and harmless to humans. Furthermore, this imaging technology is low-cost and can lead to quick diagnosis. MWI uses the contrast among various tissues to detect malignant tumours, which are measured to have higher dielectric permittivity as compared with healthy breast tissue [123]. The tissue dielectric contrast can be estimated using radar-based or tomographic reconstruction algorithms that are applied to the acquired data [124]. Various setups have been considered for microwave breast imaging. These can be distinguished in two main categories: robotic and multi-static systems. Robotic systems are generally easier to calibrate but presents an increased noise floor due to the mechanical movement of the antennas around the breast. Multi-static systems are very fast in terms of data acquisition time because they consist of large number of antennas which are positioned around the breast at fixed locations. These antennas are typically driven either by a n-port vector network analyser (VNA)

or by a n-port switching matrix connected to a two port VNA [118]. The hardware configuration of multi-static systems can be differentiated according to various factors, such as the type of acquired signals, the patient positioning, the acquisition surface and the use of coupling media [12].

5.2.2 Preliminary Design of a Multi-Static System for Microwave Breast Cancer Imaging

In this section, a preliminary design of the multi-static system for microwave breast cancer imaging developed by MITOS Medical Technologies [118] is presented. This system includes a cylindrical array embedded into a solid dielectric platform surrounding a breast phantom. The platform consists of two cylinders. The outer cylinder is made of acrylic polymers with alumina trihydrate composite and includes 24 Vivaldi antennas. The CST model of the Vivaldi antenna used to perform microwave measurements is shown in Figure 5.11. This antenna is printed on a 1.6 mm thick FR-4 substrate (ϵ = 4.3) and operates in the 1-6 GHz frequency range. The inner cylinder of the system is made of cast polyamide and it is curved as a breast shaped cup. This last cylinder is interchangeable, depending on the patient's breast size. The loss tangent of both materials are negligibly low in the 2-4 GHz frequency range and the averaged dielectric permittivity is 3, which is much lower as compared to skin's permittivity but relatively close to breast fat tissue. Thus, the platform not only has the function of supporting the breast on site, eliminating measurements' uncertainties due to the breast position, but it also improves the impedance-matching between the antennas and the breast [118]. The system is driven by a n-port VNA including PXI based configurable systems.

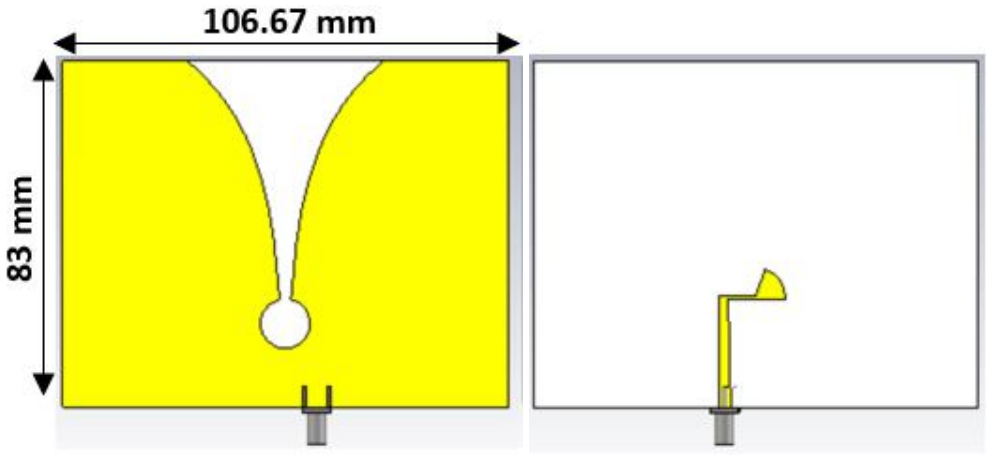

FIGURE 5.11: (**a**) Front view of the Vivaldi antennas developed by MITOS Medical Technologies and (**b**) back side of the antenna.

5.2.3 Metasurface-Enhanced Vivaldi Antenna

In this section, a new MTS-enhanced Vivaldi antenna for the system described in Section 5.3.2 is proposed. In particular, the frequency response of the Vivaldi antenna shown in Figure 5.11 has been improved according to the requirements, to achieve a deep resonance at 5 GHz, which is an optimal frequency for this system to reconstruct images. This was done by adding resonating structures on the antenna's substrate.

The double square split-ring resonator (DS-SRR) used for the new antenna's design is shown in Figure 5.12b. This includes two PEC square loops (thickness = 0.3 mm) with a 0.5 mm gap capacitance. The gap between the edge of the external loop and the edge of the internal loop is 0.45 mm. The distance between two DS-SRRs printed on the antenna's substrate is 0.3 mm. As in Chapter 4, a common resonator shape was used to improve the matching of the antenna at a specific frequency. This was done by manually optimizing the size, position and number of the DS-SRRs. First, iterative simulations were run to achieve a deep resonance at 5 GHz. In particular, the number of unit cells and their distribution was changed to vary the operating frequency of the antenna. Then, the dimensions of the metal wires of a single DS-SRR have been refined through CST's "Trust Region Framework" algorithm by setting a minimum resonance at 5 GHz as a goal.

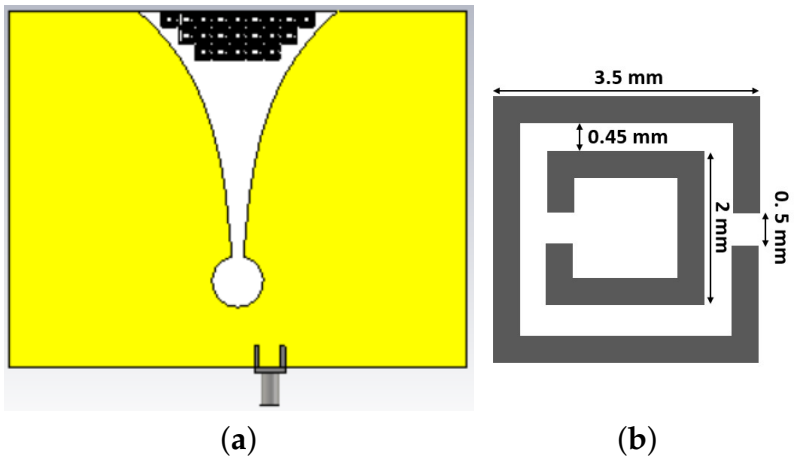

FIGURE 5.12: (**a**) MTS-enhanced Vivaldi antenna and (**b**) DS-SRR printed on its front side.

To examine the performance of the new antenna, reflection coefficient, gain and directivity were calculated over the 1-6 GHz frequency range by using CST. As shown in Figure 5.13, a deep resonance (-42 dB) at 5 GHz is obtained when the resonators are added to front side of the Vivaldi antenna. Gain and directivity are also slightly improved in the 3.5-6 GHz frequency range (Figure 5.14).

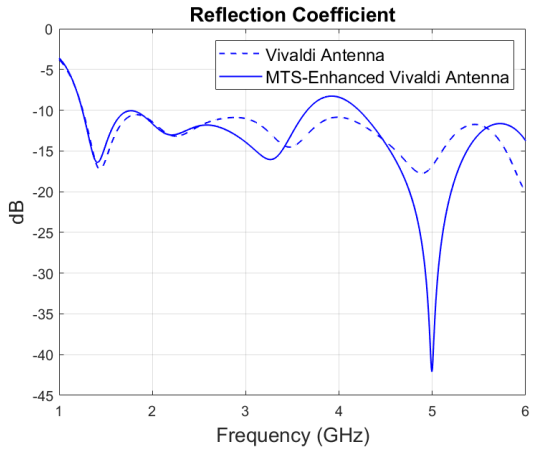

FIGURE 5.13: Reflection coefficient for the Vivaldi antenna developed by MITOS Medical Technologies (blue dashed lines) and its MTS-enhanced version, with DS-SRRs printed on the front side (blue solid lines).

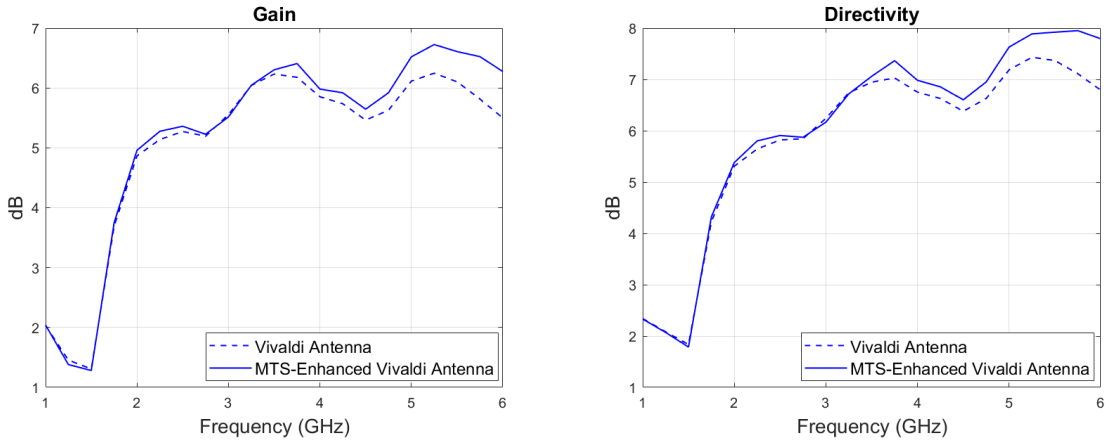

FIGURE 5.14: (**a**) Gain and (**b**) directivity plotted as function of frequency for the Vivaldi antenna developed by MITOS (blue dashed lines) and its MTS-enhanced version (blue solid lines).

5.2.4 8-Antenna System for Breast Cancer Imaging

To further investigate whether the MTS-enhanced antenna had the capability to improve breast cancer detection, MITOS's multi-static system for microwave breast cancer imaging was modelled in CST and 8 MTS-enhanced antennas were integrated in the setup. The propagation of EM waves was studied for a breast phantom model, which includes only average breast tissue ("no target" scenario) and in the presence of a tumour-like target inside the breast volume ("with target" scenario). For each system, the S-parameters were measured over the 1–6 GHz frequency range and the antennas' reflection coefficient was obtained. In addition, the signal difference "with target - no target" (in dB) was calculated at relevant frequencies and images of the

inclusions were reconstructed through KCL's radar-based algorithm.

Simulated Setup

Figure 5.15a shows the simulated setup and its dimensions. The system consists of a cylindrical 8-antenna array embedded into a solid dielectric platform consisting of two concentric cylinders. The outer cylinder is made of acrylic (ϵ = 2.53; tanδ = 0.0119) and contains 8 radial slots where the antennas are positioned. The inner cylinder (ϵ = 3; tanδ = 0.0119) is curved as a breast shaped cup and contains the breast phantom. This second cylinder has the mechanical function of sustaining the breast, eliminating

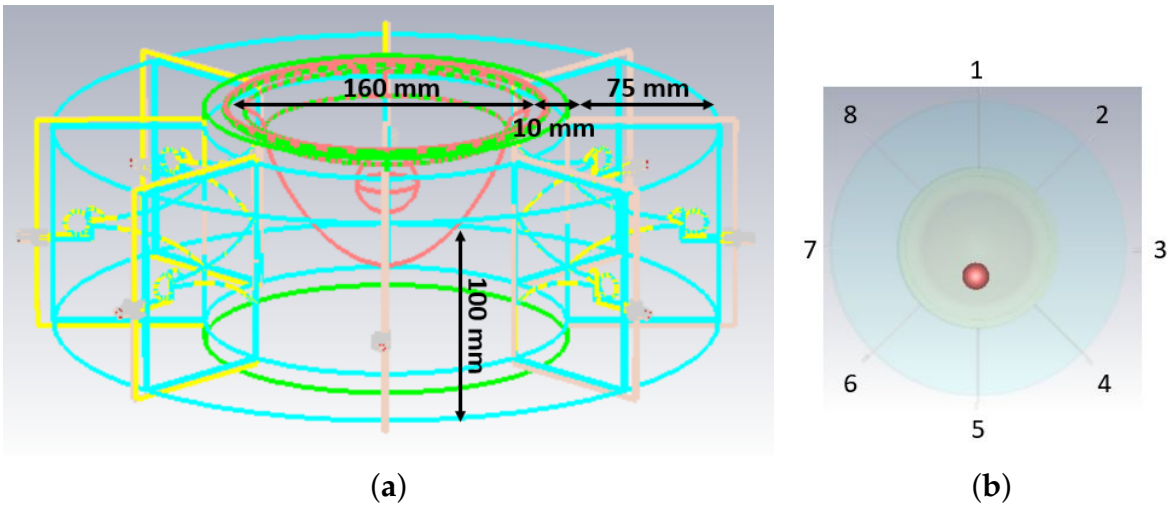

FIGURE 5.15: (**a**) Wire frame of the simulated setup with its dimensions and (**b**) tumour-mimicking target inserted in the breast phantom and placed in front of antenna 5. The breast phantom is characterized by dielectric properties fixed at 3 GHz [106]. The antennas are numbered clockwise starting from the antenna opposite to the target.

measurement's uncertainties due to movements and breast position. Furthermore, it improves the impedance-matching between the antennas and the breast. The breast phantom is characterized by dielectric properties fixed at 3 GHz (ϵ = 30.81; tanδ = 0.19). These properties were averaged between glandular tissue (ϵ = 56.40) and fat (ϵ = 5.22) [106]. The tumour-mimicking target (ϵ = 59; σ = 1.2 S/m) consists of a 30 mm diameter sphere which was placed in front of antenna 5, as shown in Figure 5.15b.

5.2.5 Results

As shown in Figure 5.16, the simulation results indicate that the reflection coefficient of the Vivaldi antennas is significantly reduced in the presence of the resonators. Furthermore, Figure 5.17 shows that there is a slight improvement in transmission in the

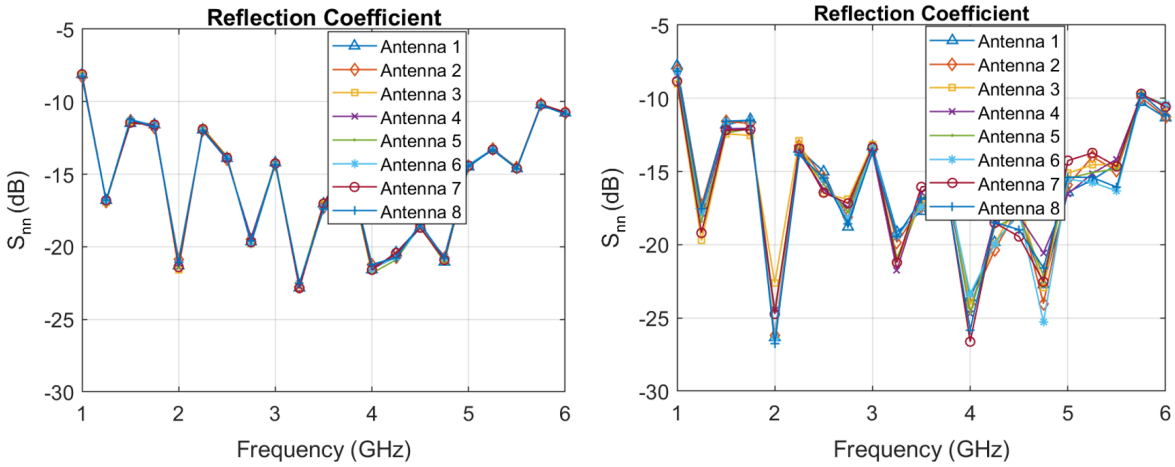

FIGURE 5.16: Reflection coefficient for the "with target" configuration for (**a**) the 8-Vivaldi antenna array and (**b**) the 8-MTS-enhanced Vivaldi antenna array. The reflection coefficient is significantly reduced when the MTS resonating structures are added on top of the Vivaldi antennas. For all the antennas in the array, the reflection parameter is reduced by around 5 dB at 2 GHz, 4 GHz and 5 GHz.

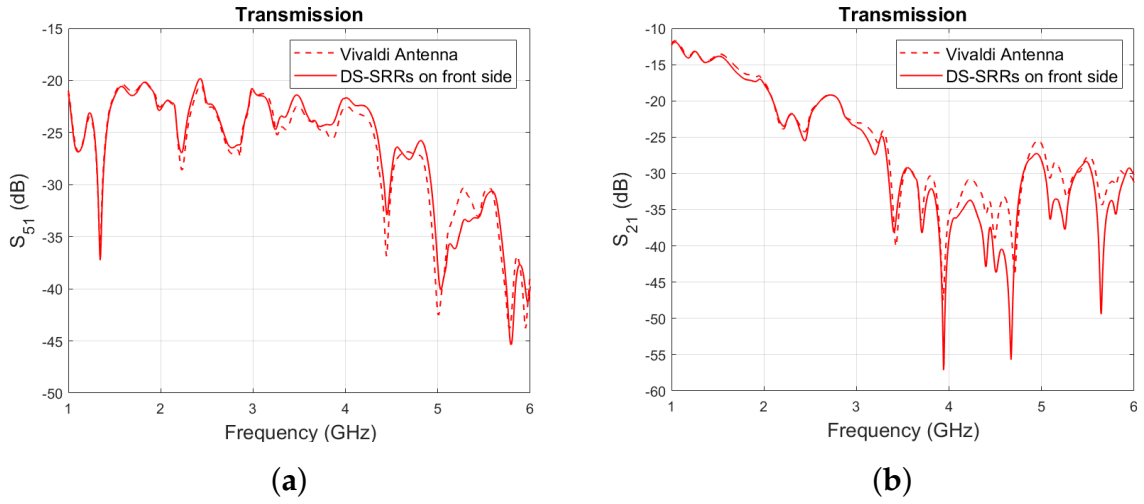

FIGURE 5.17: (**a**) S_{51} parameter for the "no target" configuration with (solid lines) and without DS-SRRs (dashed lines). A slight improvement in transmission across the breast diameter is observed. (**b**) S_{21} parameter for the "no target" configuration with (solid lines) and without DS-SRRs (dashed lines). Transmission between antenna 1 and antenna 2 is reduced by 5 dB over the 4-5 GHz frequency range. This indicates that the coupling effects between two MTS-enhanced neighbouring antennas decrease in the presence of the resonators.

direction of the breast diameter, which is also the direction containing the tumour-mimicking target. Transmission between antenna 1 and antenna 2 is contrarily reduced, indicating that the coupling effects between two MTS-enhanced neighbouring

antennas decrease in the presence of the resonators. The signal difference "with target - no target" (in dB) is shown in Figure 5.18. This difference is plotted as a function of

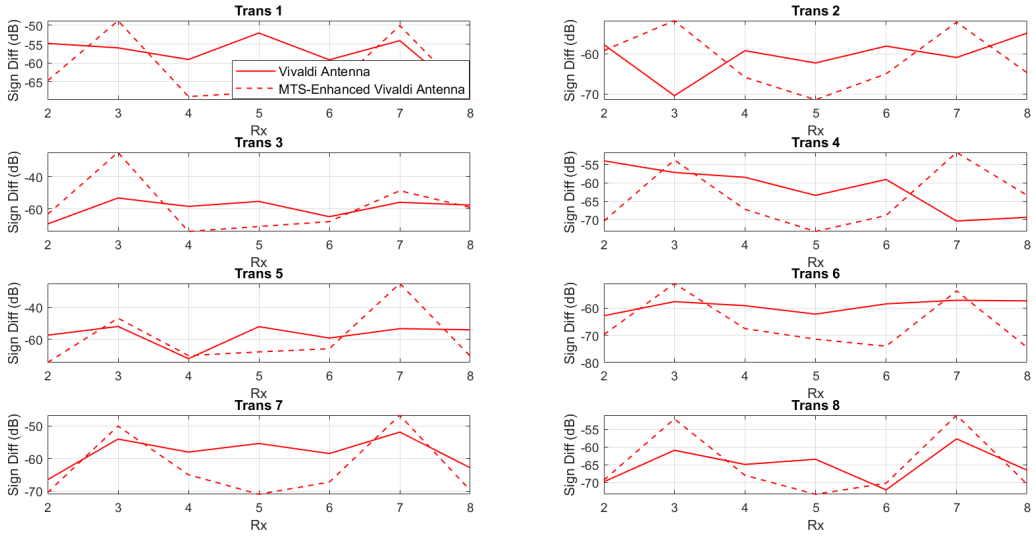

(**a**)

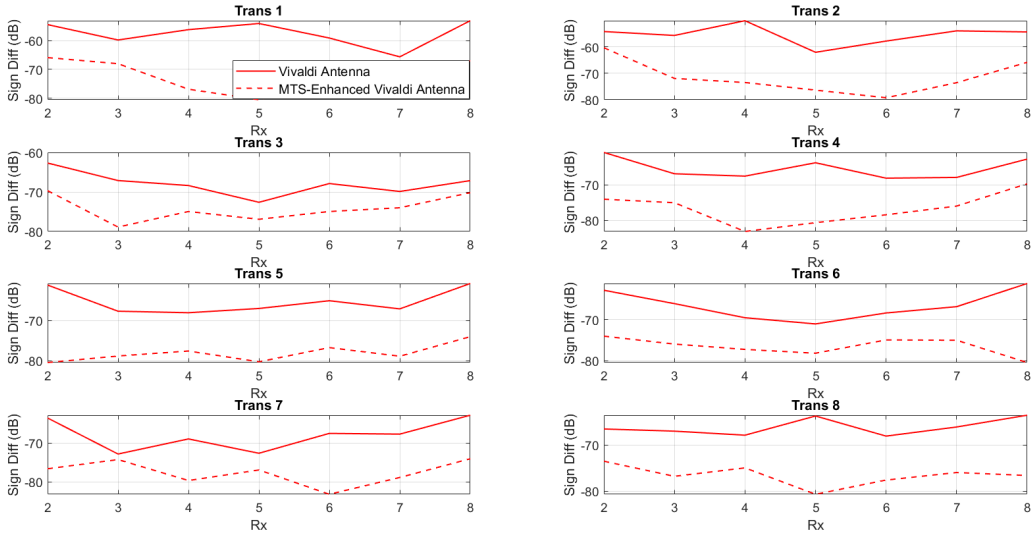

(**b**)

FIGURE 5.18: Signal difference "with target - no target" (dB) as a function of the receivers' location, plotted at (**a**) 4.5 GHz and (**b**) 5 GHz for the Vivaldi antenna-array (dashed lines) and the MTS-enhanced Vivaldi antenna-array (solid lines). The numbering of the antennas is clockwise, as shown in Figure 5.15. For each transmitter, the "weak" signal scattered from the target is enhanced for most of the receivers' locations. For example, when antenna 5 (i.e., Trans 5, which is in front of the tumour-mimicking target) is transmitting, the differential signal at 5 GHz is improved by around 15 dB for all the receiving positions.

the receivers' location, at 4.5 GHz and 5 GHz. The signal backscattered by the tumour-mimicking target is noticeably enhanced (up to 30 dB) due to the presence of resonators.

Images of the tumour-mimicking target reconstructed through the HP-based algorithm are shown in Figure 5.19. These results clearly indicate that the proposed MTS-enhanced antenna enables a correct detection and localization of the target. As noted in Chapter 3, the MTS-enhanced antenna might improve the detection and localization of the target by increasing the target's response relative to other signal artefacts (see pre-normalised images in Figure 5.19).

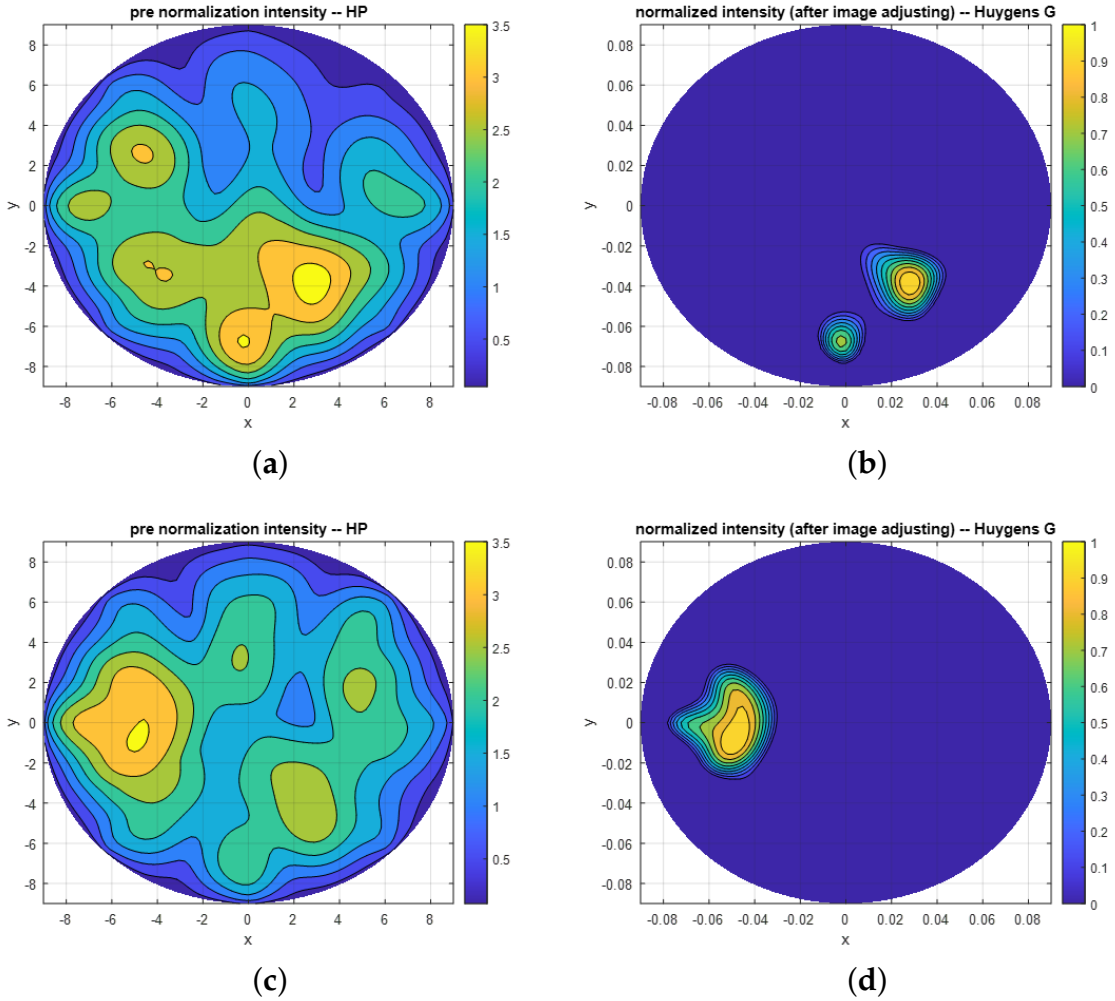

FIGURE 5.19: (**a**) Pre-normalised and (**b**) normalised images of the tumour-mimicking target reconstructed via the HP algorithm for the Vivaldi antenna-array. (**c**) Pre-normalised and (**d**) normalised images of the tumour-mimicking target for the MTS-enhanced antenna-array.

5.3 Conclusions

In conclusion, this chapter highlighted that it is feasible to apply MTS technology to improve the performance of medical devices for monitoring and screening applications. More specifically, the purpose of the study presented in Section 5.1 was to investigate the feasibility of developing a portable, compact and ergonomic microwave brain imaging scanner for CVA imaging. To this end, a new array based on 12 monopoles operating in air, in contact with an impedance matching MTS, was proposed. Then, the signal backscattered by a blood-mimicking target was calculated and images of the blood inclusion were reconstructed through the HP-based algorithm. The results indicate that it is possible to detect a blood-mimicking target placed inside the brain volume of a simple head model without using a thick and bulky matching medium. This is probably due to the enhanced target's response obtained in the presence of the MTS superstrate loading.

Section 5.2 proposes a MTS-enhanced Vivaldi antenna for breast cancer screening. This antenna presents a reduced reflection coefficient and increased gain and directivity. Furthermore, the results shown in Section 5.2.5 clearly indicate that transmission through the breast phantom increases due to the presence of the resonators, whereas the coupling effects between two neighbouring MTS-enhanced antennas are reduced. Moreover, the new antenna enhances the signals scattered from a tumour-mimicking target, which is relevant to this near-field imaging application, as it may help in enabling tumour's detection. Thus, we can attribute the target's identification in Figure 5.20d to the DS-SRRs added on the Vivaldi antenna's substrate.

Chapter 6

Metasurfaces for Therapeutical Applications

As for Chapter 5, all the numerical studies presented in this chapter were performed during two of the four secondments planned by the EMERALD consortium. In the following sections, new metasurface (MTS) designs were proposed to monitor therapeutical applications, including ultra-wideband (UWB) hyperthermia and microwave thermal ablation (MTA). Both the MTS were designed to enhance the signal backscattered by a heated area during these cancer treatments. More specifically, the first section presents an impedance-matching MTS designed to operate in front of the dipole antenna developed by TUIL (Technische Universität Ilmenau, Germany). The second section is focused on MTA and presents a new split-ring resonator (SRR) tailored to enhance the performance of the antipodal Vivaldi antenna developed by CNR-IREA and Sapienza University of Rome (Italy).

6.1 Impedance-Matching Metasurface for Hyperthermia Monitoring

In this section, a potential hardware advancement for a UWB hyperthermia monitoring prototype is proposed. Hyperthermia is a type of treatment in which the body is exposed to high temperatures (between 41°C and 48°C) in order to damage cancer cells [125]. To ensure there is no harm to the healthy tissues, accurate temperature monitoring is needed. A way to perform accurate monitoring is through imaging the distribution of temperature inside the treated tissue. The results shown in this section demonstrate the feasibility of improving temperature change detection by incorporating an impedance-matching MTS in the hyperthermia monitoring system developed by TUIL [126].

6.1.1 Hyperthermia for Head and Neck Cancer

Cancers known as head and neck cancers usually begin in the squamous cells on the mucosal surfaces of the head and neck, such as those inside the mouth, throat and voice box. Squamous cell carcinoma of the head and neck usually spreads locally and/or to the lymph nodes in the neck [127].

Depending on several factors, such as the type and stage of cancer and general health condition, many cancer treatments are available. Conventional cancer treatments are surgery, chemotherapy, radiation therapy, immunotherapy and targeted drug therapy [128]. Lately, hyperthermia (or thermotherapy) has been reconsidered as a successful treatment method, able to lead to positive outcomes when used together with conventional cancer treatments [129]. Due to its effectiveness, this treatment has attracted the interest of many research groups, and several devices have been developed to treat head and neck cancer [130–133].

During hyperthermia, temperature monitoring is needed to control the temperature inside the tumour and prevent damaging healthy cells, providing patient's safety. The most widely used method of continuous temperature measurement in thermotherapy is the implementation of optical catheters in the treated area [134]. This method is low-cost and fast, but it provides information about the temperature from only a few points. Furthermore, these invasive probes generally cause pain and patient's discomfort. As a hyperthermia session lasts from 45 to 60 minutes and is usually repeated weekly, for months [135], a non-invasive temperature monitoring is preferable. This can be performed using techniques such as magnetic resonance imaging (MRI), ultrasound, microwave radiometry and microwave imaging (MWI). [136].

As the tissue's dielectric properties change during thermal treatment due the water content, changes in the scattering behaviour of the heated area can be detected through MWI [137]. UWB radar technique is particularly preferred for this application because it employs a wide frequency band for measuring the signals backscattered by the area under treatment. Although it would be sufficient to estimate the permittivity of the heated cancerous tissue within an optimal frequency range, it may be indeed important to use frequencies outside this range to estimate the temperature in undesired hot spots that can appear in surrounding organs during the heating process [126]. Another advantage is that, while microwave tomography (MWT) estimates the dielectric properties' changes through solving an inverse electromagnetic (EM) scattering problem, UWB radar-based imaging algorithms are less computationally complex to implement, as they detect and localize strong scatterers by means of coherent summation of the reflected signal energy [126].

6.1.2 M-sequence UWB Radar Technology

In this section, the M-sequence radar technology developed by TUIL is presented. This technology uses pseudo-noise stimulation signals (M-sequences) generated by high-speed digital shift registers. As the energy of the pseudo-noise stimulus is distributed equally over time, relatively low magnitude signals are emitted. Thus, the reduced voltage exposure of the object under investigation makes this technology suitable for medical applications [136]. The M-sequence multiple-input multiple-output (MIMO) radar device shown in Figure 6.1 has a bandwidth of 6.5 GHz and includes 8 transmitters and 16 receivers, which results in 128 channels. A total of 24 passive bow-tie dipole antennas are placed in contact with a neck phantom, arranged in 8 groups of 3 antennas, with each group displaced by 45° around the phantom and at different heights. The bow-tie antennas are implemented on FR-4 substrates (0.8 mm thick, with dimensions of 10 mm by 5.6 mm) and differentially fed by passive baluns. A rotational scanner is used to rotate the antenna array around the phantom and increase the amount of measurement channels [126].

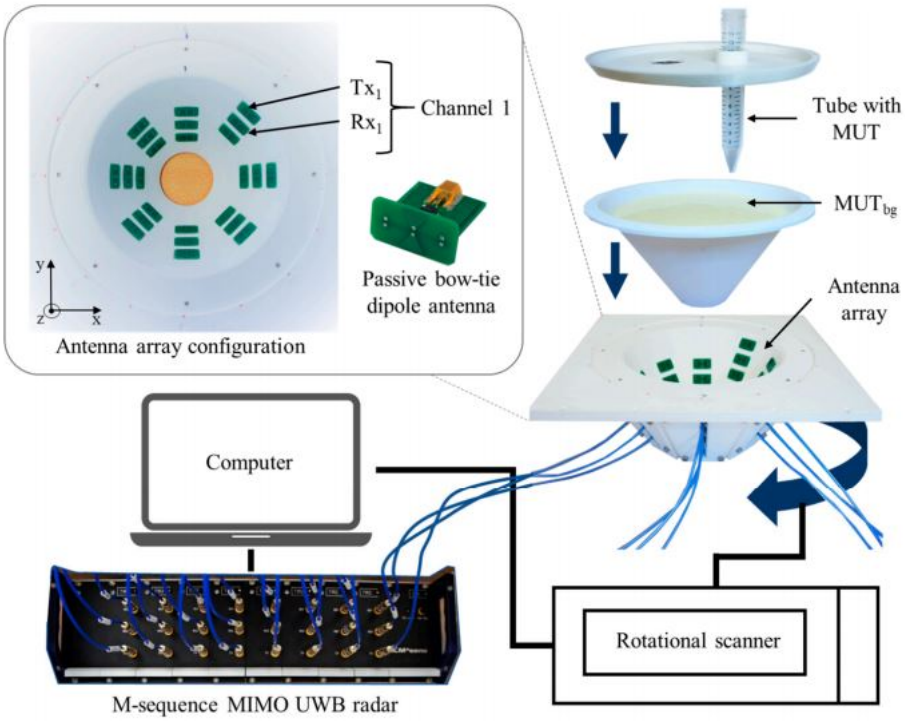

FIGURE 6.1: Measurement setup for preliminary investigations towards tissue temperature estimation developed by TUIL. *Credit: TUIL (Technische Universität Ilmenau, Ilmenau, Germany)* [126].

The measurement setup includes a 3D printed polylactic acid cup and a plastic lab tube filled with a tumour-mimicking material (a mixture of distilled water and pure acetone), which is the material under test (MUT). The cup has a shape of a truncated

cone with an upper diameter of 15 cm, lower diameter of 5 cm and height of 8.5 cm and is filled with a background material (an emulsion of fat and water), which has the dielectric properties of average neck tissue. The temperature changes in the heated tumour are mimicked by directly changing the permittivity of the tumour-mimicking material. In particular, a mixture of 30 vol% acetone and 70 vol% distilled water mimics the tumour's dielectric properties before the heating process, whereas the temperature's rising is resembled by lower acetone concentrations [126].

6.1.3 Metasurface Design

In this section, we investigate the feasibility of improving temperature change detection through MTS technology. To this end, an innovative Jerusalem cross-shaped MTS design was modelled for operating in contact with a neck phantom. To validate the impedance-matching concept, several simulation studies were performed and the MTS geometry was optimized to maximize transmission across the phantom. Then, a full MTS structure was integrated into a simplified version of the measurement system shown in Figure 6.1 and the MTS's interaction with EM waves was studied in CST Microwave Studio®.

Metasurface Unit Cell

The Jerusalem cross-based MTS film shown in Figure 6.2a was optimized for operating as an impedance-matching layer to reduce reflection and enhance transmission of microwave energy into a body region such as the neck. This MTS unit cell is based on a square unit cell, which comprises a Jerusalem cross-shaped metal lattice (PEC) printed on a 0.1 mm Rogers 3010 TM high-dielectric substrate (ϵ = 11.2; tanδ = 0.0022). The unit cell was first incorporated in the simplified planar model shown in Figure 6.2, including Lazebnik's phantom with 40% oil content (ϵ = 25 and σ = 0.9 S/m at a fixed frequency of 2 GHz) [103]. The CST's optimizer tool "Trust Region Framework" algorithm was used to tune the MTS performance, setting minimum reflection in the 0.5–3.5 GHz frequency range as a goal. The interaction of this setup with a normally incident plane wave of linear polarization was modelled in the 0.5–3.5 GHz frequency range and the S-parameters were calculated, with and without MTS, considering "Port 1" before the MTS and "Port 2" after the phantom layer. The S-Parameters plotted in Figure 6.2b show an improvement in transmission due to the MTS (about 2 dB at central frequency 2 GHz). Moreover, reflection is significantly reduced over all the frequency range in the presence of the MTS.

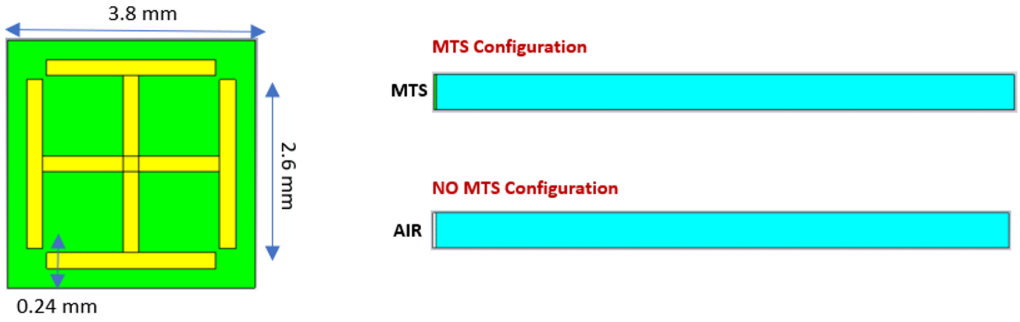

(a)

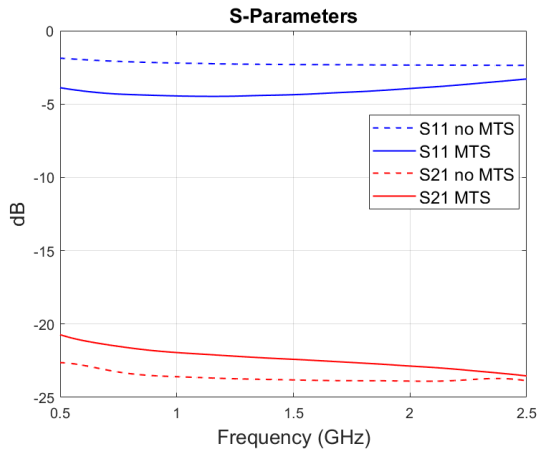

(b)

FIGURE 6.2: (**a**) MTS unit cell and planar setup including Lazebnik's phantom. (**b**) S-Parameters calculated for the "MTS" configuration (solid lines) and the "no MTS" configuration (dashed lines). In the "no MTS" configuration, the MTS is replaced with air.

Full Metasurface Structure and 8-Port Setup

Based on the unit cell results, a MTS periodic structure was also studied. This structure was included in an 8-port system comprising an octagonal plastic mould filled with a 40% oil Lazebnik's phantom. Eight transceivers were arranged in an array surrounding the phantom's block, as shown in Figure 6.3b. To investigate the feasibility of improving hyperthermia monitoring through our MTS geometry, a 5×3 unit cell MTS film was placed adjacent to the substrate of each dipole and in contact with the phantom block.

The setup was modelled in the 0.5-4 GHz frequency range and the S-Parameters were calculated, with and without MTS. The plots in Figure 6.4 show that the reflection coefficient of the antenna is significantly reduced and the transmission parameters are enhanced due to the presence of the MTS. In particular, the reflection coefficient is

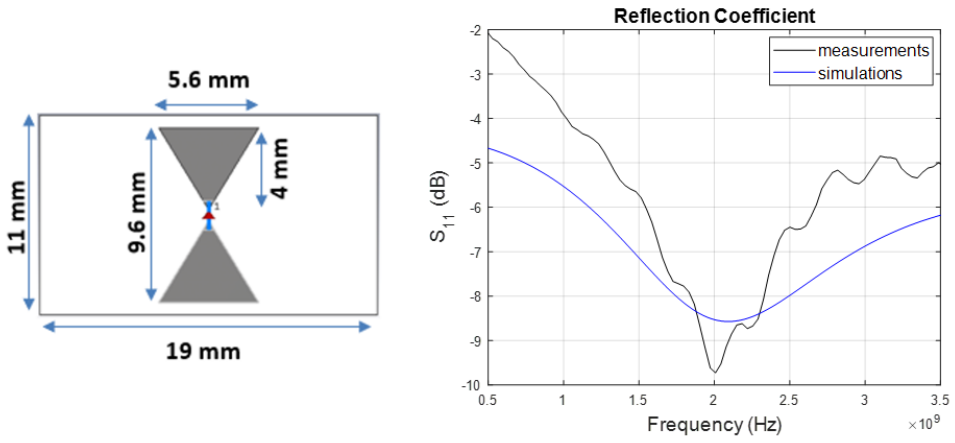

(**a**)

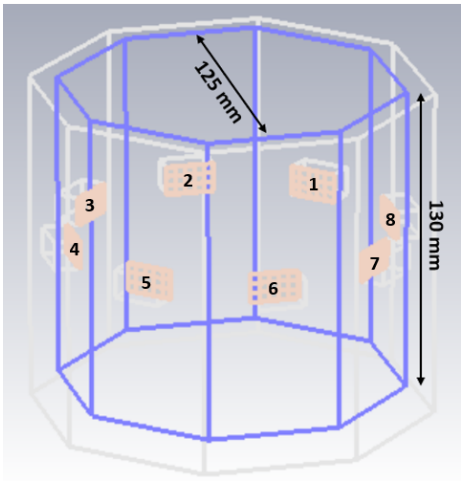

(**b**)

FIGURE 6.3: (**a**) Simulated passive dipole antenna with its dimensions (**b**) Wire frame of the 8-Port setup, comprising an octagonal plastic mould filled with Lazebnik's phantom and an 8-antenna array.

about -14 dB at 3.25 GHz and the transmission parameters are enhanced up to 8 dB due to the presence of the MTS.

6.1.4 16-Port Setup

To investigate whether the proposed MTS could improve the detection of the "weak" signal backscatter from a tumour-mimicking target and the signal differences due to changes in permittivity in the tumour area, similarly to the 8-port system, a 16-port setup was modelled. As shown in Figure 6.5, 16 transceivers were arranged in two rows of 8 transmitters and positioned on Lazebnik's phantom. The propagation of the

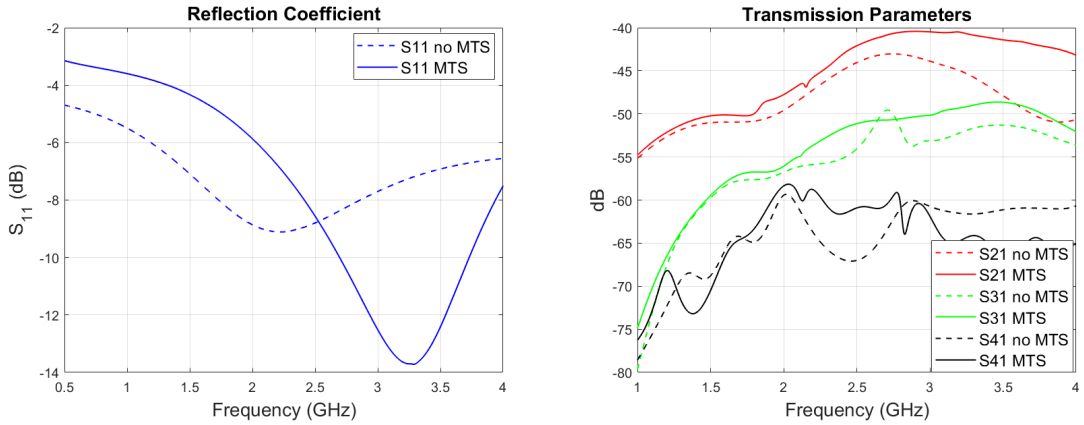

(**a**) (**b**)

FIGURE 6.4: (**a**) S_{11} parameter for the setup shown in Figure 6.3b calculated with (solid lines) and without MTS (dashed lines). The antenna's resonance is significantly reduced (-14 dB at 3.25 GHz) and shifted towards higher frequencies. (**b**) Transmission parameters for the setup shown in Figure 6.3b calculated with (solid lines) and without MTS (dashed lines). The S_{21} and S_{31} parameters are overall enhanced over the 1-4 GHz frequency range, with improvements up to 8 dB due to the presence of the MTS. The S_{41} parameter calculated for the"MTS" case is noticeably improved in the 1.7-2.7 GHz frequency range.

EM waves for the 16-antenna array was studied for the three configurations listed in Table 6.1, with and without MTS.

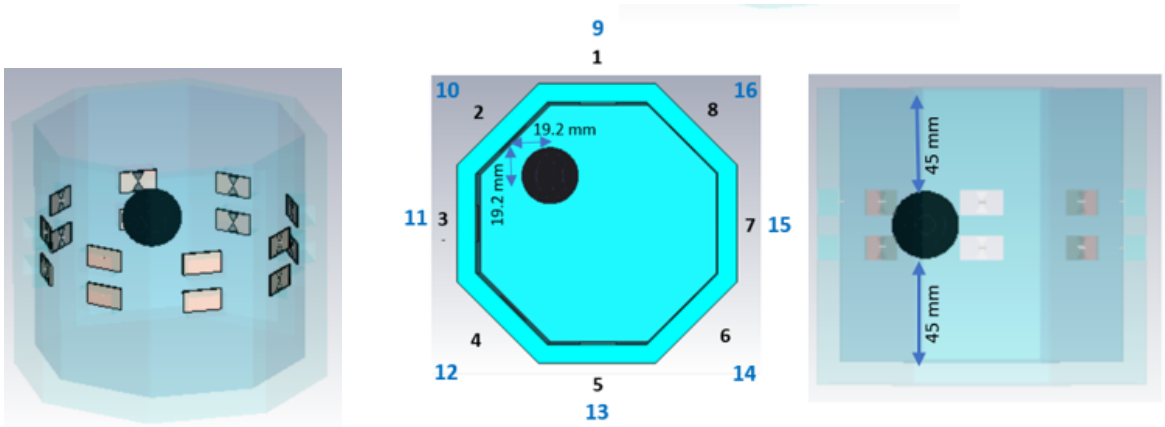

(**a**) (**b**)

FIGURE 6.5: (**a**) 16-Port setup, comprising an octagonal plastic mould filled with Lazebnik's phantom and a 16-antenna array. (**b**) Top and lateral view of the system.

The first configuration consists of a phantom including a "not heated" tumour-mimicking target, whereas the second configuration comprises a phantom including a "heated" tumour-mimicking target. Both the tumour-mimicking targets have a diameter of 30 mm and are positioned in the xz plane, at phantom's medium height, in

front of antenna 2. The third configuration comprises a neck phantom only, without any types of inclusion. The S-Parameters were measured in the 0.5-3.5 GHz frequency range and two differential signals were calculated at relevant frequencies (with and without MTS): the "not heated tumour-mimicking target-no target" (in dB) differential signal, which correspond to the signal backscattered by the "not heated" tumour-mimicking target, and the "heated tumour-mimicking target - not heated tumour-mimicking target" (in dB) differential signal, which is due to the temperature's variations in the tumour area itself.

TABLE 6.1: 16-Port system's configurations

Configuration	**Inclusion**	ϵ	σ
1	"not heated" tumour-mimicking target	59	1.2 S/m
2	"heated" tumour-mimicking target	57	1.4 S/m
3	no target	25	0.9 S/m

6.1.5 Results

The differential signals computed for the 16-port setup described in Section 5.2.4 are shown in the graphs below. These signals are plotted as function of the receivers' position at equally spaced frequencies in the interval 2-3.5 GHz. The receivers are numbered anticlockwise, starting from the top row of antennas, as shown in the top view of Figure 6.5b. The "not heated tumour-mimicking target - no target" (in dB) plotted in Figure 6.6, with and without MTS, indicates that a significant enhancement of the "weak" signal scattered from a "not heated" tumour-mimicking target is achieved in the presence of the MTS. As shown in Figure 6.6 and Figure 6.7, when the MTS is placed on the dipoles' substrate, it leads to an overall improvement (up to 30 dB) of the signal backscattered by the tumour inclusion.

Moreover, to validate the sensitivity of the MTS-system to variations in the tumour's permittivity and conductivity, we computed the "heated tumour-mimicking target - not heated tumour-mimicking target" (in dB) signal difference. The plots shown in Figure 6.8 and Figure 6.9 demonstrate that the "weak" signal backscattered by a variation in the tumour's properties due to a change in temperature is enhanced when the MTS is integrated in the setup.

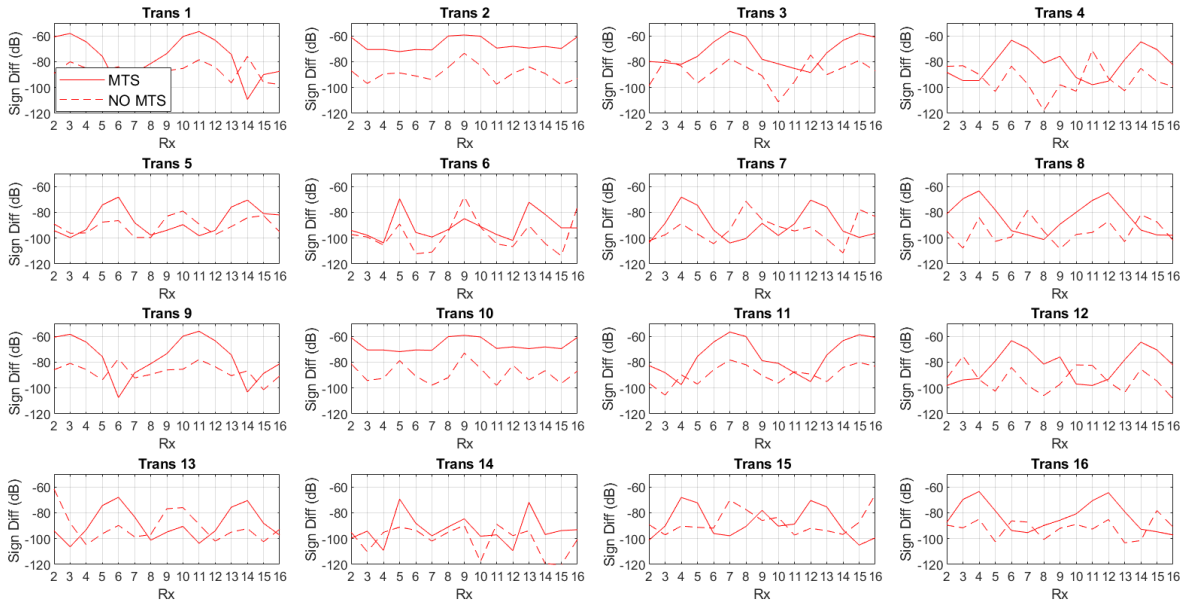

(**a**)

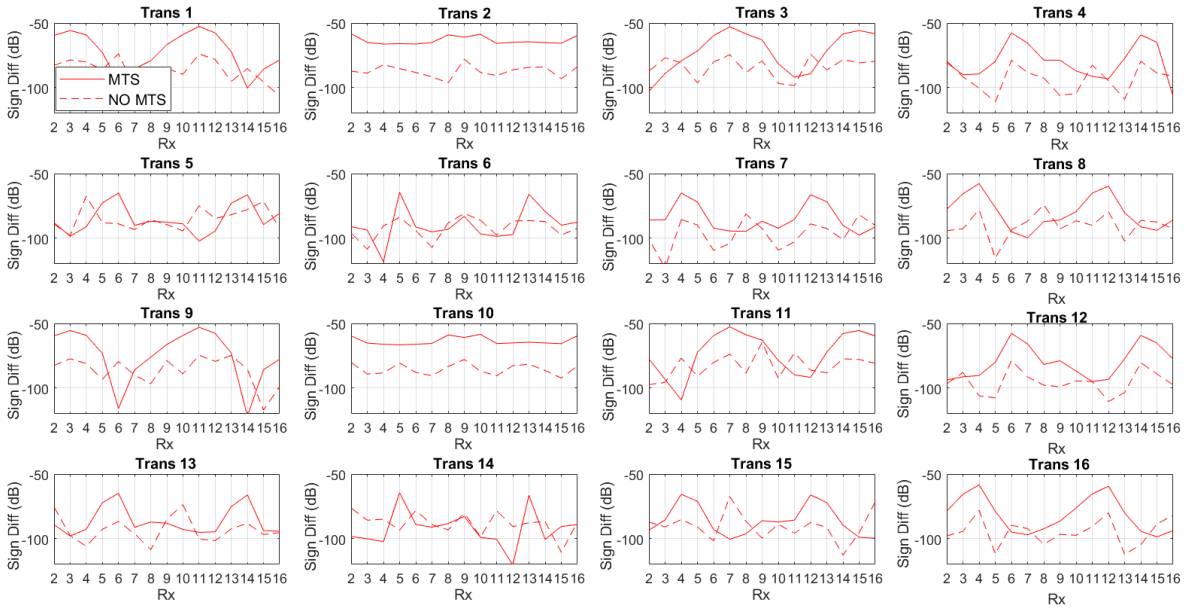

(**b**)

FIGURE 6.6: "not heated tumour-mimicking target - no target" signal difference (dB) calculated at (**a**) 2 GHz and (**b**) 2.5 GHz with (solid lines) and without MTS (dashed lines). This signal difference is plotted for each transmitter, as function of the receivers' location. An overall improvement of the signal backscattered by the target (up to 20 dB) is achieved in the presence of the MTS. For transmitter 2 and transmitter 10, which are the transmitters radiating in front of the target, the differential signal is enhanced for all the receivers' locations.

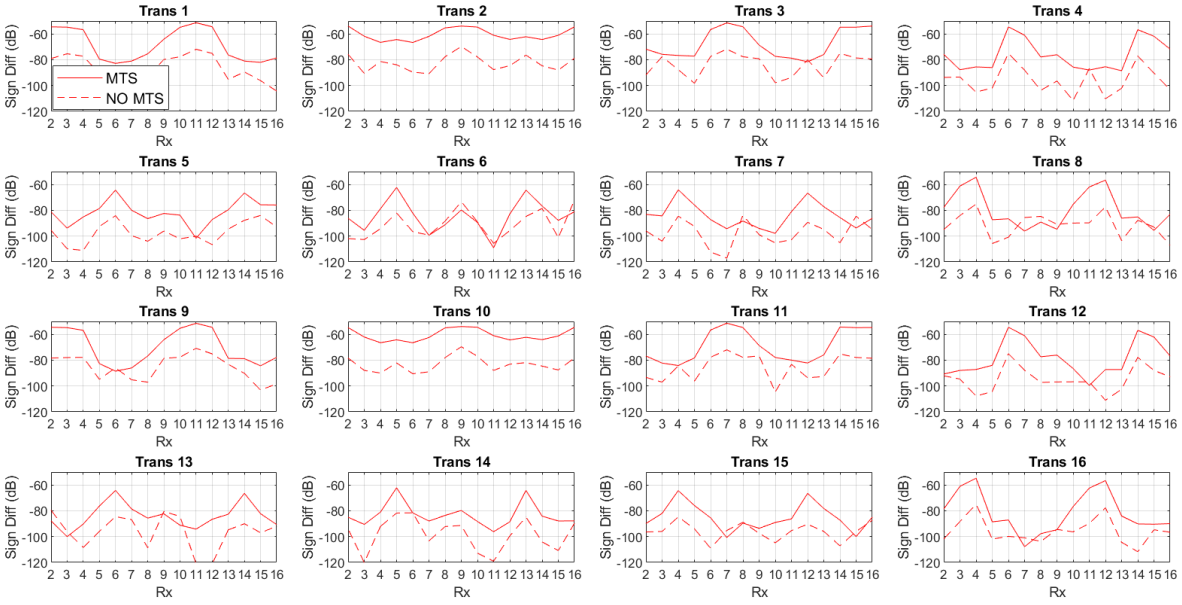

(**a**)

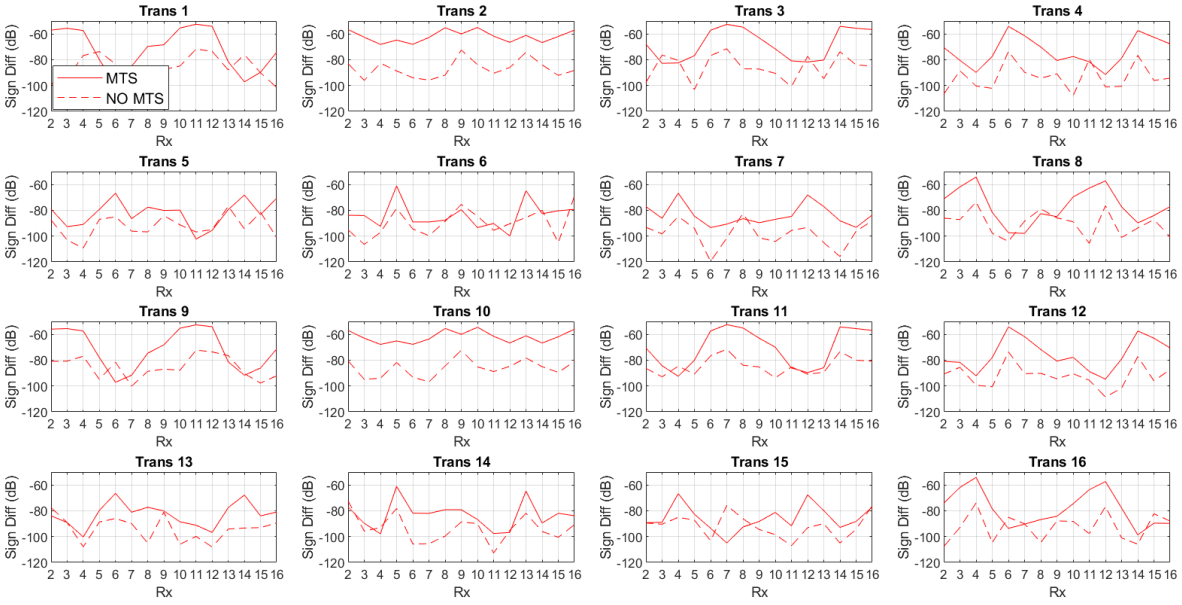

(**b**)

FIGURE 6.7: "not heated tumour-mimicking target - no target" signal difference (dB) calculated at (**a**) 3 GHz and (**b**) 3.5 GHz with (solid lines) and without MTS (dashed lines). This signal difference is plotted for each transmitter, as function of the receivers' location. An overall improvement of the signal backscattered by the target (up to 30 dB) is achieved in the presence of the MTS. For transmitter 2 and transmitter 10, which are the transmitters radiating in front of the target, the differential signal is enhanced for all the receivers' locations.

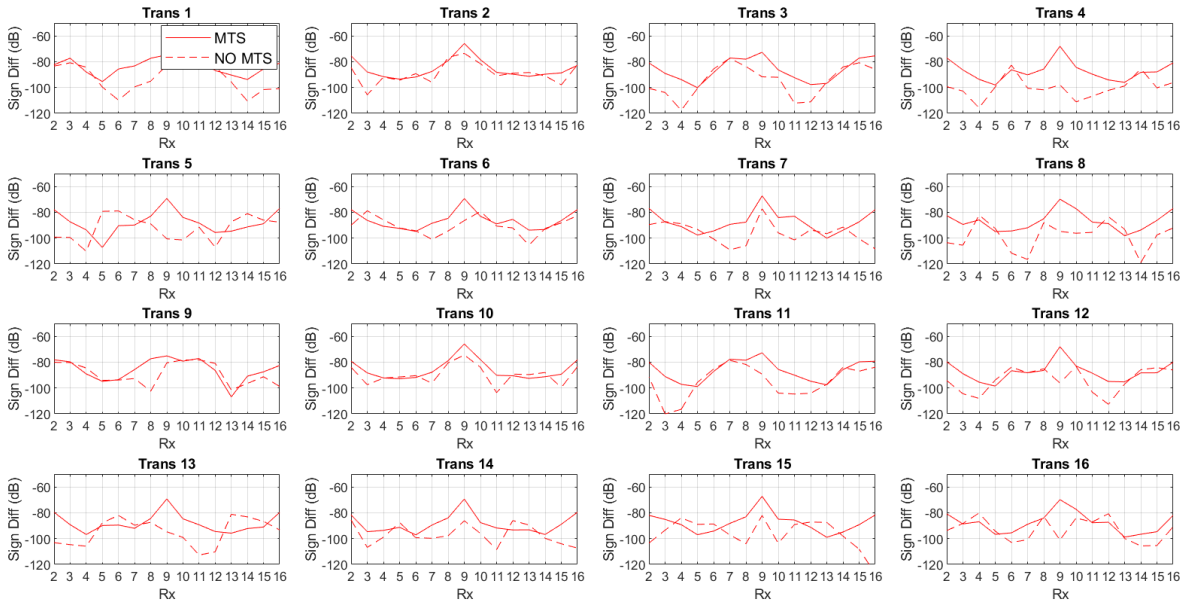

(**a**)

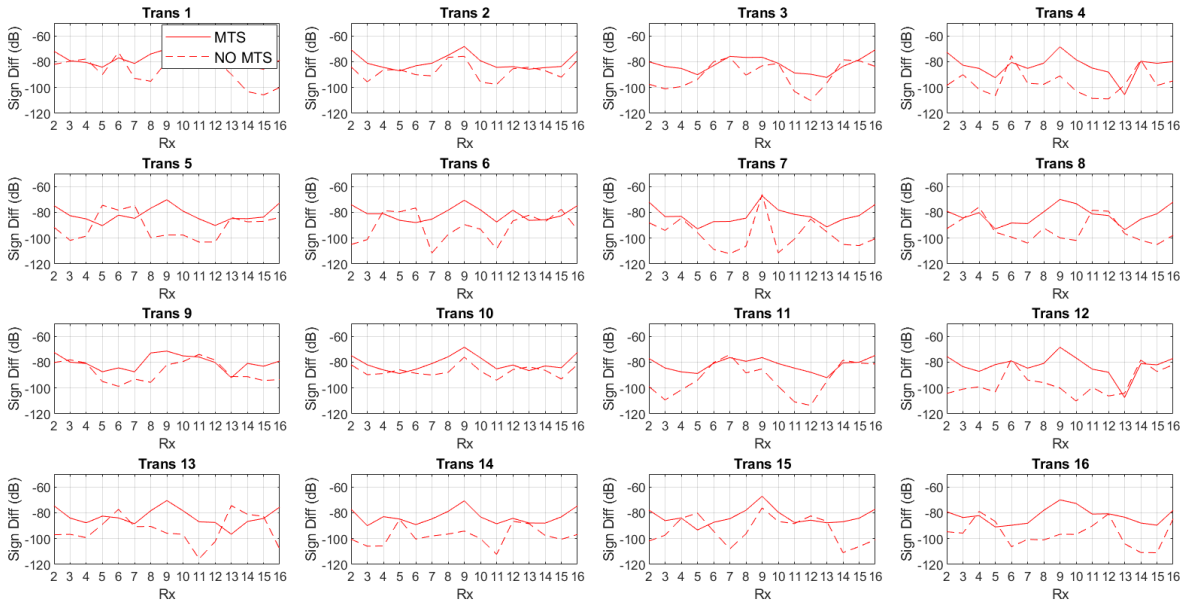

(**b**)

FIGURE 6.8: "heated tumour-mimicking target - not heated tumour-mimicking target " signal difference (dB) calculated at (**a**) 2 GHz and (**b**) 2.5 GHz with (solid lines) and without MTS (dashed lines). An overall improvement of the signal backscattered by variations in the tumour's dielectric properties is achieved in the presence of the MTS. This improvement (up to 30 dB) can be observed for several receivers' locations and might contribute to differentiate between "heated" and "not heated" cancerous tissue.

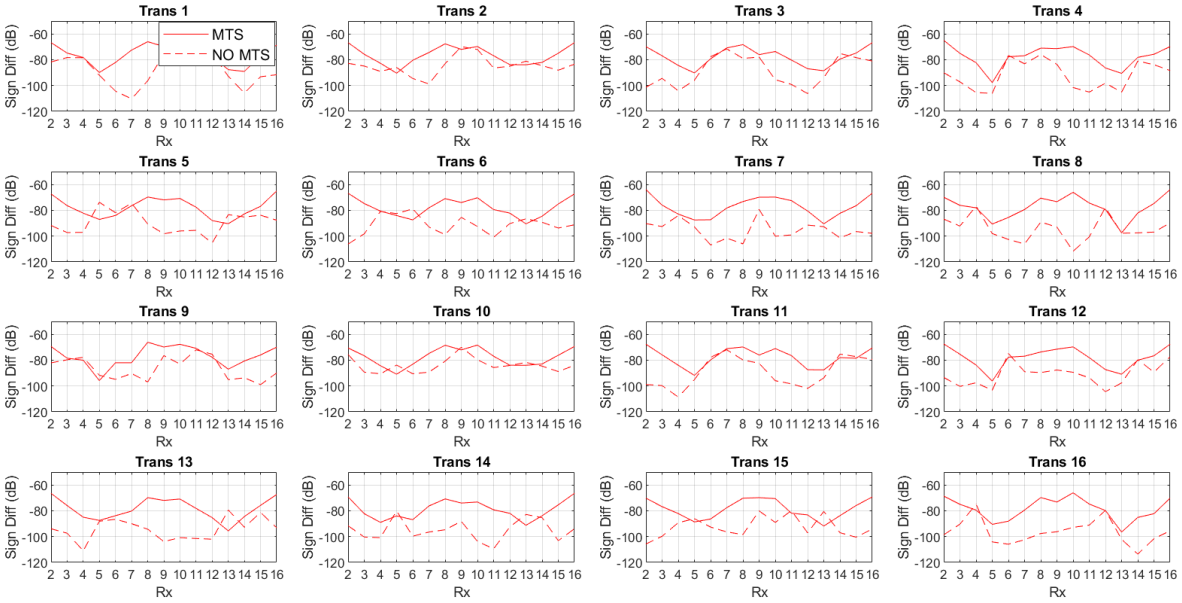

(**a**)

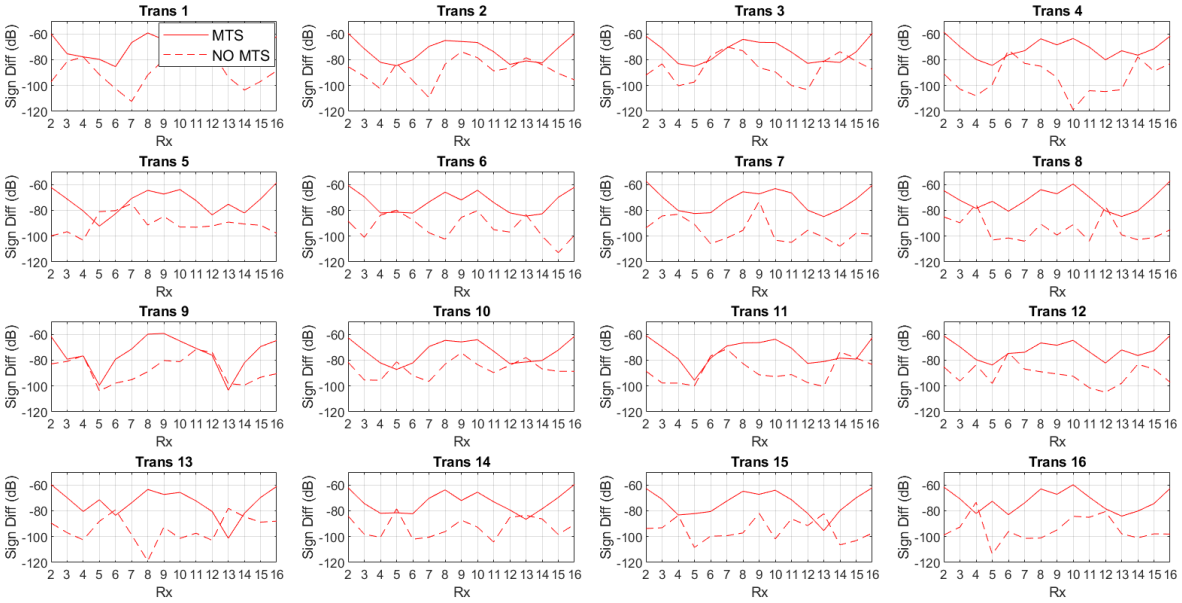

(**b**)

FIGURE 6.9: "heated tumour-mimicking target - not heated tumour-mimicking target " signal difference (dB) calculated at (**a**) 3 GHz and (**b**) 3.5 GHz with (solid lines) and without MTS (dashed lines). An overall improvement of the signal backscattered by variations in the tumour's dielectric properties is achieved in the presence of the MTS. This improvement (up to 30 dB) can be observed for several receivers' locations and might contribute to differentiate between "heated" and "not heated" cancerous tissue.

6.2 Feasibility Study of Enhancing Liver's Ablation Monitoring through Metamaterial Technology

In this section, the design of the MTA monitoring system developed by CNR-IREA and Sapienza University of Rome is described. Then, a feasibility study of enhancing the efficacy of this system through MTS technology is presented. In particular, a MTS film is proposed as a hardware advancement towards the realisation of a more accurate MWT system for temperature monitoring during MTA.

6.2.1 Microwave Thermal Ablation for Liver Cancer

Liver cancer is the fifth most common malignancy in men and the ninth most common cancer in women worldwide [138]. As a result of the peak of infection with hepatitis B and C viruses in the 1950s to 1980s, the incidence of primary liver cancer (PLC) is now increasing and will likely increase for decades in several developed countries [139]. Clinical studies have shown that PLC can be surgically treated only if detected at a presymptomatic stage [140]. However, only 5% to 15% of patients are early diagnosed and eligible for surgical removal [141]. Other treatment options for more advanced stages include trans-arterial chemoembolization (TACE) and chemotherapy with oral dosing of sorafenib, which is the most accepted treatment for late-stage cases. However, fewer than one-third of patients benefit from this treatment, as patients may have toxicity issues and develop drug resistance after a few months of treatment [141].

MTA is a recent promising cancer treatment able to destroy liver cancerous cells with a minimally invasive approach. During this treatment, a microwave antenna is placed directly into the tumour area with imaging guidance. Then, EM microwaves are emitted in the tissue to produce heat and induce cellular death via coagulation and necrosis [142]. During MTA, temperature monitoring of the ablation region is needed to avoid damaging healthy cells. For this purpose, several imaging modalities have been used, such as computed tomography (CT) and MRI. Currently, MRI is the most used technique for real time temperature monitoring, as it provides high-resolution temperature distributions and it is more suitable than CT for long time exposures [143].

An emerging imaging method which might be used for thermal ablation monitoring is MWT. The basic principle of this technique is to record the field backscattered during the ablation treatment thorough an array of antennas positioned externally to the patient's body. The variations of the recorded data between different time instants are then processed through an inverse scattering algorithm and an image of the

changes occurring in the EM properties of the heated area is produced [144]. MWT is a valid alternative to the current imaging modalities as it is a non-ionising low-cost technology which could be made compact and portable and thus compatible with MTA devices. For this reason, numerous research groups have put efforts in the development of new MWI devices for real-time monitoring during thermal ablation in different anatomical regions such as liver [145–147], breast [148], and brain [149].

6.2.2 Design of a Microwave Imaging System to Monitor Thermal Ablation of Liver Tumours

In this section, the design of the MWI system for thermal ablation monitoring developed by CNR-IREA and Sapienza University of Rome is presented. This system comprises compact antipodal Vivaldi antennas (AVAs) operating in the 500 MHz to 5 GHz frequency range. The proposed antennas are immersed in a liquid matching medium with a permittivity value close to 23, chosen such that the largest possible portion of the EM power enters the abdomen and provide an adequate backscattered signal after interacting with the liver.

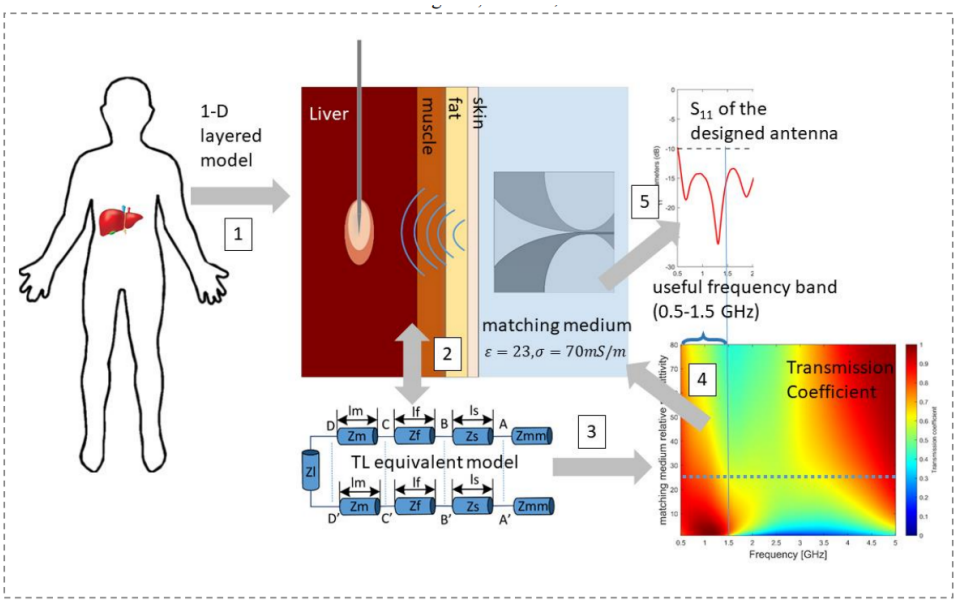

FIGURE 6.10: Design guidelines of the MTA monitoring system reported in [146]. First, the operating frequency and matching medium are identified by using transmission line equivalence to improve the match between the probing field and the human abdomen. Then, an antipodal Vivaldi antenna is designed and optimized to operate in the identified conditions. *Credit: CNR-IREA (Institute for the Electromagnetic Sensing of the Environment and National Research Council of Italy, Naples, Italy) and Sapienza University of Rome (Rome, Italy).*

Antipodal Vivaldi Antenna

The AVA developed by CNR-IREA and Sapienza University of Rome is shown in Figure 6.11a. As this antenna was initially designed to operate in air, the connector's pin was covered with an epoxy resin of permittivity equal to 4 and dimensions of 4.76 mm × 5.75 mm × 2.77 mm in order to overcome mismatching issues [146]. The SMA connector of the antenna is shown in Figure 6.11b.

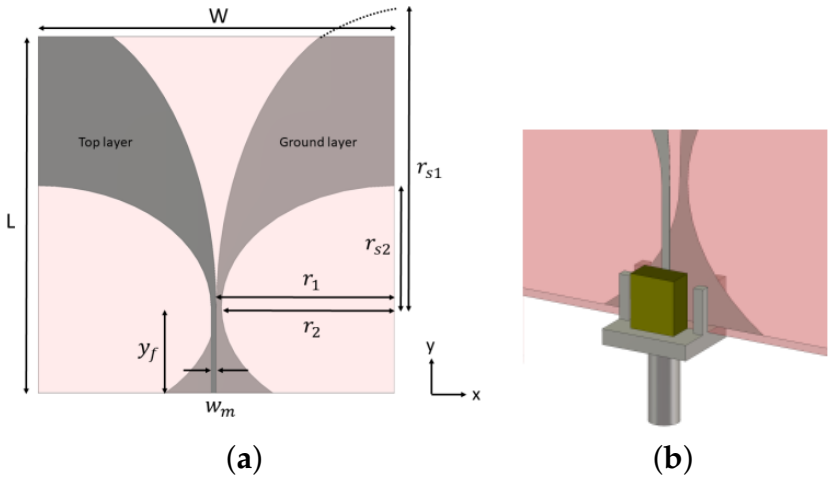

FIGURE 6.11: (**a**) Antipodal Vivaldi antenna. W=60 mm, L=60 mm, w_m=0.9 mm, y_f=14.5 mm, r_1=30 mm, r_2=29.1 mm, r_{s1}=50.1 mm, r_{s2}=20.37 mm and (**b**) SMA connector whose pin is covered with epoxy resin on the back side of the antenna [146]. *Credit: CNR-IREA (Institute for the Electromagnetic Sensing of the Environment and National Research Council of Italy, Naples, Italy) and Sapienza University of Rome (Rome, Italy).*

The reflection coefficient of the antenna tested on an abdomen phantom consisting of a stack of tissue slabs is shown in Figure 6.12b. The phantom block includes layers of skin (thickness$_s$ = 2.3), fat (thickness$_f$ = 12.2 mm) and muscle (thickness$_m$ = 20.2 mm). The last layer represents the liver (thickness$_l$ = 80 mm) and contains a target mimicking the ablated area (ϵ = 26.67 and σ = 1.26 S/m). Dimensions and position of the ablated liver are reported in Figure 6.12a. For this simulation, the dielectric properties of the tissues were taken from [106] and fixed at central frequency 2.5 GHz.

6.2.3 Metasurface Design

Split Ring Resonator

The purpose of this study is enhancing the impedance-matching of the AVA shown in Figure 6.11 at low frequencies, when loaded with biological tissue. A similar study was conducted in [150], where a MM slab based on a SRR array was designed to improve the focusing and penetration depth in human biological tissue. To this end, a

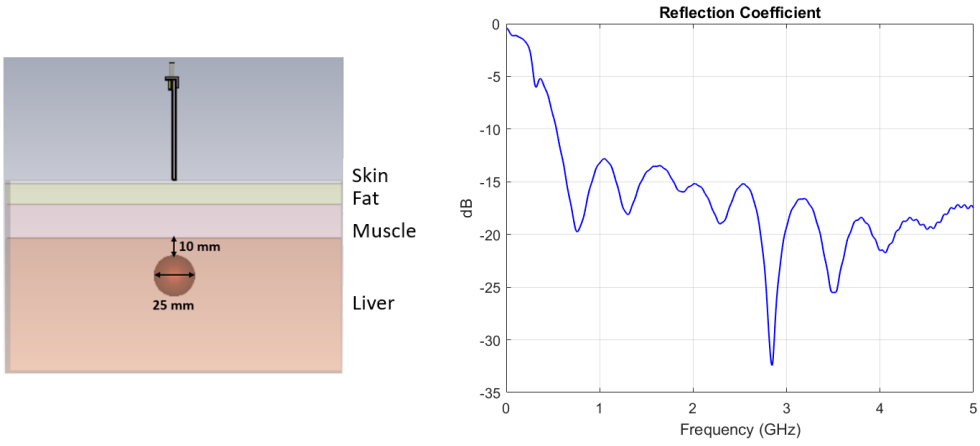

(**a**) (**b**)

FIGURE 6.12: (**a**) Abdomen phantom with target mimicking the ablated liver tissue. The phantom includes a first thin layer of skin, then fat (in yellow) and muscle (pink). The last layer (in orange) represents the liver. (**b**) Reflection coefficient of the AVA in front of the abdomen phantom containing an ablated area.

SRR was designed and the SRR's dimensions were tailored in order to set its resonant frequency at 500 MHz, which is a frequency where the S_{11} of the AVA does not fall below -10dB. The resonator was designed using "SRR Calculator Software" tool [151]. First, the thickness (0.1 mm) and the permittivity ($\epsilon = 10$) of the substrate were chosen. Then, the optimal design parameters for the metal structure were calculated. Setting the substrate's thickness and permittivity as constants during the optimization, allow us to fix the third dimension of the metafilm, without taking into account any variation of the substrate's thickness due to changes in permittivity. Figure 6.13 shows the SRR's design and its equivalent LC circuit with resonant frequency $f_0 = 500$ MHz.

Full Metasurface Structure and 1-Port System

After designing the resonator element, a MTS structure made of three SRRs was tested on the abdomen phantom using CST. This structure was centred on the skin slab, as shown in Figure 6.14a. To assess the MTS's impact on the AVA's near-field characteristics, the reflection coefficient of the antenna was calculated with and without MTS. The results suggest that the AVA's performance is greatly enhanced at lower frequencies. In particular, a deep resonance (-34 dB) at 500 MHz is shown in the presence of the MTS.

Furthermore, the E-field distribution shown in Figure 6.15 indicates that the MTS has a focusing effect, allowing better field's penetration through the phantom's layers and increasing the E-field intensity in the target's region. The impact of the MTS on the

AVA's near-field radiation properties might be attributed to the unit cell's behaviour in correspondence of its resonant frequency.

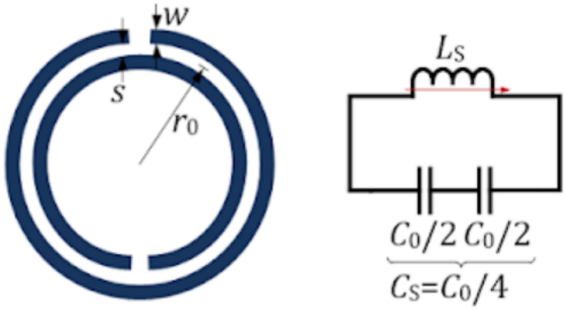

(**a**) (**b**)

FIGURE 6.13: (**a**) Split-Ring Resonator (SRR). w=1 mm, s=1 mm, r_0=23.4 mm. (**b**) Equivalent LC circuit. $C_0 = 2\pi r_0 C_{pul}$ is the total capacitance between the two rings, where C_{pul} is the per-unit-length capacitance of a CPS line. The resulting series capacitance C_S of the equivalent circuit is given by two capacitors of $C_0/2$ in series, that is C_S=$C_0/4$. The series inductance can be approximated by that of a single ring of width w and r_o (average radius). The resonant frequency of the SRR is given by: $f_0 = 1/2\pi\sqrt{LsCs}$.

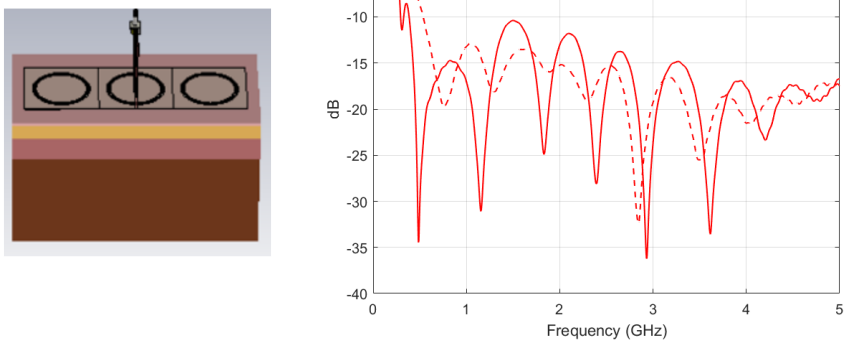

(**a**) (**b**)

FIGURE 6.14: (**a**) Full MTS structure placed on abdomen phantom and (**b**) reflection coefficient of the AVA with and without MTS. The phantom does not include the ablated area.

6.2.4 Multiple-Port System

In order to investigate whether the proposed MTS could enhance the "weak" signal backscattered by an ablated area, preliminary simulations of a multiple-port system

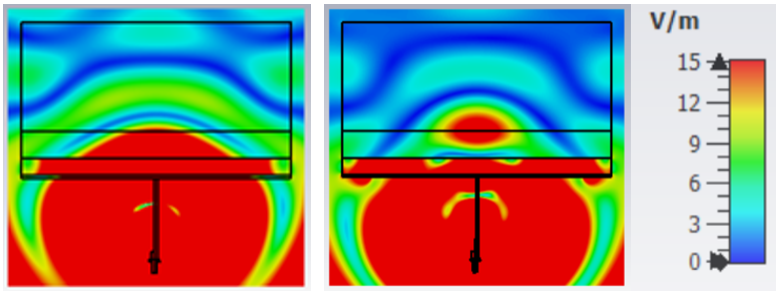

FIGURE 6.15: E-Field plotted on a transverse section of the phantom without MTS (left) and with MTS (right).

were carried on. This system is shown in Figure 6.16a and includes 5 AVAs placed at a distance of 23 mm, as reported in [147]. The EM wave propagation was studied for an abdomen phantom including a target mimicking the ablated area ("with target" scenario) and for a phantom without inclusions ("no target" scenario). The S-Parameters for reflection and transmission were calculated over the 0.5-2.5 GHz frequency range, with and without MTS. Then, the signal difference "with target - no target" (in dB) was calculated at five equally spaced frequencies in the 0.5-2.5 GHz frequency range and plotted as function of the receivers' location. The plots in Figure 6.16 show the

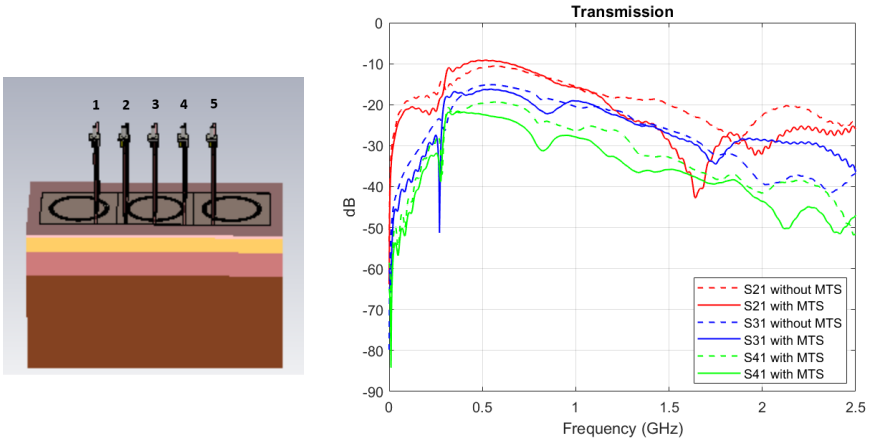

(**a**) (**b**)

FIGURE 6.16: (**a**) 5-Port setup and reflection coefficient for the antennas measured in the "no target" configuration. (**b**) S_{21}, S_{31} and S_{41} parameters calculated with and without MTS for the setup shown in (a). The transmission parameters are reduced due to the presence of the SRRs. This indicates that the coupling effects between two neighbouring antennas decrease when the antennas resonate in front of the MTS structure.

transmission parameters between antenna 1 and antennas 2, 3 and 4, calculated with and without MTS. These plots suggest that the coupling effects between two neighbouring antennas decrease when the antennas resonate in front of the MTS structure. This is probably due to the SRRs. When the antenna radiation frequency is within the

range for which the permeability is negative (SRR's resonant frequency), the component of the EM field parallel to the SRRs plane is evanescent and sideward radiation is "forbidden". Thus, the main lobe of the antenna radiation pattern is improved, while the side lobes are attenuated. For the same reason, we have a focusing effect [150].

The S-parameters for reflection shown in Figure 6.17b indicate that the MTS has an impact on the resonance of the antennas. The reflection coefficients of most of the antennas are reduced at lower frequencies with respect to the "no MTS" case scenario. Furthermore, the graphs in Figure 6.18 and Figure 6.19 show that the differential signal "with target - no target" (in dB) is overall enhanced when the antennas radiate in front of the MTS. This suggests that the MTS is capable of enhancing "weak" signals which may be useful for our application.

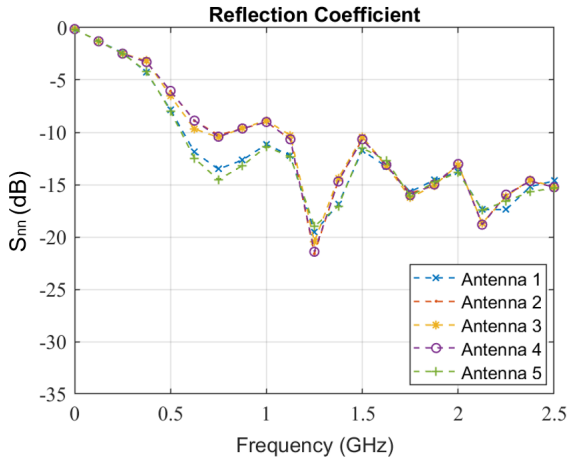

(**a**)

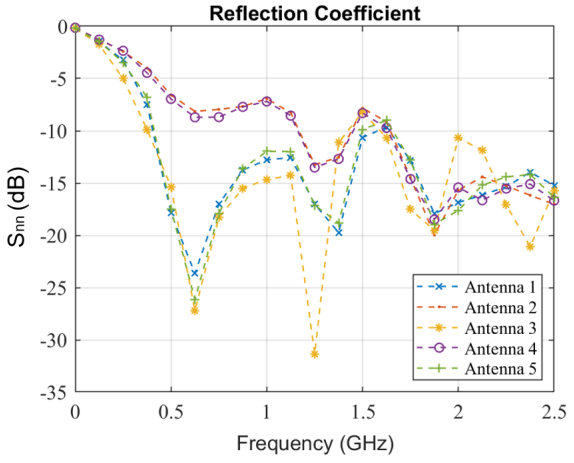

(**b**)

FIGURE 6.17: Reflection coefficient for all the antennas of the setup shown in Figure 6.16a, calculated (**a**) without MTS and (**b**) with MTS. The reflection coefficients for antennas 1, 3 and 5 are significantly reduced at lower frequencies (0.5-0.7 GHz frequency range). Antenna 2 and antenna 4 do not show the same behaviour, as they are differently located with respect to the MTS film.

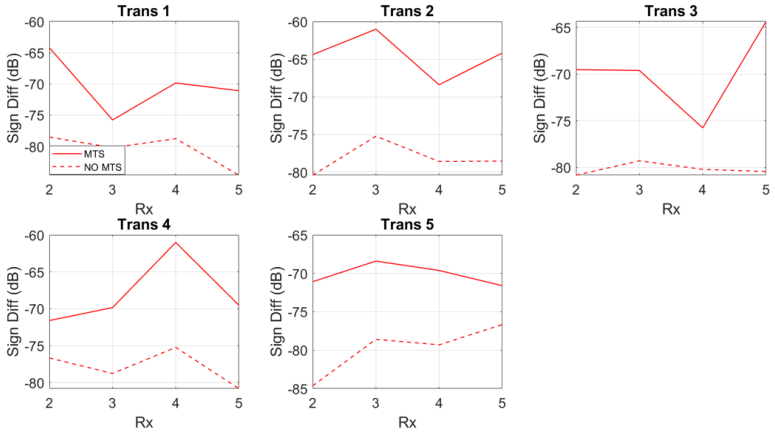

(**a**)

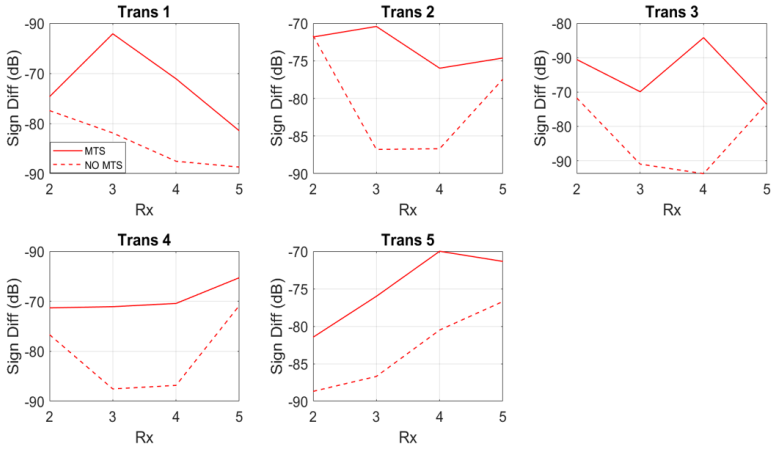

(**b**)

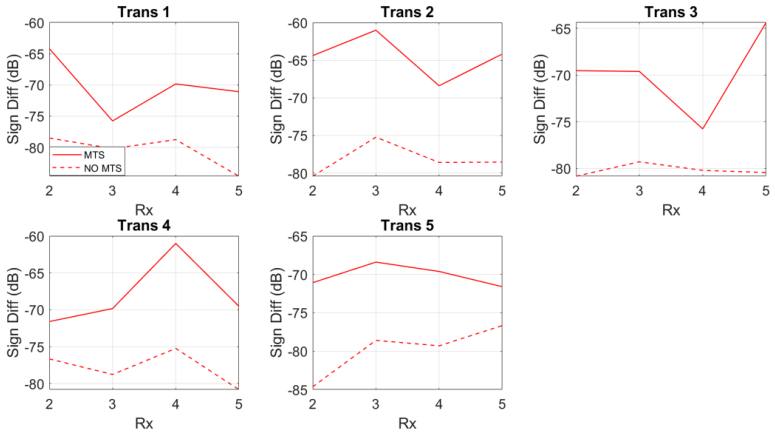

(**c**)

FIGURE 6.18: Signal difference "with target - no target" (dB) with (solid lines) and without (dashed lines) MTS, plotted as function of the receivers' location, calculated at (**a**) 0.5 GHz, (**b**) 1 GHz and (**c**) 1.5 GHz. The differential signal "with target - no target" (dB) is overall enhanced (up to 15 dB for transmitter 3 at 1.5 GHz) when the antennas radiate in front of the MTS. This enhancement is consistent for all the receivers' positions and suggests that the MTS enables the detection of "weak" signals backscattered by the target.

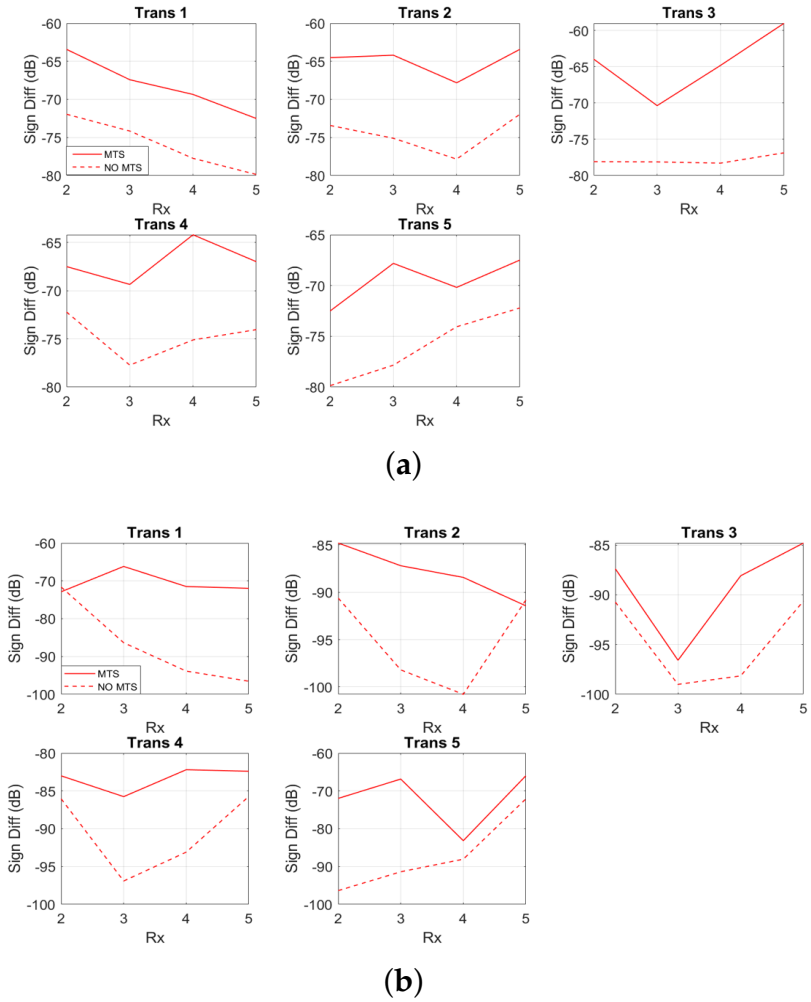

FIGURE 6.19: Signal difference "with target - no target" (dB) with (solid lines) and without (dashed lines) MTS, plotted as function of the receivers' location, calculated at (**a**) 2 GHz and (**b**) 2.5 GHz. The differential signal "with target - no target" (dB) is overall enhanced (up to 12 dB for transmitter 2 at 2.5 GHz) when the antennas radiate in front of the MTS. This enhancement is consistent for all the receivers' positions and suggests that the MTS enables the detection of "weak" signals backscattered by the target.

6.3 Conclusions

In conclusion, the results presented in this chapter suggest that MTS technology might benefit cancer treatment-related therapeutical applications. More specifically, Section 6.1 investigated the feasibility of developing an impedance-matching MTS to enhance UWB hyperthermia monitoring. The results shown in this section demonstrate that the proposed MTS film improves the signals scattered from a "not heated" tumour-mimicking target, which may help in enabling tumour's detection. Moreover, the MTS

enhances the "weak" signals due to the difference in the tumour's dielectric properties. This might contribute to detecting temperature changes in the tumour area and differentiating between "heated" and "not heated" cancerous tissue. Therefore, MTS technology might be an advantageous component in the development of functional UWB hyperthermia monitoring devices.

The main goal of the study presented in Section 6.2 was to improve the near-field performance of the AVA for thermal ablation monitoring developed by CNR-IREA and Sapienza University of Rome. To this end, a MTS structure capable of reducing the reflection coefficient of the antenna at low frequencies and focusing the E-field inside an abdomen phantom model was designed. Then, a multiple-port system was studied. The simulation results show that the signal backscattered by a target mimicking an ablated area is overall increased in the presence of the MTS. This indicates that the MTS is capable of enhancing "weak" signals which may be useful for ablation monitoring. Therefore, the results presented in the second section of this chapter suggest that the proposed MTS might improve small-size antennas' near-field characteristic and thus, be a powerful element towards the development of compact and ergonomic imaging systems.

Chapter 7

Summary and Future Work

This chapter summarizes the results presented in this thesis and proposes future directions to develop the research further.

7.1 Summary of the Results

This thesis has presented hardware advances towards the development of innovative microwave imaging (MWI) prototypes. In particular, the feasibility of enhancing brain stroke detection using metasurface (MTS) technology has been extensively investigated through theory, full-wave simulations and experiments. Furthermore, several numerical studies have been carried out to investigate the impact of employing MTSs on different hardware. In this context, new MTS films have been proposed for a wide range of clinical applications, including cerebrovascular imaging (CVA), ultra-wideband (UWB) hyperthermia monitoring, breast cancer detection and microwave thermal ablation (MTA).

Chapter 1 has presented the subject of study, the clinical motivation for the proposed research and a literature review relevant to MWI for brain stroke detection and the use of metamaterials (MMs) and MTSs for imaging applications. The final section of this chapter includes the contribution of this work to the field of research and a list of relevant publications.

Chapter 2 has reviewed the theory on which this thesis is based. First, a more detailed review on MMs and MM modelling has been proposed. Then, basic concepts on MWI and radar and tomographic imaging algorithms have been introduced.

Chapter 3 has shown the MTS design modelled to be integrated into the custom-made brain imaging prototype developed by King's College London. This design has been tested through full-wave simulations and experiments using several setups and antenna types. First, a series of simulation studies were performed to analyse the MTS unit cell's performance when immersed in a 90% glycerol-water mixture and in contact with the skin. Then, two full MTS structures based on the proposed unit cell were studied:

(a) A 15×18 unit cell MTS was incorporated in an experimental two-port setup. This first design improved transmission through a simplified planar head model and enhanced the signal scattered from a cylindrical blood target introduced in the system.

(b) A 5×6 unit cell MTS was tested on two different monopole antennas.

(i) The simulation and experimental investigation conducted for the triangular patch antenna has demonstrated that the MTS permits a considerable performance enhancement in the image reconstruction process. In particular, an improvement in the detection and localization of a h-stroke mimicking target placed in the brain phantom volume has been obtained using microwave tomography (MWT) and radar-based algorithms.

(ii) The simulation and experimental studies carried out for the spear patch antenna have shown similar results. The signal backscattered from a blood-mimicking target inside the brain volume increases significantly when the MTS is employed. This improvement translates into higher-quality reconstruction images of both h-stroke and i-stroke targets, using radar and tomographic algorithms.

Chapter 4 has investigated the feasibility of developing a compact and ergonomic microwave brain imaging scanner using a new MTS-enhanced printed square monopole antenna (PSMA) array operating in air. The simulation results presented in this chapter indicate that it is feasible to detect a blood-mimicking target placed inside the brain volume of a simple head model without using a bulky immersion liquid.

Chapter 5 has presented further microwave applications of MTS technology for medical devices. The first clinical application is related to CVA imaging (Politecnico di Torino). As in Chapter 4, a new array based on monopoles operating in contact with a MTS superstrate loading was proposed in order to avoid the use of a thick block of matching medium. The second application is related to UWB hyperthermia monitoring (Technische Universität Ilmenau). The results presented in Section 5.2.5 suggest that integrating MTS layers in an hyperthermia monitoring setup might contribute to detecting temperature changes in the tumour area and differentiating between “heated” and “not heated” cancerous tissue. Then, a MTS-enhanced antenna for breast cancer detection has been proposed. In particular, lines of double square split-ring resonators (DS-SRRs) have been added on the substrate of MITOS’s Vivaldi antenna to reduce the antenna’s reflection coefficient and improve transmission through a breast phantom. Lastly, the near-field performance of the antipodal Vivaldi (AVA) for thermal ablation monitoring developed by CNR-IREA and Sapienza

University of Rome was improved by modelling a MTS structure capable of reducing the reflection coefficient of the antenna at low frequencies and focusing the E-field inside an abdomen phantom model. Both for the Vivaldi antenna and the AVA, simulation results for multi-port systems have shown that the signal backscattered by a target mimicking the area of interest (breast tumour and ablated area, respectively) is overall increased in the presence of the proposed resonators. This indicates that SRRs are capable of enhancing "weak" signals which may be useful both for early cancer detection and therapeutical monitoring.

In conclusion, the results presented throughout all the thesis suggest that the proposed MTS films might improve small-size antennas' near-field characteristic and hence, be a powerful element towards the development of portable, compact and ergonomic imaging systems. Thus, MTSs can greatly benefit MWI, providing a significant hardware advance towards the realisation of new systems with the desired clinical accuracy.

7.2 Future Work

The most immediate continuation of this work would be conducting additional experimental studies using more complex setups. Regarding the antenna arrays immersed in the coupling liquid, it would be relevant to validate the MTS design using the 3D version of the radar and tomographic algorithms, by employing a 24-antenna array distributed in two or three rows around the head phantom. Another possible development of this research would be optimizing the MTS-enhanced PSMA presented in Chapter 4 and test it experimentally in order to assess the feasibility of applying the imaging algorithms without employing any matching medium. This will lead towards the development of portable and ergonomic prototypes to use in emergency situations.

In addition, before evaluating the MTS-enhanced systems with clinical data, it would be preferable to perform experimental tests with more realistic inhomogeneous brain phantoms. For instance, an option could be using digital volumetric brain phantoms with complex structure and different tissues (e.g. white and grey matter, bone, muscle and skin). Developing more complex phantoms will permit to mimic the head's internal structure more realistically and have a better understanding of the applicability extent of the radar and tomographic algorithms for brain stroke detection.

Another relevant point would be developing a hybrid image processing algorithm, combining the strongest features of both DBIM-TwIST and Huygens method. For instance, as for the HP-based algorithms best reconstructions are produced using a lower frequency range (0.6-0.8 GHz), while the DBIM-TwIST performs the best at

higher frequencies (1-1.5 GHz), a hybrid imaging algorithm could make use of both the lower and higher measured frequency bands for an optimum image reconstruction. A further challenge to address would be overcoming the "no target" reference scenario used for image subtraction, which is unavailable in real-life clinical scenarios. Furthermore, as the near-field antenna behaviour strongly determines how the received signals affect the effectiveness of the imaging algorithms [152], the implementation of the MTS in the algorithms must be evaluated.

Regarding the hardware, an interesting direction of research would be investigating the feasibility of developing tunable MTSs to actively varying the performance of the MWI antennas. Tunable dielectric MTSs are MTSs whose properties can be changed by external influence (e.g. by control voltage, temperature, magnetic field, pressure, or strain). For example, in the medical field, it has been already demonstrated how tunable hybrid MTSs can locally enhance the magnetic field of an external RF coil being precisely tuned to the Larmor frequency of a clinical MRI scanner. The Larmor frequency refers to the rate of precession of the magnetic moment of the proton around the external magnetic field. This frequency is important because it is the frequency at which the hydrogen nucleus will absorb energy. The absorption of that energy will cause the proton to alter its alignment. Thus, by varying the magnetic field across the body with a magnetic field gradient, the corresponding variation of the Larmor frequency can be used to encode the position. In [153], tunability is achieved by changing properties of the MTS's dielectric parts to enhance the local image quality at this specific frequency. In the microwave regime, voltage-driven elements, such as diodes, varactors and transistors, have been widely used to design active meta-atoms to achieve dynamically tunable EM responses, thanks to their miniaturized sizes (compatible with passive metallic resonators). Since each meta-atom can be independently controlled by the tunable element embedded, one can assemble these meta-atoms to form an inhomogeneous MTS with phase and amplitude profiles accurately determined by the voltages applied on different meta-atoms, thus offering the meta-device desired dynamical wave-manipulation functionalities [154]. In the field of MWI for monitoring applications, it would be interesting to study how to actively tune the MTS's response in order to vary the operational frequency of the MWI antennas. This could be useful to achieve optimal image reconstructions at different frequencies.

Appendix A

S-Parameters for Microwave Networks Characterization

A.1 Scattering Parameters

This appendix introduces the concept of S-Parameters (or scattering parameters), which are used to characterise microwave networks. These parameters relate the voltage waves incident on the ports of a microwave network to those reflected from the ports. They can be obtained using network analysis techniques or measured with a VNA. Considering the n-port network shown in Figure A.1, where V_n^+ is the voltage of the incident wave on port n and V_n^- is the voltage of the reflected wave from the port n, the relation between the incident and reflected voltage waves can be expressed as:

$$\begin{bmatrix} V_1^- \\ V_2^- \\ ... \\ V_n^- \end{bmatrix} = \begin{bmatrix} S_{11} & S_{12} & ... & S_{1n} \\ S_{21} & S_{22} & ... & S_{2n} \\ ... & ... & S_{33} & ... \\ S_{n1} & S_{n2} & ... & S_{nn} \end{bmatrix} \begin{bmatrix} V_1^+ \\ V_2^+ \\ ... \\ V_n^+ \end{bmatrix} \tag{A.1}$$

or $V^- = [S]V^+$, in compact form. The scattering matrix $[S]$ contains all the S-Parameters and provides a complete description of the network. A specific element of $[S]$ can be determined as:

$$S_{ij} = \frac{V_i^-}{V_j^+} \tag{A.2}$$

calculated for $V_k^+ = 0$, with k≠j.

In words, S_{ij} is found by driving port j with an incident wave of voltage V_j^+ and measuring the reflected wave amplitude V_i^-, which comes out of port i. The incident waves on all the ports except the jth port are set to zero (all the ports are terminated in matched loads to avoid reflections). Thus, S_{ii} is the reflection coefficient seen looking into port i when all the other ports are terminated in matched loads, and S_{ij} is

the transmission coefficient from port j to port i when all the ports are terminated in matched loads [155].

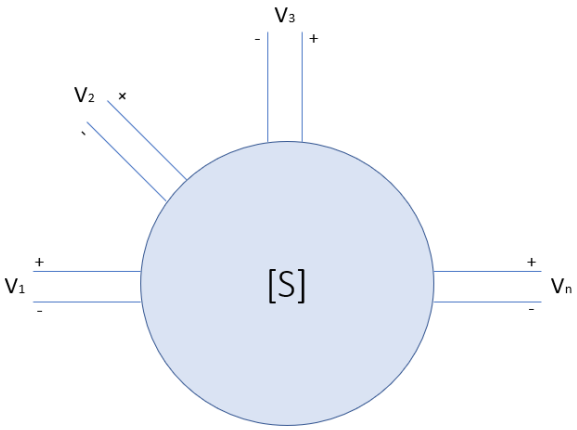

FIGURE A.1: Example of n-port network which could be described using S-Parameters.

A.2 ABCD matrix

As discussed above, S-parameters can be used to characterise a microwave network with an arbitrary number of ports, However, many microwave networks can be broken down to a cascade of two-port networks. In these cases, the use of an ABCD matrix reduces the mathematical complexity and facilitates the analysis of the networks.

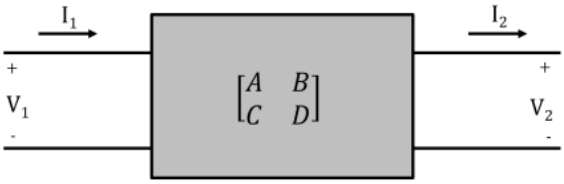

FIGURE A.2: Two-port network described by an ABCD matrix, where V are the voltages and I the currents at each port.

The ABCD matrix is a 2×2 transmission matrix defined as:

$$\begin{bmatrix} V_1 \\ V_2 \end{bmatrix} = \begin{bmatrix} A & B \\ C & D \end{bmatrix} \begin{bmatrix} I_1 \\ I_2 \end{bmatrix} \tag{A.3}$$

where V are the voltages and I are the currents as show in Figure A.2. The multiplication of the different ABCD matrixes of each network element determines the ABCD matrix of the two-port network [155].

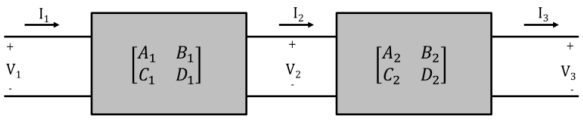

FIGURE A.3: Two-port elements in cascade.

$$\begin{bmatrix} A & B \\ C & D \end{bmatrix} = \begin{bmatrix} A_1 & B_1 \\ C_1 & D_1 \end{bmatrix} \begin{bmatrix} A_2 & B_2 \\ C_2 & D_2 \end{bmatrix} \tag{A.4}$$

A.3 S-Parameters to ABCD Parameters Conversion

The S-parameters for a two-port network are related with the ABCD parameters by the following conversion equations:

$$\begin{aligned} S_{11} &= \frac{A + \frac{B}{Z_0} - CZ_0 - D}{A + \frac{B}{Z_0} + CZ_0 + D} \qquad S_{21} = \frac{2}{A + \frac{B}{Z_0} + CZ_0 + D} \\ S_{12} &= \frac{2(AD - BC)}{A + \frac{B}{Z_0} + CZ_0 + D} \qquad S_{22} = \frac{-A + \frac{B}{Z_0} - CZ_0 + D}{A + \frac{B}{Z_0} + CZ_0 + D} \end{aligned} \tag{A.5}$$

$$\begin{aligned} A &= \frac{(1 + S_{11})(1 - S_{22}) + S_{12}S_{21}}{2S_{21}} \qquad C = \frac{(1 - S_{11})(1 - S_{22}) - S_{12}S_{21}}{2S_{21}Z_0} \\ B &= \frac{(1 + S_{11})(1 + S_{22})S_{12}S_{21}}{2S_{21}} Z_0 \qquad D = \frac{(1 - S_{11})(1 + S_{22}) + S_{12}S_{21}}{2S_{21}} \end{aligned} \tag{A.6}$$

where Z_0 is the the characteristic impedance [155].

Appendix B

Fundamental Parameters of Antennas

This appendix presents some of the parameters necessary to describe the performance of an antenna. These basic concepts are reported in [156]. The parameters' definitions (in quotation marks) are from *IEEE Standard Definitions of Terms for Antennas* (IEEE Std 145-1983).

B.1 Radiation Pattern

The radiation pattern of an antenna is defined as "a mathematical function or a graphical representation of the radiation properties of the antenna as a function of space coordinates". The radiation property of most concern is the 2D or 3D-spatial distribution of radiated energy as a function of the observer's position along a path or surface of constant radius. A convenient set of coordinates is shown in Figure B.1.

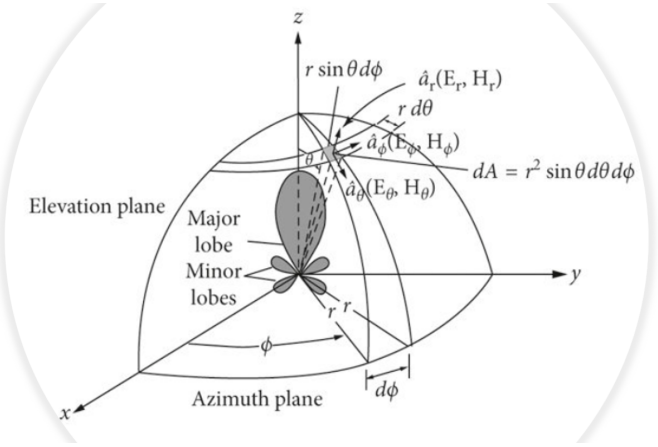

FIGURE B.1: Coordinate system for antenna analysis.

For the most practical applications, a few plots of the pattern as a function of θ for some particular values of ϕ, plus a few plots as a function of ϕ for some particular values of θ, give most of the needed information.

B.1.1 Field Regions

The space surrounding an antenna is usually subdivided into three regions:

- Reactive near-field
- Radiating near-field (Fresnel)
- Far-field (Fraunhofer)

The *reactive near-field region* is defined as "that portion of the near-field region immediately surrounding the antenna wherein the reactive field predominates". The *radiating near-field region* is "that region of the field of an antenna between the reactive near-field and the far-field region, wherein radiation fields predominate and wherein the angular field distribution is dependent upon the distance from the antenna". Finally, the *far-field region* is defined as "that region of the field of an antenna where the angular field distribution is essentially independent of the distance from the antenna".

B.2 Radiation Intensity

The radiation intensity in a given direction is defined as "the power radiated from an antenna per unit solid angle". In mathematical form it is expressed as:

$$U = r^2 W_{rad} \tag{B.1}$$

where U is the radiation intensity (W/solid angle) and W_{rad} is the radiation density (W/m^2).

B.3 Directivity

The directivity of an antenna is defined as "the ratio of the radiation intensity in a given direction from the antenna to the radiation intensity averaged over all directions. The average radiation intensity is equal to the total power radiated by the antenna divided by 4π. If the direction is not specified, the direction of maximum radiation intensity is implied". In mathematical form, it can be written as:

$$D = \frac{U}{U_0} = \frac{4\pi U}{P_{rad}} \tag{B.2}$$

B.4 Gain

The gain of an antenna is closely related to its directivity but it is a measure that takes into account also the efficiency of the antenna. The *absolute gain* of an antenna (in a given direction) is defined as "the ratio of intensity, in a given direction, to the radiation intensity that would be obtained if the power accepted by the antenna were radiated isotropically. The radiation intensity corresponding to the isotropically radiated power is equal to the power accepted (input) by the antenna divided by 4π".

$$\text{gain} = 4\pi \frac{U(\theta, \phi)}{P_{in}} \tag{B.3}$$

The *relative gain* is "the ratio of the power gain in a given direction to the power gain of a reference antenna in its referenced direction". In most cases, the reference antenna is a lossless isotropic source. When the direction is not stated, the power gain is usually taken in the direction of maximum radiation.

B.5 Antenna Efficiency

The total antenna efficiency e_0 is used to take into account losses at the input terminals and within the structure of the antenna. Such losses may be conduction or dielectric losses or due to reflections (because of the mismatch between the transmission line and the antenna). The overall efficiency can be written as:

$$e_0 = e_r e_c e_d \tag{B.4}$$

where e_r is the reflection (mismatch) efficiency, e_c is the conduction efficiency and e_d is the dielectric efficiency.

The conduction and dielectric losses of an antenna are very difficult to compute and in most cases they are measured. However, they are difficult to separate and they are usually lumped together to form the e_{cd} efficiency. The resistance R_L is used to represent the conduction-dielectric losses. The conduction-dielectric efficiency e_{cd} is defined as the ratio of the power delivered to the radiation resistance R_r to the power delivered to R_r and R_L. Thus, the radiation efficiency can be written as:

$$e_{cd} = \frac{R_r}{R_L + R_r} \tag{B.5}$$

Appendix C

Material Characterization

This appendix introduces the concepts of permittivity and permeability and provides insight into the Debye model, which can be used to represent the dispersive properties of tissues.

C.1 Permittivity and Permeability

Permittivity and permeability are two measures used in electromagnetism. Permittivity measures the ability of a material to store energy when an external electric field is applied. Permeability is a measure of the ability of a material to support the formation of a magnetic field. The permittivity of a homogeneous isotropic material is equal to the ratio of the electric displacement field to the electric field (E). It can be expressed as $\epsilon = \frac{D}{E}$, where D is the electric displacement field. Usually, the permittivity of a material is expressed as a relative permittivity, which is a dimensionless quantity. Relative permittivity, also known as the dielectric constant, is the ratio of the absolute permittivity of a material to the vacuum permittivity ($\epsilon_0 = 8.85 \times 10^{-12} Fm^{-1}$). This relationship can be expressed as $\epsilon_r = \frac{\epsilon}{\epsilon_0}$.

ϵ is a complex variable. The real part (ϵ') represents the quantity of energy that can be stored by the material when exposed to an external electric field, while the imaginary part (ϵ'') is a measure of the losses of the material. The ratio between the imaginary part and the real part of permittivity (loss tangent) is typically used to represent the relative losses of the material.

$$\epsilon = \epsilon' - j\epsilon'' \tag{C.1}$$

$$\tan\delta = \frac{\epsilon'}{\epsilon''} \tag{C.2}$$

The permeability of a material is usually denoted by the symbol μ and is equal to the ratio of the magnetic flux density to the magnetic field strength. It can be expressed as $\mu = \frac{B}{H}$. The permeability of free space, also known as the permeability constant,

vacuum permeability or magnetic constant of free space, is usually denoted by the symbol μ_0 and its value is $4\pi 10^{-7} Hm^{-1}$. The ratio of the permeability of a given medium to the permeability of free space is known as relative permeability: $\mu_r = \frac{\mu}{\mu_0}$. Similar to the permittivity, the permeability is a complex variable. The real part (μ') is related to the energy storage and the imaginary part (μ'') is a representation of the power dissipation.

$$\mu_r = \mu' - j\mu'' \tag{C.3}$$

For the natural occurring materials, including body tissues, the relative permeability has a value close to 1.

C.2 Debye Model

One of the most common models used to describe the dielectric behaviour of biological materials or aqueous solutions is the Debye relaxation model. This model was introduced by and named after the physicist Peter Debye (1913). It describes the dielectric relaxation response of an ideal, non-interacting population of dipoles to an alternating external electric field. This is usually expressed in the complex permittivity ϵ of a medium as a function of the field's angular frequency ω:

$$\epsilon(\omega) = \epsilon_\infty + \frac{\epsilon_s - \epsilon_\infty}{1 + j\omega\tau} \tag{C.4}$$

where ϵ_∞ is the permittivity at $\omega \gg 1$ (permittivity at the high frequency limit), ϵ_s is the permittivity at $\omega \ll 1$ (static, low frequency permittivity) and τ is the relaxation time of the medium. The relaxation time is the time required by the molecular dipoles of the medium to align with the dielectric field for the system to return to the equilibrium state. Separating Equation 2.6 into the real part (ϵ') and the imaginary part (ϵ'') of the complex dielectric permittivity yields:

$$\epsilon' = \epsilon_\infty + \frac{\epsilon_s - \epsilon_\infty}{1 + \omega^2\tau^2} \tag{C.5}$$

$$\epsilon'' = \epsilon_\infty + \frac{(\epsilon_s - \epsilon_\infty)\omega\tau}{1 + \omega^2\tau^2} \tag{C.6}$$

The dielectric loss is represented by the loss tangent:

$$\tan\delta = \frac{\epsilon''}{\epsilon'} = \frac{(\epsilon_s - \epsilon_\infty)\omega\tau}{\epsilon_s + \epsilon_\infty\omega^2\tau^2} \tag{C.7}$$

Bibliography

[1] Transparency Market Research. *Mobile Imaging Services Market*. URL: https://www.transparencymarketresearch.com/mobile-imaging-services.html (visited on 10/03/2021).

[2] Valery L. Feigin et al. "Worldwide stroke incidence and early case fatality reported in 56 population-based studies: a systematic review". In: *Lancet Neurol.* 8.4 (2009), pp. 355–369.

[3] Christopher Lewandowski and William Barsan. "Treatment of acute ischemic stroke". In: *Ann. Emerg. Med.* 37.2 (2001), pp. 202–216.

[4] Edward C. Jauch et al. "Guidelines for the early management of patients with acute ischemic stroke: A guideline for healthcare professionals from the American Heart Association/American Stroke Association". In: *Stroke* 44.3 (2013), pp. 870–947.

[5] Mayo Clinic. *Stroke*. URL: https://www.mayoclinic.org/diseases-conditions/stroke/diagnosis-treatment/drc-20350119 (visited on 12/03/2021).

[6] Stroke Association. *Haemorrhagic stroke*. URL: https://www.stroke.org.uk/what-is-stroke/types-of-stroke/haemorrhagic-stroke (visited on 12/03/2021).

[7] Richard F. Keep, Ya Hua, and Guohua Xi. "Intracerebral haemorrhage: Mechanisms of injury and therapeutic targets". In: *Lancet Neurol.* 11.8 (2012), pp. 720–731.

[8] Beadaa J. Mohammed et al. "Microwave system for head imaging". In: *IEEE Trans. Instrum. Meas.* 63.1 (2014), pp. 117–123.

[9] Yu-Hsuan Shao et al. "Exposure to Tomographic Scans and Cancer Risks". In: *JNCI Cancer Spectr.* 4.1 (2020), pp. 1–7.

[10] Josef Vymazal et al. "Comparison of CT and MR imaging in ischemic stroke". In: *Insights Imaging* 3.6 (2012), pp. 619–627.

[11] Rosa Scapaticci et al. "Design and Numerical Characterization of a Low-Complexity Microwave Device for Brain Stroke Monitoring". In: *IEEE Trans. Antennas Propag.* 66.12 (2018), pp. 7328–7338.

[12] Natalia K. Nikolova. "Microwave Imaging for Breast Cancer". In: *IEEE Microw. Mag.* 12 (2011), pp. 78–94.

[13] Rohit Chandra et al. "On the Opportunities and Challenges in Microwave Medical Sensing and Imaging". In: *IEEE Trans. Biomed. Eng.* 62.7 (2015), pp. 1667–1682.

[14] Panagiotis Kosmas and Lorenzo Crocco. "Introduction to special issue on Electromagnetic technologies for medical diagnostics: Fundamental issues, clinical applications and perspectives." In: *Diagnostics, 9(1)* (2019).

[15] Serguei V. Semenov et al. "Microwave-Tomographic Imaging of the High Dielectric-Contrast Objects Using Different Image-Reconstruction Approaches". In: *IEEE Trans. Microw. Theory Techn.* 53.7 (2005), pp. 2284–2294.

[16] David W. Winters et al. "Three-Dimensional Microwave Breast Imaging : Dispersive Dielectric Properties Estimation Using Patient-Specific Basis Functions". In: *IEEE Trans. Med. Imag.* 28.7 (2009), pp. 969–981.

[17] Wei Guo, Syed Ahsan, and Panagiotis Kosmas. "Portable Microwave Imaging Head Scanners for Intracranial Haemorrhagic Detection". In: *Asia-Pacific Microwave Conference (APMC), Singapore, 10-13 December 2019*.

[18] Mikael Persson et al. "Microwave-based stroke diagnosis making global prehospital thrombolytic treatment possible". In: *IEEE Trans. Biomed. Eng.* 61.11 (2014), pp. 2806–2817.

[19] Markus Hopfer et al. "Electromagnetic tomography for detection, differentiation, and monitoring of brain stroke: A virtual data and human head phantom study". In: *IEEE Trans. Antennas Propag.* 59.5 (2017), pp. 86–97.

[20] Ahmed T. Mobashsher and Amin M. Abbosh. "On-site Rapid Diagnosis of Intracranial Hematoma using Portable Multi-slice Microwave Imaging System". In: *Sci. Rep.* 6 (2016), pp. 1–17.

[21] Serguei V. Semenov and Douglas R. Corfield. "Microwave Tomography for Brain Imaging : Feasibility Assessment for Stroke Detection". In: *Int. J. Antennas Propag.* 2008 (2008), pp. 1–8.

[22] Rosa Scapaticci et al. "A Feasibility Study on Microwave Imaging for Brain Stroke Monitoring". In: *Prog. Electromagn. Res.* (2014), pp. 305–324.

[23] Serguei V. Semenov et al. "Electromagnetic tomography for brain imaging: Initial assessment for stroke detection". In: *IEEE Biomedical Circuits and Systems Conference: Engineering for Healthy Minds and Able Bodies (BioCAS), Atlanta, Georgia, U.S.A., 22-24 October 2015*.

[24] Paul M. Meaney et al. "Surface Wave Multipath Signals in Near-Field Microwave Imaging". In: *Int. J. Biomed. Imag.* 2012 (2012), pp. 1–11.

[25] Helena Cano-Garcia, Panagiotis Kosmas, and Efthymios Kallos. "Enhancing electromagnetic transmission through biological tissues at millimeter waves using subwavelength metamaterial antireflection coatings". In: *9th International Congress on Advanced Electromagnetic Materials in Microwaves and Optics, METAMATERIALS 2015, Oxford, UK, 7-12 September 2015*.

[26] Helena Cano-Garcia, Panagiotis Kosmas, and Efthymios Kallos. "Demonstration of enhancing the transmission of 60 GHz waves through biological tissue using thin metamaterial antireflection coatings". In: *10th International Congress on Advanced Electromagnetic Materials in Microwaves and Optics, METAMATERIALS 2016, Heraklion, Crete, Greece, 19-22 September 2016*.

[27] Hou Tong Chen et al. "Antireflection coating using metamaterials and identification of its mechanism". In: *Phys. Rev. Lett.* 105.7 (2010), pp. 1–4.

[28] Hou Tong Chen et al. "A Numerical Investigation of Metamaterial Antireflection Coatings". In: *Terahertz Sci. Technol.* 3.2 (2010), pp. 66–73.

[29] Margarita Puentes Vargas. *Planar Metamaterial Based Microwave Sensor Arrays for Biomedical Analysis and Treatment*. Springer International Publishing, Switzerland, 2014. Chap. 2, pp. 7–31.

[30] Hee J. Lee and Jong G. Yook. "Biosensing using split-ring resonators at microwave regime". In: *Appl. Phys. Lett.* 92.25 (2008), pp. 10–13.

[31] Luigi La Spada, Filiberto Bilotti, and Lucio Vegni. "Metamaterial biosensor for cancer detection". In: *IEEE Sensors Proceedings, Limerik, Ireland, 28-31 October 2011*.

[32] Sathish Sugumaran et al. "Biosensors and Bioelectronics Nanostructured materials with plasmonic nanobiosensors for early cancer detection: a past and future prospect". In: *Biosens. Bioelectron.* 100 (2018), pp. 361–373.

[33] Koray Aydin et al. "Investigation of magnetic resonances for different split-ring resonator parameters and designs". In: *New J. Phys.* 7 (2005), pp. 1–15.

[34] Manuel J. Freire, Ricardo Marques, and Lukas Jelinek. "Experimental demonstration of a μ=-1 metamaterial lens for magnetic resonance imaging". In: *Appl. Phys. Lett* 93.23 (2008), pp. 1–4.

[35] Marcos A. Lopez et al. "Nonlinear split-ring metamaterial slabs for magnetic resonance imaging". In: *Appl. Phys. Lett.* 98.13 (2011), pp. 1–3.

[36] Alexey P. Slobozhanyuk et al. “Enhancement of Magnetic Resonance Imaging with Metasurfaces”. In: *Adv. Mater.* 28.9 (2016), pp. 1832–1838.

[37] Dmitry Isakov et al. “A Split Ring Resonator Dielectric Probe for Near-Field Dielectric Imaging”. In: *Sci. Rep.* 7.1 (2017), pp. 1–9.

[38] Saptarshi Mukherjee et al. “Design of a Split-Ring Resonator Sensor for Near-Field Microwave Imaging”. In: *IEEE Sensors J.* 18.17 (2018), pp. 7066–7076.

[39] Saptarshi Mukherjee et al. “Enhancement of microwave imaging using a metamaterial lens”. In: *IEEE Sensors J.* 20 (2019), pp. 1–11.

[40] Okan Yurduseven et al. “Printed Aperiodic Cavity for Computational and Microwave Imaging”. In: *IEEE Microw. Wireless Compon. Lett.* 26.5 (2016), pp. 367–369.

[41] Jonah N. Gollub et al. “Large Metasurface Aperture for Millimeter Wave Computational Imaging at the Human-Scale”. In: *Sci. Rep.* 7 (2017), pp. 1–10.

[42] Joseph N. Mait, Gary W. Euliss, and Ravindra A. Athale. “Computational imaging”. In: *Adv. Opt. Photonics* 10.2 (2018), p. 409.

[43] Okan Yurduseven and David R. Smith. “A reconfigurable millimeter-wave spotlight metasurface aperture integrated with a frequency-diverse microwave imager for security screening”. In: *Proc. SPIE* 10634 (2018), pp. 1–9.

[44] Matteo Pastorino. *Microwave Imaging*. John Wiley & Sons, Inc., Hoboken, New Jersey, U.S.A., 2010, pp. 264–277.

[45] Quanlong Yang et al. “Efficient flat metasurface lens for terahertz imaging”. In: *Opt. Express* 22.21 (2014), p. 25931.

[46] Gang Wang, Jieran Fang, and Xiaoting Dong. “Resolution of near-field microwave target detection and imaging by using flat LHM lens”. In: *IEEE Trans. Antennas Propag. Propag.* 55 (2007), pp. 3534–3541.

[47] Maria Koutsoupidou and Irene S. Karanasiou. “Matching Medium based on Split-Ring Resonators for Microwave Breast Imaging”. In: *IEEE International Symposium on Biomedical Imaging (ISBI), New York, U.S.A., 16-19 April 2015*.

[48] Hou Tong Chen, Antoinette J. Taylor, and Nanfang Yu. “A review of metasurfaces: Physics and applications”. In: *Rep. Prog. Phys.* 79.7 (2016).

[49] Syed S. Bukhari, J. Vardaxoglou, and William Whittow. “A metasurfaces review: Definitions and applications”. In: *Appl. Sci. (Switzerland)* 9.13 (2019).

[50] Christopher L. Holloway et al. “An overview of the theory and applications of metasurfaces: The two-dimensional equivalents of metamaterials”. In: *IEEE Trans. Antennas Propag.* 54.2 (2012), pp. 10–35.

[51] Victor G. Veselago. "The electrodynamics of substance with simultaneously negative values of ϵ and μ". In: *Sov. Phys. Usp* 10.4 (1968).

[52] John B. Pendry et al. "Magnetism from Conductors and Enhanced Nonlinear Phenomena". In: *IEEE Trans. Microw. Theory Techn.* 47.11 (1999), pp. 2075–2084.

[53] Richard A. Shelby, David R. Smith, and Sheldon Schultz. "Experimental verification of a negative index of refraction". In: *Science* 292.5514 (2001), pp. 77–79.

[54] Ruopeng Liu et al. "Negative index material composed of electric and magnetic resonators". In: *Appl. Phys. Lett.* 90.26 (2007), pp. 1–4.

[55] David R. Smith et al. "Gradient Index Metamaterials". In: *Phys. Rev.* 71.3 (2005).

[56] John B. Pendry, David Schurig, and David R. Smith. "Controlling electromagnetic fields". In: *Science* 312.5781 (2006), pp. 1780–1782.

[57] David Schurig, David. R. Smith, and Jonah B. Pendry. "Metamaterial Electromagnetic Cloak at Microwave Frequencies". In: *Science* 314.5801 (2006), pp. 977–980.

[58] Laszlo Solymar and Ekaterina Shamonina. *Waves in Metamaterials*. OXFORD University Press, Oxford, UK, 2009, pp. 58–59.

[59] Nader Engheta and Richard W. Ziolkowski. *Metamaterials*. Wiley-Interscience, John Wiley & Sons, Inc., Hoboken, New Jersey, U.S.A., 2006, pp. 13–18.

[60] Richard W. Ziolkowski and Allison D. Kipple. "Application of Double Negative Materials to Increase the Power Radiated by Electrically Small Antennas". In: *IEEE Trans. Antennas Propag.* 51.10 I (2003), pp. 2626–2640.

[61] Richard W. Ziolkowski and Allison D. Kipple. "Reciprocity between the effects of resonant scattering and enhanced radiated power by electrically small antennas in the presence of nested metamaterial shells". In: *Phys. Rev. E Stat. Nonlin. Soft Matter Phys.* 72.3 (2005).

[62] Richard W. Ziolkowski and Aycan Erentok. "Metamaterial-based efficient electrically small antennas". In: *IEEE Trans. Antennas Propag.* 54.7 (2006), pp. 2113–2130.

[63] Jing Jing Yang, Ming Huang, and Jin Hui Peng. "Directive emission obtained by Mu and Epsilon-Near-Zero metamaterials". In: *Radioengineering* 18.2 (2009), pp. 124–128.

[64] Hang Zhou et al. "A high-directive patch antenna based on all-dielectric near-zero-index metamaterial superstrates". In: *J. Electromagn. Waves Appl.* 24.10 (2010), pp. 1387–1396.

[65] Richard W. Ziolkowski. "Metamaterial-based antennas: Research and developments". In: *IEICE Trans. Electron.* E89-C.9 (2006), pp. 1267–1275.

[66] Jason C. Soric et al. "Omnidirectional metamaterial antennas based on ϵ-near-zero channel matching". In: *IEEE Trans. Antennas Propag.* 61.1 (2013), pp. 33–44.

[67] Helena Cano-garcia. "Non-invasive Glucose Sensing in Millimitre Waves Using Impedance Matching Metamaterials". PhD thesis. King's College London, London, UK, 2018.

[68] Filippo Capolino. *Theory and phenomena of metamaterials*. CRC Press, Taylor and Francis Group, LLC, Boca Raton, Florida, U.S.A., 2009, (31)23–(31)27.

[69] Olli Luukkonen et al. "Simple and Accurate Analytical Model of Planar Grids and High-Impedance Surfaces Comprising Metal Strips or Patches". In: *IEEE Trans. Antennas Propag.* 56 (2008), pp. 1624–1632.

[70] Lev D. Landau and Evgeny M. Lifshitz. *Electrodynamics of Continuos Media*. Pergamon Press, Oxford, UK, 1984.

[71] Tie Jun Cui, David R. Smith, and Ruopeng Liu. *Metamaterials: Theory, Design and Applications*. Springer, New York, U.S.A., 2009, p. 14.

[72] Ruopeng Liu et al. "Broadband Ground-Plane Cloak". In: *Science* (2009), pp. 366–370.

[73] Ruopeng Liu et al. "Description and explanation of electromagnetic behaviors in artificial metamaterials based on effective medium theory". In: *Phys. Rev. E Stat. Nonlin. Soft Matter Phys.* 76.2 (2007), pp. 1–8.

[74] *CST Microwave Studio 2016 - Workflow & Solver Overview*. CST - Computer Simulation Technology AG, Darmstadt, Germany, 2016.

[75] Simone Genovesi et al. "Metasurface matching layers for enhanced electric field penetration into the human body". In: *IEEE Access* 8 (2020), pp. 197745–197756.

[76] Fengyuan Yang et al. "Near-Reflectionless Wireless Transmission into the Body with Cascaded Metasurfaces". In: *IEEE Trans. Antennas Propag.* 70.9 (2022).

[77] Daniela Gasperini et al. "Analytical Approach for Metasurface Matching Layer Design for Electric Field Maximization in Biological Tissues". In: *16th International Congress on Advanced Electromagnetic Materials in Microwaves and Optics – Metamaterials 2022 Siena, Italy, 11-16 September 2022*.

[78] Bruce Fischl and Andres M Dale. "Measuring the thickness of the human cerebral cortex from magnetic resonance images." In: *PNAS* 97.20 (2000), pp. 11050–11055.

[79] Karan Chopra et al. "A comprehensive examination of topographic thickness of skin in the human face". In: *Aesthetic Surg. J.* 35.8 (2015), pp. 1007–1013.

[80] Elizabeth M. Lillie et al. "Estimation of skull table thickness with clinical CT and validation with microCT". In: *J. Anat.* 226.1 (2015), pp. 73–80.

[81] Niels Lynnerup, Jacob G Astrup, and Birgitte Sejrsen. "Thickness of the human cranial diploe in relation to age, sex and general body build". In: *Head Face Med.* 1.1 (2005), pp. 1–13.

[82] Constantine A. Balanis. *Advanced Engineering Electromagnetics*. John Wileys and Sons, 1989.

[83] Ahmed T. Mobashsher and Amin M. Abbosh. "Developments of tomography and radar-based head imaging systems". In: *International Symposium on Antennas and Propagation (ISAP), Hobart, Tasmania, Australia, 9-12 November 2015*.

[84] W. C. Chew. *Waves and Fields in Inhomogenous Media*. Wiley-IEEE Press, 1995.

[85] Pan Lu. "Development of Novel Algorithms for Microwave Medical Imaging Applications". PhD thesis. King's College London, London, UK, 2023.

[86] Jacob D. Shea et al. "Three-dimensional microwave imaging of realistic numerical breast phantoms via a multiple-frequency inverse scattering technique". In: *Med. Phys.* 37.8 (2010), pp. 4210–4226.

[87] José M Bioucas-dias et al. "A New TwIST : Two-Step Iterative Shrinkage / Thresholding Algorithms for Image Restoration". In: *IEEE Trans. Image Process.* 16.12 (2007), pp. 2992–3004.

[88] Zhenzhuang Miao and Panagiotis Kosmas. "Microwave breast imaging based on an optimized two-step iterative shrinkage/thresholding method". In: *9th European Conference on Antennas and Propagation (EuCAP), Lisbon, Portugal, 13-17 April 2015*.

[89] Zhenzhuang Miao and Panagiotis Kosmas. "Multiple-Frequency DBIM-TwIST Algorithm for Microwave Breast Imaging". In: *IEEE Trans. Antennas Propag.* 65.5 (2017), pp. 2507–2516.

[90] Maciej Klemm et al. "Radar-based breast cancer detection using a hemispherical antenna array - Experimental results". In: *IEEE Trans. Antennas Propag.* 57.6 (2009), pp. 1692–1704.

[91] Xu Li et al. "Microwave imaging via space-time beamforming: Experimental investigation of tumor detection in multilayer breast phantoms". In: *IEEE Trans. Microw. Theory Techn.* 52.8 II (2004), pp. 1856–1865.

[92] Hooi Been Lim et al. "Confocal microwave imaging for breast cancer detection: Delay-multiply-and-sum image reconstruction algorithm". In: *IEEE Trans. Biom. Eng.* 55.6 (2008), pp. 1697–1704.

[93] Panagiotis Kosmas and Carey M. Rappaport. "Time reversal with the FDTD method for microwave breast cancer detection". In: *IEEE Trans. Microw. Theory Techn.* 53.7 (2005), pp. 2317–2323.

[94] Peter Enders. "Huygens' Principle as Universal Model of Propagation". In: *Lat. Am. J. Phys. Educ.* 3.1 (2009), pp. 19–32.

[95] Navid Ghavami. "Ultra-Wideband Imaging Techniques for Medical Applications". PhD thesis. Oxford University, Oxford, UK, 2012.

[96] Navid Ghavami et al. "UWB microwave imaging of objects with canonical shape". In: *IEEE Trans. Antennas Propag.* 60.1 (2012), pp. 231–239.

[97] Navid Ghavami et al. "Non-iterative beamforming based on Huygens principle for multistatic ultrawide band radar: Application to breast imaging". In: *IET Microw. Antennas Propag.* 9.12 (2015), pp. 1233–1240.

[98] Navid Ghavami et al. "Huygens principle based UWB microwave imaging method for skin cancer detection". In: *International Symposium on Communication Systems, Networks and Digital Signal Processing (CSNDSP), Prague, Czech Republic, 20-23 July 2016*.

[99] Gianluigi Tiberi et al. "Ultrawideband microwave imaging of cylindrical objects with inclusions". In: *IET Microw. Antennas Propag.* 5.12 (2011), pp. 1440–1446.

[100] Syed Ahsan et al. "Experimental comparison of two printed monopole antenna designs for microwave tomography". In: *Asia-Pacific Microwave Conference Proceedings (APMC), New Delhi, India, 10-13 December 2019*.

[101] Wei Guo et al. "Printed Monopole Antenna Designs for a Microwave Head Scanner". In: *18th Mediterranean Microwave Symposium (MMS), Istanbul, Turkey, 31 October-2 November 2018*, pp. 384–386.

[102] Syed Ahsan et al. "Multiple-Frequency Microwave Tomography System". In: *Sensors* 18 (2018), pp. 1–13.

[103] Mariya Lazebnik et al. "Tissue-mimicking phantom materials for narrowband and ultrawideband microwave applications". In: *Phys. Med. Biol.* 50.18 (2005), pp. 4245–4258.

[104] Syed Ahsan et al. "Advances towards the Development of a Brain Microwave Imaging Scanner". In: *13th European Conference on Antennas and Propagation (EuCAP), Krakow, Poland, 31 March-5 April 2019*.

[105] Eleonora Razzicchia et al. "Feasibility study of enhancing microwave brain imaging using metamaterials". In: *Sensors* 19.24 (2019), pp. 1–17.

[106] Daniele Andreuccetti. *An internet resource for the calculation of the dielectric properties of body tissues in the frequency range 10 Hz-100 GHz*. URL: http://niremf.ifac.cnr.it/tissprop/ (visited on 10/10/2018).

[107] Filippo Costa and Agostino Monorchio. "An Overview of Equivalent Circuit Modeling Techniques of Frequency Selective Surfaces and Metasurfaces". In: *Appl. Comoput. Electromagn. Soc. J.* 29 (2014), pp. 960–976.

[108] Syed Ahsan. "Design of a Microwave Tomography System for Medical Imaging Applications". PhD thesis. King's College London, London, UK.

[109] Colleen J. Fox et al. "Characterization of an Implicitly Resistively-Loaded Monopole Antenna in Lossy Liquid Media". In: *Int. J. Antennas Propag .* (2008), pp. 1–9.

[110] Olympia Karadima et al. "Experimental Validation of Microwave Tomography with the DBIM-TwIST Algorithm for Brain Stroke Detection and Classification". In: *Sensors* 20.3 (2020).

[111] Navid Ghavami, Ioannis Sotiriou, and Panagiotis Kosmas. "Preliminary experimental validation of radar imaging for stroke detection with phantoms". In: *2019 Photonics and Electromagnetics Research Symposium (PIERS), Rome, Italy, 17-20 June 2019*.

[112] Navid Ghavami et al. "The Use of Metasurfaces to Enhance Microwave Imaging: Experimental Validation for Tomographic and Radar-Based Algorithms". In: *IEEE Open J. Antennas Propag.* 3 (2022), pp. 89–100.

[113] Behnaz Sohani et al. "Developing artefact removal algorithms to process data from a microwave imaging device for haemorrhagic stroke detection". In: *Sensors* 20.19 (2020), pp. 1–15.

[114] Zhenzhuang Miao et al. "Application of the DBIM-TwIST Algorithm to Experimental Microwave Imaging Data". In: *11th European Conference on Antennas and Propagation (EUCAP), Paris, France, 19-24 March 2017*.

[115] Joao M. Felicio et al. "Antenna design and near-field characterization for medical microwave imaging applications". In: *IEEE Transactions on Antennas and Propagation* 67.7 (2019), pp. 4811–4824.

[116] David O. Rodriguez-Duarte et al. "Brick-Shaped Antenna Module for Microwave Brain Imaging Systems". In: *IEEE Antennas Wirel. Propag. Lett.* 19.12 (2020), pp. 2057–2061.

[117] Olympia Karadima, Eleonora Razzicchia, and Panagiotis Kosmas. "Image Improvement Through Metamaterial Technology for Brain Stroke Detection". In: *14th European Conference on Antennas and Propagation (EuCAP), Copenaghen, Denrmark, 15-20 March 2020*.

[118] Ibrahim Akduman, Mehmet Cayoren, and Hulya Sahinturk. "A New Multi-Static System for Microwave Breast Cancer Imaging: Preliminary Design". In: *Mediterrean Microwave Symposium (MMS), Hammamet, Tunisia, 31 October-2 Novemeber 2019*.

[119] Breast Cancer UK. *Breast Cancer Statistics - Facts & Figures*. URL: https://www.breastcanceruk.org.uk (visited on 04/02/2022).

[120] Cathy Coleman. "Early Detection and Screening for Breast Cancer". In: *Semin. Oncol. Nurs.* 33.2 (2017), pp. 141–155.

[121] Centers for Disease Control and Prevention. *Breast Cancer Screening Tests*. URL: https://www.cdc.gov/cancer/breast/basic{_}info/screening.htm (visited on 04/23/2022).

[122] American Cancer Society. *Limitations of Mammograms*. URL: https://www.cancer.org/cancer/breast-cancer/screening-tests-and-early-detection/mammograms/limitations-of-mammograms.html (visited on 04/23/2022).

[123] Sollip Kwon and Seungjun Lee. "Recent Advances in Microwave Imaging for Breast Cancer Detection". In: *Int. J. Biomed. Imaging* 2016 (2016).

[124] Paulo De Azevedo-Marques Mazzoncini et al. *Medical Image Analysis and Informatics: Computer-Aided Diagnosis and Therapy*. CRC Press, Taylor and Francis Group, LLC, Boca Raton, Florida, U.S.A., 2017, pp. 451–466.

[125] Gian Franco Baronzio and Dieter E. Hager. *Hyperthermia In Cancer Treatment: A Primer*. Landes Bioscience and Springer Science+Business Media, New York, U.S.A., 2006, p. 2.

[126] Alexandra Prokhorova, Sebastian Ley, and Marko Helbig. "Quantitative interpretation of uwb radar images for non-invasive tissue temperature estimation during hyperthermia". In: *Diagnostics* 11.5 (2021).

[127] National Cancer Institute. *What Is Cancer?* URL: https://www.cancer.gov/about-cancer/understanding/what-is-cancer (visited on 03/20/2022).

[128] Mayo Clininc. *Cancer Treatment*. URL: https://www.mayoclinic.org/tests-procedures/cancer-treatment/about/pac-20393344 (visited on 03/20/2022).

[129] Gianfranco Baronzio et al. "A Brief Overview of Hyperthermia in Cancer Treatment". In: *J. Integr. Oncol.* 03.01 (2014), pp. 1–10.

[130] Ondrej Fiser, Ilja Merunka, and Jan Vrba. "Waveguide applicator system for head and neck hyperthermia treatment". In: *J. Electr. Eng. Technol.* 11.6 (2016), pp. 1744–1753.

[131] Gerda M. Verduijn et al. "Deep hyperthermia with the HYPERcollar system combined with irradiation for advanced head and neck carcinoma–a feasibility study". In: *Int. J. Hyperth.* 34.7 (2018), pp. 994–1001.

[132] Gerben Schooneveldt et al. "Hyperthermia treatment planning including convective flow in cerebrospinal fluid for brain tumour hyperthermia treatment using a novel dedicated paediatric brain applicator". In: *Cancers* 11.8 (2019).

[133] Massimiliano Zanoli and Hana D. Trefná. "Iterative time-reversal for multi-frequency hyperthermia". In: *Phys. Med. Biol.* 66.4 (2021).

[134] Emiliano Schena et al. "Fiber optic sensors for temperature monitoring during thermal treatments: An overview". In: *Sensors* 16.7 (2016), pp. 1–20.

[135] Temple Health. *Hyperthermia*. URL: https://www.templehealth.org/services/radiation-oncology/hyperthermia (visited on 04/20/2022).

[136] Ondrej Fiser et al. "Microwave non-invasive temperature monitoring using UWB radar for cancer treatment by hyperthermia". In: *Prog. Electromagn. Res. M* 162 (2018), pp. 1–14.

[137] Sebastian Ley et al. "Ultra-wideband temperature dependent dielectric spectroscopy of porcine tissue and blood in the microwave frequency range". In: *Sensors* 19.7 (2019).

[138] World Cancer Research Fund International. *Liver cancer statistics*. URL: https://www.wcrf.org/cancer-trends/liver-cancer-statistics/ (visited on 03/03/2022).

[139] Xavier F. Bosch et al. "Primary liver cancer: Worldwide incidence and trends". In: *Gastroenterology* 127.5 SUPPL. 1 (2004), pp. 5–16.

[140] Binghui Yang et al. "Prospective study of early detection for primary liver cancer". In: *J. Cancer Res. Clin. Oncol.* 123.6 (1997), pp. 357–360.

[141] David Anwanwan et al. "Challenges in liver cancer and possible treatment approaches". In: *Biochim. Biophys. Acta Rev. Cancer* 1873.1 (2020), p. 188314.

[142] Caroline J. Simon, Damian E. Dupuy, and William W. Mayo-Smith. "Microwave ablation: Principles and applications". In: *Radiographics* 25.25 SUPPL. 1 (2005), pp. 69–83.

[143] Bruno Quesson, Jacco A. De Zwart, and Chrit T.W. Moonen. "Magnetic resonance temperature imaging for guidance of thermotherapy". In: *J. Magn. Reson. Imaging* 12.4 (2000), pp. 525–533.

[144] Rosa Scapaticci et al. "Monitoring Thermal Ablation via Microwave Tomography: An Ex Vivo Experimental Assessment". In: *Diagnostics* 8.4 (2018), p. 81.

[145] Rosa Scapaticci et al. "Exploiting Microwave Imaging Methods for Real-Time Monitoring of Thermal Ablation". In: *Int. J. Antennas Propag.* 2017 (2017).

[146] Mengchu Wang, Lorenzo Crocco, and Marta Cavagnaro. "On the Design of a Microwave Imaging System to Monitor Thermal Ablation of Liver Tumors". In: *IEEE J. Electromagn. RF Microw. Med. Biol.* 5.3 (2021), pp. 231–237.

[147] Mengchu Wang et al. "Towards a microwave imaging system for continuous monitoring of liver tumor ablation: Design and in silico validation of an experimental setup". In: *Diagnostics* 11.5 (2021).

[148] Kazuki Kanazawa et al. "Microwave Imaging Algorithm Based on Waveform Reconstruction for Microwave Ablation Treatment". In: *IEEE Trans. Antennas Propag.* 68.7 (2020), pp. 5613–5625.

[149] Guanbo Chen et al. "Real-Time Three-Dimensional Microwave Monitoring of Interstitial Thermal Therapy". In: *IEEE Trans. Biomed. Eng.* 65.3 (2018), pp. 528–538.

[150] Vincenza Portosi, Antonella Maria Loconsole, and Francesco Prudenzano. "A split ring resonator-based metamaterial for microwave impedance matching with biological tissue". In: *Appl. Sci.* 10.19 (2020), pp. 1–14.

[151] *Split Ring Resonator (SRR) Calculator*. URL: https://srrcalculator.blogspot.com/p/calculator.html (visited on 07/20/2021).

[152] Joao M. Felicio et al. "Antenna design and near-field characterization for medical microwave imaging applications". In: *IEEE Trans. Antennas Propag.* 67.7 (2019), pp. 4811–4824.

[153] Alena V. Shchelokova et al. "Locally Enhanced Image Quality with Tunable Hybrid Metasurfaces". In: *Phys. Rev. Appl.* 9.1 (2018).

[154] Qiong He, Shulin Sun, and Lei Zhou. "Tunable/Reconfigurable Metasurfaces: Physics and Applications". In: *Research* 2019 (2019), pp. 1–16.

[155] David M. Pozar. *Microwave Engineering*. John Wiley & Sons, Inc., New York, U.S.A., 1998, pp. 196–198.

[156] Constantine A. Balanis. *Antenna Theory: Analysis and Design*. Wiley-Interscience, John Wiley & Sons, Inc., Hoboken, New Jersey, U.S.A., 2005, pp. 28–78.